The role of heterochromatin markers in lytic human herpesvirus egress and maturation.

Laurel Kelnhofer-Millevolte

A dissertation

submitted in partial fulfillment of the

requirements for the degree of

Doctor of Philosophy

University of Washington

2025

Reading Committee:

Daphne C. Avgousti, Chair

Adam P. Geballe

Susan M. Parkhurst

Program Authorized to Offer Degree:

Molecular and Cellular Biology

©Copyright 2025

Laurel Kelnhofer-Millevolte

University of Washington

Abstract

The role of heterochromatin markers in lytic human herpesvirus egress and maturation

Laurel Kelnhofer-Millevolte

Chair of the Supervisory Committee:

Daphne C. Avgousti

Molecular and Cellular Biology (Medicine)

The human herpesviruses are large, double-stranded DNA viruses known for their persistent latent phase. Within the herpesvirus family there are 3 subfamilies; alphaherpesviruses, classified as such because of their more rapid replication and latency in neurons; betaherpesviruses, known for slow replication cycles and latency in myeloid cells; and gammaherpesviruses, oncogenic viruses with a more variable replication cycle and latency in lymphocytes. Many of these human herpesviruses cause human disease ranging from sores and mild “cold-like” symptoms to encephalitis, congenital defects, and cancers. All herpesviruses replicate in the host nucleus, assemble capsids then egress out of the nucleus, mature through acquisition of tegument proteins and secondary envelopment, and finally bud out of the host
cell.

The virus must contend with components of the host nucleus to replicate, including the host chromatin. Chromatin consists of DNA, RNA, and proteins that maintain the DNA structure. Host chromatin is organized into units called nucleosomes that consist of approximately 147bp of DNA wrapped around an octamer of histone proteins. The structural and transcriptional control of the chromatin is tightly

regulated and closely linked. Transcriptionally active, open chromatin is referred to as euchromatin, while tightly packed, transcriptionally repressed chromatin is referred to as heterochromatin. Chromatin state is controlled by incorporation of histone variants and post-translational modification of histone tails, also called histone marks. Trimethylation of histone 3 at the 9th and 27th lysine residue (H3K9me3 and H3K27me3 respectively) and histone variant macroH2A are common markers of heterochromatin.

Over the course of lytic herpesvirus infection, host chromatin undergoes extensive gross remodeling as chromatin is marginalized to the nuclear periphery to accommodate viral replication and later to provide structural support during nuclear egress. However, the specific role of heterochromatin in these lytic infections remain unknown. In this thesis, I will show that host heterochromatin markers have unique roles in lytic herpesvirus infection. To this end, I will first show the heterochromatin marker macroH2A1 supports the formation of heterochromatin channels required for the alphaherpesvirus, Herpes Simplex Virus-1 (HSV-1), to efficiently reach the nuclear membrane and egress. Next, I will show that histone post-translational modification , H3K27me3, directs capsid docking on the nuclear membrane and subsequent Us3 phosphorylation for efficient nuclear budding of HSV-1 virions. Finally, I will show that macroH2A1 plays a dramatically different role in HCMV lytic replication, by regulating expression of dormant host genes required for maturation, while H3K27me3 reduction had minimal effect on HCMV progeny production. This thesis work expands our understanding of chromatin control of cellular processes, especially during cellular stress, and the biology of lytic replication of two important human pathogens.

Table of Contents

List of Figures

Acknowledgements

I would like to acknowledge several people for their technical assistance throughout the work presented in this thesis. First, I would like to acknowledge Hannah Lewis for assistance with much of the work presented in chapter 2. I would like to acknowledge Mia Brinkley for assistance with the western blot images presented in chapter 2, and the harvesting of samples for RNA sequencing in chapter 4. I would like to acknowledge Lea Wilson and Daniel Nguyen for technical help, especially virus and cell line maintenance for the work performed in chapter 3 and 4. I would like to acknowledge Srinivas Ramachandran, at the University of Colorado, for assistance with data processing for CUT&Tag experiments presented in chapter 2 and RNA sequencing presented in chapter 4. I would like to acknowledge Katarzyna Kulej, at Memorial Sloan Kettering Cancer Center, and Matthew Weitzman, at the Children's Hospital of Philadelphia, for access to mass-spectrometry data used to guide experiments in chapter 3, especially the peptide pulldown presented in Figure 3.9. Thank you to the participants in the Fred Hutch Thursday morning Virus Group, for the extensive feedback throughout this work.

I would like to thank several members of the core faculties at the Fred Hutch Cancer Center for the advice and technical support that made much of this thesis work possible. Thanks to Alex Zevin and Alyssa Dawson for assistance in and technical support on RNA sequencing experiments. A huge thank you to Steve MacFarlane for the preparation of electron microscopy samples and the extensive patience teaching me to image the sections. Thanks to Caleigh Azumaya for technical assistance with TEM imaging as well. Thanks to Julien Dubrulle for assisting with the coding to quantify TEM images. A huge thank you to Lena Schroeder and Hoku West-Foyle for their boundless enthusiasm and countless consultations on imaging and image quantification.

This research was supported by the Electron Microscopy Shared Resource, RRID:SCR_022611. The EMSR, CISR, and Genomics core are supported in part by the Fred Hutch/University of Washington Cancer Consortium (P30 CA015704). This study was also

supported by start-up funds from the RNA Bioscience Initiative at the University of Colorado School of Medicine (S. Ramachandran), the Fred Hutch (D.C. Avgousti), National Institutes of Health funding to E.A. Arnold (AI083203), A.P. Geballe (AI145945), S. Ramachandran (GM133434), and D.C. Avgousti (GM133441), and the University of Washington Magnuson Scholarship to L.E. Kelnhofer-Millevolte.

Next, I would like to thank my committee for their extensive and invaluable expertise and contributions to this work. I would like to thank Leslie Goo for her support and energy as my original Graduate School Representative. I would like to thank Michael Lagunoff for stepping into my committee last minute, for his insight on the herpesvirus replication cycles, and for the networking support at the International Herpesvirus Workshops I attended. I would like to thank Stephen Tapscott for asking the tricky questions during my committee meetings and keeping me to the MSTP timeline. I would like extend a huge thank you to Susan Parkhurst for serving on my reading committee, stepping in as my Graduate School Representative, extensive feedback and support on the 3 published manuscripts that comprise the majority of this thesis, and several consults on presenting and quantifying my TEM images. Lastly, I would like to extend a huge thank you to Adam Geballe, despite telling me you would not be my co-mentor, your support has been truly career-saving, Thank you for serving on my reading committee, the endless supply of advice and reagents for my CMV project, acting as my role model as a joyous and fulfilled physician-scientist even as you transition to retirement, and for acting as my no longer reluctant in-person mentor throughout the unforeseen twist of my time in the Avgousti lab (including housing me for my final experiments of grad school).

I would next like to thank all the MSTP directors, Marshall Horwitz, Mary-Claire King, Stephen Tapscott, and Heather Cheng. It is truly amazing to be in program where the directors are so incredibly supportive and deeply care about each and everyone of their students an individual. Thank you for all the support and advice these last 6 years. Thank you to the MCB directors during

my time in the program Celeste Berg, Nina Salama, and Julian Simon. Lastly, thank you to the extensive network of administrative support at UW and the Fred Hutch. Denise Barnes, Maia Low, Alice Ven, Andrea Brocato, Mel Leavens, Carolina Chambers, Bao-Han Nguyen, Jasmine Gonzalez, James Adams, Luna Yu, Kacee French, and Sara Carlson. With extra shout-outs to Luna Yu, Maia Low, and Sara Carlson for keeping everything in grad school running as smoothly as possible.

On a more personal note, I would like to thank all the past and present members of the Avgousti Lab. Thanks to Kelsey Lynch, a fellow southeast Indiana lady, for all the technical support; but more importantly the enthusiasm for science and the energy you put into making the Avgousti Lab culture so appealing with spirit days and happy hours during the tough months of the COVID pandemic. Thank you to Melanie Dillon, whose glowing review of the lab was the reason I found Daphne as a potential mentor, for keeping the lab afloat my first year and for your role in the amazing lab culture. Thank you to Mia Brinkley, it was an honor to watch you grow as a scientist, thank you for everything you did to keep the lab running, but more importantly to help keep me sane during some of the roughest points in my grad school experience. I hope you find the same level of support in your grad school experience as well. Thank you to Edward Arnold, it was really amazing to experience all the ups and downs of grad school with you as a fellow student. Thank you to Julian Smith, not only for the technical assistance in finishing this project, but also for bringing a fresh batch of energy into the lab when we really needed it. Thank you to Robin Kaii, your friendship is one of best things to come out of grad school. Thank you to Allison Veishlow for being my “lab mom” and the support that comes with that title. Thank you to “my kids” Daniel Nguyen and Lea Wilson thank you for being my mentees, you are both incredibly talented, enthusiastic, motivated, and passionate. You both brought such amazing energy to my team, even if it did make me feel a million years old. I can’t wait to see what you both continue on to do. Finally, a huge thank you to Hannah Lewis. You truly built the entire foundation for this work. Thank

you so much for all the energy you put into mentoring me even as you worked to finish graduate school yourself.

Thank you to all the mentors I have had Xinyu Zhao and Yu Gao, for teaching me such a strong foundational base on most the molecular biology techniques out there. Thank you to Matthew Reynolds and Jason Weinfurter for giving me the space to try out being an independent scientist and the support getting into graduate school. Thank you to Alexis Kaushansky and Jesse Bloom for the incredible opportunities to rotate in your labs. Thank you to my clinical mentor Jon Ilgen for keeping me connected to medicine during graduate school and the work to prepare me to return to the clinic. And thank you to Daphne Avgousti, I am so fortunate that you were willing to take me on as a graduate student despite everything that was going on in your personal life. While the writing, presentation, and scientific mentorship helped me grow into the scientist I have become, it is the personal mentorship I value the most. I consider myself so incredibly blessed to have such an honest and kind mentor who I felt comfortable talking to from the beginning. Thank you for all the time you put into me and my career, from helping remind me the alphabet and working to delete “this” from my vocabulary, to helping me become a calmer and more considered person with Greek mythology and philosophy stories. Thank you for always having an ear and tissue box ready regardless of what was going on in your life. And thank you for showing me what it means to be a strong, confident woman in science.

Finally, I would like to thank some people who made me who I am as a person. Thank you to my family, especially my mom and dad, for the sacrifices you made to get me here. Thank you for the support in everything I have done, including the millions of essays you read. Thank you to my high school friends Natalie Pottschmidt and Courtney Unkrich for the unending support and laughter for well over a decade now. Thank you to my MSTP cohort for going through this crazy journey as my close friends. A special thanks to some of the women in the program; Alex Willcox, Rechel Geiger, Sophie Blackburn, Marina Han, Siegan McKellar, Naomi Yamamoto, and Courtney

Vishy. I am so blessed to be among some of the kindest, smartest, strongest ladies in the world. I would like to acknowledge my dogs, Gerty, Boo, and Matilda, for the source of joy they are in my life, and for being the most attentive audience and often the only ones listening.

And most importantly, I would like to thank my husband Gus Millevolte for literally everything. I am so lucky to have your support. I couldn't have done this without you. Thank you for being my best friend and my go-to person.

Chapter 1: Introduction

* This chapter is adapted and expanded from my review article "Controlling Much? Viral Control of Host Chromatin Dynamics. Annual Review of Virology. Sep;11(1):171-191; Kelnhofer-Millevolte LE, Arnold EA, Nguyen DH, Avgousti DC (2024)". This chapter is reproduced here as it is licensed under a Creative Commons Attribution 4.0 International License, allowing for unrestricted use provided the original source is cited. "We" is used throughout the publication. I wrote the sections on chromatin, Herpes simplex virus, cytomegalovirus, and conclusion of the original manuscript and collected immunofluorescence images in Figure 1.1. Edward Arnold originally drafted the adenovirus section, which I have edited and condensed to fit the scope desired for this thesis. He also collected the immunofluorescence images in Figure 1.2. Figure 1.3 was created in close collaboration with Daniel Nguyen. The work here was supervised and edited by Daphne Avgousti.

Abstract:

Viruses are exemplary molecular biologists and have been integral to scientific discovery for generations. It is therefore no surprise that nuclear replicating viruses have evolved to systematically take over host cell function through astoundingly specific nuclear and chromatin hijacking. In this chapter, we focus on nuclear replicating DNA viruses — herpesviruses and adenoviruses — as key examples of viral invasion in the nucleus. We concentrate on critical components of nuclear architecture, such as chromatin and the nucleolus, to illustrate the complexity of the virus-host battle for resources in the nucleus. We conclude with a discussion of the technological advances that have enabled the discoveries we describe and upcoming steps in this burgeoning field.

1.1 Chromatin organization in the nucleus.

Chromatin, which is a combination of DNA, RNA, and proteins, specifically refers to the state of host DNA prior to condensing during prophase into the more widely recognized chromosome. Host chromatin is organized into units called nucleosomes that consist of approximately 147bp of DNA wrapped around an octamer of histone proteins (1). Post-translational modifications on these histone

proteins, including methylation and acetylation, are integral to regulation of gene expression and have been extensively reviewed (2). Regions of chromatin that are transcriptionally active are broadly classified as euchromatin, while regions that are transcriptionally repressed are called heterochromatin (2, 3). Some regions of heterochromatin, such as telomeres and centromeres, are maintained in a permanently inactive state and referred to as constitutive heterochromatin (4). Conversely, other regions of heterochromatin, termed facultative heterochromatin, are dynamically expressed at different times and are associated with histone modifications such as trimethylation on the lysine 27 residue of histone H3 (H3K27me3), H3K9me3, and the histone variant macroH2A (5, 6). These histone modifications (or 'marks') are critical for defining the local conformation of chromatin, thereby dictating access to genes for expression or repression as needed by the cell. For example, once a cell has differentiated and expression of developmental genes is no longer needed, these genes must be repressed to support cell identity. Conversely, immune signaling genes are expressed in response to stimulus and must be poised for rapid induction to defend the cell when needed. The combination of histone marks on a gene locus can also have important outcomes on how that gene may be expressed, often referred to as a histone code or crosstalk language (7, 8). As chromatin marks come together and influence local and global compaction, the three-dimensional nuclear landscape takes shape.

The histone mark H3K27me3, is a marker of facultative chromatin. As such it is a dynamic mark associated with transcriptional repression (9). The H3K27me3 mark is deposited by the enhancer of Zeste 2 (EZH2) methyltransferase component (10) of the Polycomb Repressive Complex 2 (PRC2) (11) Additional components of the PRC2 complex include Embryonic Ectoderm Development (EED) and Suppressor of Zeste 12 (SUZ12) (12). In addition to transcriptional control, PCR2 deposition of H3K27me3 supports formation of large chromatin loops (13) Loss of H3K27me3 around the nuclear periphery is associated with abnormal nuclear morphology (14). EZH2 mutations and H3K27me3 dysregulation are associated with many cancers (15, 16).

MacroH2A is a histone variant that substitutes for the canonical H2A histone within the nucleosome that frequently colocalizes with H3K27me3. MacroH2A broadly refers to three forms: two splice variants macroH2A1.1 and macroH2A1.2 and a separate gene macroH2A2 (17, 18). MacroH2A1 was initially discovered on the inactivated X chromosome together with H3K27me3, suggesting it is primarily involved in transcriptional silencing (18, 19). Additionally, macroH2A1 was found to co-localize with other markers of heterochromatin such as H3K9me3(20). MacroH2A1 contains 3 protein domains: the histone fold region, which has a high degree of homology with H2A; a linker region; and a C-terminal macrodomain (21). The linker region is important for oligomerization of the protein, suggesting this region is responsible for heterochromatin formation in cells (22). The macrodomain of macroH2A1.1 binds NAD+ derivatives suggesting it acts as a metabolic sensor (23). Importantly, loss of macroH2A1 and macroH2A2 results in significantly less heterochromatin in the nuclear periphery of cells (24), suggesting that macroH2A-dependent heterochromatin is critical for nuclear integrity. It has also been suggested that this maintenance of nuclear architecture is a result of macroH2A1 interacting with lamin B1 (25). In fact, the dysregulation of macroH2A transcripts has been associated with multiple types of cancer (26–28). Therefore, macroH2A1-dependent structural support of the nucleus is important for cell health, and dysregulation of macroH2A1-dependent heterochromatin can lead to disease.

Advances in sequencing and chromatin capture technologies have brought the importance of global chromatin architecture to the forefront of molecular biology (Table 1). These techniques have aided the discovery of complex folding of the chromatin in a highly specific and well-regulated manner. Chromatin folding is often reported as “looping” (29, 30) and enables regions of DNA that are several kilobases away in primary sequence to interact in three dimensions. Uncovering this layer of complexity has revealed that enhancers, promoters, and other regulatory elements may have overlapping function (31). Further, studying 3D interactions within the genome showed that transcriptional activation may not occur as isolated events but rather in ‘hubs’ or frequently interacting regions (FIREs) that consolidate resources to specific physical locations for greater efficiency (32). Larger regions of interaction are

referred to as topologically associating domains (TADs) (33), spanning over 800 kilobases on average with around 2200 TADs per genome, and multiple combinations of histone marks per TAD (34). TADs are further organized into active A compartments or more silent B compartments, which in turn make up chromosome territories (35). In addition to compartmentalizing gene regulation, these larger areas also physically support the structure of the nucleus (36).

Viral infection requires host cell resources. The requirement of host resources necessitates control of the host genome and the host chromatin. As such, viral infection leads to disruption of normal chromatin function at many levels, from hijacking histone modifying enzymes to exploiting global changes in nuclear morphology. One key protein involved in the organization of chromatin that will be discussed in this chapter as it pertains to viral infection is the CCCTC-binding factor, CTCF. CTCF is a best known as a transcription factor but has multiple roles as a repressor and insulator and defines the boundaries between chromatin domains or TADs (37). The structural role of CTCF is largely due to its interaction with the cohesin protein complex (35), a ring complex that recognizes CTCF and helps stabilize loops and TADs (38). CTCF action brings enhancer regions into close physical proximity with promotors to drive transcription, though it can also insulate genes from enhancers to repress transcription. Because of this critical role in TAD maintenance and gene expression, many viruses exploit CTCF and chromatin looping to regulate their own gene expression.

1.2 Other components of nuclear integrity.

Surrounding the chromatin and supporting the nuclear membrane is a meshwork of proteins collectively called the lamina. The lamina is composed of two types of lamin: splice isoforms Lamin A or C, and Lamin B encoded by a separate gene. Lamin A/C with Lamin B supports the nuclear membrane and interacts with additional proteins such as Emerin, SUN1, and BAF (39). These components are part of the linker of nucleoskeleton and cytoskeleton (LINC) complex that anchors the chromatin to the nuclear envelope and reinforces the structure (40). When the nucleus undergoes mitosis, the lamina is phosphorylated and rearranged to facilitate division (41). Mutation of these key proteins can cause

disruption to the lamina structure and lead to diseases known as laminopathies (42). Enveloped nuclear replicating viruses like herpesviruses are too large to enter or exit through the nuclear pores. Thus, the nuclear lamina presents a barrier to nuclear virus infection. To overcome this block, viruses have evolved mechanisms to disrupt the lamina to facilitate infection, recently reviewed in depth (43).

Within the nucleus also resides the well-defined nucleolus where ribosomal RNA (rRNA) is transcribed and ribosomes are assembled. It is currently thought that the nucleolus exists as a phase-separated sub-compartment of the nucleus that houses RNA and proteins mainly associated with ribosomal biogenesis (44). Nucleolar morphology reflects cellular health as increased nucleolar volume is associated with cancers (45) whereas decreased nucleolar volume was observed in neurons with neurodegenerative disease (46). Studies focused on nucleolar function have defined nucleolar involvement in spindle formation, nuclear structure, cell cycle control and stress sensing (47–49), underscoring the importance of this compartment in nuclear integrity. As viral infection takes over the nucleus, the nucleolus becomes a critical player both in sequestering proteins and as a powerhouse for the assembly of viral progeny.

1.3 Herpes Simplex Virus reorganization of the nucleus.

The herpesvirus family consists of alpha-, beta-, and gamma- subfamilies, includes 8 known human viruses and infect invertebrates, birds, and mammals. The known human herpesviruses include Herpes Simplex Virus-1 and –2 (HSV-1, HSV-2), Varicella-zoster virus (VZV)- the causative agent of chicken pox and shingles, Cytomegalovirus (CMV), human herpes virus 6 and 7 (HHV-6 and HHV-7), and two oncologic viruses Epstein-Barr virus (EBV) and Kaposi's sarcoma-associated herpesvirus (KSHV)(50) . The herpesviruses are ancient and believed to have infected a common ancestor of all animals and evolved with their hosts. This has led to viruses that are highly specific for their hosts and commonly causing only minor symptoms in their host species (51) .

Herpes Simplex Virus-1 (HSV-1) and Herpes Simplex Virus-2 (HSV-2) are closely related alphaherpesviruses that are estimated to infect up to 2/3rd of the world's population (52). Like all

herpesviruses, HSV has lytic and latent phases, allowing the virus to persist through the lifetime of the host (53). Once infection is established, HSV-1 and 2 maintain latency in the trigeminal and sacral ganglia, respectively, reactivating occasionally when stress triggers activation of lytic gene promoters (53, 54). Initial infection and reactivation in HSV-1 usually present as oral sores whereas HSV-2 is more frequently associated with genital sores in healthy individuals. As population demographics shift, HSV-1 is becoming more represented as a sexually transmitted disease (55). Typically, infection and reactivation of HSV are painful for individuals though mortality is limited. In contrast, severe complications can occur in immunocompromised individuals and neonates (56). Acyclovir or acyclovir-derived drugs that inhibit viral replication as a nucleoside analog are the primary treatment used for HSV infection (57). Acyclovir can reduce viral symptoms, but there is still no curative therapy for HSV. HSV-1 is more commonly used as a model system for herpesviruses. Due to its close homology, HSV-2 is likely to share similar biology. In this chapter, I will refer to HSV-1 and HSV-2 collectively as HSV.

For over a half-century, biologists have used HSV-1 as a model system for herpesviruses and for nuclear disruption. Early electron microscopy (EM) work described the most notable features of infection as the disruption of the nucleolus and “a progressive reduction of chromatin” (58) and these large-scale disruptions were consistent across cell types (59–61). Because DNA was not actually lost, it was concluded that chromatin was redistributed rather than reduced. In addition to nucleolus loss and chromatin marginalization, the host nucleus dramatically increases in size over the course of infection (62–64) (Figure 1.1). In 2000, Monier *et al.*
generated 3D imaging by combining EM and confocal microscopy to demonstrate this increase (62). Simpson-Holley *et al.* confirmed this finding and went further to identify host and viral factors involved, notably showing that the increase in nuclear volume is dependent on nuclear G-actin (64). Inhibiting G-actin prevented nuclear expansion, whereas inhibiting the cytosolic F-actin did not affect nuclear expansion during infection. These early observations built a solid foundation for more recent

technological advances in biophysical techniques like atomic force microscopy and 3D imaging to be applied to investigating changes in the nucleus induced by HSV.

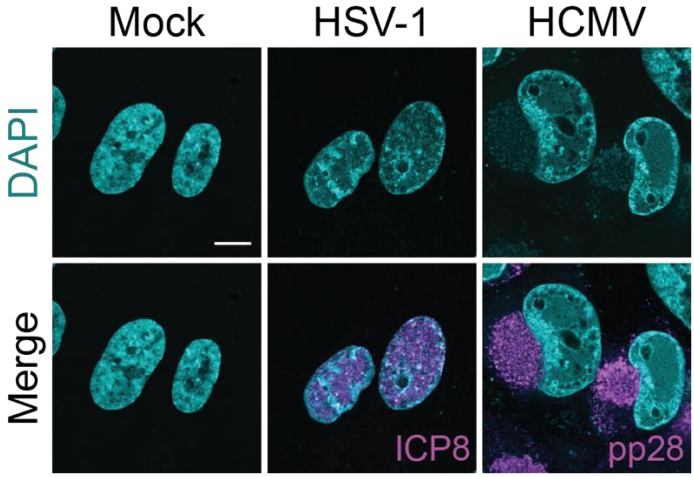

Figure 1.1. Herpesvirus infection leads to host chromatin disruption.

Immunofluorescence images demonstrating lytic infections of HSV-1 (*syn17+*, 10 hours post infection) and CMV (Towne, 3 days post infection) in primary HFF cells. DAPI is shown in cyan, viral proteins (ICP8 for HSV-1 and pp28 for CMV) are shown in magenta. Scale bar represents 10 μm.

1.4. Chromatin as a barrier to HSV infection.

As soon as the HSV-1 genome enters the nucleus, the host chromatin begins to respond. In fact, injection of the bare HSV-1 genome into an isolated nucleus causes the immediate stiffening of chromatin around the nuclear periphery, measured by atomic force microscopy (65). As infection progresses and replication begins, host chromatin becomes marginalized to the nuclear periphery (62, 64). While visualization implies the physical movement of chromatin, recent work suggests that new heterochromatin is formed in the nuclear periphery by the repression hundreds of housekeeping genes (see section 2.1.1) (66). Because viral replication centers (VRCs) continue to expand, it is thought that nuclear expansion is likely due to a need to accommodate these VRCs. Counterintuitively, small spaces on the order of a few hundred nanometers between chromosome territories, termed ‘corrals’, increase in size during infection (67). Progeny capsids diffuse through these corrals to reach the inner

nuclear membrane and begin egress (68). The movement of capsids through regions co-staining with chromatin is significantly slower than movement through regions without chromatin, indicating that host chromatin is a potential barrier to nuclear egress.

Egress from the nuclear compartment is facilitated by the nuclear egress complex (NEC), comprised of viral UL31 and UL34, and supported by viral kinase Us3 (69–71). Once phosphorylation of lamin B1 by viral Us3 and host PKC causes depolymerization of the lamina, capsids dock at the inner nuclear membrane (INM) and bud into the perinuclear space (72, 73). Just before reaching the INM, progeny HSV-1 capsids in the nuclear periphery associate with regions of less dense chromatin, or channels (74). Densely stained chromatin surrounds these channels, suggesting that host heterochromatin is important for their formation. In uninfected cells, heterochromatin markers macroH2A1 and H3K27me3 at the nuclear periphery support nuclear integrity (75, 76). Depletion of these markers causes progeny capsids to diffuse more slowly and accumulate in the host nucleus, resulting in lower viral titers (66). Thus, host chromatin acts as a physical barrier to HSV-1 egress in multiple ways.

1.5 Host chromatin response to lytic HSV infection.

Chromatin dynamics on the host genome regulate the transcription of genes for essential host processes and antiviral responses. During viral infection, the host cell responds by halting nonessential transcription while upregulating defense genes. For example, upon detection of an invading virus through pathogen associated molecular patterns (PAMPs), the host cell drives interferon transcription which in turn initiates a cascade of interferon stimulated gene (ISG) expression to defend the infected organism (77, 78). The DNA sensing ISG known as IFI16 causes H3K9me3 to increase specifically on the viral genome at lytic gene promoters in an ICP0 dependent manner (79, 80). This interesting finding indicates that IFI16 promotes deposition of silencing marks on the incoming viral genome to prevent transcription of viral genes. While interferon responses are silenced, lytic HSV-1 DNA is marked with H3K4me3 and H3K9Ac, consistent with active viral transcription (81, 82). This highlights the complexity of the post-translation histone modifications in pro-viral and anti-viral transcription.

During lytic infection, CTCF is recruited to viral replication compartments and is required for HSV-1 transcription (83). It is thought that CTCF arranges chromatin in a manner that brings enhancers physically nearer to lytic viral genes, thus driving transcription of essential viral genes. Indeed, knockdown of cohesin complex components causes reduced lytic gene transcription and lower recruitment of RNA Polymerase II (RNA Pol II) to viral lytic genes (84). Thus, reduced RNA Pol II recruitment could be a result of more physical distance between enhancers and viral transcription start sites. These findings support a model in which CTCF and cohesin mediated chromatin folding activate viral lytic genes.

1.6 Chromatin dynamics during HSV latency and reactivation.

During latency, heterochromatin marks associate with HSV-1 genomes (85, 86). The polycomb repressive complex 2 (PRC2) and H3K27me3 begin associating with the HSV-1 genome *in vivo* several days after latency is established (87). In fact, inhibition of the H3K9me3 demethylase or H3K27me3 demethylase reduces reactivation in mouse models because reducing the removal of the corresponding silencing mark promotes the repressive state of the latent HSV-1 genome (88, 89). EZH2 or Enhancer of zeste homolog 2 is the PRC2 subunit that deposits the H3K27me3 mark (90). Arbuckle *et al.* found that EZH2 inhibition induces expression of a set of ISGs that in turn reduce HSV-1 transcription while also promoting host defenses (91). Thus, small molecule inhibitors to epigenetic modifications offer a promising avenue for treatment to prevent HSV reactivation.

Latent HSV also takes advantage of CTCF function. During latent infection, CTCF associates with the latency associated transcript (LAT), whose tightly controlled transcription regulates reactivation. Remarkably, there are seven CCCTC sites on the LAT gene. Upon deletion of one CCCTC site, LAT becomes increasingly associated with repressive histone marks (92). While a more repressive chromatin state would be predicted to produce lower LAT levels and promote reactivation, mutation of this specific CTCF binding site on the LAT gene resulted in less reactivation. Conversely, depletion of

other sites often resulted in more reactivation (93–95). Thus, the outcome of loss of CTCF binding is likely dependent on which of specific site is affected. These findings indicate that the interaction of viral genomes with host factors like CTCF during latency and reactivation has many facets that are yet to be deciphered.

1.7 Nucleolar disruption during HSV infection.

Early in HSV-1 infection the nucleolus becomes more electron dense, appearing compact before fragmenting later during viral replication (58). Nucleolar proteins including nucleolin, fibrillarin, B23, and upstream binding factor (UBF) become diffuse throughout the nucleus during infection (96–98). The redistribution of nucleolar proteins B23 and nucleolin is dependent on the HSV protein UL24 (97, 98). Loss of UL24 or knockdown of nucleolin results in reduced titers and increased nuclear capsids, suggesting the inability to disrupt the nucleolus may be detrimental to egress. Viral proteins VP22 and Us11 also interact with nucleolin (99, 100), but their role in nucleolar rearrangement is less clear. As study of the nucleolus progresses, it will be interesting to follow how virus infection affects nucleolar biology and how nucleolar discoveries may indicate areas of viral vulnerabilities.

1.8 Cytomegalovirus rearrangement of the nuclear compartment.

Cytomegalovirus (CMV) is a betaherpesvirus defined by a slow lytic replication cycle. CMV infects a majority of the world's population with seropositivity reaching greater than 90% depending on the country of study (101). Many CMV infections are asymptomatic or result only in minor cold-like symptoms (102). Perhaps due to this low severity of illness, CMV is less well-known than other herpesviruses in the general population. Nevertheless, CMV is one of the leading infectious causes of birth defects with congenital CMV occurring in an estimated 1 in 200 births. As many as 20% of these congenital infections result in disabilities, most commonly deafness (103). The latent phase of CMV is established in monocyte precursors and CMV reactivation can cause severe disease in immunocompromised individuals. CMV infection is a major source of complications following bone

marrow or solid organ transplant (104) and a common culprit of morbidity in AIDS patients (105). In these cases of severe disease, treatment options are limited (106).

CMV infection causes large-scale cellular rearrangement during lytic infection. This rearrangement includes reorganization of the host Golgi and endosomes to form a cytoplasmic viral-induced assembly compartment (vIAC) where virions undergo maturation (107). At the same time the vIAC is formed, the host nucleus acquires a distinct kidney-bean shape that wraps around the vIAC, with host chromatin polarized towards the vIAC (108) (Figure 1.1). These cellular changes are critical for progeny production because high levels of infectious CMV progeny cannot be produced without nuclear remodeling and the formation of a compact, spherical vIAC (109, 110). Interestingly, expression of CMV nuclear egress complex (NEC) proteins UL50 and UL53 are sufficient to initiate remodeling of host nuclei (111). Thus, nuclear structure is intimately tied to viral productivity and research in this area is likely to uncover important results relevant for multiple viruses.

1.9 Reorganization of host chromatin during CMV infection.

One of the first proteins expressed by CMV is immediate early protein 1 (IE1), a transcriptional activator that promotes viral gene expression and replication (112, 113). IE1 directly interacts with host core histones through preferential binding of the acidic patch on-H2B region (113). This interaction causes disruption of host chromatin architecture and was suggested to impair higher order compaction of the host genome (114). Furthermore, this interaction may serve to promote inheritance of latent CMV genomes through tethering (115). These results suggest that IE1 evolved to harness host chromatin structure to promote infection, though the direct benefit to viral progeny production remains unclear.

On a global scale, it is becoming increasingly clear that CMV infection causes specific reorganization of host chromatin. Proctor *et al.* and others showed that chromatin associated with heterochromatin markers H3K9me2 and me3 polarized towards the vIAC and was excluded from the viral replication compartment (108, 116). In contrast, chromatin associated with active marker H3K4me3 and heterochromatin marker H3K27me3 are not polarized and remain diffuse in the nucleus (108). In

addition to affecting histone mark arrangement within the nucleus, CMV infection causes reduction in transcription and mRNA processing of core histones (117). Together these studies suggest that control of histone levels and their modifications may be a critical aspect of CMV infection that have yet to be fully revealed.

1.10 Chromatin factors on the CMV genome during lytic and latent infection.

During lytic replication, CMV genomes are marked with both active and repressive histone modifications at different stages of infection (116, 118–120). These stages are sequentially separated into expression of immediate-early (IE), early (E), and late (L) gene transcripts.

During the first phase of infection and transcription of IE genes, repressive marks are associated with genes that are expressed later, namely E and L gene promoters (121, 122). Thus, premature expression of E and L genes is avoided by utilizing the host repressive machinery associated with marks like H3K27me3 (119, 120). As IE gene transcription begins, active marks H3K9Ac and H3K14Ac are deposited on the Major Immediate Early Promoter (MIEP). Further, IE1 prolongs viral transcription by inhibiting cellular deacetylase activity at active viral promotors (123). Following viral replication, additional active marks are deposited on CMV E and L gene promoters while repressive marks at these promoters are reduced (118), promoting a shift in transcription towards a later stage of infection. Interestingly, the MIEP includes a CTCF binding site that upon deletion enhances IE transcript levels, indicating that CTCF acts as an insulator in this setting (124). Further, depletion of CTCF results in a 50-fold increase in progeny production during lytic infection (124), highlighting the importance of this factor during CMV infection.

The CTCF binding site in the MIEP of CMV is also important during latency as CTCF binds in the MIEP to repress IE1 and IE2. Furthermore, a viral encoded protein Us28 induces increased expression of CTCF during latent infection, likely to help maintain latency (125). EZH2 inhibition results in strong reactivation of CMV, indicating that H3K27me3 on the viral genome also supports latency (126). These

findings underscore that CMV latency is dependent on host factors actively maintaining heterochromatin.

1.11 Nucleolar dynamics during CMV infection.

In CMV infected cells, dense fibrous structures that resemble the nucleolus persist through viral replication and can outline the regions producing viral capsids (127, 128). Despite the apparent maintenance of nucleolar structure during CMV infection, core nucleolar proteins become diffuse throughout the nucleus beginning early in infection. Late gene expression results in mislocalization of nucleolin, which is required for targeting viral UL44 to sites of viral replication to promote DNA synthesis (129). Loss of nucleolin results in reduced viral titers, suggesting that either nucleolin or the nucleolus is important for CMV replication. The viral protein UL31 (not homologous with HSV UL31 discussed earlier) may play a key role in this nucleolar reorganization by promoting mislocalization of nucleolin and UBF (130). Thus, it is clear that several nucleolar proteins are important for viral replication even though further study is needed to fully understand the role of nucleolar structure during CMV infection.

1.12 DNA-virus infection in the nucleus.

Herpesviruses are not the only viruses that hijack host chromatin and nuclear structure to reproduce. Another DNA-virus with well-studied in chromatin manipulation is adenovirus. Adenoviruses are small double-stranded DNA viruses that cause multiple diseases, including gastroenteritis, conjunctivitis, and respiratory infections (53). While generally viewed to cause a self-limiting infection, adenoviruses are particularly harmful for immunocompromised individuals, especially those undergoing stem cell-therapy and organ transplants (131, 132). Worryingly, in the past few years, there have been several reported cases of acute hepatitis in children, most of whom tested positive for adenovirus infection (133, 134). While the exact cause of hepatitis cannot be definitively attributed to adenovirus, this trend shows that there is much we have yet to understand about how adenovirus causes disease. Though there is an adenovirus vaccine to a few adenovirus subtypes, it is not commonly distributed outside the US military (135) and adenovirus treatments are limited (136).

At the structural level of the nucleus, adenovirus infection induces several changes. Adenovirus infection causes a general enlargement of the nucleus, which has been reported in many cases and is easily visualized by DAPI staining in immunofluorescence microscopy (137, 138) (Figure 1.2). Adenovirus infection takes over the nucleus and forms replication centers that are sites of genome accumulation, transcription, and RNA splicing and are near sites of newly formed virions (139). Replication centers begin as several small foci throughout the nucleus, visualized by staining of the viral ssDNA binding protein, DBP (139). As infection progresses, these replication centers grow and form larger ring-like centers. At late stages of infection, a large late viral accumulation center (LVAC) marked by protein V forms and occupies most of the center of nucleus (140). Recently, Pfitzner *et al.* showed using TEM and FRAP that the LVAC is full of a para-crystalline array of virions in a rigid, immobile structure (140). These replication compartments together with the LVAC occupy most of the nucleus, likely providing sufficient space for the production of thousands of progeny virions. At the chromatin level, adenoviruses express multiple proteins that change the chromatin landscape of the host cell. Most notable of these proteins are E1A and protein VII.

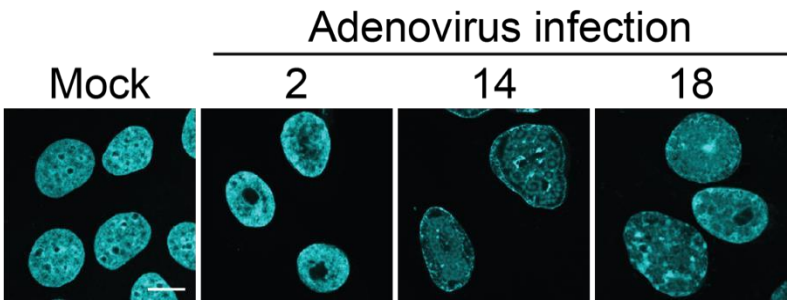

Figure 1.2. Adenovirus infection causes host chromatin reorganization during infection. Immunofluorescence images showing adenovirus type 5 infection in A549 lung epithelial cells with changes to DAPI appearance (cyan) over the course of infection. Time points in hours post infection as indicated. Scale bar represents 10 μm.

1.13 Summary

Nuclear replicating viruses perturb both genomic and nuclear architecture to generate viral progeny (Figure 1.3). Advances in techniques for sequencing and imaging have significantly advanced our

understanding of virus infection in the nucleus (summarized in Table 1). The literature discussed here highlights the complex dual role of chromatin as the transcriptional source of the resident genome and a physical structure in the nucleus during viral infection. The next steps in the field utilizing recent gene-editing advances together with increasingly sophisticated bioinformatics pipelines will allow for tracking viral-induced changes to chromatin structure and transcription throughout infection. Particularly, it is the combination of multiple techniques that will allow for a wholistic understanding of the impact viral infection has on the nucleus, and conversely, how chromatin mechanisms have evolved to combat virus infection.

Although we have focused on herpesviruses and adenoviruses in this chapter, similar techniques have revealed how viruses generally manipulate host chromatin and biology. For example, studies using Hi-C and super-resolution microscopy identified that hepatitis B virus closely associates with H3K4me3-rich regions of the host genome (168, 169). Further, mass spectrometry of papillomaviruses revealed that histones packaged inside virions with the viral genome are predominantly associated with activating histone marks, suggesting that incoming viral genomes are poised for gene expression (170). Given the importance of chromatin in all aspects of cellular function, it is unsurprising that cytoplasmic RNA viruses like SARS-CoV-2 also disrupt host chromatin architecture to evade immune responses (171). Thus, the discoveries laid out here, and those that will undoubtedly surface as technology advances, have enormous potential to pinpoint host vulnerabilities and viral immune evasion strategies.

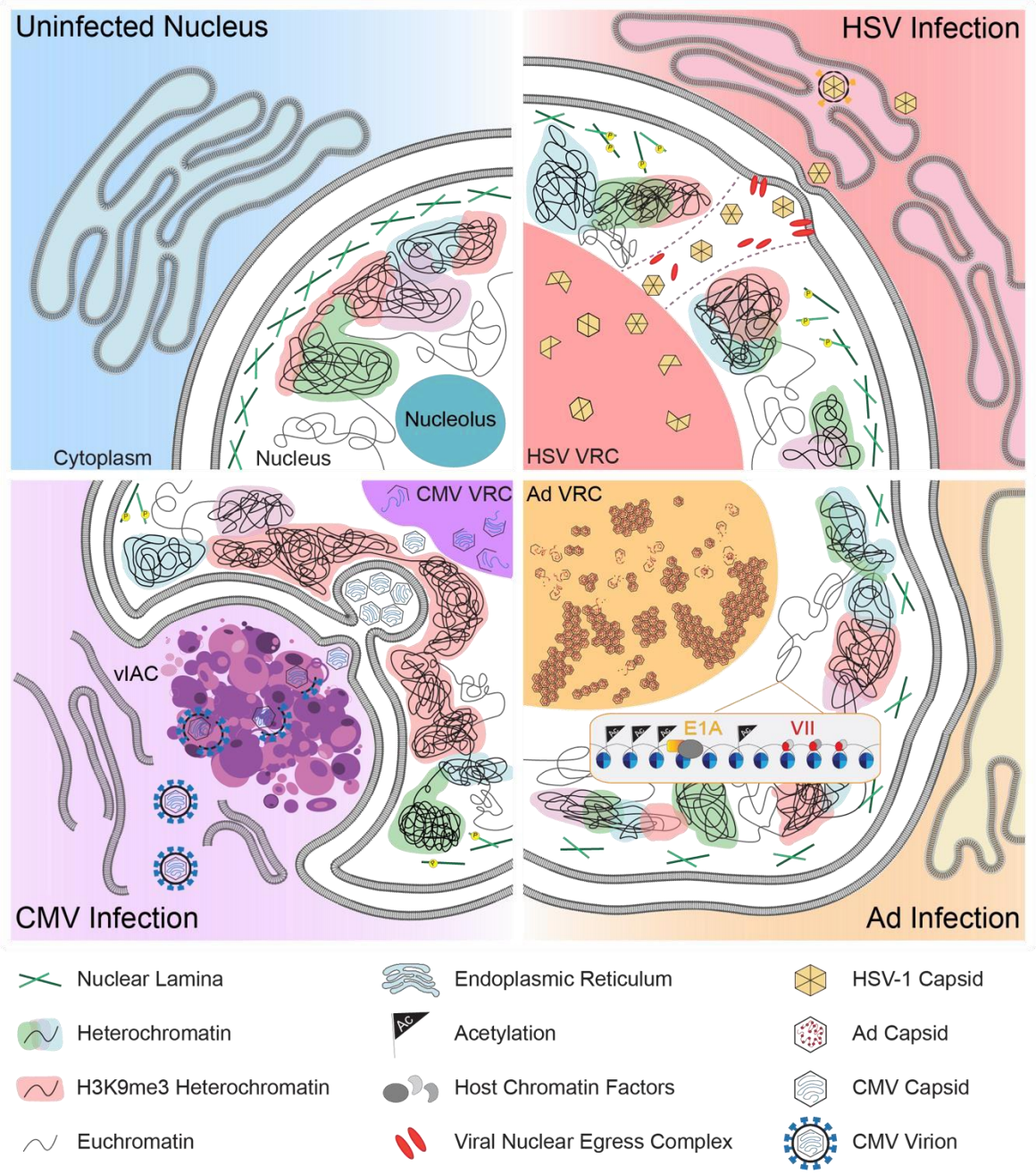

Figure 1.3. Schematic of the large-scale disruptions discussed in this thesis that occur during HSV, adenovirus, and CMV infections. In uninfected cells, heterochromatin predominantly resides along the nuclear periphery and nucleolus. The nucleolus is a phase-separated compartment where ribosomes are assembled. Nuclear lamina and peripheral heterochromatin support the nuclear envelope. In these virus infections, the nuclear volume expands and host chromatin structure is reorganized as large viral replication centers become the dominant nuclear feature. In herpes simplex virus infection, chromatin is redistributed and condensed at the periphery as new regions of heterochromatin are formed. Viral capsids pass through chromatin channels to the nuclear membrane for egress. During adenovirus infection, viral proteins E1A and protein VII remodel host chromatin and the replication center takes over the nuclear compartment to generate viral progeny, which are released in cellular lysis. In

cytomegalovirus infection, the nucleus forms a distinct kidney bean shape and H3K9me3associated heterochromatin is polarized toward the cytoplasmic viral-induced assembly compartment, where egressing virions mature. Structures depicted are described in the key. Abbreviations: Ad, adenovirus; CMV, cytomegalovirus; HSV, herpes simplex virus; vIAC, viral-induced assembly compartment; VRC, viral replication center.

Chapter 1 Table 1. Description of current technologies used to study how viruses manipulate host chromatin and nuclear architecture.

Technique Examples	Purpose	Comments
Genomic Techniques		
Chromatin Immuno-precipitation (ChIP)	To investigate localization of proteins on the genome. - Primarily used to map transcription factors and histone modifications. - Requires a specific antibody and is challenging to normalize replicating viral genomes. - High numbers of cells are required.	(87, 172)
Cleavage Under Targets and Tagmentation (CUT&Tag)/ CUT&Run	To investigate localization of proteins on the genome with higher resolution and lower background compared to ChIP. - Uses intact nuclei to reflect the native chromatin state more accurately. - Requires fewer cells than ChIP, but still relies on antibody specificity.	(66, 173)
Chromosome Confirmation Capture (3C)/4C	To examine the 3D structure of chromatin at a specific region. - Can be used to identify physical interactions between viral and host chromatin. - Requires advanced bioinformatics, and large amounts of cells.	(174, 175)
HiC	To investigate all the chromatin interactions in a cell in an unbiased manner. - Similar to 3C/4C in that it requires advanced bioinformatics and large numbers of cells. - Can be costly to sequence at the depth required to make biological conclusions.	(169)
Imaging Techniques		
Confocal Microscopy / Live imaging	To investigate subnuclear localization of host and viral proteins and visualize how they change during infection. - Z stacks can be acquired for 3-D rendering. - Relies on specific antibodies that can have cross reactivity with viral proteins.	(62, 67, 68, 137)

Super Resolution microscopy	To visualize intermolecular interactions with resolution beyond the diffraction barrier.	- Requires specialized equipment and extensive protocols.	(168)
Electron Microscopy	To visualize cellular organelles and structures using an electron beam.	- Micrographs of densities have high resolution and can detect individual capsids and heterochromatin. - Requires specialized equipment and 3D rendering is challenging.	(66, 176)
Combination/Other Techniques			
Mass Spectrometry	To identify proteins and their post-translational modifications using the mass to charge ratio.	- Datasets obtained from isolated proteomes or proteomic analysis can be very powerful to define changes to host cells during infection. - Requires specialized equipment and analysis.	(177, 178)
Isolation of proteins on nascent DNA (iPOND)	To determine the proteins associated with replicating DNA genomes via EdU incorporation.	- Can be used to identify proteins interacting with viral genomes during replication. - Requires in depth follow up via western blotting or mass spectrometry. - Requires large numbers of cells.	(160, 179)
Atomic Force Microscopy	To determine physical properties of a sample using a probe to apply force.	- Can be used to determine changes to nuclei upon infection or virion stability. Requires specialized equipment and analysis.	(65)

Chapter 2: HSV-1 exploits host heterochromatin for nuclear egress

* This chapter is adapted from Lewis HC,* Kelnhofer-Millevolte LE,* Brinkley MR, Arbach HE, Arnold EA, Ramachandran S, Avgousti DC. (2023) HSV-1 exploits host heterochromatin for egress. *Journal of Cell Biology.* 22 (9): e202304106. This chapter is reproduced here as it is licensed under a Creative Commons Attribution 4.0 International License, allowing for unrestricted use provided the original source is cited. "We" is used throughout the publication. In close collaboration with Hannah Lewis, I designed and performed experiments, wrote, and created figures for the original manuscript. Mia Brinkley assisted with experiments and figure editing. Edward Arnold and Han Arbach assisted with experiments. Sequencing analysis and text describing analysis was kindly performed by Srinivas Ramachandran. The work here was supervised and edited by Daphne Avgousti.

Abstract

Herpes simplex virus (HSV-1) progeny form in the nucleus and exit to successfully infect other cells. Newly formed capsids navigate complex chromatin architecture to reach the inner nuclear membrane (INM) and egress. Here, we demonstrate by transmission electron microscopy (TEM) that HSV-1 capsids traverse heterochromatin associated with trimethylation on histone H3 lysine 27 (H3K27me3) and histone variant macroH2A1. Through chromatin profiling during infection, we revealed global redistribution of these marks whereby massive host genomic regions bound by macroH2A1 and H3K27me3 correlate with decreased host transcription in active compartments. We found that loss of these markers resulted in significantly lower viral titers but did not impact viral genome or protein accumulation. Strikingly, we discovered that loss of macroH2A1 or H3K27me3 resulted in nuclear trapping of capsids. Finally, by live-capsid tracking, we quantified this decreased capsid movement. Thus, our work demonstrates that HSV-1 takes advantage of the dynamic nature of host heterochromatin formation during infection for efficient nuclear egress.

2.1 Introduction

Nuclear-replicating viruses must contend with host chromatin to establish a successful infection. Like most DNA viruses, herpes simplex virus (HSV-1) takes advantage of host chromatin factors both by incorporating histones onto its genome to promote gene expression (1) and by reorganizing host chromatin during infection (2,3,4). In response to infection, changes to histone modifications on interferon response genes can also hinder HSV-1 gene expression (5). HSV-1 progeny capsids egress from the nucleus by a unique mechanism of budding into the inner nuclear membrane and then fusing with the outer nuclear membrane for further maturation in the cytosol (6,7). Thus, host chromatin that accumulates in the nuclear periphery during HSV-1 infection creates a potential barrier for capsids to egress from the nucleus. The redistribution of host chromatin during infection allows for capsids to traverse the nucleus such that the transport of HSV-1 capsids through chromatin is the rate-limiting step of nuclear egress (8). The progress of HSV-1 infection is also associated with areas of less dense chromatin in the nuclear periphery, also termed channels (9). However, it is not known if these channels are necessary for viral egress and the mechanisms by which they form are unclear. Heterochromatin density and subnuclear localization are affected by the presence and ratio of specific histone modifications. In uninfected cells, histone modifications such as trimethylation of histone H3 lysine 27 (H3K27me3) and the histone variant macroH2A1, among others, delineate heterochromatin regions that are largely localized to the nuclear periphery. H3K27me3 is deposited by the EZH2 enzyme (10), a member of the polycomb repressive complex (PRC2) (11). This modification is bound by PRC2, leading to modification of adjacent nucleosomes, which results in formation of heterochromatin domains that repress transcription. MacroH2A, the largest of the histone variants, consists of a canonical histone fold domain, a small linker region and a C-terminal 25 kDa macro domain that is thought to protrude from the nucleosome (12). There are three isoforms referred to collectively as macroH2A: macroH2A1.1, macroH2A1.2 and macroH2A2. MacroH2A1.1 and macroH2A1.2 are splice variants of the same gene that differ by one exon resulting in a 28-amino acid difference in the macro domain. MacroH2A1 was found to be downregulated in melanoma (13),

suggesting a key role in the maintenance of genome integrity. Importantly, loss of macroH2A1 and macroH2A2 results in a significant decrease in heterochromatin in the nuclear periphery observed by electron microscopy (14). Furthermore, macroH2A1 also demarcates regions of host chromatin that associate with the nuclear lamina (15), termed lamina-associated domains (LADs), highlighting its importance in linking chromatin with the nuclear envelope to support nuclear integrity.

In this study, we visualized HSV-1 nuclear egress by transmission electron microscopy (TEM) and found that capsids reach the inner nuclear membrane in regions of less densely stained chromatin. Therefore, we hypothesized that HSV-1 exploits host heterochromatin dynamics to successfully egress from the nuclear compartment. We examined chromatin structure by TEM in the absence of heterochromatin markers macroH2A1 and H3K27me3 and discovered that peripheral heterochromatin is largely dependent on these marks. We used chromatin profiling of macroH2A1 and H3K27me3 during HSV-1 infection to define the specific host genomic regions bound by these markers and found that they demarcate broad regions of heterochromatin that form in transcriptionally active compartments. Importantly, we found that the loss of macroH2A1 results in significantly lower viral titers but does not impair viral transcription, protein production, or replication in both lab adapted and clinical isolates of HSV-1. Furthermore, by inhibiting EZH2 deposition of H3K27me3, we found that reduction of H3K27me3 also leads to a significant decrease in viral titers but did not affect viral protein or genome accumulation. Finally, we determined by TEM that loss of macroH2A1 or H3K27me3 results in significantly more viral capsids trapped in the nuclear compartment, pinpointing the importance of heterochromatin dynamics in viral nuclear egress. Our study is the first to demonstrate that HSV-1 infection takes advantage of heterochromatin changes to successfully egress from the nuclear compartment.

Results

2.2 HSV-1 capsids associate with regions of less dense chromatin

To investigate the journey of HSV-1 capsids to the inner nuclear membrane, we used transmission electron microscopy (TEM) to image nuclei and examined heterochromatin formation in primary and diploid human foreskin fibroblast (HFF) cells. In uninfected cells, we observed dark staining, characteristic of dense heterochromatin, in the nuclear periphery (Figure 2.1a, arrowhead). Upon infection with HSV-1, we observed capsids interacting with the inner nuclear membrane primarily in regions of low-density chromatin indicated by lighter staining (Figure 2.1b, arrows). These results are consistent with a previous report in African green monkey kidney cells (Vero) showing that viral capsids can reach the inner nuclear membrane via channels in the marginalized chromatin. Because heterochromatin in the nuclear periphery was dependent on macroH2A presence in hepatoma cells (16,17), and macroH2A1 commonly overlaps with H3K27me3, we chose to examine heterochromatin formation in the absence of these markers in HFFs.

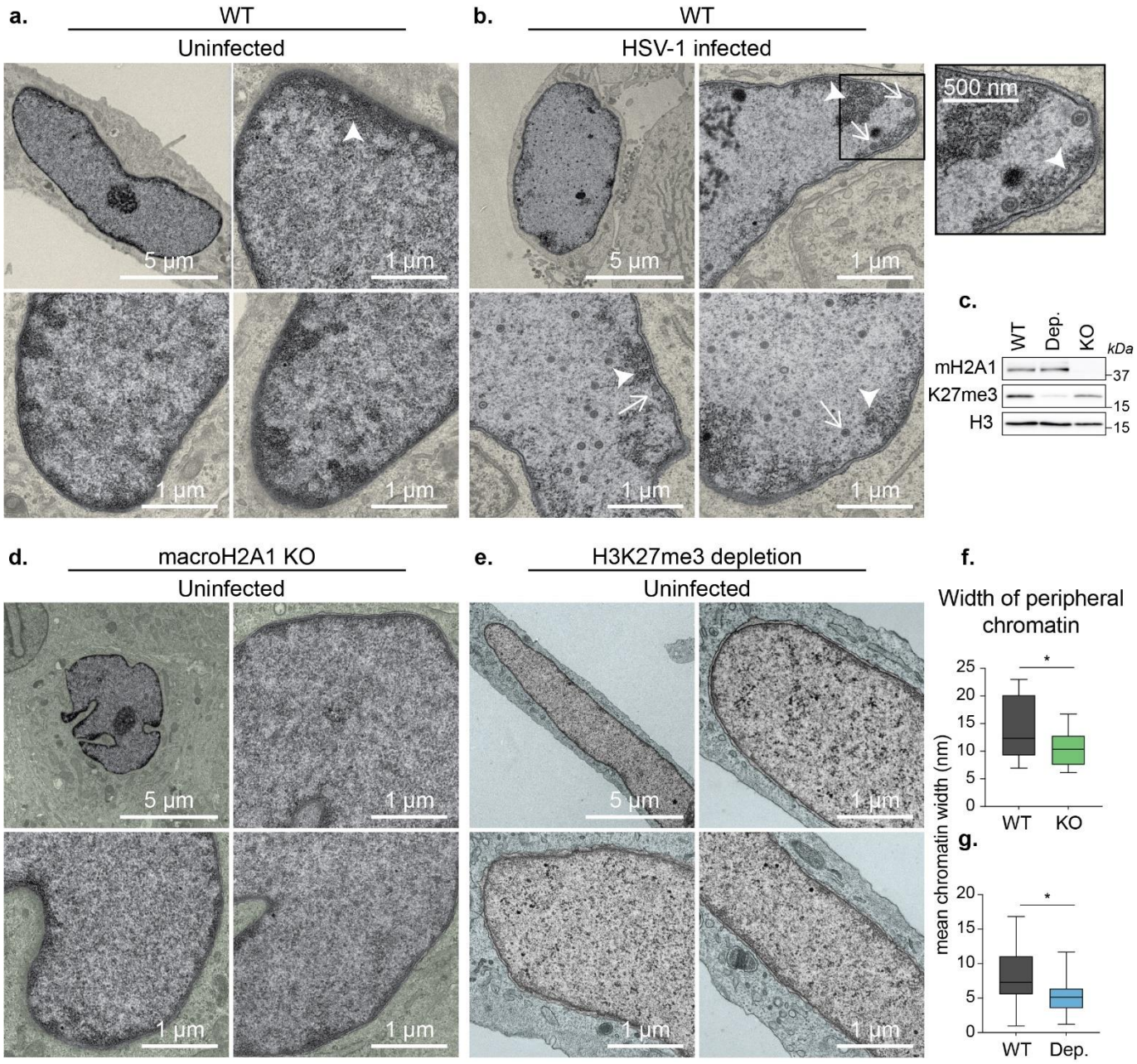

Figure 2.1. HSV-1 capsids navigate through regions of less dense chromatin to reach the inner nuclear membrane in HFF cells. A) Transmission electron microscopy (TEM) images of representative uninfected nuclei in WT HFF-Ts. Regions outside of the nucleus are colorized yellow. Dark regions represent high density chromatin (arrowhead). Scale bars as indicated. B) TEM images of representative WT nuclei at 18 hours post-infection (hpi) with HSV-1. Inset shows enlarged view of respective boxed area. Arrowhead indicates high density chromatin, arrows indicate HSV-1 capsids. C)Representative western blots with proteins as

indicated showing macroH2A1 knock-out (mH2A1 KO) and H3K27me3 depletion (Dep.). D) TEM images of representative uninfected nuclei in macroH2A1 knockout HFF-T cells. Regions outside of the nucleus are colorized green. E) TEM images of representative uninfected nuclei in H3K27me3 depleted conditions. Regions outside of the nucleus are colorized blue. F) Quantification of peripheral heterochromatin width in nuclei from A and D. Width was measured in nm from the nuclear periphery via binary thresholding from intensity profiles sampled every 10 pixels. Mean width was plotted for each nucleus. p= 0.0275 (n=16 WT, n=22 macroH2A1 KO) by unpaired t-test. For the box plot, the box marks upper and lower quartiles, center line marks median, and error bars denote minimum and maximum values for the population. G) Quantification as in (f) in nuclei from A and E. p= 0.0144 (n= 22 WT, n=20 H3K27me3 depleted) by unpaired t-test. For the box plot, the box marks upper and lower quartiles, center line marks median, and error bars denote minimum and maximum values for the population.

2.3 Heterochromatin markers macroH2A1 and H3K27me3 support densely stained regions in the nuclear periphery

We used CRISPR-Cas9 to knock-out (KO) expression of the *macroH2A1* gene in hTERT-immortalized HFF cells (HFF-T) cells, which resulted in the loss of total macroH2A1 (Figure 2.1 c), termed macroH2A1 KO cells. To reduce H3K27me3 levels, we targeted the EZH2 enzyme that deposits this mark (18) using a well-characterized inhibitor called tazemetostat (EPZ-6438) (19). We treated cells with 10 μM of tazemetostat or DMSO control for 3 days to allow for steady-state reduction of H3K27me3 (Figure 2.1c). We found by TEM that macroH2A1 KO cells and H3K27me3 depleted cells had strikingly less heterochromatin in the nuclear periphery than WT cells (Figure 2.1d and e). We quantified the width of heterochromatin at the nuclear periphery in each cell type through binary thresholding of the intensity of electron-dense regions and found that loss of macroH2A1 results in a significant reduction in peripheral heterochromatin (Figure 2.1 f and g). It is important to note that in cells with observed decreased heterochromatin that there is not a decrease in total chromatin. These cells are simply not able to condense their chromatin to a degree that it would be visible by TEM. Importantly, the genomic regions bound by macroH2A1 and H3K27me3 are sufficiently massive that changes are visible by TEM. Therefore, we next examined the genomic distribution of these markers by chromatin profiling.

2.4 MacroH2A1 and H3K27me3 bind broad regions of the host genome that are redistributed during infection

We hypothesized that macroH2A1 and H3K27me3 are deposited at specific genomic loci on the host genome during infection to promote the formation of heterochromatin. To test this hypothesis, we used CUT&Tag (20) to profile the genomic localization of macroH2A1 at 4, 8 and 12 hours post infection (hpi) in wild-type (WT) and macroH2A1 KO HFF-T cells. MacroH2A1 KO cells showed no expression of total macroH2A1, macroH2A1.1 or macroH2A1.2; however, macroH2A2 levels were unchanged (Figure 2.2 b-c). We also examined the chromatin profile of H3K27me3 under these conditions. On the human genome, we observed clear enrichment of macroH2A1 and H3K27me3 compared to IgG in WT cells (Figure 2.2 d-f). The enrichment of macroH2A1 and H3K27me3 was observed as large domains, many of which were gained upon viral infection (Figure 2.3 a), suggesting that the host landscape is altered upon infection. These gains were reflected in an increase in total protein levels measured by mass-spectrometry (Figure 2.2 a). Since large regions are not amenable to traditional peak-based analysis, we instead used domain-based analysis. With the minimum domain size of 1 kb, we observed ~50,000 H3K27me3 domains and ~70,000 macroH2A1 domains genome wide across the conditions we profiled (Figure 2.2 f). We observed less than 10 macroH2A1 domains in the datasets generated from macroH2A1 KO cells, indicating that our algorithm was identifying robust domains (Figure 2.2 f). Furthermore, there is high correlation in macroH2A1 domain enrichments between macroH2A1 CUT&Tag in WT cells, and between H3K27me3 datasets themselves in both WT and macroH2A1 KO. MacroH2A1 CUT&Tag from macroH2A1 KO cells has lowest correlation coefficients in comparisons across the board (Figure 2.2 g). This implies a clear loss of signal in macroH2A1 CUT&Tag from macroH2A1 KO cells, but concordant signals from macroH2A1 CUT&Tag in WT, and H3K27me3 from WT and macroH2A1 KO cells at domains defined just using WT macroH2A1 time series. To identify regions in the genome where macroH2A1 was changing with infection, we first defined non-overlapping sections of the genome where macroH2A1 domains were observed in at least one of the datasets. We then calculated the change in enrichment of macroH2A1 in these sections across the infection time

course. We used k-means clustering during the time course of infection compared to mock to identify patterns of macroH2A1 gain or loss during infection (Figure 2.3 b). With k=6, we observed two clusters to substantially gain macroH2A1 over the course of infection (Clusters 5 and 6, Figure 2.3 b left and c). Clusters 1-3 had significant decreases in macroH2A1, whereas cluster 4 had a minor increase (Figure 2.3 b left and 2.2 c). We then asked how these macroH2A1-defined clusters behaved with respect to H3K27me3 and found that the overall trends across clusters were preserved in H3K27me3 (Figure 2.3 b right, and 2.3 d), suggesting that H3K27me3 is largely enriched in the same broad regions. Thus, our clustering analysis demonstrates significant redistribution of H3K27me3 and macroH2A1 on the host genome during HSV-1 infection.

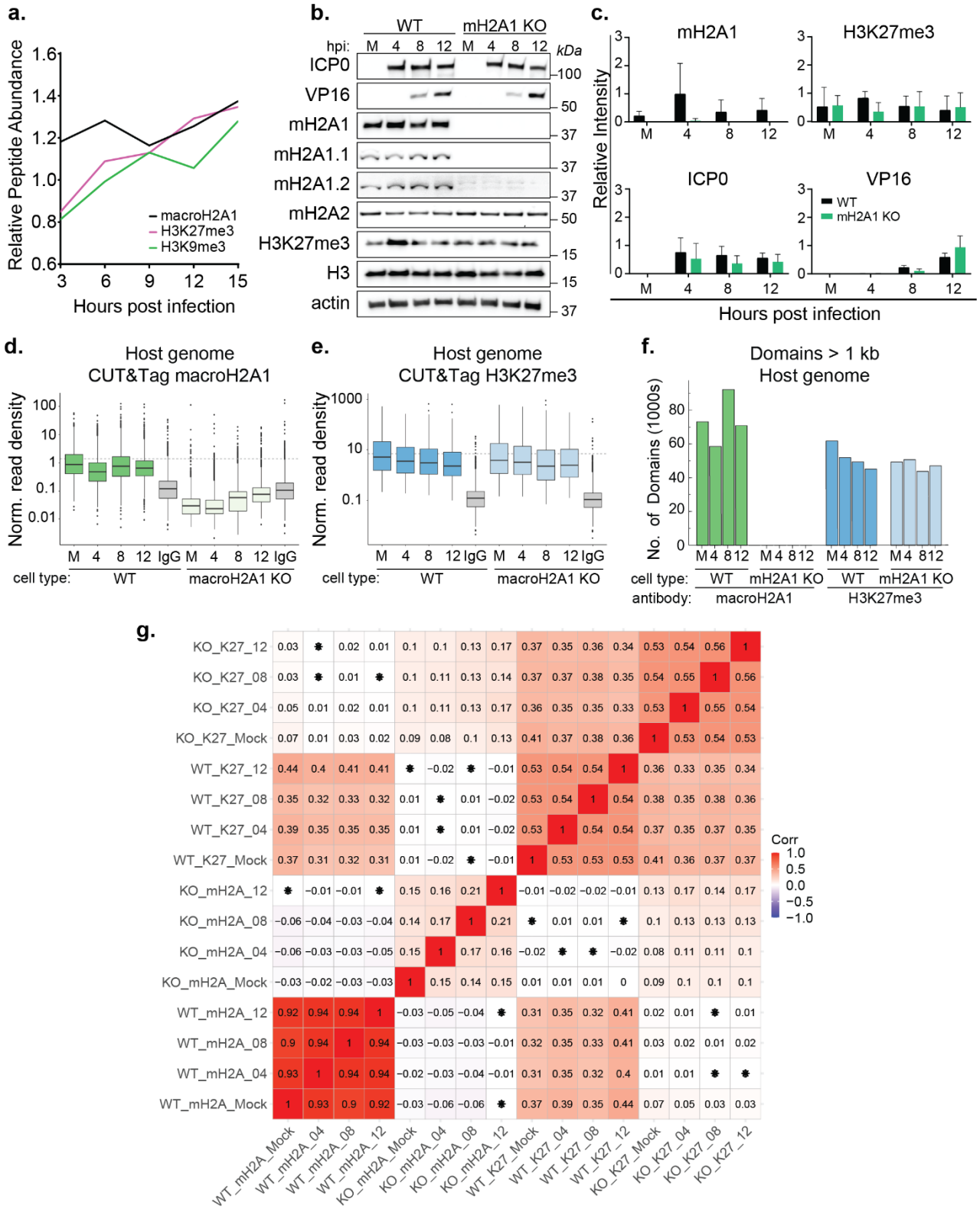
a.
Relative Peptide Abundance
Hours post infection
macroH2A1
H3K27me3
H3K9me3
b.
WT
mH2A1 KO
hpi:
kDa
ICP0
VP16
mH2A1
mH2A1.1
mH2A1.2
mH2A2
H3K27me3
H3
actin
c.
mH2A1
H3K27me3
ICP0
VP16
Relative Intensity
Hours post infection
d.
Host genome
CUT&Tag macroH2A1
Norm. read density
cell type:
WT
macroH2A1 KO
e.
Host genome
CUT&Tag H3K27me3
f.
Domains > 1 kb
Host genome
No. of Domains (1000s)
antibody:
macroH2A1
H3K27me3
g.
Corr

Figure 2.2 Quantification of macroH2A1 and H3K27me3 enrichment on host genomes during HSV-1 infection. A) Relative peptide abundance of macroH2A1, H3K27me3, and H3K9me3 over the course of HSV-1 infection in primary HFFs from three biological replicates normalized to mock peptide counts (original data from (3)). B) Representative western blots of total viral and host proteins as indicated at mock(M) 4, 8, and 12 hpi with HSV-1 in WT and macroH2A1 KO HFF-T cells. H3 and actin are shown as loading controls. C) Mean relative intensity of total macroH2A1, H3K27me3, ICP0, and VP16 as indicated. Error bars show ± SD of three replicates of western blots as in (b). D) Spike-in normalized CUT&Tag read density of macroH2A1 on WT and macroH2A1 KO HFF-T host genomes during HSV-1 infection. M indicates mock infected cells; 4,8,12 indicate 4,8,12 hpi. For box plots the lower and upper hinges correspond to the first and third quartiles (the 25th and 75th percentiles). The upper whisker extends from the hinge to the largest value no further than 1.5 * IQR from the hinge (where IQR is the inter-quartile range, or distance between the first and third quartiles). The lower whisker extends from the hinge to the smallest value at most 1.5 * IQR of the hinge. Data beyond the end of the whiskers are called “outlying” points and are plotted individually. E) Spike-in normalized CUT&Tag read density of H3K27me3 on WT and macroH2A1 KO host genomes during HSV-1 infection presented as in (d). F) Total number of macroH2A1 and H3K27me3 domains over 1 kb as measured by CUT&Tag of WT and macroH2A1 KO host genomes during HSV-1 infection. G) Correlation matrix of host genome enrichment from all datasets at domains as defined in Fig 2. Pearson correlation coefficient is plotted both as a heatmap and the values are printed inside each cell. If the p-value of a correlation coefficient is not significant, there is an asterisk over the number in that cell.

To determine whether H3K27me3 deposition was dependent on macroH2A1, we also examined H3K27me3 enrichment in domains in the absence of macroH2A1. We plotted the H3K27me3 changes at the WT clusters for macroH2A1 KO cells and found that the trends of H3K27me3 were similar between WT and macroH2A1 KO cells (Figure 2.3 e and f). This result suggests that H3K27me3 deposition is independent of macroH2A1. In summary, HSV-1 infection results in formation of new heterochromatin domains that span ~10-100s of kilobases. Importantly, our results demonstrate that heterochromatin accumulating in the nuclear periphery during HSV-1 infection represents *new* regions of heterochromatin that are macroH2A1 and H3K27me3 dependent.

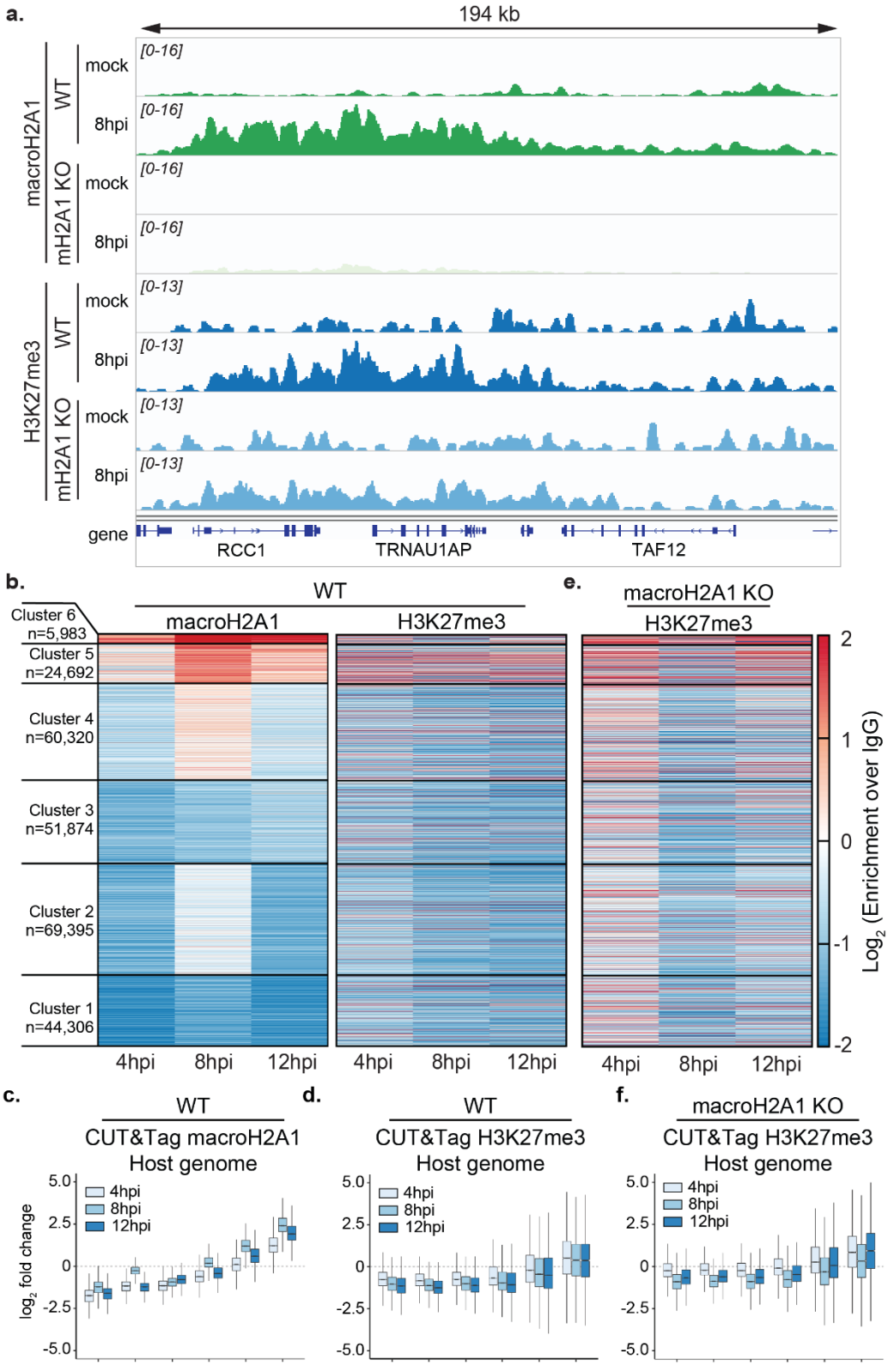
a.
194 kb
macroH2A1
WT
mock
8hpi
mH2A1 KO
mock
8hpi
H3K27me3
WT
mock
8hpi
mH2A1 KO
mock
8hpi
[0-16]
[0-13]
gene
RCC1
TRNAU1AP
TAF12
b.
WT
macroH2A1
H3K27me3
Cluster 6 n=5,983
Cluster 5 n=24,692
Cluster 4 n=60,320
Cluster 3 n=51,874
Cluster 2 n=69,395
Cluster 1 n=44,306
4hpi
8hpi
12hpi
e.
macroH2A1 KO
H3K27me3
Log2 (Enrichment over IgG)
c.
WT
CUT&Tag macroH2A1
Host genome
log2 fold change
d.
WT
CUT&Tag H3K27me3
Host genome
f.
macroH2A1 KO
CUT&Tag H3K27me3
Host genome

Figure 2.3. MacroH2A1 and H3K27me3 bind broad chromatin regions on the host genome that are redistributed over the course of HSV-1 infection. A) Representative genome browser snapshots of spike-in normalized CUT&Tag enrichment of macroH2A1 and H3K27me3 showing increases at 8 hpi of HSV-1 infection as measured by CUT&Tag in WT, or macroH2A1 KO HFF-T cells as indicated. The region shown is found on chromosome 1. B) Changes in log2 enrichment of spike-in normalized CUT&Tag of macroH2A1 and H3K27me3 over IgG compared to mock treatment are shown as a heatmap. Each line in the heatmap represents a domain of macroH2A1. C) Quantification of heat maps from (b) showing macroH2A1 enrichment in WT HFF-T cells across each cluster. D) Quantification of heat maps from (b) showing H3K27me3 enrichment in clusters defined by macroH2A1 in HFF-T cells. E) Changes in log2 enrichment as in (b) of H3K27me3 over IgG in macroH2A1 KO HFF-T cells. F) Quantification as in (c) in macroH2A1 KO HFF-T cells.

In contrast, the macroH2A1 CUT&Tag on the viral genome showed similar enrichments in both WT and macroH2A1 KO cells. Further, the H3K27me3 signal on the viral genomes also mirrored the IgG control. These results indicated that there was a significant background signal from the viral genome that could not be accounted for (Figure 2.4 a-d). Furthermore, there is high correlation between all datasets regardless of the antibody or genetic background (Figure 2.4 e) implying that there is the same signal from the viral genome regardless of experimental condition, and most probably represents non-specific tagmentation. We performed immunofluorescence on macroH2A1 KO, H3K27me3-depleted and respective control cells (Figure 2.4 f-g). We observed no cross reactivity of antibodies in macroH2A1 KO and H3K27me3depleted cells and minimal colocalization of these heterochromatin marks with ICP8 (HSV-1 DNA binding protein (21)). Therefore, we disregarded viral genome reads in our dataset and focused instead on the host genome. Taken together, these results indicate that multiple forms of heterochromatin were gained at specific host genomic loci during HSV-1 infection.

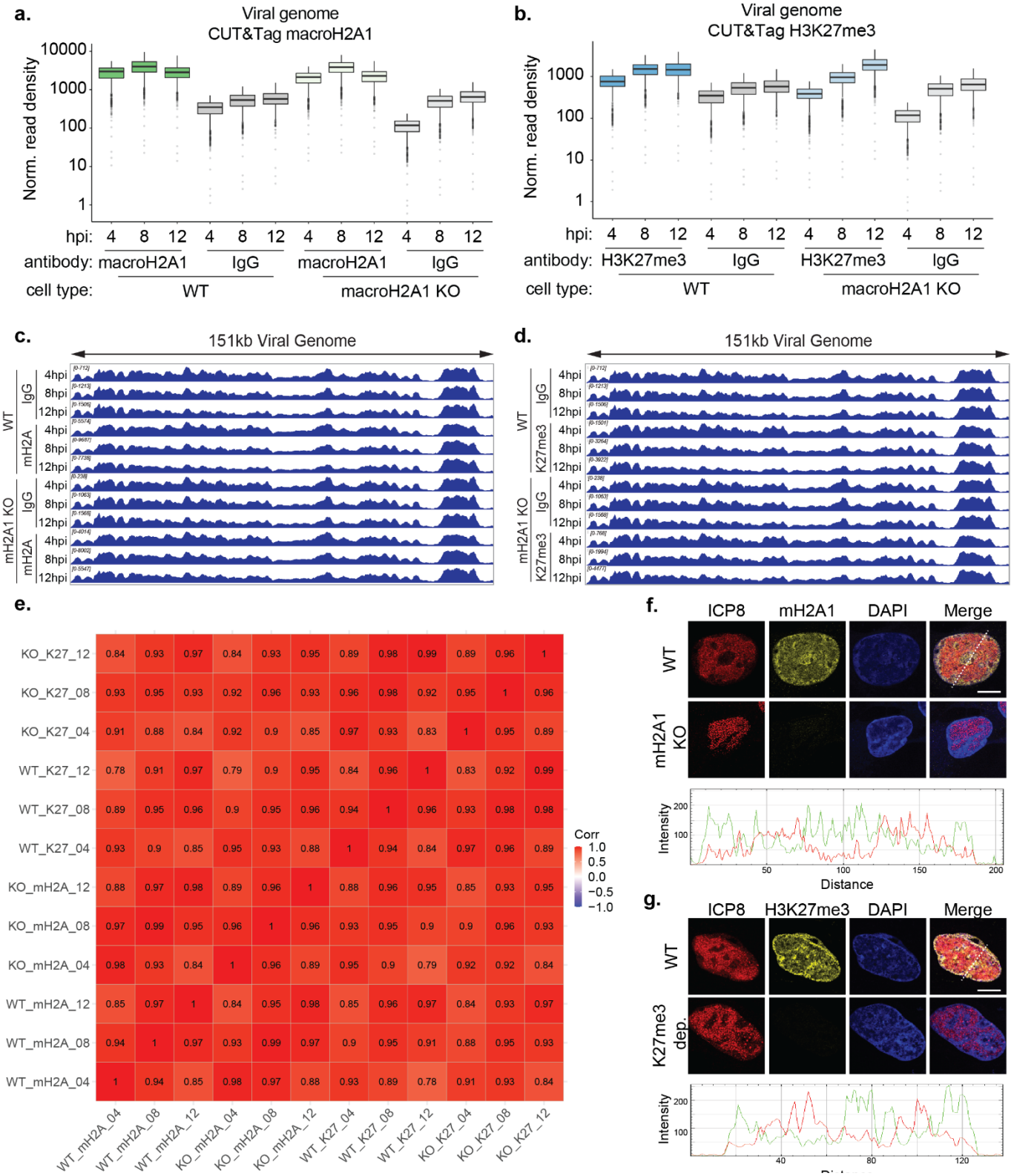
a.
Viral genome
CUT&Tag macroH2A1
Norm. read density
10000
1000
100
10
1
hpi: 4 8 12 4 8 12 4 8 12 4 8 12
antibody: macroH2A1 IgG macroH2A1 IgG
cell type: WT macroH2A1 KO
b.
Viral genome
CUT&Tag H3K27me3
Norm. read density
1000
100
10
1
hpi: 4 8 12 4 8 12 4 8 12 4 8 12
antibody: H3K27me3 IgG H3K27me3 IgG
cell type: WT macroH2A1 KO
c.
151kb Viral Genome
WT
IgG
mH2A
mH2A1 KO
4hpi
8hpi
12hpi
d.
151kb Viral Genome
WT
IgG
K27me3
mH2A1 KO
K27me3
4hpi
8hpi
12hpi
e.
KO_K27_12 0.84 0.93 0.97 0.84 0.93 0.95 0.89 0.98 0.99 0.89 0.96 1
KO_K27_08 0.93 0.95 0.93 0.92 0.96 0.93 0.96 0.98 0.92 0.95 1 0.96
KO_K27_04 0.91 0.88 0.84 0.92 0.9 0.85 0.97 0.93 0.83 1 0.95 0.89
WT_K27_12 0.78 0.91 0.97 0.79 0.9 0.95 0.84 0.96 1 0.83 0.92 0.99
WT_K27_08 0.89 0.95 0.96 0.9 0.95 0.96 0.94 1 0.96 0.93 0.98 0.98
WT_K27_04 0.93 0.9 0.85 0.95 0.93 0.88 1 0.94 0.84 0.97 0.96 0.89
KO_mH2A_12 0.88 0.97 0.98 0.89 0.96 1 0.88 0.96 0.95 0.85 0.93 0.95
KO_mH2A_08 0.97 0.99 0.95 0.96 1 0.96 0.93 0.95 0.9 0.9 0.96 0.93
KO_mH2A_04 0.98 0.93 0.84 1 0.96 0.89 0.95 0.9 0.79 0.92 0.92 0.84
WT_mH2A_12 0.85 0.97 1 0.84 0.95 0.98 0.85 0.96 0.97 0.84 0.93 0.97
WT_mH2A_08 0.94 1 0.97 0.93 0.99 0.97 0.9 0.95 0.91 0.88 0.95 0.93
WT_mH2A_04 1 0.94 0.85 0.98 0.97 0.88 0.93 0.89 0.78 0.91 0.93 0.84
WT_mH2A_04 WT_mH2A_08 WT_mH2A_12 KO_mH2A_04 KO_mH2A_08 KO_mH2A_12 WT_K27_04 WT_K27_08 WT_K27_12 KO_K27_04 KO_K27_08 KO_K27_12
Corr
1.0
0.5
0.0
−0.5
−1.0
f.
ICP8 mH2A1 DAPI Merge
WT
mH2A1 KO
Intensity
200
100
50 100 150 200
Distance
g.
ICP8 H3K27me3 DAPI Merge
WT
K27me3 dep.
Intensity
200
100
40 80 120

Figure 2.4. Quantification of macroH2A1 and H3K27me3 enrichment on viral genomes during HSV1 infection. A) Spike-in normalized CUT&Tag read density of macroH2A1 on HSV-1 genomes during infection of WT and macroH2A1 KO HFF-T cells. The lower and upper hinges correspond to the first and third quartiles (the 25th and 75th percentiles). The upper whisker extends from the hinge to the largest value no further than 1.5 * IQR from the hinge (where IQR is the inter-quartile range, or distance between the first and third quartiles). The lower whisker extends from the hinge to the smallest value at most 1.5 * IQR of the hinge. Data beyond the end of the whiskers are called “outlying” points and are plotted individually. B) Spike-in normalized CUT&Tag read density of H3K27me3 on HSV-1 genomes during infection of WT and macroH2A1 KO HFF-T cells. Data graphed as in (a). C) Genome browser snapshots of spike-in normalized CUT&Tag enrichment of macroH2A1 on viral genomes in WT or macroH2A1 KO HFF-T cells as indicated. The full viral genome is shown. D) Genome browser snapshots of spike-in normalized CUT&Tag enrichment of H3K27me3 on viral genomes in WT or macroH2A1 KO HFF-T cells as indicated. The full viral genome is shown. The same IgG control was used to generate IgG WT and KO control graphs for S2c-d. E) Correlation matrix of CUT&Tag signals aligned to the viral genome from all datasets. Pearson correlation coefficient is plotted both as a heatmap and printed inside each cell. If the p-value of a correlation coefficient is not significant, there is an asterisk over the number in that cell. F) (Top) Representative Immunofluorescence of total macroH2A1 (yellow), viral DNA binding protein ICP8 (red), and DAPI (blue) at 10 hpi in WT and macroH2A1 KO HFF-T cells infected with HSV-1. Scale bar is 10 μm. (Bottom) Histogram of macroH2A1 (green) and ICP8 (red) intensity at dotted transect line. G) (Top) Representative Immunofluorescence of H3K27me3 (yellow), ICP8 (red), and DAPI (blue) at 10 hpi in HSV-1 infected WT and H3K27me3 depleted HFF-T cells. (Bottom) Histogram of H3K27me3 (green) and ICP8 (red) intensity at dotted transect line.

2.5 MacroH2A1 and H3K27me3 deposition correlates with decreased transcription in active compartments

To investigate the transcriptional output of newly formed macroH2A1 and H3K27me3-bound regions, we performed RNA-seq on WT and macroH2A1 KO cells over the course of HSV-1 infection and calculated fold changes in RNA levels at each time point over the mock control. We identified genes that are contained within domains in each cluster defined in Figure 2.3 and plotted the distribution of RNA fold changes of the genes grouped by the clusters to which they belonged (Figure 2.5 a and c). We found that total RNA levels anti-correlate with macroH2A1 presence: clusters 1-3 had an increase in RNA levels, whereas clusters 4-6 had a decrease in RNA levels over the course of infection (Figure 2.5 a and c). Strikingly, the gene expression changes in macroH2A1 KO cells mirror that of WT cells, leading us to conclude that macroH2A1 deposition is not driving changes in total RNA (Figure 2.5 b-c).

Because macroH2A1 and H3K27me3-bound regions span a large portion of the host genome, we asked whether any specific gene ontology (GO) categories were over-represented for the genes in each macroH2A1-defined cluster (Figure 2.5 d). Genes in clusters 1 and 2 (with decreased macroH2A1 and increased expression) were associated with response to dsRNA and inflammatory responses, as expected during viral infection. Surprisingly, clusters 4-6, with increasing macroH2A1, consisted mostly of housekeeping genes. Taken together, these results indicate that macroH2A1 deposition is downstream of transcription changes. Thus, the deposition of macroH2A1 is not directly affecting the expression of specific genes that would be pro- or antiviral, but rather it is likely that these changes in transcription are a result of the stress response to infection.

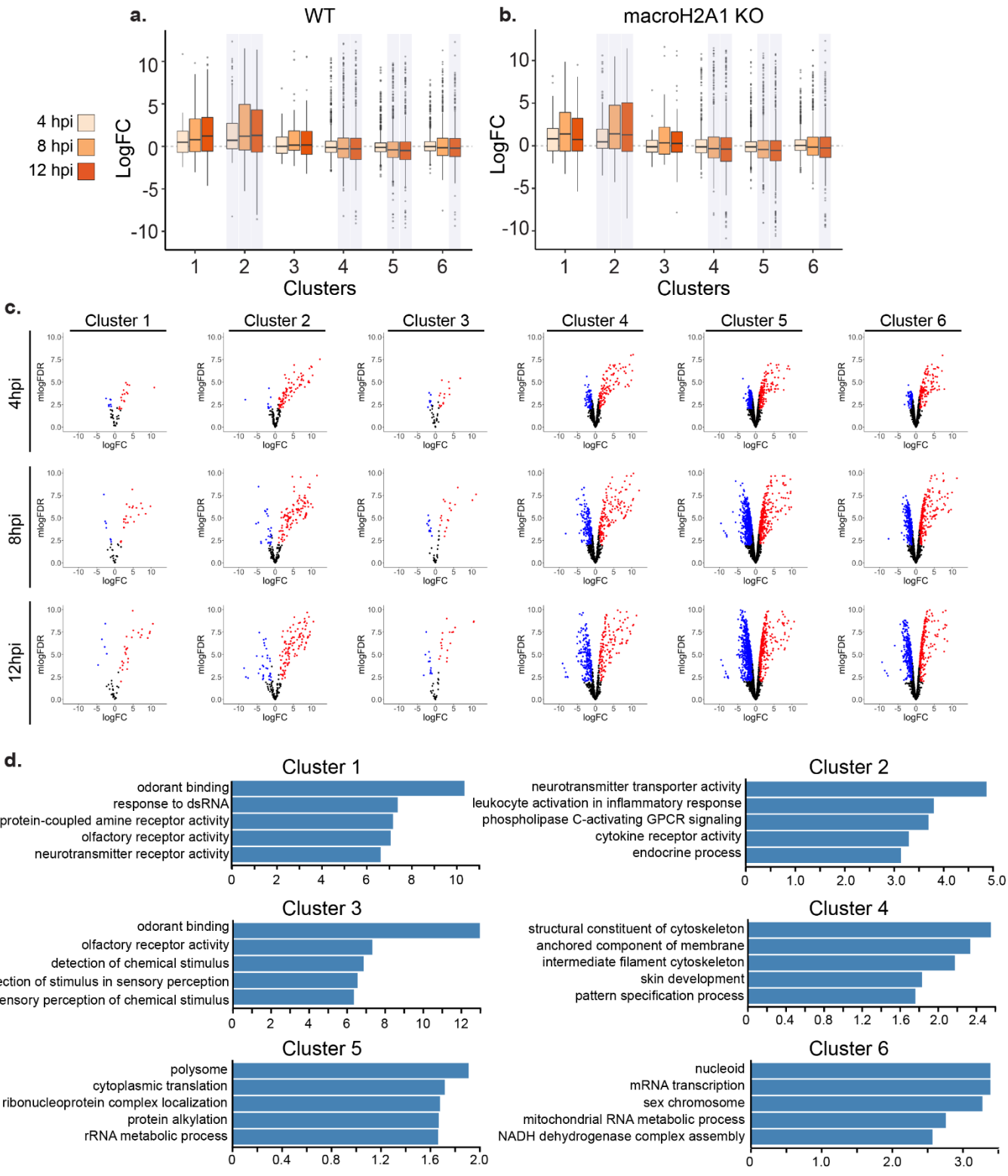
a.
WT
b.
macroH2A1 KO
4 hpi
8 hpi
12 hpi
LogFC
Clusters
c.
Cluster 1
Cluster 2
Cluster 3
Cluster 4
Cluster 5
Cluster 6
4hpi
8hpi
12hpi
mlogFDR
logFC
d.
Cluster 1
odorant binding
response to dsRNA
G protein-coupled amine receptor activity
olfactory receptor activity
neurotransmitter receptor activity
Cluster 2
neurotransmitter transporter activity
leukocyte activation in inflammatory response
phospholipase C-activating GPCR signaling
cytokine receptor activity
endocrine process
Cluster 3
odorant binding
olfactory receptor activity
detection of chemical stimulus
detection of stimulus in sensory perception
sensory perception of chemical stimulus
Cluster 4
structural constituent of cytoskeleton
anchored component of membrane
intermediate filament cytoskeleton
skin development
pattern specification process
Cluster 5
polysome
cytoplasmic translation
ribonucleoprotein complex localization
protein alkylation
rRNA metabolic process
Cluster 6
nucleoid
mRNA transcription
sex chromosome
mitochondrial RNA metabolic process
NADH dehydrogenase complex assembly

Figure 2.5. MacroH2A1 and H3K27me3 presence on host genomes correlates with decreased transcription. A) Box plots of total host RNA from RNA-seq in HFF-T WT for genes overlapping clusters from Figure 2. Kolmogrov-Smirnov test (in R) was performed comparing logCPM values of genes at each time point with logCPM values of genes from mock dataset for each cluster. The p-values were corrected for multiple testing, and the time points and clusters with corrected p-value less than 0.05 are shaded. B) Same as (a) for macroH2A1 KO HFF-T cells. C) Host differential RNA levels between WT and macroH2A1 KO HFF-T cells from RNA-seq at 4-,8-, and 12 hpi by cluster as indicated. N = 3 biological replicates. Volcano plot for host genes in each cluster is plotted as in Fig 3a with log(Fold Change) on x-axis and -1xlog(False Discovery Rate) plotted on the y-axis. Points without significant change in expression are plotted in black, significant reduction in expression are plotted in blue, and significant increase in expression are plotted in red. D) Enrichment gene sets from gene ontology (GO) analysis of genes belonging to each cluster as indicated. P-value <0.001 and FDR was <0.05 for all shown GO clusters.

To determine whether these changes in RNA reflected changes in transcription, we analyzed published 4sU-RNA-labeling data during HSV-1 infection (22). The time course comparison revealed that in clusters 5 and 6, where we found an increase in macroH2A1 and H3K27me3 presence during infection, the 4sU-labeled RNA decreased at 8hpi compared to mock, indicating that the gain in heterochromatin correlates with a reduction in active transcription (Figure 2.6 a). Anticorrelation between transcription and heterochromatin gain is also seen in clusters 1, 2, and 3, which feature a loss of macroH2A1 and H3K27me3, and show a significant increase in active transcription. Interestingly, cluster 4 diverged between total RNA and 4sU-RNA data: 4sU-RNA increased whereas total RNA decreased. This indication of active transcription explains why cluster 4 features a weak macroH2A1 gain. Taken together, these results indicate that macroH2A1 and H3K27me3 presence correlates with a decrease in transcription in active regions. Interestingly, this 4sU-RNA labeling dataset also included cells treated with heat shock and salt stress. We analyzed these conditions and found that under these treatments, once again clusters 5-6 had reduced transcript levels (Figure 2.6 b-c). These results strongly indicate that the global changes in transcription, which we defined by redistribution of macroH2A1, are a universal stress response.

Finally, we asked if the gain or loss of macroH2A1 happened across previously defined genome compartments (23). We determined the distribution of the eigenvector corresponding to A/B compartments for IMR90 Hi-C data from the 4DN project (24). Here, positive values correspond to the A compartment, which features higher gene density and accessible or active chromatin, whereas negative values correspond to the B compartment, which features inactive chromatin. All clusters except cluster 2 are significantly biased towards one of the compartments: clusters 1 and 3 are significantly biased towards compartment B, whereas clusters 4-6 are significantly biased towards compartment A (Figure 2.6 d). Strikingly, the median of the clusters increases moving from Cluster 1 to Cluster 6, correlating with macroH2A1 gain. Thus, macroH2A1 gains and losses happen in distinct genomic compartments upon HSV-1 infection. In summary, macroH2A1 and H3K27me3 gain correlates with decreased transcription over the course of HSV-1 infection or stress response in transcriptionally active compartments.

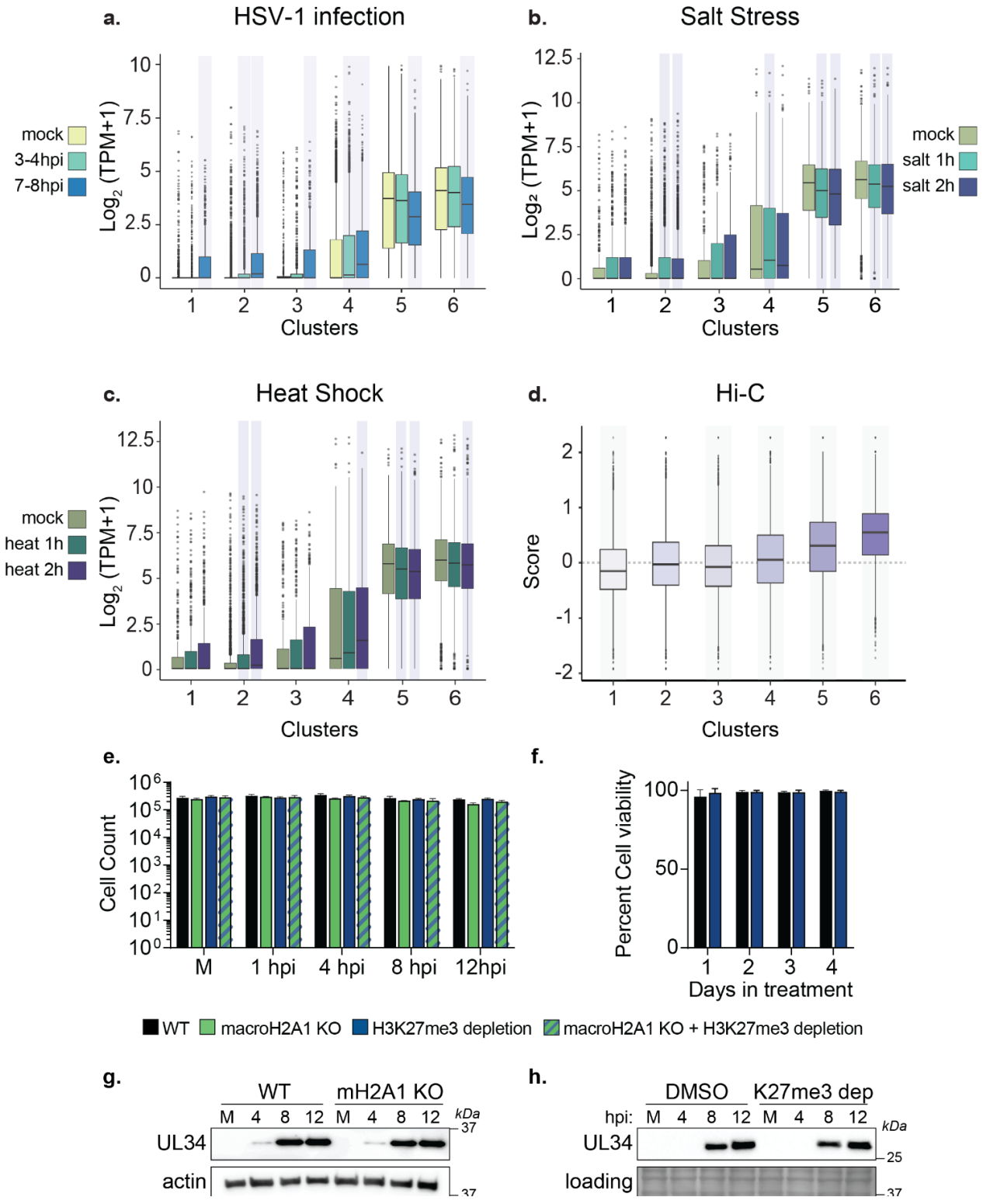
a.
HSV-1 infection
mock
3-4hpi
7-8hpi
Log2 (TPM+1)
Clusters
b.
Salt Stress
mock
salt 1h
salt 2h
c.
Heat Shock
mock
heat 1h
heat 2h
d.
Hi-C
Score
e.
Cell Count
M
1 hpi
4 hpi
8 hpi
12hpi
f.
Percent Cell viability
Days in treatment
WT
macroH2A1 KO
H3K27me3 depletion
macroH2A1 KO + H3K27me3 depletion
g.
WT
mH2A1 KO
kDa
UL34
actin
h.
DMSO
K27me3 dep
hpi:
UL34
loading

Figure 2.6. Clusters with more macroH2A1 and decreasing transcription during HSV-1 infection also show less transcription after salt stress or heat shock and correlate with active compartments. A) 4sU-RNA counts for genes from(22) overlapping with clusters from Figure 2 shown as box plots. Kolmogrov-Smirnov test (in R) was performed comparing logCPM values of genes at each time point with logCPM values of genes from mock dataset for each cluster. The p-values were corrected for multiple testing, and the time points and clusters with corrected p-value less than 0.05 are shaded. For all box plots in this figure, lower and upper hinges correspond to the first and third quartiles (the 25th and 75th percentiles). The upper whisker extends from the hinge to the largest value no further than 1.5 * IQR from the hinge (where IQR is the inter-quartile range, or distance between the first and third quartiles). The lower whisker extends from the hinge to the smallest value at most 1.5 * IQR of the hinge. Data beyond the end of the whiskers are called “outlying” points and are plotted individually. B) Replicate RPKM values from published 4sU-RNA-seq data(22) (GSE100469) from HFF treated with 80mM KCl (increase in final concentration) for 1 and 2 hours were converted to TPM, averaged, and intersected with gene lists for each of the six clusters. The distribution of the log2(TPM+1) for genes in each cluster is shown as boxplots. C) Same as (b) for heat stress (44^{o}C) also from GSE100469. D) Box plots of Hi-C eigenvector scores of regions overlapping with clusters from Figure 2. The Hi-C compartment eigen vector scores were obtained from 4DN project website. Wilcoxon signed rank test with alternate hypothesis that the true location is not equal to 0 was performed on the distribution of eigen vector scores for each cluster. The p-values were corrected for multiple testing, and the clusters with corrected p-value less than 0.05 are shaded. Bonferroni correction was used for p-value adjustments. E) Cell counts for experiments as described in Figure 3b-h. N = 3 biological replicates. No significance by paired t-test. Error bars represent the SEM of three biological replicates. F) Cell viability of HFF-T in DMSO or 10 μM Tazemetostat for 4 days post treatment. N = 3 biological replicates. No significance by paired t-test. Error bars represent the SEM of three biological replicates. G) Representative western blots of HSV-1 protein UL34 in WT and macroH2A1 KO HFF-T cells during HSV-1 infection at mock infected (M) or 4-, 8-, and 12 hpi. Actin is shown as loading control. H) Representative western blots of HSV-1 protein UL34 in WT and H3K27me3 depleted cells during HSV-1 infection at mock infected (M) or 4-, 8-, and 12 hpi. Ponceau stain is shown as loading control.

2.6 Loss of macroH2A1 or H3K27me3 results in reduced viral progeny but does not affect viral genome or protein accumulation

To determine the impact of macroH2A1 in HSV-1 infection, we infected WT and macroH2A1 KO HFF-T cells with HSV-1. First, we used RNA-seq to compare viral transcripts in WT and macroH2A1 KO cells. We found no significant change in viral transcripts at 4-, 8-, or 12 hpi between the two cell types (Figure 2.7 a). Next, we examined viral protein accumulation and observed similar levels of ICP0 (immediate early (25)), VP16 (early (26)) and glycoprotein H (gH, late (27)) in both wild type (WT) and macroH2A1

KO cells (Figure 2.7 b). We also examined the impact of H3K27me3 on HSV-1 infection by treatment with tazemetostat to inhibit EZH2 and deplete H3K27me3 levels (as in Figure 2.1). Tazemetostat treatment at 10 μM for multiple days did not impact cell counts or cell viability (Figure 2.6 e-f). To examine any synergistic effects of both heterochromatin markers, we treated both WT and macroH2A1 KO cells with tazemetostat. We found that accumulation of viral proteins ICP0, VP16, and gH were not affected by the reduction of H3K27me3, with or without macroH2A1 (Figure 2.7 b-d and Figure 2.6 g-h). Consistent with our findings, a previous report also showed no change in viral transcripts when THP-1 cells were treated with 10 μM tazemetostat prior to infection(28). These data indicate that despite changes to heterochromatin dynamics, viral RNA and protein production is not affected by the loss of macroH2A1. Additionally, depletion of H3K27me3 does not impact viral protein production.

We next examined HSV-1 replication under the same conditions and measured viral genome accumulation by droplet digital PCR (ddPCR). We observed no significant difference in viral genome accumulation between WT and macroH2A1 KO cells (Figure 2.7 e, black and green bars), indicating that neither HSV-1 replication nor protein production is affected by macroH2A1 loss. We found that reduction of H3K27me3 did not significantly affect viral genome accumulation compared to control (Figure 2.7 e, black and blue bars). We observed no additional decrease in viral genomes in macroH2A1 KO cells treated with the inhibitor, suggesting that regardless of H3K27me3 levels, loss of macroH2A1 does not impact viral replication as we observed above (Figure 2.7 e, striped bars).

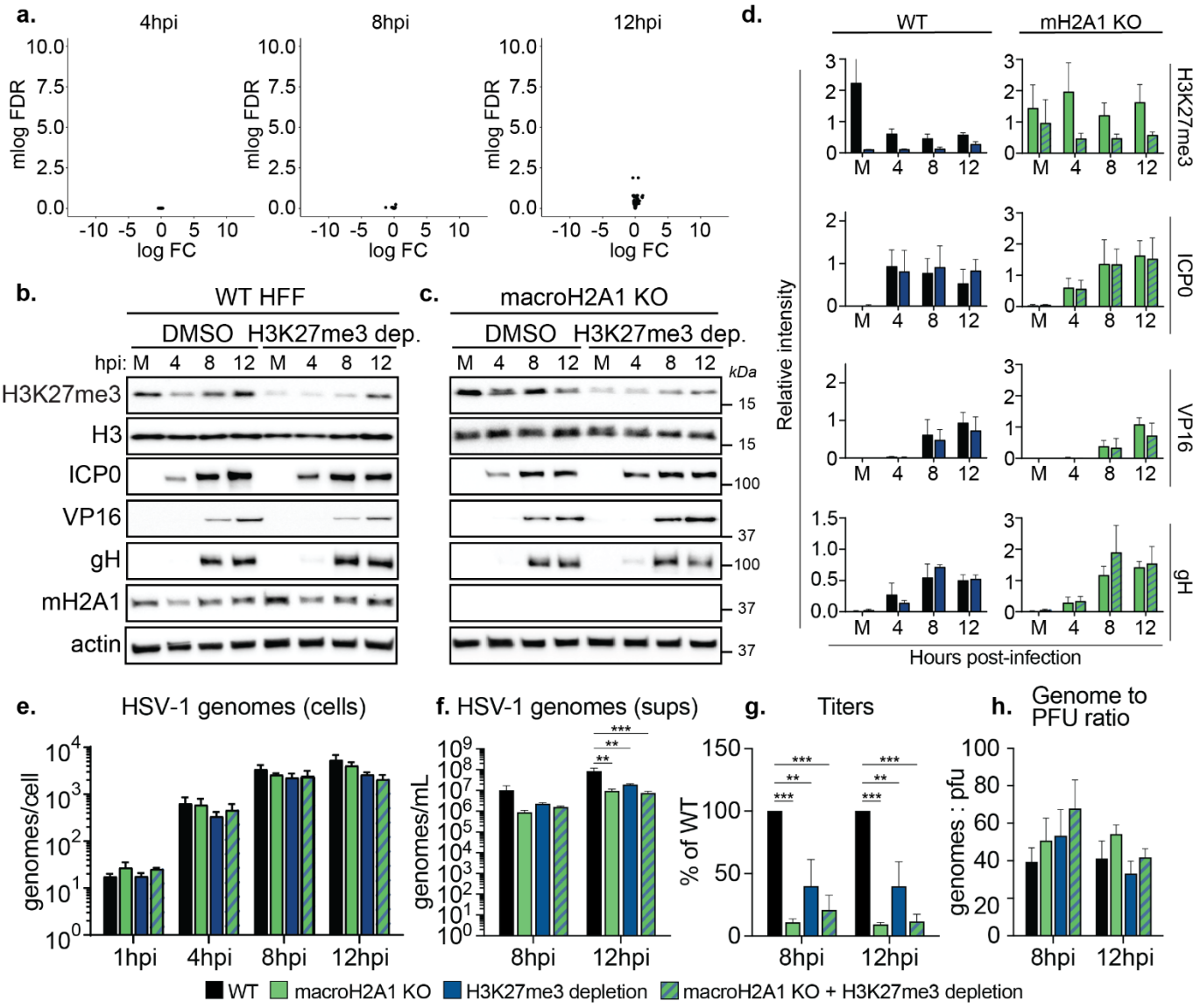

Figure 2.7. HSV-1 requires heterochromatin marks macroH2A1 and H3K27me3 for progeny production but not replication or protein production. A) Volcano plots comparing differential viral RNA levels between WT and macroH2A1 KO HFF-T cells from RNA-seq at 4-,8-, and 12 hpi. N = 3 biological replicates. Genes are plotted with log(Fold Change) on x-axis and -1xlog(False Discovery Rate) plotted on the y-axis. Points without significant change in expression are plotted in black. There are no significantly changing genes. B) Representative western blots of proteins shown as indicated upon H3K27me3 depletion or DMSO control treated HFF-T cells during HSV-1 infection at mock infected (M) or 4-, 8-, and 12 hpi. Actin and H3 are shown as loading controls. C) Representative western blots as in (b) for macroH2A1 KO HFF-T cells. D) Mean relative intensity of H3K27me3, ICP0, VP16, and gH normalized to H3

quantified from western blots as in (b) and (c) as indicated from WT or macroH2A1 KO. Error bars represent ± SD of three biological replicates. E) Droplet digital (ddPCR) quantification of HSV-1 genomes extracted from infected cells as indicated for each time point. Error bars represent the SEM of three biological replicates. No significance by Dunnett's multiple comparisons test. F) ddPCR quantification of HSV-1 genomes released from cells treated as indicated and isolated from supernatants (sups). Error bars represent the SEM of three biological replicates, ** $p < 0.01$, *** $p < 0.001$ by Dunnett's multiple comparisons test. G) Infectious progeny produced from HSV-1 infected cells treated as indicated and quantified by plaque assay. Viral yield is indicated as the percent yield compared to WT at each indicated time point. Error bars represent the SEM of three biological replicates, ** $p < 0.01$, *** $p < 0.001$ by Dunnett's multiple comparisons test. H) Genome to PFU ratio 8 and 12 hpi in indicated conditions as measured by paired plaque assays and ddPCR of genomes isolated from supernatants as in (f). Error bars represent the SEM of three biological replicates, no significance by Dunnett's multiple comparison test.

To determine the impact of macroH2A1 or H3K27me3 loss on viral progeny production, we measured viral genome accumulation in the supernatant. We discovered a 9-fold decrease in the levels of HSV-1 genomes produced in the supernatant of macroH2A1 KO cells compared to those produced from WT cells at 12 hpi (Figure 2.7 f, green and black bars). We found a significant 4-fold decrease at 12 hpi from tazemetostat-treated cells compared to DMSO-treated (Figure 2.7 f, blue bars). Because viral genomes measured in the supernatant could also capture defective particles, we also measured infectious progeny by plaque assay. We further discovered that infectious progeny produced from macroH2A1 KO cells were dramatically decreased compared to those produced from WT cells at 8 and 12 hpi (Figure 2.7 g, green and black bars). Infectious progeny production was also significantly decreased at 12 hpi in cells with depleted H3K27me3 (Figure 2.7 g black and blue bars). Interestingly, H3K27me3 reduction in macroH2A1 KO cells did not result in any additional defects, suggesting the two markers function in the same genetic pathway (Figure 2.7 e-g, striped bars). Furthermore, we did not observe any significant differences in the ratio of genomes to plaque forming units (pfu) upon loss of macroH2A1, H3K27me3, or both, compared to control conditions (Figure 2.7 h), indicating that loss of these markers does not result in significantly more defective particles. This effect was consistent across cell types with similar results observed in macroH2A1 KO RPE cells (Figure 2.8 a-g). These

data indicate that loss of macroH2A1 leads to a significant defect in infectious viral progeny but not viral protein, RNA, or genome accumulation. Similarly, depletion of H3K27me3 results in a significant reduction in infectious progeny but no significant changes in viral protein or genome accumulation. Therefore, we conclude that macroH2A1 and H3K27me3 are important either for proper capsid assembly or efficient viral egress.

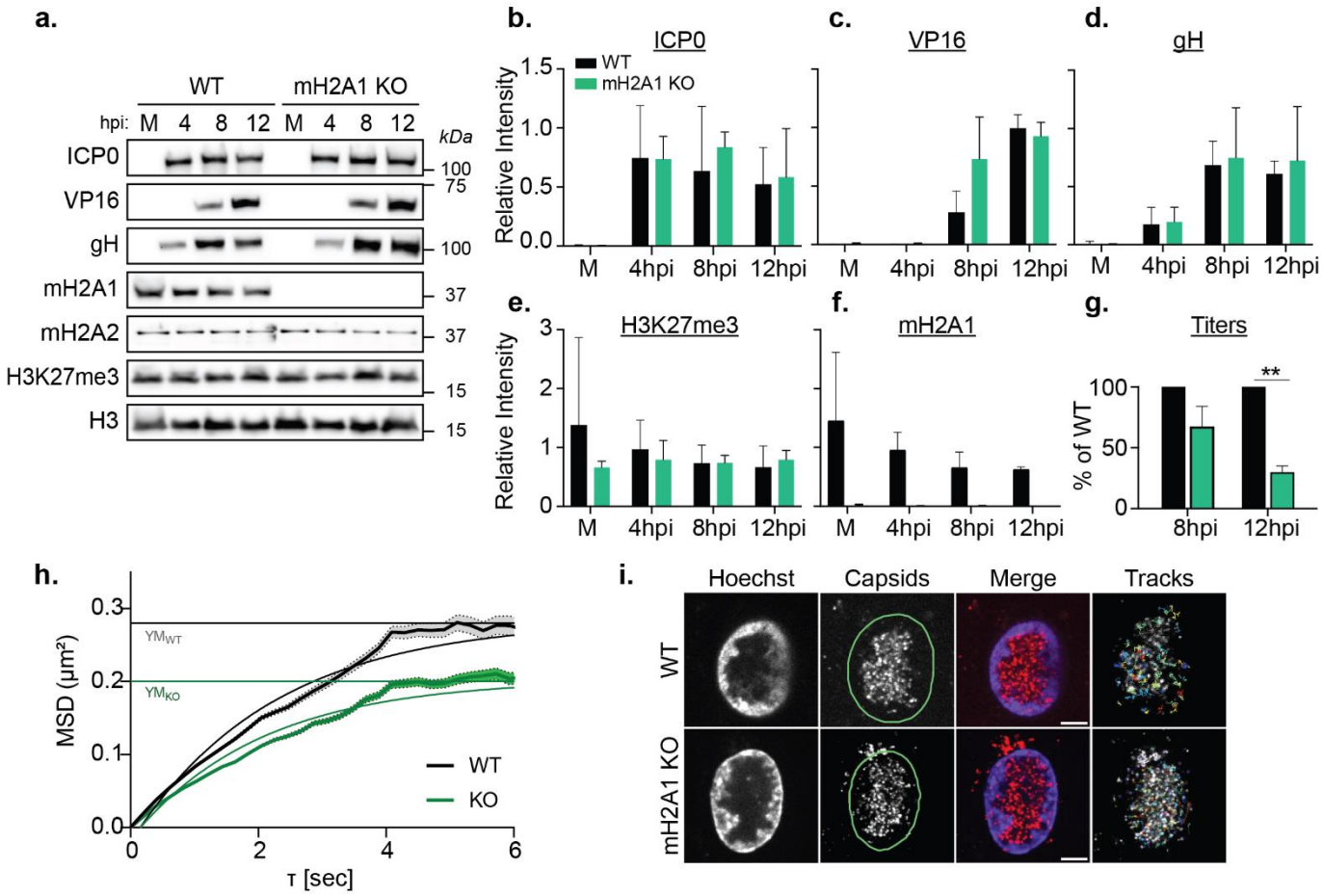

Figure 2.8. MacroH2A1 is also required for efficient viral egress, but not protein production, in RPE cells. A) Western blot of proteins as indicated in mock(M) or 4-, 8-, and 12 hpi in WT and macroH2A1 KO RPE cells. H3 is shown as a loading control. B) Mean relative

intensity of ICP0 over H3 at indicated timepoints during HSV-1 infection in WT or macroH2A1 KO RPEs as in (a). Error bars represent ± SD from three biological replicates. C) Same as (b) for VP16. D) Same as (b) for gH. E) Same as (b) for H3K27me3. F) Same as (b) for macroH2A1. G) Infectious progeny produced by WT or macroH2A1 knockout RPE cells quantified by plaque assay on cell-free supernatant. Viral yield calculated as in Fig 3g for conditions as indicated, ** p. < 0.01 by unpaired t-test. Error bars represent the SEM of three biological replicates. H) Average mean squared displacement (MSD) plots +/- SEM of nuclear capsid tracks in HSV-1 mCherry-VP26 infected WT or macroH2A1 KO RPE cells at 8 hpi. Non-linear fits of mean MSD plots and exponential plateau as dotted lines (YM) are indicated. I) Representative live-cell images of HSV-1 mCherry-VP26 infected WT or macroH2A1 KO RPE nuclei at 6 hpi and corresponding tracks from singleparticle tracking used for MSD analysis in (h). Scale bar is 5 μm.

2.7 Clinical HSV-1 isolates also require macroH2A1 for progeny production, but not replication or protein production.

To determine how robust the requirement for macroH2A1-dependent chromatin is for HSV-1 egress, we used clinical HSV-1 viruses isolated from “low-shedding” or “high-shedding” patients. We measured protein accumulation at 4, 8, and 12 hpi and viral genome accumulation in cells and supernatant by ddPCR. We found that there was no significant change in viral protein or viral genome accumulation for either clinical isolate in macroH2A1 KO cells (Figure 2.9 a-d). We measured viral genomes in the supernatant and found that there was a modest reduction in HSV-1 genomes in the supernatant of macroH2A1 KO cells compared to control cells (Figure 2.9 e, green bars). For both clinical isolates, we found that macroH2A1 KO cells produced significantly fewer progeny than WT cells at 12 hpi (Figure 2.9 f). Taken together, these results indicate that egress of clinically isolated HSV-1 is also dependent on macroH2A1.

It is important to note that while we measured significantly lower infectious progeny produced from the infected macroH2A1 KO cells, we do not detect a corresponding increase in intracellular genomes. This is likely because we reached the maximum detection limit of our system at 8hpi such that there is no significant difference in the genomes detected between 8 and 12hpi (Figure 2.7 e and Figure 2.9 d), consistent with the notion that chromatin is the

bottleneck for HSV-1 egress.

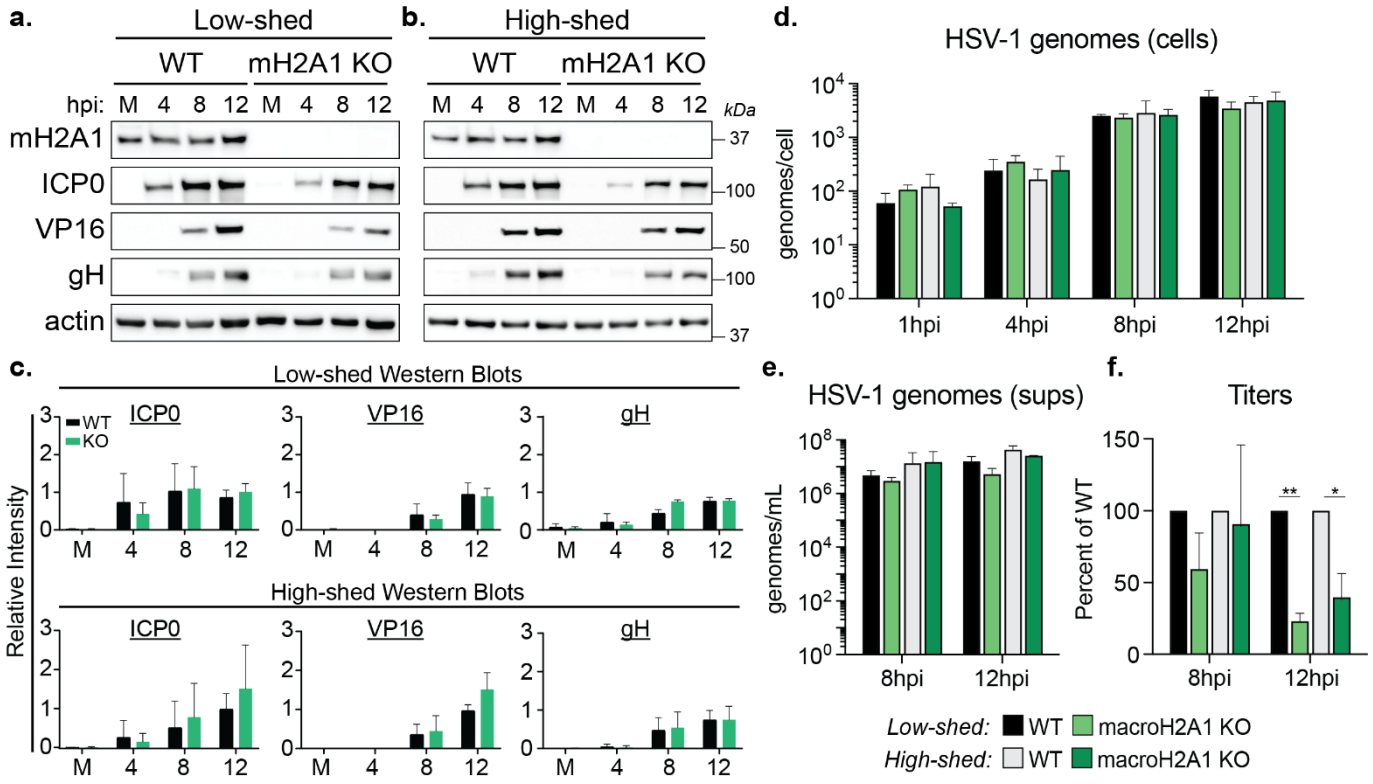

Figure 2.9. Clinical HSV-1 isolates also require heterochromatin mark macroH2A1 for progeny production but not replication or protein production. A) Western blots of proteins as indicated for mock (M) 4-, 8-, and 12-hpi in WT and macroH2A1 KO cells infected with a low-shedding HSV-1 clinical isolate. B) Western blot as in (a) for a high-shedding HSV-1 clinical isolate. C) Mean relative intensity of ICP0, VP16, and gH from low-shed (top) or high-shed (bottom) clinical isolate western blots. Error bars represent ± SD of three biological replicates, no significance by unpaired t-test. D) ddPCR quantification of HSV-1 genomes extracted from infected cells as indicated for each time point in WT and macroH2A1 KO cells infected with HSV-1 low- and high-shedding clinical isolates. Error bars represent the SEM of three biological replicates. No significance by Tukey's multiple comparisons test. E) ddPCR quantification of HSV-1 genomes released from cells infected with clinical isolates of HSV-1 as indicated and isolated from supernatants (sups). Error bars represent the SEM of three biological replicates. No significance by Tukey's multiple comparisons test. F) Infectious progeny of cells as indicated infected with clinical HSV-1 isolates quantified by plaque assay. Viral yield is indicated as the percent yield compared to WT, error bars represent the SEM of three biological replicates, * $p. < 0.05$, ** $p < 0.01$ by Tukey's multiple comparisons test.

2.8 MacroH2A1 or H3K27me3-dependent heterochromatin is critical for efficient HSV-1 nuclear egress.

Our results indicate that HSV-1 capsids in the nucleus access the nuclear membrane through channels bracketed by highly dense chromatin at the nuclear periphery (Figure 2.1), consistent with previous reports in other cell types (9, 16). We found that loss of macroH2A1 or depletion of H3K27me3 resulted in decreased heterochromatin in the nuclear periphery (Figure 2.1) and caused a decrease in infectious virus progeny released from infected cells (Figure 2.7 and 2.9). Therefore, we hypothesized that efficient HSV-1 egress out of the nuclear compartment requires macroH2A1- or H3K27me3-dependent heterochromatin in the nuclear periphery. To test this, we infected macroH2A1 KO cells, visualized nuclei by TEM and quantified capsids in the nucleus (Figure 2.10 a). We found that infected macroH2A1 KO nuclei have significantly more HSV-1 capsids than those of WT cells (Figure 2.10 b, WT control cells seen in Figure 2.1 b), indicating that loss of macroH2A1-dependent heterochromatin is detrimental for efficient nuclear egress. Similarly, we used tazemetostat treatment to deplete H3K27me3 levels to a steady state, infected cells with HSV-1, and visualized capsids in the nuclei of infected cells by TEM. Strikingly, we found that significantly more capsids accumulated at the nuclear membrane compared to control cells (Figure 2.10 c, WT control cells seen in Figure 2.1 b). We quantified this difference by counting the number of capsids that accumulated at the inner nuclear membrane (INM) at any one location and found that significantly more capsids lined up at the INM upon H3K27me3 depletion (Figure 2.10 d).

To determine whether capsid assembly was impacted by heterochromatin disruption, we quantified capsid type as a proportion of the total capsids from our TEM. Herpesvirus infection produces three subtypes of capsids: A capsids that are empty, B capsids which contain scaffolding proteins, and C capsids that contain viral DNA and are considered the precursor to infectious virions (29, 30) (Figure 2.10 e). We quantified the proportion of each capsid type in WT and macroH2A1 KO cells and found no difference in the proportion of each capsid type (Figure 2.10 f). We carried out the same analysis upon

infection in H3K27me3-depleted cells and similarly found no difference in the proportion of capsid type (Figure 2.10 g). Furthermore, we examined the levels of viral nuclear egress complex (NEC) component UL34 to investigate whether loss of this important factor may explain the decreased titers. We did not observe any change in UL34 levels by western blot upon loss of macroH2A1 nor depletion of H3K27me3 (Figure 2.6 g-h), indicating that this is unlikely to account for the phenotype. Together, these results indicate that neither capsid formation nor NEC component levels are impacted by disruption of host heterochromatin. Rather, we conclude that it is the ability of the capsids to egress from the nuclear compartment that is dependent on heterochromatin. Taken together, these data demonstrate that macroH2A1 and H3K27me3-dependent heterochromatin is critical for efficient nuclear egress.

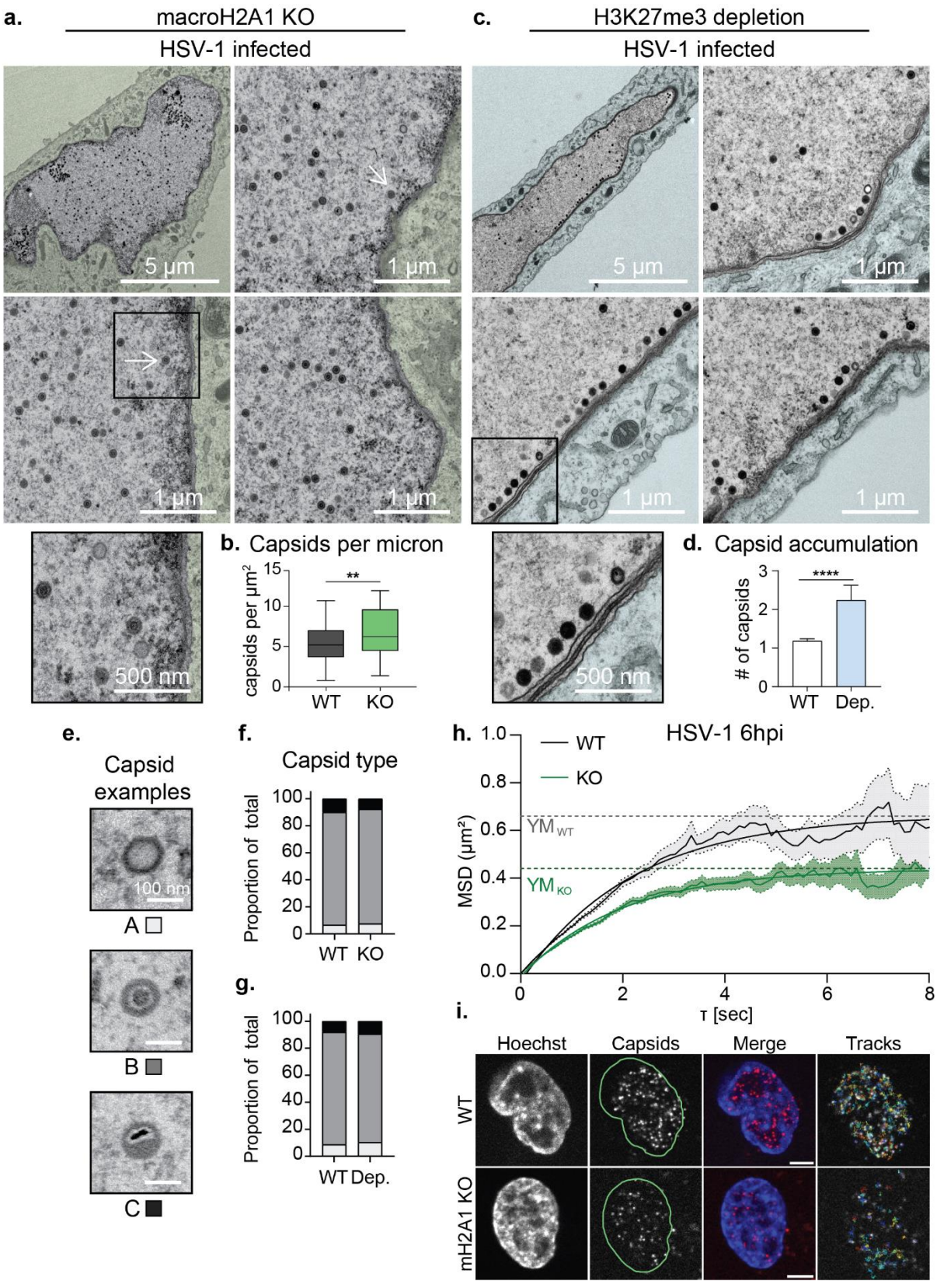
a.
macroH2A1 KO
HSV-1 infected
5 µm
1 µm
1 µm
1 µm
500 nm
b. Capsids per micron
capsids per µm²
15
10
5
0
**
WT
KO
c.
H3K27me3 depletion
HSV-1 infected
5 µm
1 µm
1 µm
1 µm
500 nm
d. Capsid accumulation
# of capsids
3
2
1
0
****
WT
Dep.
e.
Capsid examples
100 nm
A
B
C
f.
Capsid type
Proportion of total
100
80
60
40
20
0
WT
KO
g.
Proportion of total
100
80
60
40
20
0
WT
Dep.
h.
HSV-1 6hpi
WT
KO
MSD (µm²)
1.0
0.8
0.6
0.4
0.2
0.0
YM WT
YM KO
0
2
4
6
8
τ [sec]
i.
Hoechst
Capsids
Merge
Tracks
WT
mH2A1 KO

Figure 2.10. HSV-1 requires macroH2A1- and H3K27me3-dependent heterochromatin for movement through host chromatin to access the inner nuclear membrane (INM). A) TEM images of representative macroH2A1 KO HFF-T nuclei infected with HSV-1 at 18 hpi. Insets show enlarged views of respective box. Arrows indicate HSV-1 capsids. Scale bars as indicated. B) Quantification of capsids within nuclei compared to Figure 1b. Number of capsids was normalized according to nucleus area in μm^2, p=0.0036 (n=40 WT, n=55 mH2A1 KO) by unpaired t-test. For the box plot, the box marks upper and lower quartiles, center line marks median, and error bars denote minimum and maximum values for the population. C) TEM images of representative H3K27me3 depleted nuclei infected with HSV-1 presented as in (a). D) Quantification of capsids accumulating at the INM. The number of capsids within 200 nm of the membrane scored per chain as capsids within 300 nm of another capsid, p=0.0008 by Mann-Whitney test (n= 61 for DMSO, n= 51 for H3K27me3 depleted). Error bars represent $\pm$ SEM of the population. E) TEM images of representative A (empty), B (intermediate; scaffolding proteins, but no genome), and C (full) HSV-1 capsids. Scale bars as noted. F) Quantification of capsid type within nuclei from (a) in WT and macroH2A1 KO cells. Values for each capsid type are shown as a proportion of total capsids. No significance by Chi-square test, n= 120 capsids per condition. G) Quantification of capsid type as in (f) in nuclei from (c) in WT and H3K27me3 depleted cells. No significance by Chi-square test, n= 120 capsids per condition. H) Average mean squared displacement (MSD) plots +/- SEM of nuclear capsid tracks in HSV-1 mCherry-VP26 infected WT or macroH2A1 KO HFF-T cells at 6 hpi. Non-linear fits of MSD plots and exponential plateau as dotted lines (YM) are indicated. MSD plots represent 1148 tracks in 6 nuclei for WT and 993 tracks in 6 nuclei for macroH2A1. Plateaus are at YM_{WT}=0.66μm^2 and YM_{KO}=0.44μm^2. I) Representative live-cell images of HSV-1 mCherry-VP26 infected WT or macroH2A1 KO HFF-T nuclei at 6 hpi and corresponding tracks from single particle tracking used for MSD analysis in (h). Scale bar is 5 μm.

We and others (8, 31) have previously shown that infection-induced chromatin modifications promote capsid translocation to the INM. Specifically: i) HSV-1 infection alters host heterochromatin such that open space is induced at heterochromatin boundaries, termed "corrals," in which viral capsids diffuse, and ii) the movement of viral capsids through the host heterochromatin is the rate-limiting step in HSV-1 nuclear egress. We therefore hypothesized that macroH2A1 was critical for the infection-induced formation of open space at heterochromatin boundaries. To test whether the egress defect was a result of restricted capsid movement, we employed live-cell imaging and single particle tracking to directly measure the effect of macroH2A1-dependent heterochromatin changes on chromatin corral size and viral capsid motility. Using an HSV-1 mutant expressing mCherry-VP26, we found that the mean squared displacement (MSD) of diffusing capsids in macroH2A1 KO cells plateaued at lower levels

than in WT cells indicating a smaller corral size (Figure 2.10 h-i). To determine the approximate reduction on corral diameter, we fitted the MSD curves using a non-linear fit with an exponential plateau in the statistical software GraphPad Prism to determine the exact values (see Materials and Methods). The plateau height YM was 0.44 μm^2 for macroH2A1 KO cells and 0.66 μm^2 for

WT cells. We calculated the corral diameter by the following equation (modified from (31))

$$d_{corral} = d_{particle} + 2 \times \sqrt{YM}$$

where d_{corral} is the corral diameter, $d_{particle}$ is the estimated HSV-1 capsid size of 125 nm(32), and YM is the plateau of the respective MSD curve. This resulted in 1.75μm mean corral diameter for WT and 1.45μm for macroH2A1 KO cells, indicating that corrals in knockout cells were about 300 nm smaller than in WT cells, restricting capsid diffusion in cellular chromatin. We observed similar limitations in capsid movement in macroH2A1 KO RPE cells with a decrease in corral size of about 165 nm compared to WT cells (Figure 2.9 h-i). These results are consistent with the finding that macroH2A1 limits chromatin plasticity both in vitro (33) and in cells (34) and support our hypothesis that macroH2A1-dependent heterochromatin is critical for the translocation of HSV-1 capsids through the host chromatin to reach the INM. Furthermore, these data support a model in which macroH2A1 supports chromatin rearrangement induced during infection (Figure 2.11).

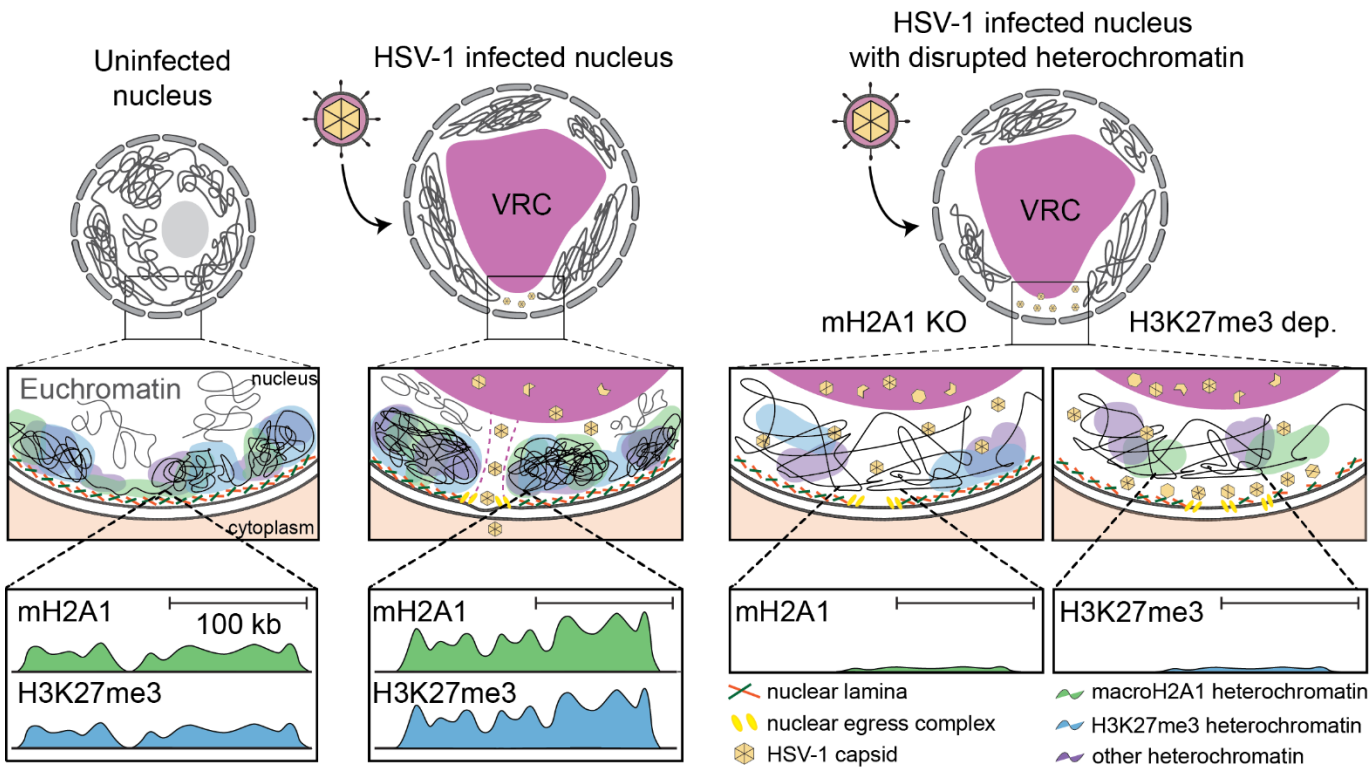

Figure 2.11. Model for heterochromatin support of HSV-1 nuclear egress. Left: Model of previously described chromatin movement during HSV-1 infection. Right: Proposed model of effects of heterochromatin disruption in HSV-1 infection.

2.9 Discussion:

Host chromatin is emerging as a newly appreciated critical barrier to viral success. Elegant studies showed that HSV-1 infection induces host chromatin redistribution to the nuclear periphery (2, 9). Here, we showed that viral capsids subsequently egress through low-density regions of chromatin indicated through less staining (Figure 2.1), consistent with reports in different cell types (16). We investigated the impact of heterochromatin markers histone variant macroH2A1 and H3K27me3 on chromatin architecture and HSV-1 infection. We found that loss of macroH2A1 resulted in significantly less heterochromatin visible in the nuclear periphery by TEM in HFF cells (Figure 2.1), similar to what was observed in hepatoma cells (14). To our knowledge, this is the first instance of TEM imaging of heterochromatin upon depletion of H3K27me3, which produced a similar phenotype to macroH2A1 KO

with significantly less heterochromatin in the nuclear periphery (Figure 2.1). Visualization of chromatin by TEM is inherently challenging, which is why we carefully compared our chromatin-disrupted conditions only to their respective controls that were processed on the same day and the same time. Our findings are consistent with those reported from other groups including the importance of macroH2A for nuclear integrity (14, 15), therefore, we are confident in our conclusion that heterochromatin is disrupted in the macroH2A1 KO and H3K27me3-depleted conditions.

We then demonstrated that macroH2A1 and H3K27me3 bind broad regions of the host genome that are redistributed during HSV-1 infection (Figure 2.3). Our chromatin profiling analysis required a custom algorithm to accommodate the massive domains created by macroH2A1 and H3K27me3, consistent with regions large enough to be visible by TEM. We demonstrated that the regions that gain macroH2A1 and H3K27me3 are primarily found in transcriptionally active compartments defined by Hi-C in uninfected cells, supporting the idea that newly formed heterochromatin is globally redistributed during HSV-1 infection. Unfortunately, as our controls strongly indicated a lack of specific signal from our viral genome reads, at this time we are unable to make conclusions about the presence or absence of these marks from the viral genome (Figure 2.4). Future technical advances will allow for chromatin profiling of viral genomes from single cells to more accurately interpret chromatin marks during infection on the lytic viral genome.

Arbuckle *et al.* showed that high dose inhibition of EZH2, the enzyme that deposits heterochromatin mark H3K27me3, caused upregulation of interferon stimulated genes (ISGs) creating an antiviral state in the cell in the absence of infection (35). This antiviral state was then shown to prevent infection of several viruses, including HSV-1, adenovirus, HCMV and ZIKA (35). This broad response suggests that it was not specific to HSV-1 but rather a blunt disruption of host heterochromatin to which the cell reacted by initiating defense mechanisms. In contrast, H3K27me3 levels can be decreased to stable levels, or a steady-state, using a low dose of inhibition over several days. Low dose inhibition of EZH2 is being developed to target cancer types with EZH2 mutations as these cancers are sensitive to

inhibition while WT cells are unaffected (36, 37). This is important because we can differentiate between blunt force inhibition of EZH2 (i.e. high dose) causing an immune response and may have off target effects on other methyltransferases, and low dose inhibition (i.e. steady-state) that decreases total heterochromatin but has little effect on other targets or global cellular processes. Further, low dose inhibition, as we used, was reported to have no impact on accumulation of HSV-1 transcripts (28). Finally, our analysis of 4sU-RNA generated from heat shock and salt stress demonstrates that there is a decrease in transcription in genes found in macroH2A1-defined clusters upon either stressor (Figure 2.6). Thus, our finding that depletion of H3K27me3 does not impact viral protein or genome accumulation is a distinct scenario from what has been previously reported. In addition, the striking phenotype of capsids lined up at the INM suggest a different mechanism of involvement of H3K27me3 compared to macroH2A1 in which capsids are trapped throughout the nucleus. It will be interesting to determine in future work how these two marks work together or in concert to promote nuclear egress. Together, these results support a model in which host heterochromatin formation creates a structural highway for HSV1 capsids to successfully access the INM and egress (Figure 2.11).

Mining of proteomics on histone marks indicates that several heterochromatin marks including H3K9me3 are also changing during HSV-1 infection (3). This suggests that there may be other mechanisms of heterochromatin dynamics at play. It will be fascinating to consider the diverse implications of heterochromatin domains not only as a means of transcriptional regulation but also as a structural component that impacts many facets of viral infection. Our finding that macroH2A1-defined clusters exhibit decreases in transcription upon heat shock and salt stress suggests that global changes to heterochromatin are likely a consequence of the cell's stress response to infection that HSV-1 exploits to access the INM. Our results strongly indicate that it is the structural aspect of heterochromatin that is important for nuclear HSV-1 egress rather than transcription of any single gene or group of genes. Therefore, we propose that deposition of macroH2A1 and H3K27me3 in specific genomic regions during HSV-1 infection supports the formation of heterochromatin through which HSV-

1 capsids travel to reach the inner nuclear membrane. Our study also provides a functional mechanism of how viral capsids can access the INM by diffusion, in the absence of an active transport mechanism (8,31, 38). It is important to note that capsids may move more freely in the replication compartments than at the periphery and our live-tracing measurements were taken in the whole nucleus, including replication compartments and periphery. Because we assessed the average MSD for all particles detected within the confocal volume, we can conclude that macroH2A1 knockout has a significant impact on the MSD, which is likely due to a portion of capsids located in the nuclear periphery. When averaged together, the movement of capsids is significantly slower in the absence of macroH2A1-dependent heterochromatin, consistent with our model. At the inner nuclear membrane, capsids are aided by the nuclear egress complex, comprised of viral proteins UL34 and UL31, to bud into the inner nuclear membrane and fuse with the outer nuclear membrane for further maturation in the cytoplasm (7). Budding into the nuclear membrane also requires nuclear lamina disruption. Multiple reports describe that not only does lamina disruption occur independently of capsid formation, but that chromatin is likely the limiting factor in viral egress (39-45).

Together with our results, this suggests that there are multiple steps in the capsid's journey to the inner nuclear membrane preceding nuclear budding. In summary, our study demonstrates that the contribution of heterochromatin to the successful egress of HSV-1 capsids is a critical aspect of viral infection.

DATA AVAILIBILITY

The data generated are available in the published article and its online supplemental material.

The CUT&Tag and RNA-seq data can be found here: Series GSE209820.

Chapter 3: Viral Kinase manipulation of host heterochromatin promotes efficient docking of the HSV-1 nuclear egress complex

*The work in this chapter represents my contributions to a manuscript in collaboration with the laboratories of Matthew Weitzman (University of Pennsylvania) and Katarzyna Kulej (Memorial Sloan Kettering Cancer Center) to be submitted in Spring 2025. "We" is used throughout the chapter as the text will contribute to a large portion of the manuscript. I designed and performed the experiments presented here with input from Daphne Avgousti, Katarzyna Kulej, Srinivas Ramachandran, and Matthew Weitzman. Mass-spectrometry data in Figure 3.7 E-F and additional data discussed in text kindly provided by Katarzyna Kulej. The work here was supervised and edited by Daphne Avgousti.

Abstract:

Herpes simplex virus (HSV-1) progeny form in the nucleus and exit to successfully infect other cells. Newly formed capsids navigate complex chromatin architecture to reach the inner nuclear membrane (INM) and egress. Here, we demonstrate by a combination of proteomics and transmission electron microscopy (TEM) that HSV-1 capsids depend on heterochromatin associated with trimethylation on histone H3 lysine 27 (H3K27me3) and phosphorylation on serine 28 (H3S28Ph) to efficiently locate and dock at the viral nuclear egress complex (NEC) in the INM. We demonstrate that the NEC, consisting of UL31 and UL34, together with viral kinases Us3 and UL13, requires dually modified H3K27me3S28ph for capsids to localize to and efficiently dock at the NEC, without which nuclear budding of viral progeny does not occur. Our work demonstrates that HSV-1 both manipulates and takes advantage of the dynamic nature of host heterochromatin formation during infection for efficient nuclear egress.

3.1 Introduction:

Chromatin, which is a combination of DNA, RNA, and proteins, specifically refers to the state of eukaryotic DNA prior to condensing during prophase into the more widely recognized chromosome. The structure of chromatin is tightly regulated as transcription of genes is linked to chromatin accessibility. Regulation of chromatin is highly dynamic, allowing the cell to respond to its environment, and controlled by high levels of redundancy, to protect the cell from aberrant gene expression. Chromatin is organized into units called nucleosomes that consist of approximately 147bp of DNA wrapped around an octamer of histone proteins (1). Posttranslational histone modifications (or 'marks') are critical for defining the local conformation of chromatin. Marks such as trimethylation on the lysine 27 residue of histone H3 (H3K27me3), H3K9me3 are commonly associated with transcriptional repression (2) while acetylation is associated with activation (3). Additional marks on the histone tail can alter the original mark, one example of these "dual marks" is the phosphorylation of H3S28 next to H3K27 di- or trimethylation leading to chromatin decompaction (4).

Chromatin regulators include enzymes that post-translationally modify histones, enzymes that support the structure of the chromatin, and enzymes that directly modify the DNA or non-histone proteins in the chromatin structure (5). Histone Acetyltransferases (HATs) and Histone Deacetylases (HDACs) add and remove acetyl groups, respectively, on histone tails (6). These HDACs are themselves controlled by post-translational modifications, such as phosphorylation inhibiting function (7). Other chromatin regulators are also controlled by phosphorylation. For example, heterochromatin protein 1 gamma (HP1γ), a non-histone protein that helps condense heterochromatin, is phosphorylated to disrupt its interaction with DNA (8). Another example, is tripartite motif protein 28 (TRIM28), also called KAP1/TIF1β, recruits HP1 γ to histone methylation to support heterochromatin (9), when phosphorylated though TRIM28 acts

to relax chromatin (10). Nuclear lamin proteins, which support the nuclear structure, also play a role in maintaining chromatin structure (11–13).

Nuclear-replicating viruses takeover host chromatin and its regulators to successfully produce progeny (14). Herpes Simplex Virus-1 (HSV-1), a nuclear-replicating double stranded DNA virus, causes gross chromatin remodeling marginalizing chromatin to the nuclear periphery (15– 17). The virus then uses a unique mechanism of nuclear egress: progeny are first encapsulated by the inner nuclear membrane forming a vesicle that then fuses with the outer nuclear membrane and is released into the cytosol for final maturation (18). In HSV-1 lytic infection, newly formed capsids pass through gaps in the heterochromatin to reach the inner nuclear membrane and bud into single-virion vesicles (16, 19–22). This nuclear egress is facilitated by viral proteins UL31 (23), UL34(24, 25), and the viral kinase Us3 (17, 26–28). UL31 and UL34 are together referred to as the nuclear egress complex or NEC. HSV-1 also encodes a second serine/threonine kinase UL13 (29, 30), which directs the NEC and activates Us3 through phosphorylation (31).

Here we sought to further investigate the mechanisms that drive the chromatin rearrangement during HSV-1 infection. Chromatin rearrangements during HSV-1 infection are important for nuclear egress (16, 19–22). To further investigate the chromatin rearrangement during HSV-1 infection, we examined changes in levels and phosphorylation of proteins that participate in chromatin remodeling in a previously published mass spectrometry data set (33). Through personal communication with collaborators, we decided to further investigate the fact that lamin b, pre-lamin A/C, HP1γ/CBX3, HDAC2, and TRIM28 levels remain relatively stable over the course of HSV-1 infection by mass spectrometry**.** In contrast, phosphorylation of levels of lamin B, pre-lamin A/C, HP1γ/CBX3, HDAC2, and TRIM28 all increase significantly during HSV-1 infection. These phosphorylation changes were observed by mass spectrometry and validated by western blot (not permitted to be shown here).

In a similar manner, the dual histone mark H3K27me3S28ph increases over the course of infection. This increase differs from the above chromatin remodeling proteins in that the H3S28ph single mark does not change significantly over the course of infection, but the dual histone mark of H3K27me2/3S28ph does significantly increase, suggesting the H3K27 methylation is important for the direction of the phosphorylation mark. This is in line with previously published reports that H3S28ph triggers the release of the PRC2 complex from chromatin, suggesting H3K27me2/3 is added prior to phosphorylation (4). Taken together, these data suggest that chromatin remodeling during HSV-1 infection is driven, at least in part, by phosphorylation events.

HSV-1 encodes 2 known protein kinases Us3 and UL13. To investigate the nature of these chromatin remodeling phosphorylation events, our collaborators performed proteomics analysis by mass spectrometry on cells infected with Us3-null, UL13 kinase-dead, or Us3null/UL13 kinase-dead HSV-1. The phosphorylation of the above chromatin-associated proteins required viral kinase Us3, UL13, or both. Thus, we concluded that viral kinases directed a majority of these chromatin remodeling phosphorylation events. And I performed follow-up studies on these observations discussed below in the results section.

In my follow-up studies I found that, the viral kinase Us3 is necessary and sufficient to cause large scale chromatin rearrangements, in heterochromatin dependent manner. I additionally, found infected H3K27me3-depleted cells phenocopy infected cells with no capsid docking(32). Taken together, we propose a model in which the dual histone mark H3K27me3S28ph directs the NEC and capsid docking for proper nuclear egress.

Results:

3.2 Us3, but not Ul13, is sufficient to rearrange chromatin and H3K27me3

Based on the extensive role of these viral kinases in the phosphorylation of chromatin remodeling proteins, we hypothesized that these viral kinases may be sufficient for specific chromatin remodeling events during HSV-1 infection. To test this hypothesis, we transfected plasmids encoding either Us3, Us3 kinase dead (Us3K220A) (34, 35) or UL13 (36) into HeLa cells and examined the chromatin structure by immunofluorescence in the presence or absence of H3K27me3 depletion. I n control cells, transfection with a plasmid expressing GFP only, we found that chromatin remains evenly distributed throughout the nucleus **(Figure 3.1 A-B).** Interestingly, we found that Us3 ectopic expression is sufficient to grossly rearrange host chromatin **(Figure 3.1 A,D).** In cells transfected to express functional Us3, chromatin becomes punctate, with an increase in intensity around the nuclear periphery **(Figure 3.1 D).** In contrast, cells transfected to express UL13 also retained even chromatin distribution, while the nuclei appeared larger than control nuclei **(Figure 3.1 A,C)**, similar to what is observed during HSV-1 infection ((15, 17)**.** This suggests that the phosphorylation events caused by UL13 are not sufficient to grossly rearrange chromatin but do impact nuclear size, while phosphorylation events caused by Us3 are sufficient to drive chromatin rearrangement.

To confirm that the chromatin rearrangement in Us3 expressing cells was a result of Us3 kinase activity, we next generated a Us3 kinase dead expression plasmid. The Us3K220A point mutation ablates kinase activity (36, 37). Cells expressing the Us3K220A mutant did not undergo chromatin rearrangement (**Figure 3.1 A,E**). Rather the chromatin remained uniformly distributed, though like UL13, the nuclei did enlarge. Thus, we found that without the kinase activity, the impact of Us3 on chromatin was lost, indicating that phosphorylation events are critical for to elicit chromatin changes.

3.3 Us3 chromatin rearrangement is enhanced when heterochromatin markers are present

As Us3 phosphorylates many proteins involved in maintaining heterochromatin structure, we next chose to investigate whether heterochromatin markers were required for Us3

rearrangement of chromatin. We have previously shown that heterochromatin markers H3K27me3 and macroH2A1 are important in HSV-1-induced chromatin rearrangement (22). H3K27me3 is deposited as the first mark in the H3K27me3S28ph dual mark increase we observed (**Figure 3.1 D**) and macroH2A1 is phosphorylated over the course of HSV-1 infection. Therefore, we hypothesized that these heterochromatin markers may play a role in Us3-induced chromatin rearrangement. To investigate this, we used tazemetostat to deplete H3K27me3 by inhibiting EZH2 and knocked out macroH2A1 by CRISPR/Cas9 as previously described (22) . We then transfected to express GFP or UL13 as described above and discovered that chromatin appeared uniform as in normal untreated cells (**Figure 3F-G**) and upon loss of the heterochromatin markers H3K27me3 and macroH2A1. Us3 expression in cells depleted of H3K27me3 caused chromatin rearrangement as in DMSO treated cells, however, the effect appeared less intense in the absence of the heterochromatin mark. Similarly, loss of macroH2A1 also resulted in a less intense chromatin rearrangement **(Figure 3.1 F-I)**. Furthermore, Us3 expression also led to formation of large H3K27me3-stained regions predominantly around the nuclear periphery **(Figure 3.2)**. These H3K27me3 regions were not present in H3K27me3-depleted cells. Together, these data suggest that Us3 is sufficient to rearrange host chromatin in a heterochromatin-supported manner.

Figure 1. HSV-1 kinase Us3, but not UL13, is sufficient to cause gross chromatin rearrangement

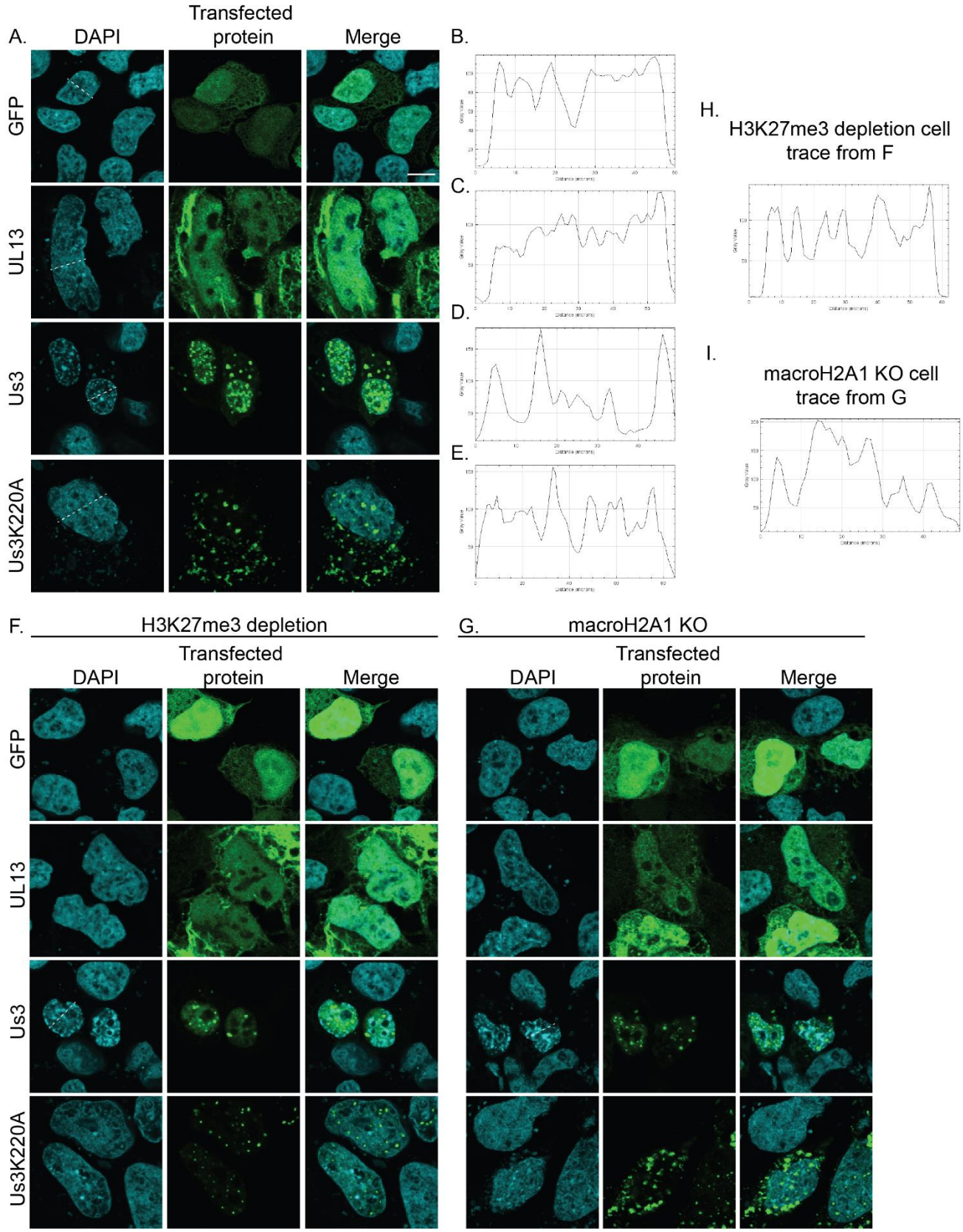

Figure 3.1. HSV-1 kinase Us3, but not UL13, is sufficient to cause gross chromatin rearrangement. A) Representative immunofluorescence images of HeLa cells transfected with plasmid expressing GFP, UL13, Us3, or Us3K220A as indicated. Chromatin is marked with DAPI. Scale bar indicates 10 μM. Dashed lines though cells indicate region for histograms of DAPI intensity in B-E. B) Histogram of DAPI intensity in HeLa cell transfected with plasmid expressing GFP. C) Histogram of DAPI intensity in HeLa cell transfected with plasmid expressing UL13. D) Histogram of DAPI intensity in HeLa cell transfected with plasmid expressing Us3. E) Histogram of DAPI intensity in HeLa cell transfected with plasmid expressing Us3K220A. F) Representative immunofluorescence images of H3K27me3 depleted HeLa cells transfected with plasmid expressing GFP, UL13, Us3, or Us3K220A as indicated. Chromatin is marked with DAPI. Dashed lines though cells indicate region for histograms of DAPI intensity in H. G) Representative immunofluorescence images of macroH2A1 knockout HeLa cells transfected with plasmid expressing GFP, UL13, Us3, or Us3K220A as indicated. Chromatin is marked with DAPI. Dashed lines though cells indicate region for histograms of DAPI intensity in I. H) Histogram of DAPI intensity in H3K27me3 depleted HeLa cell transfected with plasmid expressing Us3. I) Histogram of DAPI intensity in macroH2A1 KO HeLa cell transfected with plasmid expressing Us3.

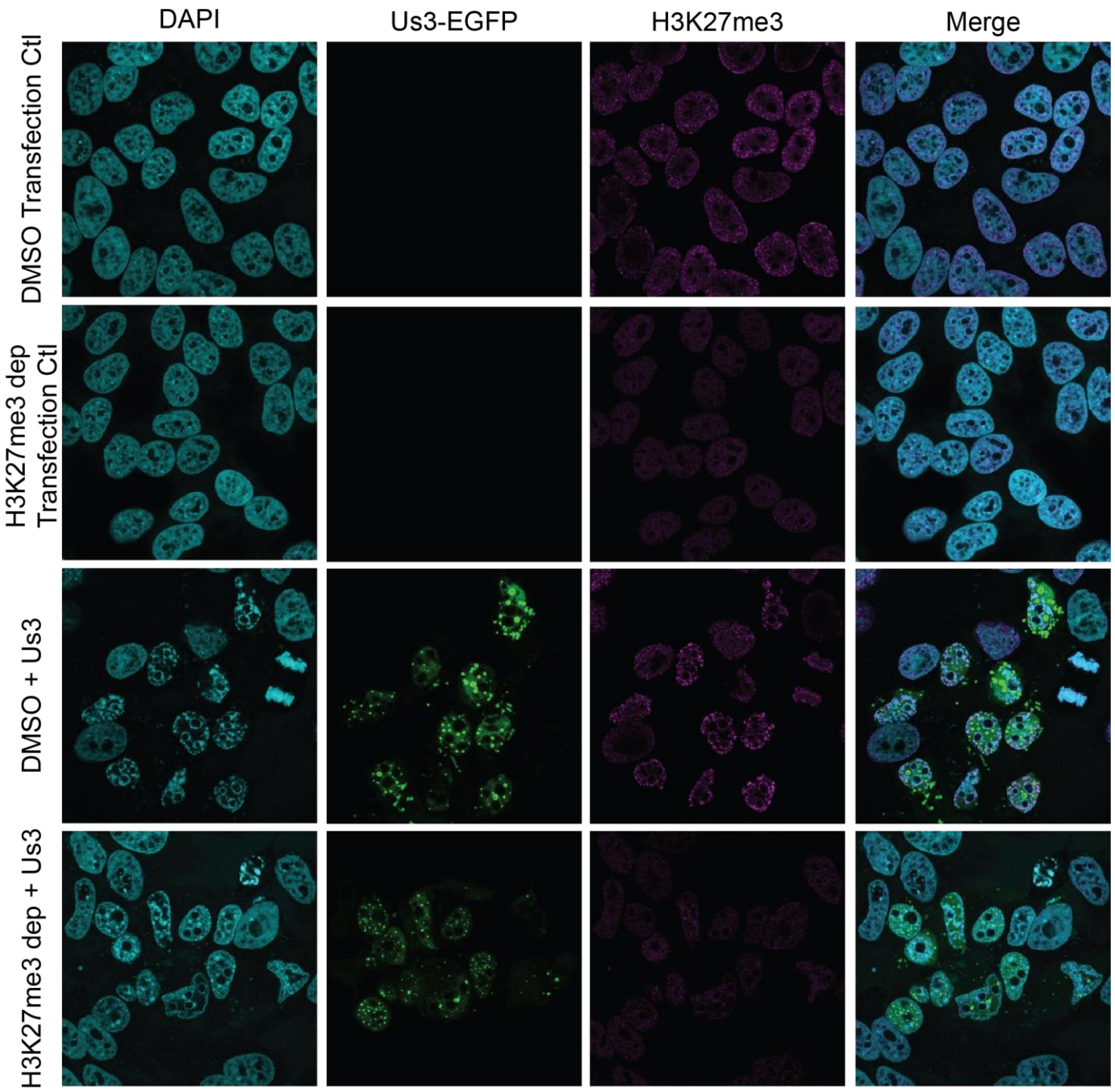

Figure 3.2. H3K27me3 is redistributed by HSV-1 Us3 expression alone. A) Representative immunofluorescence images of HeLa cells and H3K27me3 depleted HeLa transfected with plasmid containing Us3 as indicated. Chromatin is marked with DAPI. H3K27me3 is shown in magenta.

3.4 HSV-1 Us3 is necessary to arrange host chromatin, this rearrangement is also enhanced by presence of heterochromatin mark H3K27me3

Since Us3 was sufficient to rearrange the H3K27me3-associated host chromatin, we next hypothesized that Us3 is also necessary to rearrange host chromatin. To investigate this, we infected HFF-t cells with either a WT laboratory strain (syn17+) or a Us3-null strain of HSV-1 and performed immunofluorescence imaging at 18 hpi. Consistent with previously works, we saw that there were many large openings in the host chromatin in cells infected with WT HSV-1 (16). Interestingly, these chromatin openings we not present in cells infected with US3-null HSV-1 **(Figure 3.3).** Furthermore, we hypothesized that H3K27me3 may play a role in this rearrangement as well. We found that in H3K37me3-depleted cells these openings were not present when cells were infected with either WT or Us3-null HSV-1 **(Figure 3.3)**.

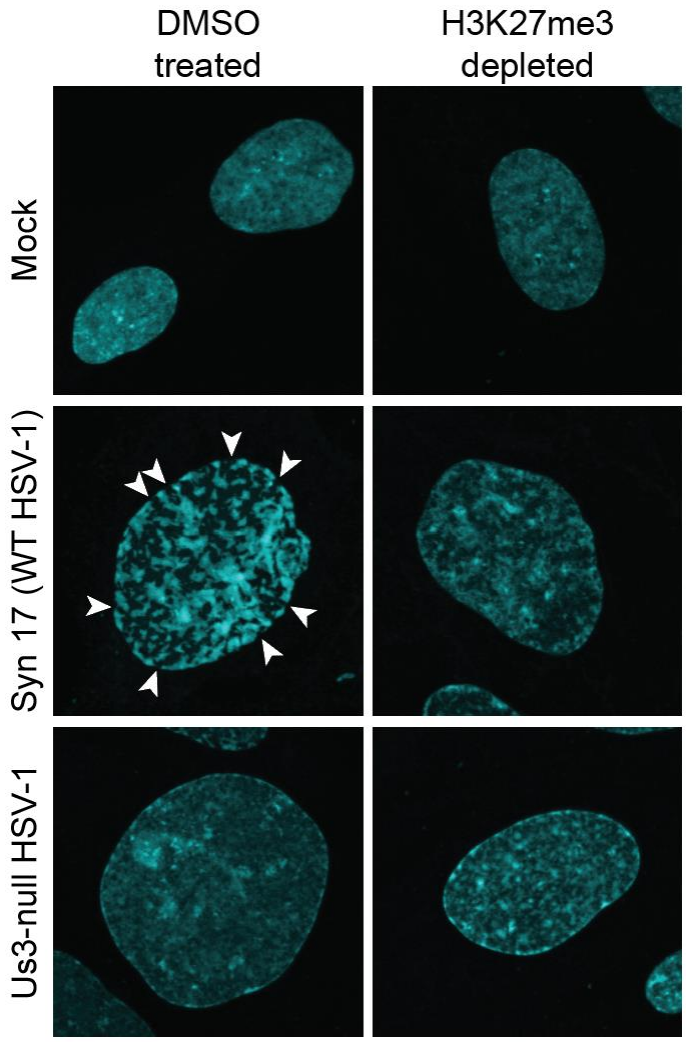

Figure 3.3 Us3 and H3K27me3 are necessary for chromatin rearrangement during HSV-1 infection. *A) Representative immunofluorescence images of HFF-t cells and H3K27me3 depleted HFF-t cells infected with WT or Us3-null HSV-1 at 18hpi as indicated. Chromatin is marked with DAPI.*

3.5 K27me3 depletion causes nuclear membrane folding in HSV-1 infected cells

Thus far we have shown that Us3 is required to phosphorylate chromatin-associated proteins and is sufficient to rearrange the host chromatin. Because Us3 plays a key role in nuclear egress (27, 34, 37), we therefore hypothesized that Us3 may directly interact with H3K27me3 to support nuclear egress. We previously showed H3K27me3 depletion inhibits efficient nuclear egress in HSV-1 and showed that HSV-1 capsids

appeared to “line up” along the edge of the nuclear membrane by TEM (22). Unexpectedly, we found that viral capsids were directly adjacent to membranes where four distinct membranes were visible **(Figure 3.4 A).** In many cases, a membrane looping was also visible directly adjacent to the capsid accumulations **(Figure 3.4 A, arrowheads)** but was not present in uninfected cells or H3K27me3-dpeleted uninfected cells (**Figure 3.4 B-C**). For clarity, we will refer to this characteristic phenotype of membrane looping as ‘infolding’, which was significantly increased in HSV-1 infected cells depleted of H3K27me3 compared to the DMSO-treated control (**Figure 3.4 D**). There were also no membrane infoldings observed in DMSO treated HSV-1 infected cells **(Figure 3.4 C)**, suggesting that H3K27me3 is a critical part of viral egress at the nuclear membrane.

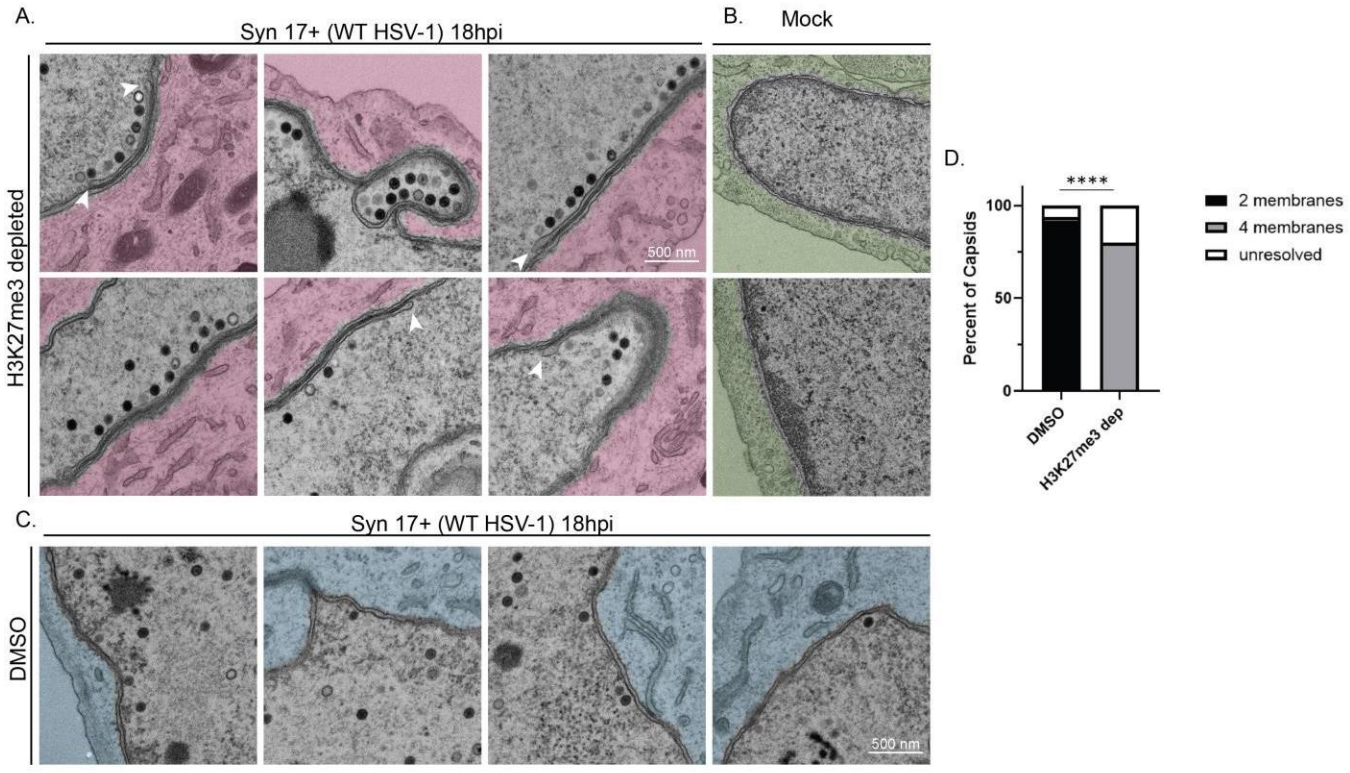

Figure 3.4. H3K27me3 depletion causes membrane infolding during HSV-1 nuclear egress. A) Representative transmission electron microscopy image of HFF cell during HSV-1 infection. B) Representative transmission electron microscopy image of uninfected HFF cell with H3K27me3 depletion. C) Representative transmission electron microscopy image of HFF cell with H3K27me3 depletion during HSV-1 infection. Arrowheads indicate membrane infoldings. D) Quantification of membranes present at each capsid interaction with the nuclear membrane. Data is shown as percentage of the capsid interactions n=48 in DMSO treated cells, n=89 in H3K27me3 depleted cells, $P < 0.0001$ chi-square test.

Because membrane infoldings were only present during infection, we next hypothesized that they are dependent on components of the nuclear egress complex (NEC). To investigate this hypothesis, we used immunofluorescence to visualize NEC component UL34, which inserts into the nuclear membrane and supports nuclear egress. We found significantly more concentrated regions of UL34 in H3K27me3-depleted cells compared to DMSO-treated cells **(Figure 3.5 A-B).** Furthermore, when we infected H3K27me3-depleted cells with UL34-null or UL31-null viruses we observed no membrane infoldings **(Figure 3.6 A-B).** Taken together, these results suggest that the observed membrane infoldings may be accumulations of UL31 and UL34.

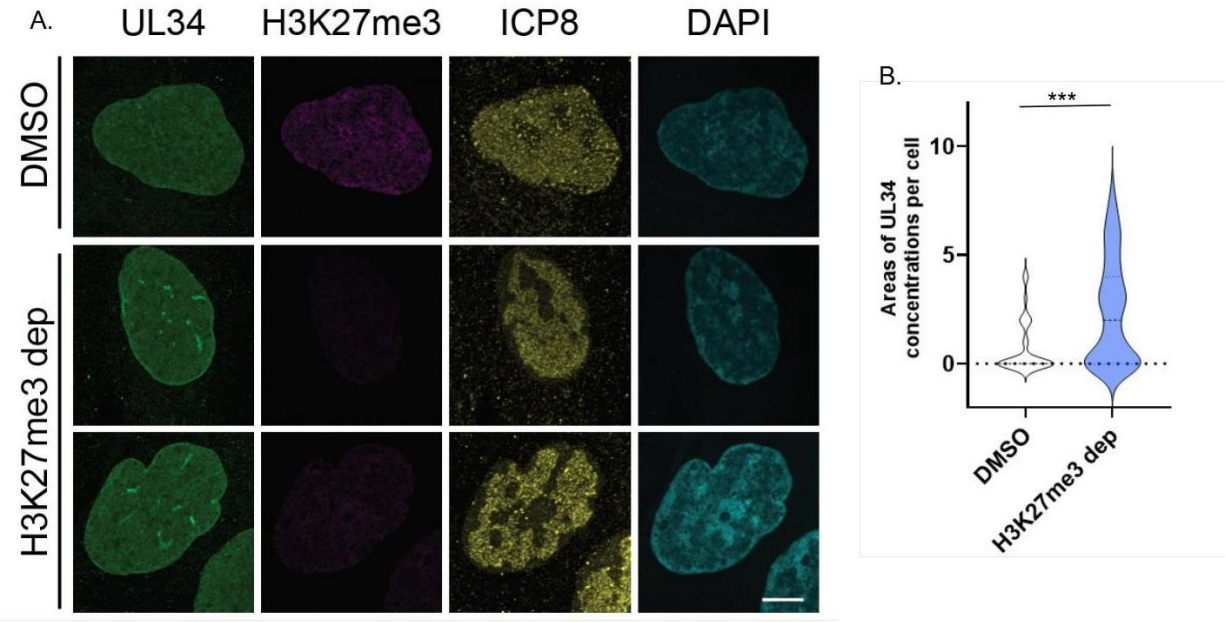

Figure 3.5. H3K27me3 depleted cells contain large concentrations of UL34. A) Representative immunofluorescence images of UL34 (green), H3K27me3 (magenta), ICP8 (yellow), and DAPI (cyan) at 10 hpi in HSV-1 infected DMSO treated and H3K27me3 depleted HFF-T cells. Scale bar indicates 10 μM. B) Scoring number of UL34 concentrations per cell. N = 30 cells ***P < 0.001 by student t-test.

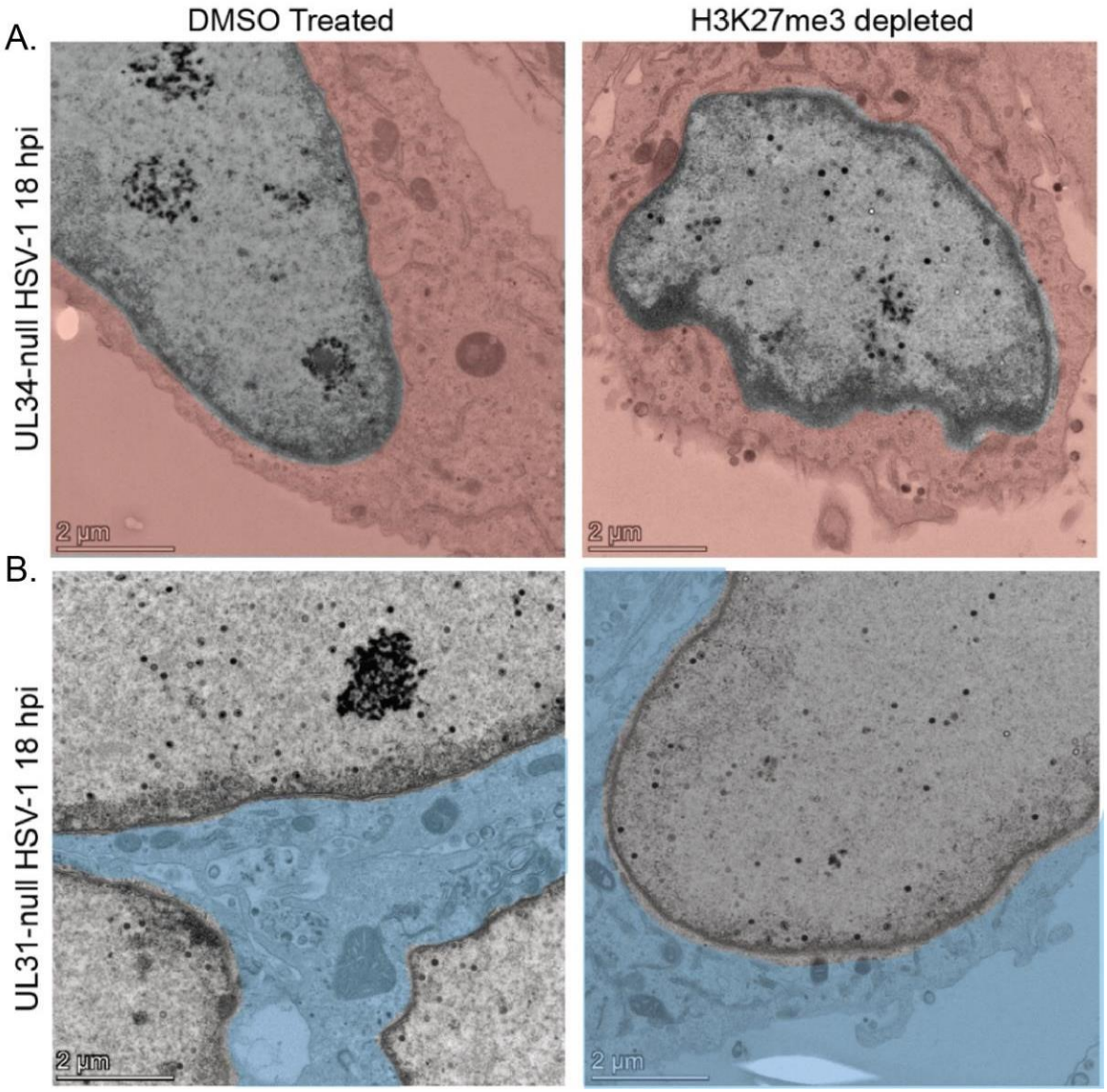

Figure 3.6. Nuclear membrane infoldings are not present in H3K27me3 depleted cells infected with NEC mutants. TEM images of representative DMSO treated (left column) or H3K27me3 depleted (right column) nuclei infected with UL 34-null (A) or UL31-null (B) HSV-1 at 18 hpi. Scale bar as indicated.

To confirm that the specificity of H3K27me3 depletion was responsible for the reduction in progeny and not an effect of EZH2 inhibition, we first only pretreated cells for 1 hour rather than 3 days prior to infection. We have found that pretreatment with Tazemetostat for less than 24 hours does not noticeably deplete H3K27me3 levels in HFF-ts. We found 1 hour pretreatment with Tazemetostat was insufficient to significantly reduce progeny (**Figure 3.7 A).** This suggests that H3K27me3 depletion prior to infection drives the reduction in progeny rather than inhibition of EZH2 during infection. We further investigated this by infecting cells pretreated for 3 days with EED226, a small molecule inhibitor PRC2 complex member EED with a similar H3K27me3 reduction profile to Tazemetostat (38). We found that EED226 and Tazemetostat reduced infectious HSV-1 progeny to the same degree. Thus, we also found that the protein in the PRC2 complex targeted by small molecule inhibitor did not affect the reduction in progeny production (**Figure 3.7 B).** Furthermore, depletion of H3K27me3 reduced infectious progeny to similar proportion when normalized to DMSO control in WT, UL13 KD, Us3null, and Us3null/UL13KD viruses (**Figure 3.8 A-D**).

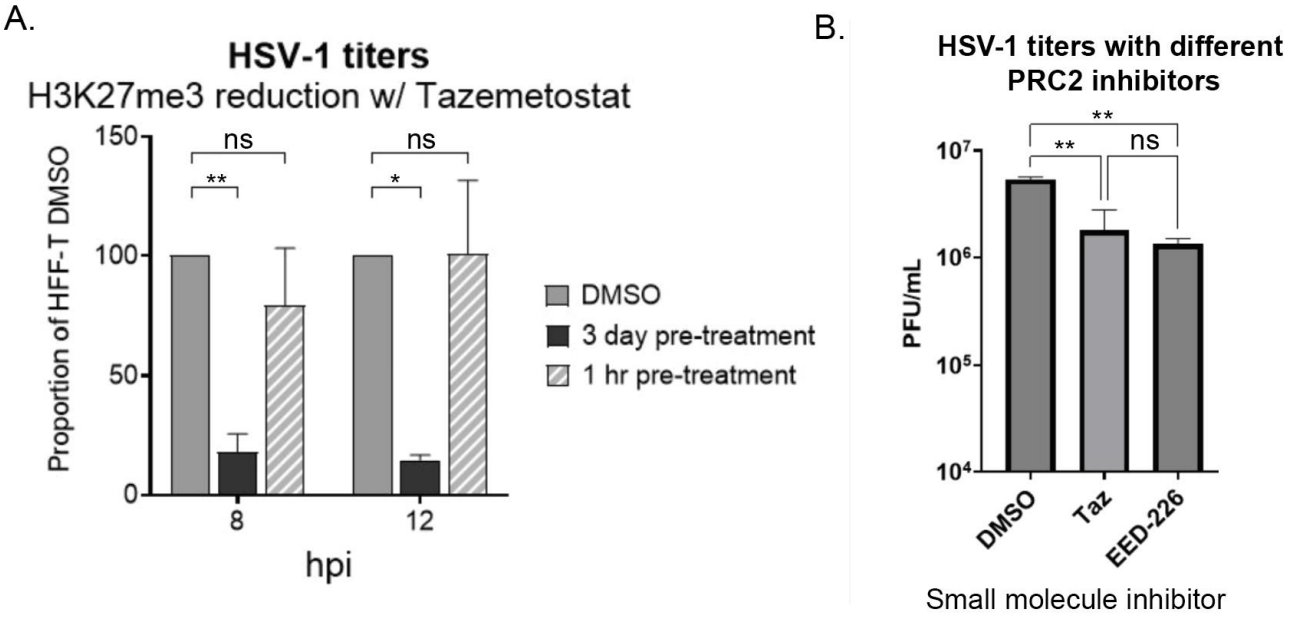

Figure 3.7. Timing of low dose PRC2 inhibitor, but not component of PRC2 complex targeted by inhibitor, impacts reduction in viral progeny production. A)

Infectious progeny produced from HSV-1 infected cells treated with Tazemetostat to inhibit PRC2 at either 3 days prior to infection or 1 hour prior to infection and quantified by plaque assay. Viral yield is indicated as the percent yield compared to WT at each indicated time point. Error bars represent the SEM of three biological replicates, *P < 0.05 **P < 0.01 by Dunnett's multiple comparisons test. B) Infectious progeny produced from HSV-1 infected cells treated for 3 days with EZH2 inhibitor Tazementostat, EED inhibitor EED-226, and DNA methylation inhibitor GSK-3484862 and quantified by plaque assay. Error bars represent the SEM of three biological replicates, **P < 0.01, ***P < 0.001 by Dunnett's multiple comparisons test.

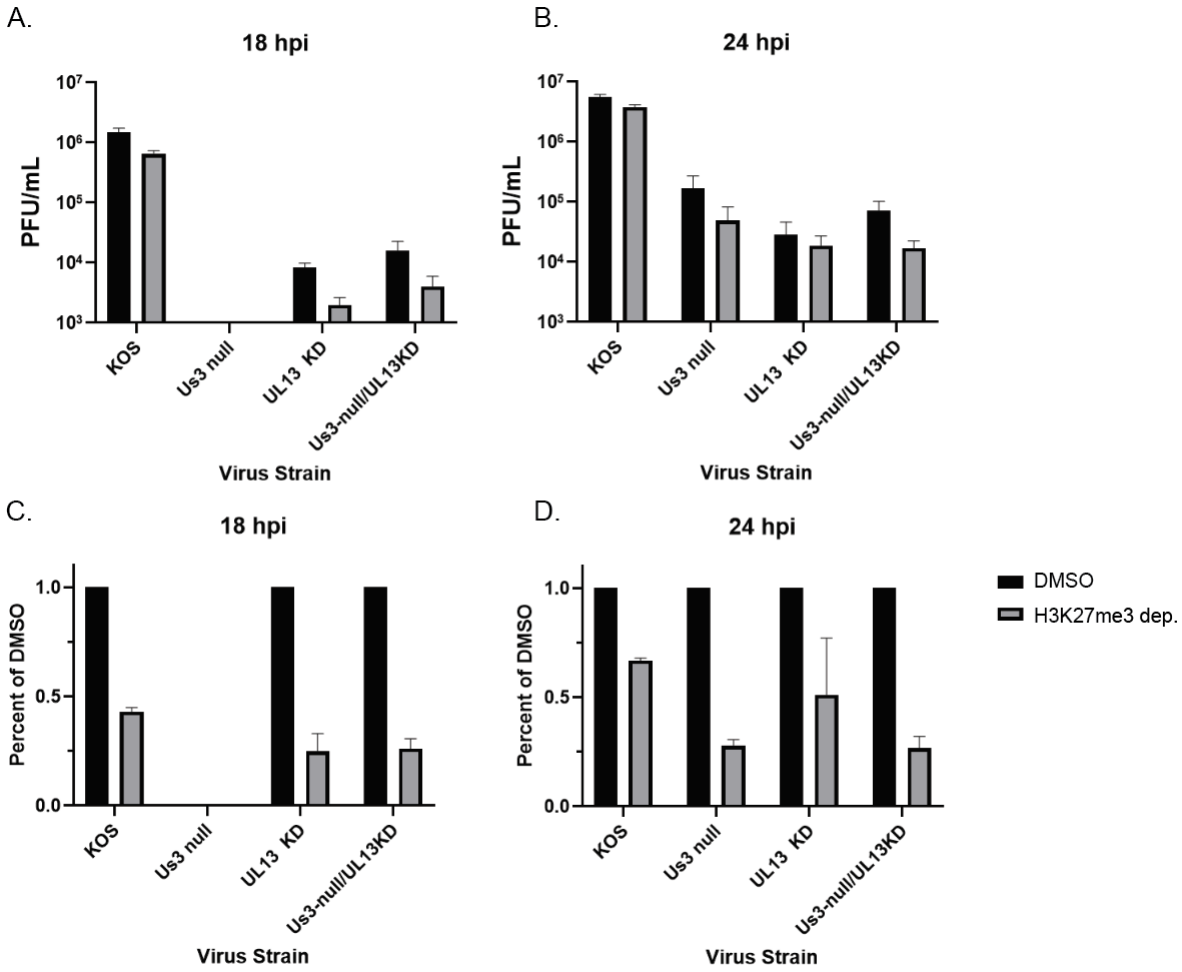

Figure 3.8. H3K27me3 depletion reduces infectious progeny to a similar degree in HSV-1 kinase mutants. A) Infectious progeny produced from HSV-1 infected DMSO treated or H3K27me3 depleted cells at 18 hpi with strain as indicated and quantified by plaque assay. B) Infectious progeny produced from HSV-1 infected DMSO treated or H3K27me3 depleted cells at 24 hpi with strain as indicated and quantified by plaque assay. C) Infectious progeny normalized to DMSO treated progeny levels at 18 hpi with strain as indicated and quantified by plaque assay. D) Infectious progeny normalized to

DMSO treated progeny levels at 24 hpi with strain as indicated and quantified by plaque assay.

3.6 H3K27me3 and Us3 are both required for efficient capsid docking and nuclear egress

Because loss of H3K27me3 results in capsids not budding efficiently into the INM, we examined the dependence of this phenotype on UL31 and UL34. Our results using the UL31-null and UL34-null viruses indicate that they are required for the membrane infolding phenotype we observe. Together, these results led us to hypothesize that HSV-1 capsids require both H3K27me3 and NEC components to efficiently dock and bud into the INM. To investigate this, we turned to Us3 as a key player in supporting HSV-1 capsid nuclear budding. We infected H3K27me3-depleted cells with a Us3-null viruses and examined the nuclear membrane by TEM. Surprisingly, infection of H3K27me3-depleted cells with Us3-null virus led to increased membrane infoldings compared to wild-type HSV-1 infection **(Figure 3.9 A).** Furthermore, there were many instances in which membrane infolding was observed with no visible capsids along the membrane. This was surprising because it is in contrast to the membrane infolding observed above which only occurred when WT HSV-1 capsids lined up at the INM in H3K27me3-depleted cells **(Figure 3.4).** Interestingly, this extensive membrane infolding strongly phenocopies what has been observed in cells infected with a virus lacking VP5, the major capsid protein, and expressing only kinase dead Us3K220A (32). The membrane infolding observed by others in VP5-null/Us3K220A infected cells was not seen in cells infected with either VP5 null or Us3-kinase dead virus (32). This observation suggests that membrane infolding only occurs when Us3 cannot trigger membrane budding through a combination of phosphorylation events and proper capsid docking. In our experiment infecting H3K27me3-depleted cells with Us3-null virus, we observed a further reduction in viral titers compared to Us3-null virus infection **(Figure 3.9 B).** Of note, in H3K27me3 depleted cells, both WT and Us3-null HSV-1 progeny were reduced by the same proportion (**Figure 3.9 C**), suggesting distinct functions. Based on the similarity in phenotype to VP5-null/Us3K220A HSV-1

infection and the further reduction of Us3-null virus titers when H3K27me3 was depleted, we conclude that H3K27me3 depletion impacts either HSV-1 capsid formation or docking of the capsids to the NEC.

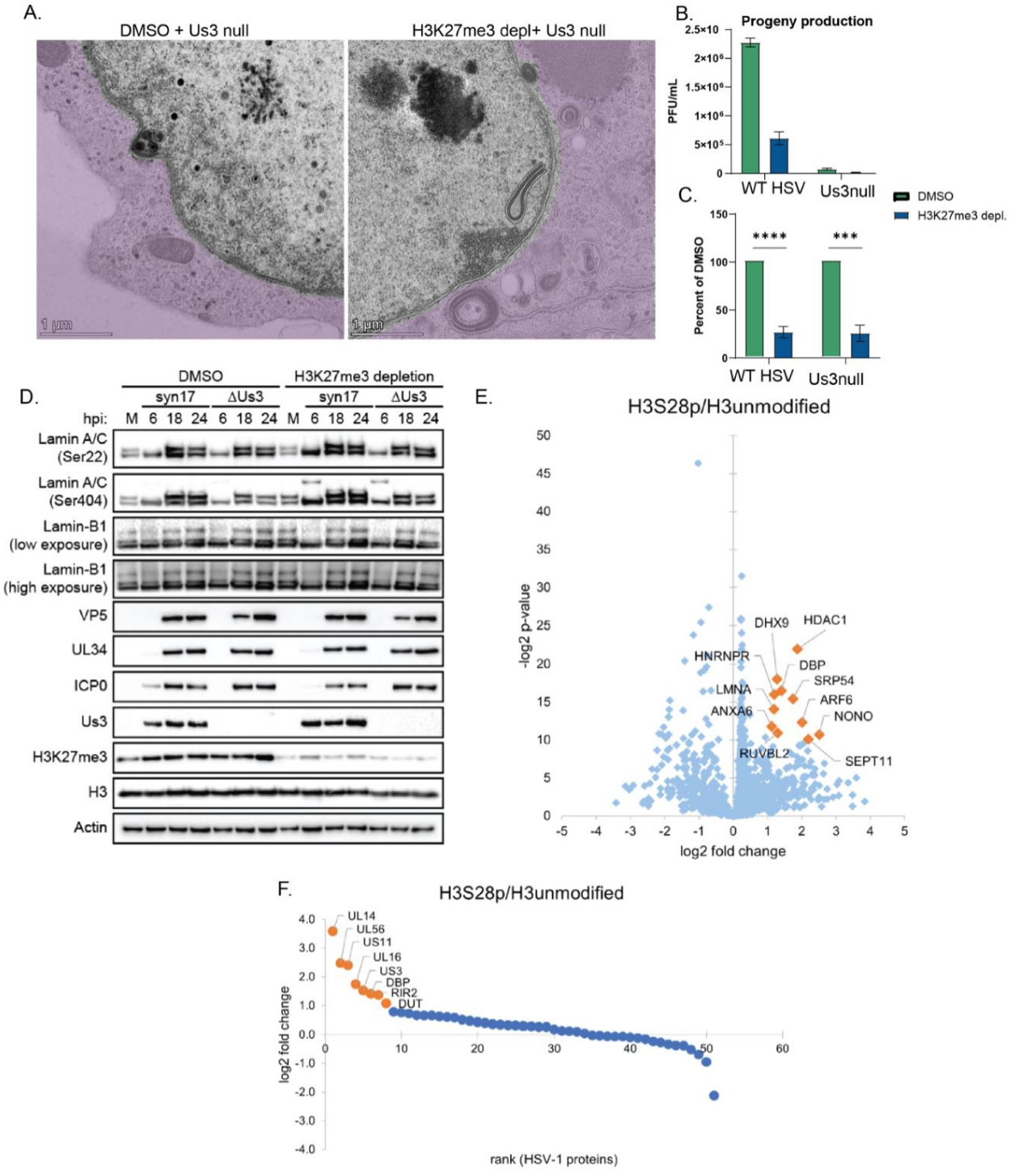

Figure 3.9 H3K27me3 and Us3 are required for efficient capsid docking and nuclear egress. A**)** TEM images of representative DMSO treated (left column) or H3K27me3 depleted (right column) nuclei infected with Us3-null 18 hpi. Scale bar as indicated. B) Infectious progeny produced from DMSO and H3K27me3 depleted cells during HSV-1 WT and Us-3 null virus infection. Error bars represent the SEM of three biological replicates, **P < 0.01, ***P < 0.001 by Dunnett's multiple comparisons test. C) Infectious progeny data from B normalized to DMSO progeny production in indicated strain. Error bars represent the SEM of three biological replicates, ***P < 0.001, ****P < 0.0001 by Dunnett's multiple comparisons test. D) Representative western blot of lamin A/C ser-22-ph, lamin A/C ser-404-ph, total Lamin-B1, viral proteins VP5, UL34, ICP0, and Us3, H3 and actin are shown as loading controls. E) Differential host protein level log fold-change from H3S28ph and H3 control peptide pull-down and follow-up mass-spectrometry. n = biological replicates. F) Differential viral protein level log fold-change from H3S28ph and H3 control peptide pull-down and follow-up mass-spectrometry. N= 3 biological replicates.

To investigate whether viral capsid protein production was inhibited by H3K27me3 depletion, we examined protein levels of VP5 (also known as major capsid protein, MCP) in both DMSO treated and H3K27me3 depleted cells and found no change in protein levels by western blot. Because the phosphorylation of lamins is essential for HSV-1 capsids to reach the INM, we also examined these levels during infection in H3K27me3-depleted cells compared to control. We found that there were no detectable changes in lamin, phosphorylated lamins, or UL34 levels in H3K27me3-depleted cells when infected with either WT or Us3-null HSV-1 **(Figure 3.9 D),** suggesting that our observed phenotype is not driven by defect in capsid production or lamin rearrangement. We also examined lamin distribution by immunofluorescence and found though there was no apparent difference in Lamin B1 or phosphor-LaminA/C distribution, we were able to detect large membrane bound vesicles seen by TEM (**Figure 3.10**)

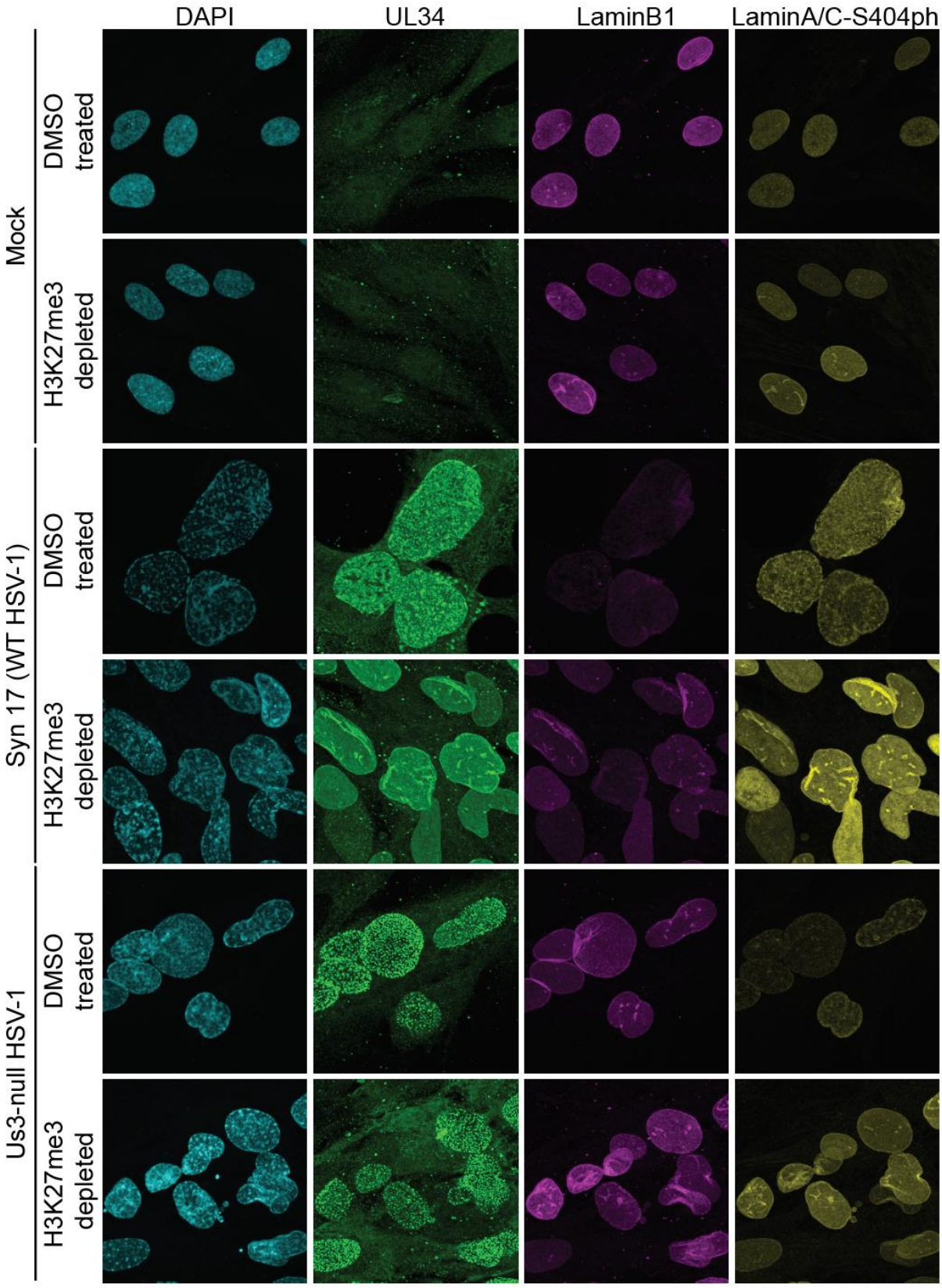
DAPI
UL34
LaminB1
LaminA/C-S404ph
Mock
DMSO treated
H3K27me3 depleted
Syn 17 (WT HSV-1)
DMSO treated
H3K27me3 depleted
Us3-null HSV-1
DMSO treated
H3K27me3 depleted

Figure 3.10 Us3 and H3K27me3 affect Lamin A/C-S404ph distribution during HSV-1 infection. Representative immunofluorescence images of HFF-t cells and H3K27me3 depleted HFF-t cells infected with WT or Us3-null HSV-1 at 18hpi as indicated. Chromatin is marked with DAPI.HSV-1 UL34 is green, LaminB1 is magenta, and LaminA/C Ser404ph is yellow.

To further confirm expression of capsid proteins is unaffected by H3K27me3 depletion, we are currently processing bulk RNA seq in DMSO and H3K27me3 depleted cells. However, it is unlikely K27me3 depletion impacts viral transcription as several other published findings with small molecule inhibitors of EZH2 that deplete H3K27me3 levels did not detect changes in viral transcript levels(39, 40). Based on these findings, we hypothesized that the phenotype we found in H3K27me3 depleted viruses infected with Us3-null virus was more likely to reflect a capsid docking defect.

To determine whether the defect is a direct result of the loss of histone modification, we next investigated the interaction of a modified histone tail with viral proteins. To do this, we incubated cellular lysate from infected cells with immobilized H3S28ph peptide and performed mass spectrometry to identify proteins interacting with H3S28ph or H3 peptide alone. H3S28ph was selected based on increase in abundance, the role of viral kinase, Us3, in egress and chromatin rearrangement, and peptide availability. We found that the H3S28ph peptide pulldown of host proteins was enriched for lamins, and several vesicle trafficking proteins, including Arf6 (41), Septin11 (SEPT11)(42), and SRP54(43) **(Figure 3.9 E).** Furthermore, the viral proteins most significantly enriched in the H3S28ph peptide pulldown include UL14, UL16, UL56, and Us3 **(Figure 3.9 F).** UL14 and UL16 knockout results in viruses with reduced nuclear egress (44, 45), and UL56 knockout has a more generally defined egress defect, though if this egress was at the nuclear stage or secondary egress was not defined (46).

Taken together, the results from this pulldown suggest that H3S28ph interacts with host and viral proteins not canonically included in the NEC designation but facilitate the docking and nuclear budding of capsids in nuclear egress.

Discussion

Integrating the data presented here, we propose a model in which the viral kinase Us3 rearranges host chromatin to allow capsids to access the nuclear membrane. The histone marks H3K27me3, and the dual mark H3K27me3S28p then help direct the capsids to dock at the nuclear membrane before the viral kinase Us3 phosphorylates additional viral and host proteins to trigger capsid egress (**Figure 3.11**). The other NEC components, UL31 and UL34, are also necessary for chromatin rearrangement during HSV-1 infection, especially near the nuclear periphery(16). Us3 driven chromatin rearrangement can be seen in the Hoescht staining of other works studying the NEC that the components, their work also suggest that UL21 directs the Us3, UL31 and UL34 HSV-1 proteins to the nuclear membrane (47).

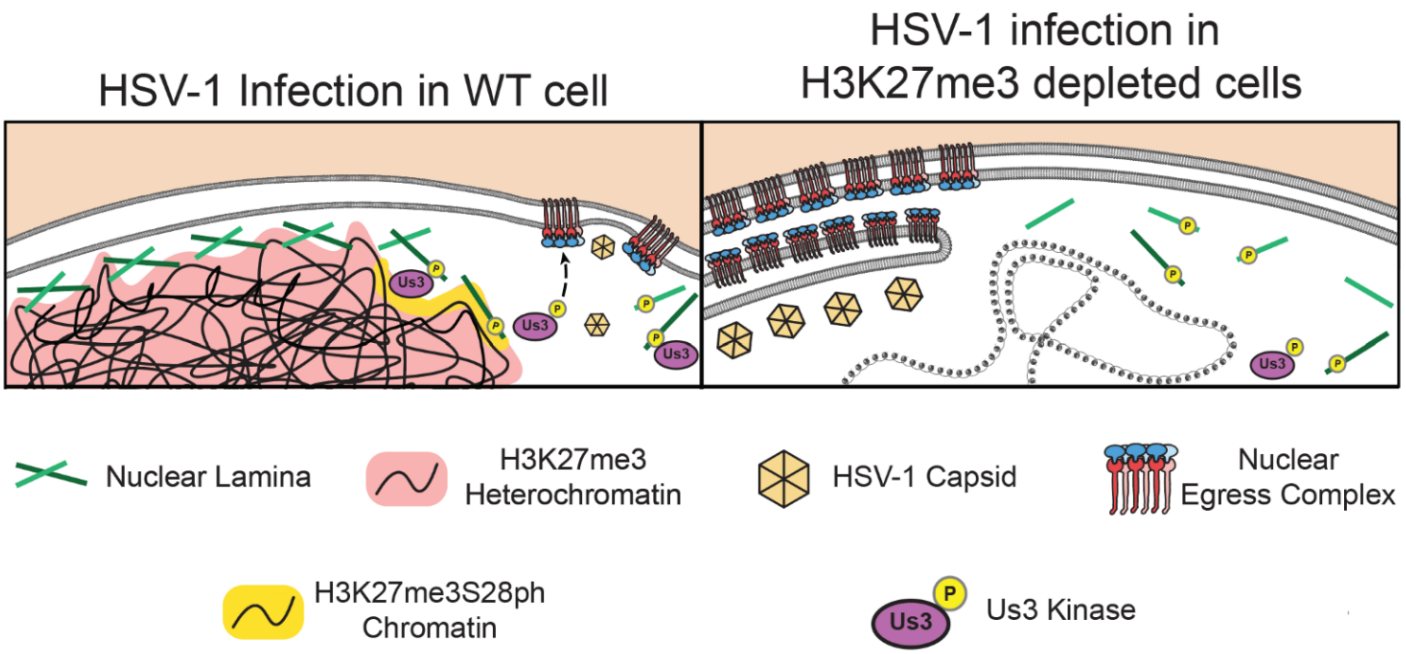

Figure 3.11 Model for H3K27me3 direction of HSV-1 nuclear egress. Left: Proposed model of phosphorylation events by Us3 and H3K27me3/H3K27me3S28ph chromatin support during HSV-1 nuclear egress. Right: Proposed model of effects of H3K27me3 heterochromatin disruption in HSV-1 nuclear egress.

In **Figure 3.9**, we show that Us3-null HSV-1 infection in H3K27me3 depleted cells phenocopies VP5-null/Us3K220A HSV-1 infection. This mutant virus highlights the potential that some capsid docking event triggers the budding process in HSV-1 nuclear egress. In H3K27me3 depleted cells, the exacerbation of membrane infolding with Us3-null virus infection suggest this release event is dependent on Us3 kinase activity. However, the presence of membrane infoldings in H3K27me3 depleted cells infected with WT HSV-1, and proportional reduction of progeny production in H3K27me3 depleted cells regardless of infection with WT or Us3-null virus suggests the phenotype is driven by H3K27me3 depletion affecting capsid docking to the NEC. In H3K27me3 depleted cells, VP5 levels are unaffected in WT and Us3-null HSV-1 infection. Virion capsid formation is not impacted by H3K27me3 depletion in WT HSV-1 infection (22). Highlighting that this phenotype is likely a capsid docking defect and not a capsid production defect. Follow-up studies should investigate how HSV-1 capsids dock to the NEC complex and the involvement of H3K27me3.

The dual histone mark H3K27me3S28ph increases on latent HSV-1 genomes just prior to reactivation (48). The H3K27me3S28ph mark is very dynamic in neuronal cells, frequently increasing in response to abnormal signaling conditions (49, 50). H3K27me3S28ph increasing on viral genomes as latent virus is reactivated may indicate this mark is concurrently increasing on host chromatin and thus helping facilitate the nuclear egress of reactivated virus as well.

Us3 and UL16, one of the top associations in H3S28ph pulldown, are key factors in neuroinvasion and neurovirulence of the alpha herpesvirus, PRV (51). The H3K27me3S28ph role in neuronal firing and role of US3 and UL16 in neurovirulence suggests that this nuclear egress phenotype may play an even more dramatic role in neuron cells compared to the HFFs used in this study. Indeed, treatment of mice with small molecules that deplete H3K27me3 significantly reduced neuroinvasion of HSV-1 infection in mice(52) . This highlights that an understanding of HSV-1 nuclear egress can help lead to drug discoveries targeting the severe diseases associated with HSV-1 such as herpetic encephalitis. (47)

Chapter 4: Human cytomegalovirus induces neuronal gene expression through IE1 for viral maturation

*The contents of this chapter are adapted from my manuscript Kelnhofer-Millevolte LE, Smith JR, Nguyen DH, Wilson LS, Lewis HC, Arnold EA, Brinkley MR, Geballe AP, Ramachandran S, Avgousti DC. Human cytomegalovirus induces neuronal gene expression for viral maturation. bioRxiv [Preprint]. 2024 Jun 13:2024.06.13.598910. doi: 10.1101/2024.06.13.598910, and currently under revision at *Nature Communications.* "We" is used throughout the publication. I designed and performed experiments, wrote, and created figures for the original manuscript. Julian Smith assisted with experimental design, performed experiments, and assisted with figure creation, especially Figure 4.X. Daniel Nguyen performed experiments and assisted with figure creation, especially Figure 4.X. Mia Brinkley, Edward Arnold, Hannah Lewis, and Lea Wilson assisted with experiments. Sequencing analysis and text describing analysis was kindly performed by Srinivas Ramachandran. Adam Geballe provided reagents and consulted on experimental design. The work here was supervised and edited by Daphne Avgousti.

Abstract

Viral invasion of the host cell causes some of the most dramatic changes in biology. Human cytomegalovirus (HCMV) extensively remodels host cells, altering nuclear shape and generating a cytoplasmic viral-induced assembly compartment (vIAC). How these striking morphology changes occur in the context of host gene regulation is still emerging. Here, we discovered that histone variant macroH2A1 is necessary for formation of infectious progeny and HCMV-induced reorganization of the host cell. Using RNA-seq we found that while all viral genes were highly expressed in the absence of macroH2A1, many HCMV-induced host genes were not. Remarkably, hundreds of these HCMV-induced macroH2A1-dependent host genes are associated with neuronal synapse formation and vesicle trafficking. Further, we found that HCMV immediate early protein, IE1, is sufficient to induce these neuronal genes, providing a mechanism of activation. Together, our findings demonstrate that HCMV

hijacks a dormant neuronal secretory pathway through chromatin manipulation for efficient virion maturation.

4.1 Introduction

Human cytomegalovirus (HCMV) is a ubiquitous herpesvirus with seropositivity ranging from 65 to 100% (1, 2). In immunocompetent individuals, HCMV is typically asymptomatic or results in mild cold-like symptoms (3). In contrast, congenital HCMV infection is one of the leading causes of infectious birth defects affecting about 1 in every 200 live births (4). Additionally, cytomegalovirus is a chief cause of morbidity and mortality in both solid organ and stem cell transplant recipients (5) and individuals with poorly controlled HIV (6).

HCMV infection of the host cell induces large scale cellular remodeling (7). The host nucleus forms a characteristic kidney-bean shape while host chromatin becomes polarized to one side (8) and large-scale cytoskeletal rearrangement causes the nucleus to spin (8, 9). Simultaneously, the Golgi, endosome, and other cellular membranes are reorganized during HCMV infection to form the viral-induced assembly compartment (vIAC) (10). Viral replication occurs in the nucleus, after which progeny capsids exit from the nucleus and pass through the vIAC for tegumentation and final maturation (11–13). Importantly, unlike other lytic herpesvirus infections, HCMV does not shut down host transcription (14), though how host gene expression is altered by HCMV remains actively under investigation.

Cellular remodeling is closely controlled by host gene expression, which in turn is regulated by histone modifications and histone variants (15–17). MacroH2A1 is a histone variant that can replace the core histone H2A. MacroH2A1 was initially discovered on the inactive X chromosome associated with transcriptional repression (18, 19). In contrast, macroH2A1 is also required for gene activation in several contexts including serum starvation response (19), smooth muscle differentiation (20), and neuronal differentiation (21). We previously showed how macroH2A1-dependent heterochromatin is critical for herpes simplex (HSV-1) egress from the nuclear compartment (22). Therefore, we hypothesized that macroH2A1 may also function in cytomegalovirus infection. Here, we demonstrate

that HCMV predominantly upregulates hundreds of exclusively neuronal genes in a macroH2A1-dependent manner, driven by viral immediate early IE1. This upregulation of neuronal genes is essential for efficient HCMV infectious progeny production and defines a new mechanism wherein HCMV has evolved to control host gene expression to promote progeny maturation and viral spread.

Results

4.2 MacroH2A1 is required for production of infectious HCMV progeny.

Due to the importance of macroH2A1 in lytic HSV-1 infection (22) and the observation that macroH2A1 mRNA levels increase during lytic HCMV infection (23), we hypothesized that macroH2A1 is also necessary for efficient HCMV lytic infection. To investigate this hypothesis, we infected wild-type human foreskin fibroblast cells (WT HFF-T) and our established macroH2A1 CRISPR knock-out cells (macroH2A1 KO HFF-T) (22) with HCMV (*Towne*) and measured infectious viral progeny. We found that HCMV grown in macroH2A1 KO cells produced approximately 30-fold fewer infectious progeny, than HCMV grown in control cells (**Figure 4.1 A, Figure 4.2 A**).

We next asked whether macroH2A1 loss affected viral protein and RNA accumulation. We measured viral protein levels by western blot of representative immediate early (IE1/2), early (UL44), late tegument (pp28 and pp65), and late envelope (gB) proteins. We found that all measured viral proteins were robustly expressed at earlier time points, and to a stronger degree in macroH2A1 KO cells (**Figure 4.1 B**).

To determine whether other viral genes not measured by western blot might explain the decrease in infectious progeny produced, we next measured the viral transcriptome by RNA sequencing. We performed bulk RNA sequencing of HCMV-infected WT and macroH2A1 KO cells at 4, 16, 24, 48, and 72 hours post infection (hpi). We found that in macroH2A1 KO cells, early gene expression was initiated by 4 hpi and that immediate early viral genes were expressed at a higher level compared to their levels in WT cells. By 16 hpi, many late viral transcripts were already expressed in macroH2A1 KO cells, while late transcripts were not expressed in WT control cells until 48 hpi (**Figure 4.1 C, Figure 4.2**

B-C). Thus, HCMV transcripts and proteins were expressed earlier and to a higher level in macroH2A1 KO cells compared to WT cells.

As increased protein and RNA expression in macroH2A1 KO cells did not explain the strong reduction in infectious progeny, we next investigated genome replication. We found that within cells, there was no significant change in viral genomes between WT and macroH2A1 KO cells measured by droplet digital PCR (ddPCR) (**Figure 4.1 D**). Similarly, we found no significant change in nuclease-resistant genomes released into the supernatant (**Figure 4.1 E**), indicating that the reduction in infectious progeny is not due to replication or egress defects but rather that viral progeny grown in macroH2A1 KO cells are defective.

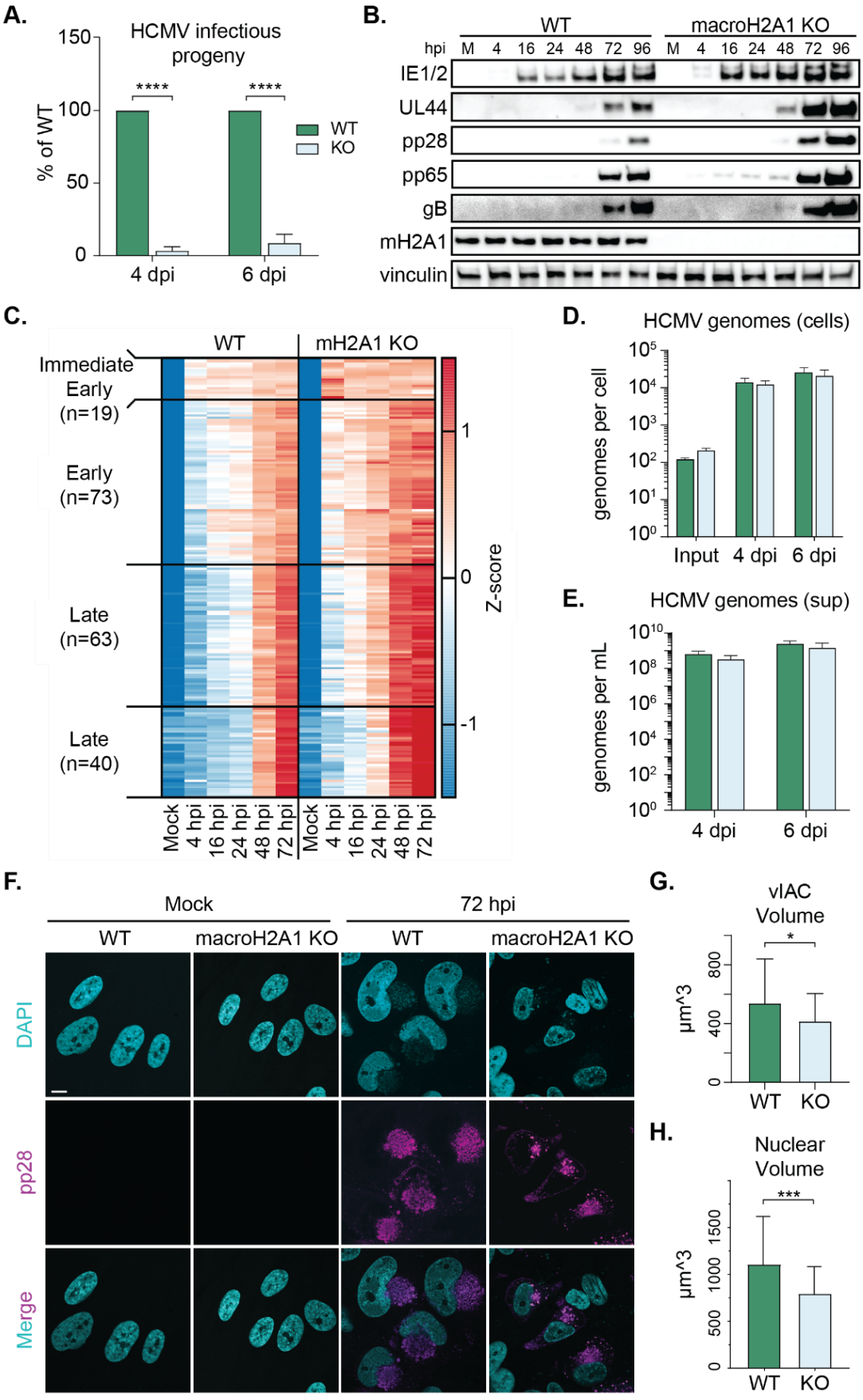
A.
HCMV infectious progeny
% of WT
150
100
50
0
****
****
WT
KO
4 dpi
6 dpi
B.
WT
macroH2A1 KO
hpi
M 4 16 24 48 72 96
M 4 16 24 48 72 96
IE1/2
UL44
pp28
pp65
gB
mH2A1
vinculin
C.
WT
mH2A1 KO
Immediate Early (n=19)
Early (n=73)
Late (n=63)
Late (n=40)
Z-score
1
0
-1
Mock
4 hpi
16 hpi
24 hpi
48 hpi
72 hpi
D.
HCMV genomes (cells)
genomes per cell
Input
4 dpi
6 dpi
E.
HCMV genomes (sup)
genomes per mL
4 dpi
6 dpi
F.
Mock
72 hpi
WT
macroH2A1 KO
WT
macroH2A1 KO
DAPI
pp28
Merge
G.
vIAC Volume
µm^3
*
WT
KO
H.
Nuclear Volume
µm^3
***
WT
KO

Figure 4.1. HCMV requires macroH2A1 for efficient production of infectious progeny, but not protein, RNA, or genome accumulation. A) Infectious progeny produced from HCMV infected WT and macroH2A1 KO HFF-T cells quantified by plaque assay at 4- or 6-days post infection (dpi) as indicated. Viral yield is indicated as the percent yield compared to wild type, with errors bars representing SEM. **** $P < 0.0001$ at both time points by unpaired T-test. N=3 biological replicates. B) Representative western blots of viral proteins in cells as in (A) during HCMV infection at 4, 16, 24, 48, 72, and 96 hours post infection (hpi) compared to mock (M). These time points correspond to immediate early gene expression (4 hpi), early gene expression (16 hpi), genome replication (24 hpi), and late gene expression (48 and 72 hpi). Vinculin is shown as loading control. C) Heat map of viral genes measured by RNA sequencing at 4, 16, 24, 48, and 72 hpi compared to mock (M). N=3 biological replicates. D) Droplet digital PCR (ddPCR) quantification of HCMV genomes extracted from infected WT and macroH2A1 KO cells at 4 hours (input), 4, and 6 dpi. Bar graphs show the mean with error bars indicating SEM. No significance at any time point by paired T-test. E) ddPCR quantification of HCMV genomes released from cells as in (D) and isolated from supernatants (sups) at 4 and 6 dpi after nuclease treatment, indicating encapsidated genomes. Error bars represent the SEM of three biological replicates. No significance at any time point by paired T-test. F) Representative immunofluorescence images of WT and macroH2A1 KO cells during HCMV infection at mock and 72 hpi. DAPI is shown in cyan, and viral protein pp28 is shown in magenta. Scale bar represents 10 μm. G) Quantification of the volume of viral induced assembly compartments (vIACs) measured by pp28 fluorescence. Bar graphs show mean with error bars indicating SEM. $P < 0.05$ by unpaired T-test. N>40 vIACs. H) Quantification of nuclear volume of WT and macroH2A1 knockout HCMV-infected cells at 72 hpi. Bar graphs show mean with error bars indicating SEM. $p < 0.001$ by unpaired T-test. N>40 cells.

4.3 MacroH2A1 is required for nuclear rearrangement and vIAC formation.

Proper maturation of HCMV progeny occurs in the vIAC. Therefore, we hypothesized that the loss of macroH2A1 results in a viral maturation defect due to a defective vIAC. We used immunofluorescence to visualize infected cells. Strikingly, we found that the vIACs were significantly smaller in macroH2A1 KO cells (**Figure 4.1 F-G, Figure 4.2 D**), the nuclei did not expand as expected, and the nuclei did not form the characteristic kidney-bean shape (**Figure 4.1 F and H, Figure 4.2 E**). Furthermore, we observed that infected macroH2A1 KO cells also retained the centrosomes and tubulin boundary between cells, suggesting that HCMV-induced syncytia are malformed in infected macroH2A1 KO cells compared to infected WT cells (**Figure 4.2 F**). Our findings demonstrate that macroH2A1 plays a key role in HCMV-induced cellular remodeling and formation of vIACs.

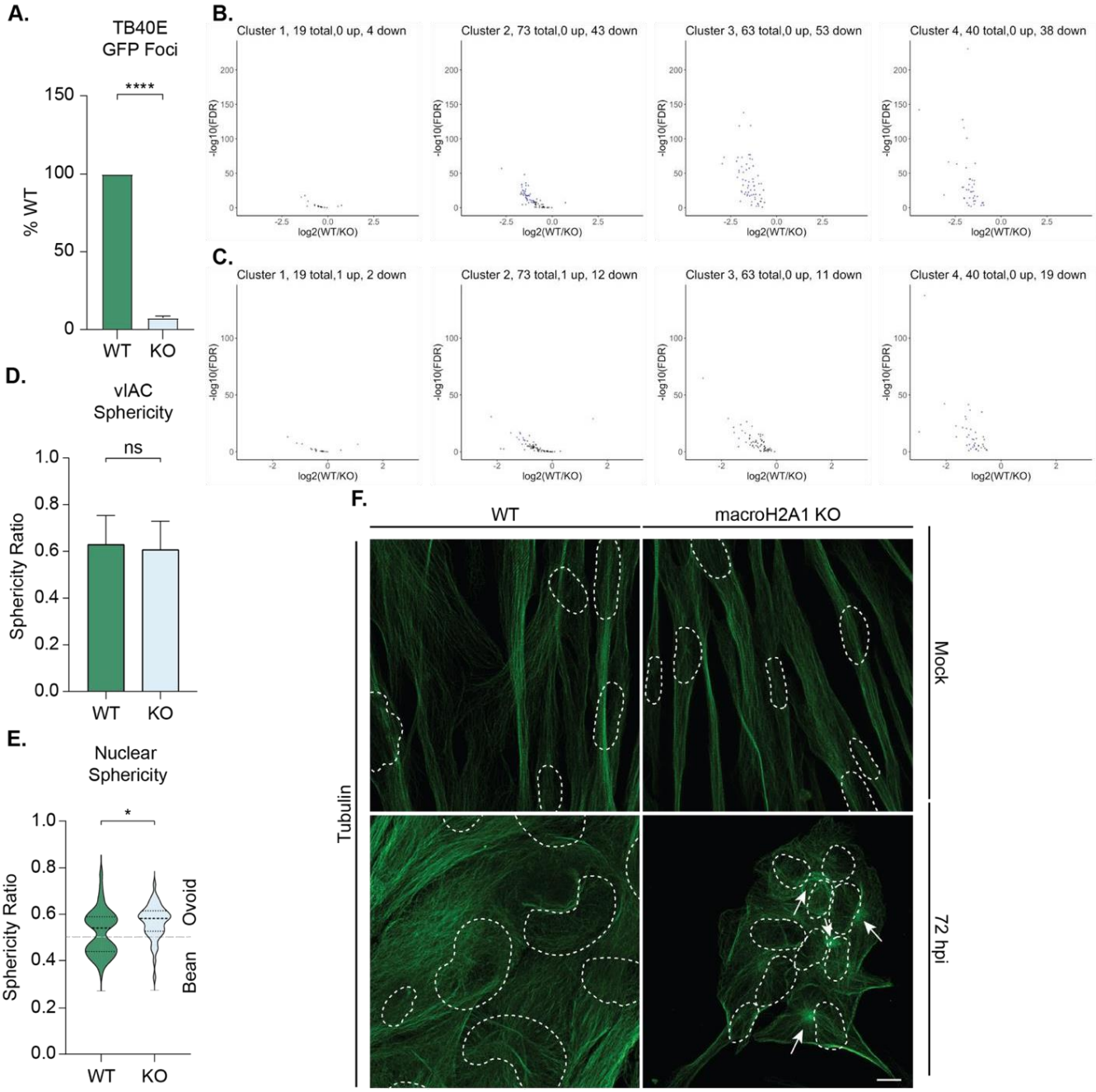

Figure 4.2. HCMV nuclear and cytoskeletal reorganization requires macroH2A1. A) Infectious progeny produced from *TB40E-GFP* HCMV infected WT and macroH2A1 KO HFF-T cells quantified by plaque assay at 4 or 6 days post infection (dpi) as indicated. Viral yield is indicated as the percent yield compared to wild type, with errors bars representing SEM. P < 0.0001 at both time points by unpaired T-test. N=3 biological replicates. B) Volcano plots where

the Log_2(Fold Change) for WT vs. macroH2A1 KO at 48 hpi is plotted against -log_{10}(FDR) for genes in clusters as marked. Significantly upregulated genes (Genes with Log2(Fold Change) >1 and FDR£0.05) are marked in red, and significantly downregulated genes (Genes with Log2(Fold Change) <1 and FDR£0.05) are marked in blue. C) Volcano plots as in (B) for gene expression at 72 hpi. D) Sphericity of viral induced assembly compartment as measured by pp28 staining. Bar graphs show mean with error bars indicating SEM. No significance by unpaired T-test. N>40 vIACs. E) Nuclear sphericity of WT and macroH2A1 KO HCMV infected cells at 72 hpi. Violin plot depicts median and quartiles in dashed lines. Division of oval and bean shape as marked. $p < 0.05$ by unpaired T-test. $N > 40$ cells. F) Representative immunofluorescence images of WT and macroH2A1 KO cells during CMV infection at mock and 72 hpi with tubulin staining in green. Arrows indicate centrosomes and dashed white lines outline nuclei. Scale bar represents 10 micrometers.

4.4 HCMV rearranges host cytosolic structures in a macroH2A1-dependent manner.

To determine if the structural rearrangements that are required for vIAC formation occur in the absence of macroH2A1, we investigated cellular organization using transmission electron microscopy (TEM). We found that while the overall cellular structure was comparable in mock-treated WT and macroH2A1 KO cells (**Figure 4.4 A**), at 4 days post infection (dpi) HCMV infected cells exhibited dramatically different cytoplasmic structures. We observed that the measurable length of endoplasmic reticulum (ER) regions was significantly shorter in WT cells compared to macroH2A1 KO cells (**Figure 4.4 B-D, Figure 4.3 A-B**). Our findings suggest that without macroH2A1, HCMV is unable to disrupt the host ER.

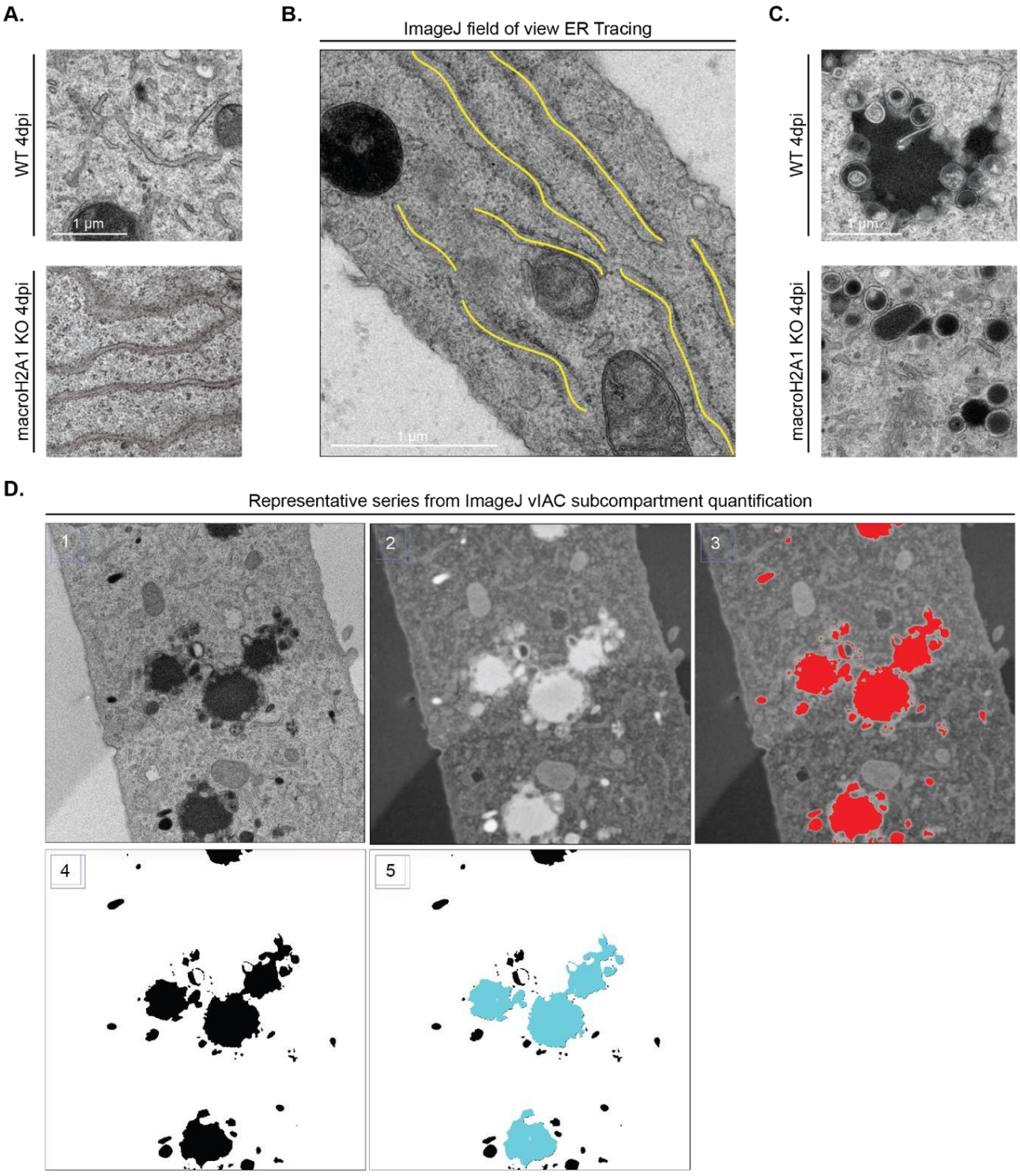
A.
B.
C.
ImageJ field of view ER Tracing
WT 4dpi
macroH2A1 KO 4dpi
1 µm
D.
Representative series from ImageJ vIAC subcompartment quantification
1
2
3
4
5

Figure 4.3. Image analysis pipeline for electron microscopy data. A) Additional transmission electron microscopy image of WT and macroH2A1 KO cells at 4 dpi with HCMV. Scale bar as indicated. B) Representative image highlighting the ER tracing in ImageJ for quantification in Figure 4.4D. Yellow lines represent traces made with "Freehand line tool", length of line was measured with ImageJ "Measure" function. C) Additional transmission electron microscopy images of vIACs from WT and macroH2A1 KO cells at 4 dpi. D) Representative images indicating the ImageJ macro for quantification of vIACs shown in Figure 4.4F. 1) Original image, 2) invert and gaussian blur, 3) thresholding to define subcompartments, 4) convert to mask and fill holes, 5) size exclusion on dense bodies and virions.

Moreover, by TEM we observed further differences in vIAC formation. In WT cells we observed the vIAC was made up of large subcompartments, consistent with previous findings (24). Each subcompartment was surrounded by a heterogeneous population of dense bodies, which are non-infectious HCMV particles comprised of enveloped viral proteins (25, 26). In contrast, the HCMV-infected macroH2A1 KO cells rarely formed these distinct large subcompartments (**Figure 4.4 E-F, Figure 4.3 C-D**). In the macroH2A1 KO cells, the largest observable subcompartments, whose area was significantly smaller than those formed in WT cells, were rarely surrounded by dense bodies (**Figure 4.4 E**). The dense bodies in the infected macroH2A1 KO cells were largely homogenous individual structures distributed throughout the cytosol, compared to the heterogenous and conglomerated dense bodies in infected WT cells. Furthermore, virus particles observed in macroH2A1 KO cells frequently appeared malformed, consistent with the finding that macroH2A1 KO cells produce defective progeny (**Figure 4.4 E,** arrowhead). Taken together, these results support our hypothesis that macroH2A1 plays a major role in HCMV-induced cellular remodeling and viral maturation.

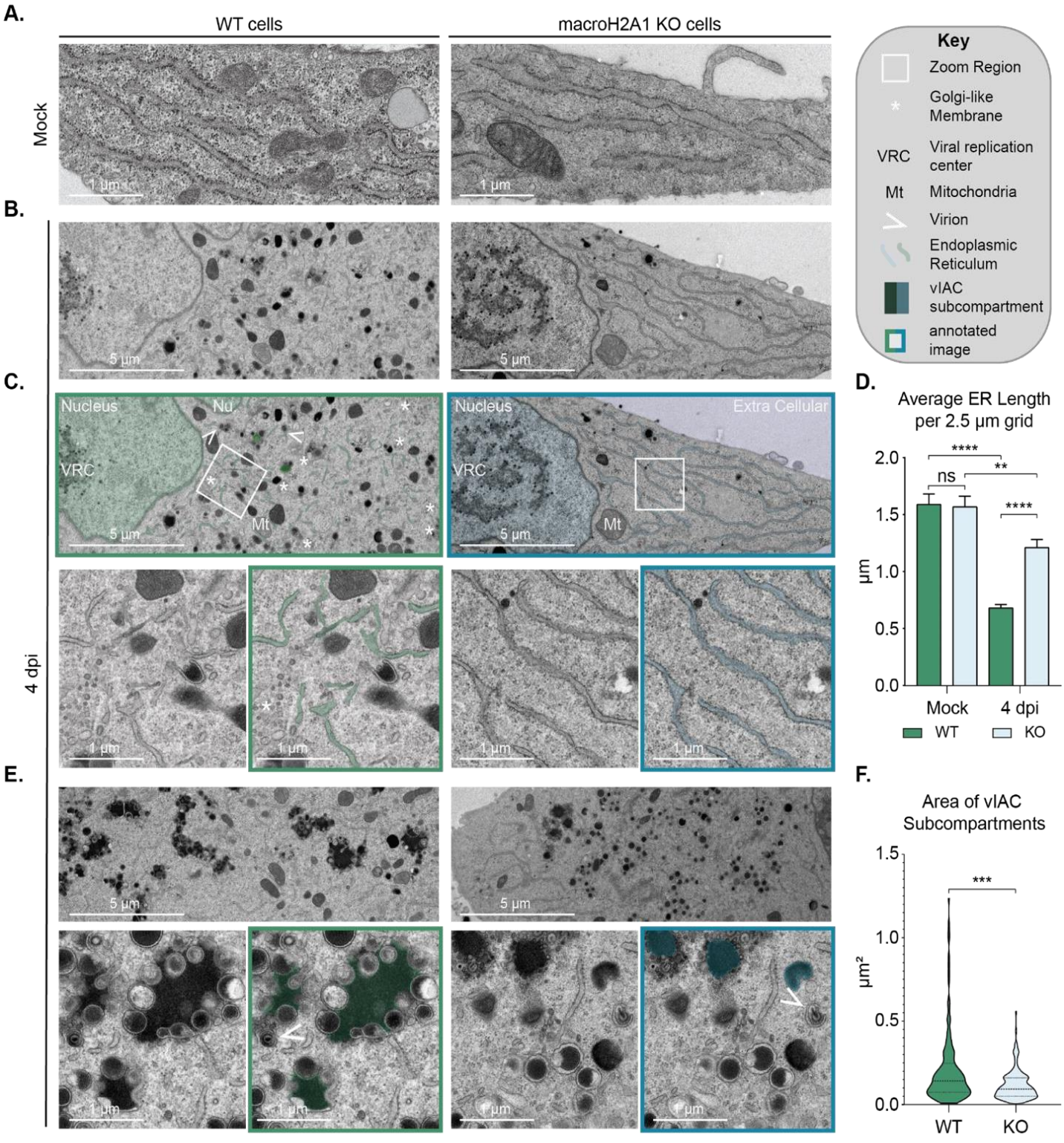
A.
WT cells
macroH2A1 KO cells
Mock
B.
C.
4 dpi
E.
Nucleus
Nu.
VRC
Mt
Extra Cellular
1 µm
5 µm
Key
Zoom Region
Golgi-like Membrane
VRC
Viral replication center
Mt
Mitochondria
Virion
Endoplasmic Reticulum
vIAC subcompartment
annotated image
D.
Average ER Length per 2.5 µm grid
µm
2.0
1.5
1.0
0.5
0.0
****
**
ns
****
Mock
4 dpi
WT
KO
F.
Area of vIAC Subcompartments
µm²
1.5
1.0
0.5
0.0
***
WT
KO

Figure 4.4. HCMV cellular remodeling and vIAC formation is dependent on macroH2A1. A) Representative transmission electron microscopy images of mock-treated WT and macroH2A1 KO HFF-T cells showing the uninfected state of the endoplasmic reticulum (ER). B) Representative transmission electron microscopy images of WT and macroH2A1 KO cells at 4 days post infection with HCMV. C) Annotation of images from (B). *Right:* Key for annotation. *Below:* Zooms of boxed regions of interest with annotated images of zoomed panels to the right. D) Average endoplasmic reticulum trace per 2.5 μm by 2.5 μm grid of WT and macroH2A1 KO cells in mock and 4 dpi. Bar graph shows mean length of ER per field of view with error bars indicating SEM. ** denotes $p < 0.01$, **** denotes $p < 0.0001$ by one-way ANOVA with subsequent Dunnett's tests of pairs of interest. N=40 grids for mock cells and 100 for infected cells. E) Representative transmission electron microscopy images viral-induced assembly compartments (vIAC) at 4dpi in WT and macroH2A1 KO cells as indicated. *Below:* Zooms from image with annotated versions to the right as in (C). F) Quantification of vIAC subcompartment area. Violin plot depicts median, and upper, and lower quartiles as dotted lines. $P < 0.001$ by paired T-test. N>100 subcompartments. Scale bars as indicated.

4.5 Loss of macroH2A1 prevents activation of neuronal genes during HCMV infection.

To profile changes in host gene expression that might lead to the observed phenotypic effects on HCMV infection upon loss of macroH2A1, we analyzed the host transcriptomes of WT and macroH2A1 KO cells during the course of HCMV infection. Principal component analysis of our RNA-seq data showed all replicates clustering close to each other, indicating reproducibility.

PC1 captured the time course of infection whereas PC2 captured the genotype (**Figure 4.5 A)**. We first identified a superset of genes that significantly changed in either one of the time points and/or one of the genotypes and then performed k-means (k=4) clustering of Z-scores of gene expression across time and genotype. This analysis captured both time-dependent and genotype-dependent changes in gene expression during HCMV infection (**Figure 4.6 A**). Cluster 1 contained genes that had mixed to low expression in mock-treated cells but steadily increased in expression over the course of infection, peaking at 72 hpi in WT but remained low in the macroH21 KO cells. Genes in this cluster were highly enriched for macroH2A1 and heterochromatin marker H3K27me3 in uninfected cells in our previously published CUT&Tag data set (22) (**Figure 4.5 B-E**). Clusters 2-4 captured time-dependent changes in expression that were mostly similar between WT and macroH2A1 KO conditions (**Figure 4.5 F-H**).

Cluster 2 contained genes that were activated at 48-72 hpi and expectedly includes genes that would assist in viral trafficking such as those associated with cellular reorganization and protein trafficking within the cell (**Figure 4.5 J**). Cluster 3 contained genes that were activated at 1624 hpi before returning to low expression. Also as expected, this cluster contains genes associated with immune response and transcription (**Figure 4.5 K**). Cluster 4 contained genes that were repressed throughout infection and contains genes associated with DNA repair, metabolic processes, and apoptosis (**Figure 4.5 L**). In striking contrast to clusters 2-4, cluster 1 genes were highly enriched for neuronal genes belonging to several Gene Ontology categories that highlighted neuronal function (**Figure 4.6 B, Figure 4.5 I**). Notably, cluster 1 genes strikingly had significantly lower expression in macroH2A1 KO cells, with large fold changes, especially at 72 hpi (**Figure 4.6 C**). Cluster 1 genes, which are the most affected by the loss of macroH2A1, suggest that HCMV induces a neuronal-like transcriptional profile that increases over the course of infection.

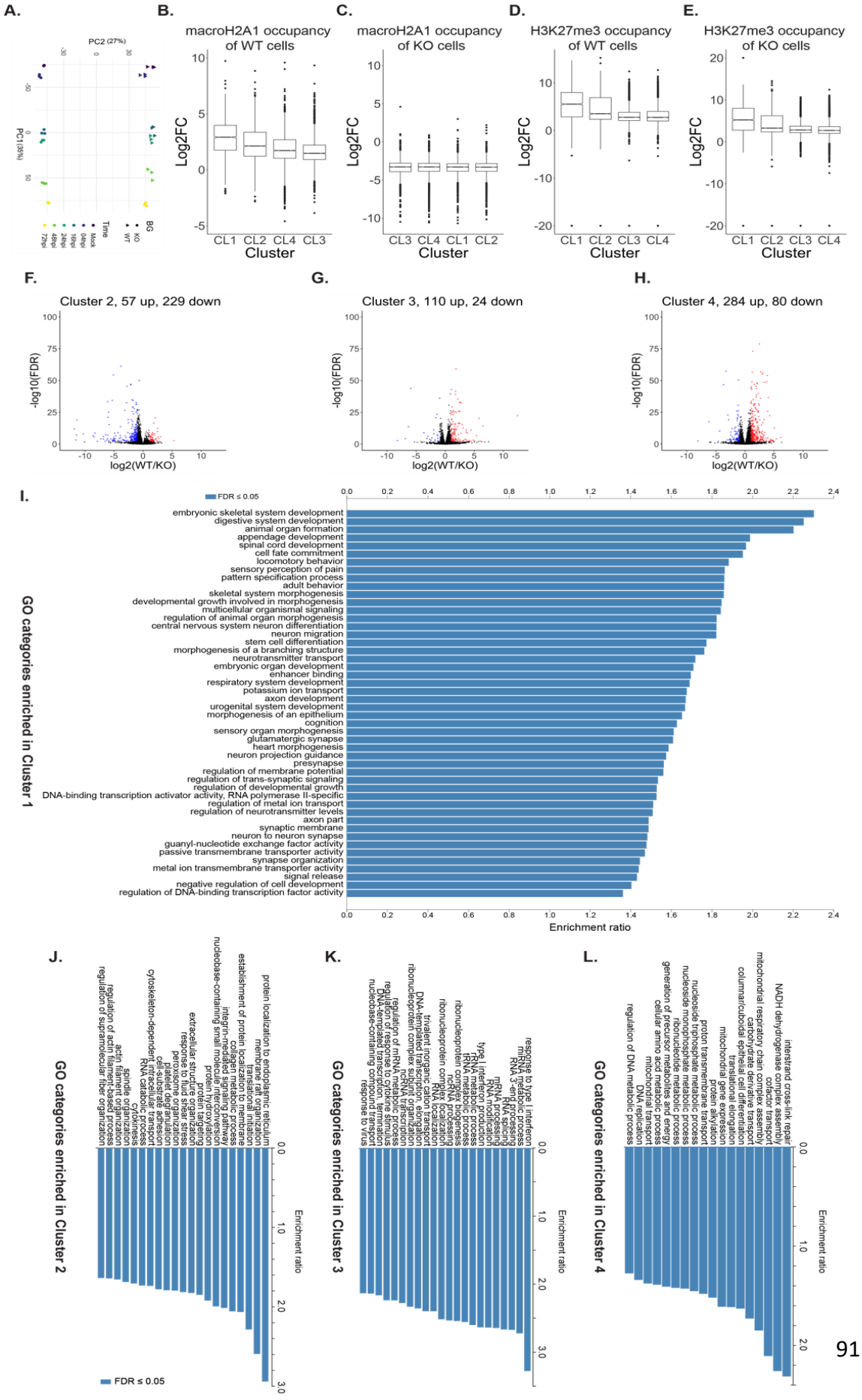
A.
B.
C.
D.
E.
macroH2A1 occupancy of WT cells
macroH2A1 occupancy of KO cells
H3K27me3 occupancy of WT cells
H3K27me3 occupancy of KO cells
Log2FC
Cluster
CL1 CL2 CL4 CL3
CL3 CL4 CL1 CL2
CL1 CL2 CL3 CL4
F.
G.
H.
Cluster 2, 57 up, 229 down
Cluster 3, 110 up, 24 down
Cluster 4, 284 up, 80 down
-log10(FDR)
log2(WT/KO)
I.
GO categories enriched in Cluster 1
FDR ≤ 0.05
embryonic skeletal system development
digestive system development
animal organ formation
appendage development
spinal cord development
cell fate commitment
locomotory behavior
sensory perception of pain
pattern specification process
adult behavior
skeletal system morphogenesis
developmental growth involved in morphogenesis
multicellular organismal signaling
regulation of animal organ morphogenesis
central nervous system neuron differentiation
neuron migration
stem cell differentiation
morphogenesis of a branching structure
neurotransmitter transport
embryonic organ development
enhancer binding
respiratory system development
potassium ion transport
axon development
urogenital system development
morphogenesis of an epithelium
cognition
sensory organ morphogenesis
glutamatergic synapse
heart morphogenesis
neuron projection guidance
presynapse
regulation of membrane potential
regulation of trans-synaptic signaling
regulation of developmental growth
DNA-binding transcription activator activity, RNA polymerase II-specific
regulation of metal ion transport
regulation of neurotransmitter levels
axon part
synaptic membrane
neuron to neuron synapse
guanyl-nucleotide exchange factor activity
passive transmembrane transporter activity
synapse organization
metal ion transmembrane transporter activity
signal release
negative regulation of cell development
regulation of DNA-binding transcription factor activity
Enrichment ratio
J.
GO categories enriched in Cluster 2
protein localization to endoplasmic reticulum
establishment of protein localization to membrane
collagen metabolic process
translational initiation
membrane raft organization
integrin-mediated signaling pathway
nucleobase-containing small molecule interconversion
protein hydroxylation
protein targeting
extracellular structure organization
response to fluid shear stress
peroxisome organization
platelet degranulation
cell-substrate adhesion
cytoskeleton-dependent cytokinesis
cytokinesis
RNA catabolic process
spindle organization
actin filament-based process
regulation of supramolecular fiber organization
Enrichment ratio
FDR ≤ 0.05
K.
GO categories enriched in Cluster 3
response to type I interferon
rRNA metabolic process
RNA 3'-end processing
RNA splicing
mRNA modification
type I interferon production
RNA metabolic process
rRNA processing
ncRNA processing
ribonucleoprotein complex biogenesis
ribonucleoprotein complex localization
DNA-templated transcription, elongation
trivalent inorganic cation transport
ribonucleoprotein complex subunit organization
regulation of mRNA metabolic process
regulation of response to cytokine stimulus
DNA-templated transcription, termination
nucleobase-containing compound transport
response to virus
Enrichment ratio
L.
GO categories enriched in Cluster 4
interstrand cross-link repair
NADH dehydrogenase complex assembly
mitochondrial respiratory chain complex assembly
cofactor transport
columnar/cuboidal epithelial cell differentiation
translational elongation
mitochondrial gene expression
protein alkylation
proton transmembrane transport
nucleoside triphosphate metabolic process
nucleoside monophosphate metabolic process
generation of precursor metabolites and energy
cellular amino acid metabolic process
mitochondrial transport
DNA replication
regulation of DNA metabolic process
Enrichment ratio

Figure 4.5. Host gene expression and chromatin states. A) Loadings of first two principal components from principal component analysis of the matrix of quantification of all genes for all 36 samples. PC1 captures the time course of infection, whereas PC2 captures the genotype. B) Log2 fold change of macroH2A CUT&Tag enrichment compared to IgG from uninfected cells at genes (from gene start to gene end) in each cluster plotted as boxplots. C) Same as (B) for macroH2A1 KO cells. D) Same as (B) for H3K27me3 CUT&Tag in WT cells. E) Same as (B) for H3K27me3 for macroH2A1 KO cells. Published macroH2A, H3K27me3, and IgG CUT&Tag data were used for (B-E). F-H) Volcano plots where the Log_2(Fold Change) for WT vs. macroH2A.1 KO at 72 hpi is plotted against -log_{10}(FDR) for genes in clusters 2 (F), 3(G), and 4 (H) shown. Significantly upregulated genes (Genes with Log2(Fold Change) >1 and FDR£0.05) are marked in red, and significantly downregulated genes (Genes with Log2(Fold Change) <1 and FDR£0.05) are marked in blue. I-L) Enrichment of GO categories with FDR<0.05 plotted for Cluster 1 (I), 2 (J), 3(K), and 4 (L).

To test the hypothesis that HCMV induces a neuronal-like phenotype that is blunted by the loss of macroH2A1, we compared our gene expression profiles to those of different cell types from ENCODE (27, 28). From ENCODE, we included expression profiles of IMR90 fibroblast cells, similar to our HFF cells, and cells differentiated from induced pluripotent stem cells to form cells in the neuronal, muscle, and liver lineages. We first generated a distance matrix and observed that IMR90 clustered with all macroH2A1 KO time points and WT mock and early time points. However, WT cells at 48 and 72 hpi cluster with the other lineages we included in the analysis (**Figure 4.6 D**). This suggests that later time points of HCMV infection cause a transition of HFF cells to a non-fibroblast identity, and this transition is suppressed in the absence of macroH2A1. To explore this further, we performed a principal component analysis of the expression matrix comprising genes from Cluster 1. PC1 captures the differences between fibroblast and non-fibroblast lineages, whereas PC3 captures the differences between neuronal and non-neuronal lineages (**Figure 4.6 E**). We found PC1 and PC3 to capture the infection time course. WT mock infected cells had similar values to IMR90 in PC1 and PC3. We observed an increase in PC1 and PC3 loadings with increasing time of infection in the direction toward neural cells. A similar trend is observed in macroH2A1 KO cells, but the starting time points (mock and 4 hpi) have much lower PC1 and PC3 loadings such that by the final time point, PC1 and PC3 values for

macroH2A1 KO cells are similar to that of mock-infected WT cells. Thus, an increase in both PC1 and PC3 observed over the course of infection captures the loss of fibroblast identity and a gain of neuronal identity in WT cells. Interestingly, in macroH2A1 KO cells, the starting point is much lower in PC1 and PC3, suggesting an inability of macroH2A1 KO cells to transition from fibroblast to neuronal identity over the course of infection. In summary, our gene expression analysis highlights the profound effect of macroH2A1 on transcriptional upregulation of many host genes during HCMV infection and that this upregulation transitions infected cells away from a fibroblast expression profile and towards a neuronal expression profile.

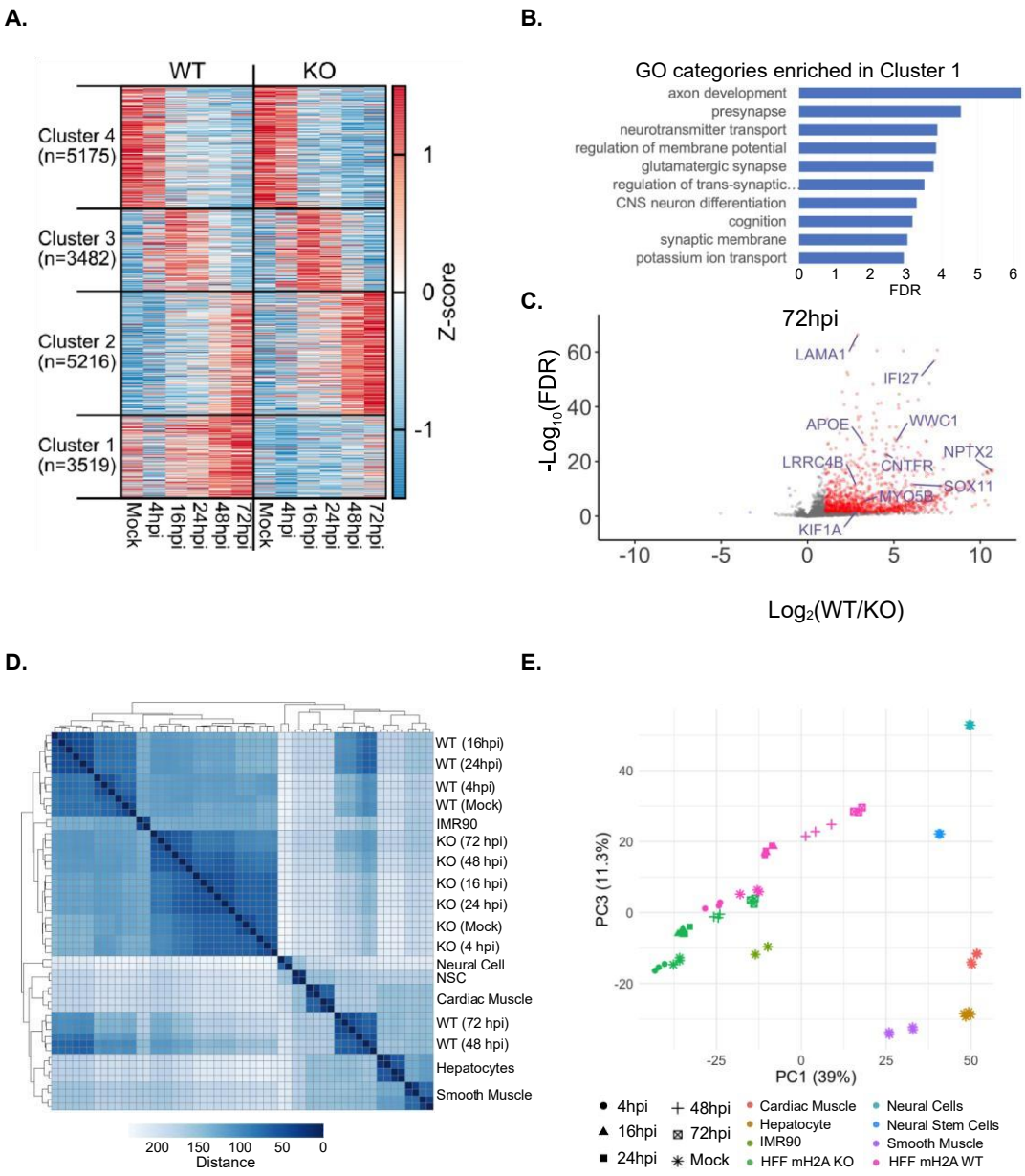

Figure 4.6. Host gene expression is altered upon loss of macroH2A1 during HCMV infection. A) K-means clustering (k=4) of gene expression changes over 72 hours of infection shown as a heatmap. Z-scores were calculated for each gene from its normalized count across the time course of CMV infection for WT and macroH2A1 KO cells. B) The -$\log_{10}$(FDR) value for enrichment of neuronal GO categories in Cluster 1. C) Volcano plot where the Log_2(Fold Change) for WT vs. macroH2A.1 KO is plotted against -$\log_{10}$(FDR) for genes in Cluster 1. Genes with Log_2(Fold Change) >1 and FDR £ 0.05 are marked in red. Neuronal genes selected for further characterization are labeled in blue. D) Matrix of Euclidean distance between normalized expression profiles of CMV infection time course for WT and macroH2A1 KO, and

other cell types. Gene expression datasets for other cell types were obtained from ENCODE. E) PCA plot showing PC1 and PC3 for the same expression profiles plotted in (D).

As macroH2A1 frequently colocalizes with H3K27me3 and cluster 1 was also enriched for H3K27me3 (**Figure 4.5 D-E**), we used the small molecule tazemetostat (an EZH2 inhibitor)(29), to deplete H3K27me3 prior to HCMV infection. We found that although H3K27me3 depletion caused a significant reduction in titer, the reduction was modest compared to that induced by loss of macroH2A1 (**Figure 4.7 A**). Furthermore, H3K27me3 depletion did not impact nuclear rearrangement or vIAC formation (**Figure 4.7 B-D**). We also investigated by western blot the induction of cluster 1 gene KIF1A, a kinesin motor for axonal transport in neurons(30), and found that its induction was not diminished significantly by the depletion of H3K27me3 (**Figure 4.7 E**). Our results suggest that while H3K27me3 is likely also important for HCMV infection, its role on cluster 1 genes appears less significant for HCMV infection than that of macroH2A1.

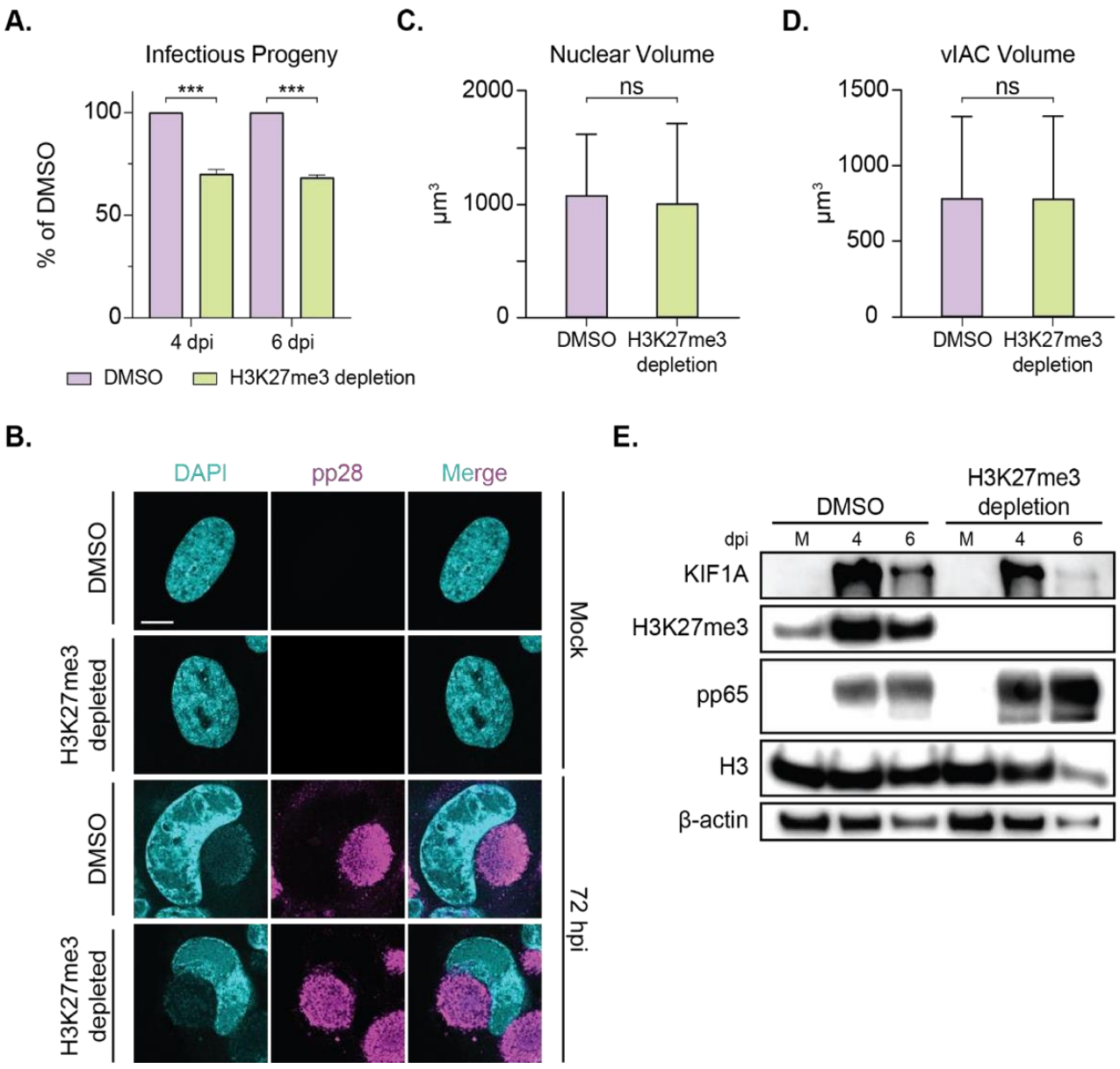

Figure 4.7. H3K27me3 is not required for cellular remodeling or KIF1A induction by HCMV. A) Infectious progeny produced from HCMV-infected WT and H3K27me3 depletion by tazemetostat cells quantified by plaque assay. Viral yield is indicated as the percent yield compared to wild type, with errors bars representing SEM. $P < 0.001$ at both time points by unpaired T-test. N=3 biological replicates at 4 dpi N=2 at 6 dpi. B) Representative immunofluorescence images of WT and H3K27me3 depleted cells during HCMV infection at mock and 72 hpi. DAPI is shown in cyan and viral protein pp28 is shown in magenta. Images are merged in bottom row. Scale bar represents 10 µm. C) Nuclear volume of WT and H3K27me3-depleted HCMV-infected cells at 72 hpi. Bar graphs show mean with error bars indicating SEM. No significance by unpaired T-test. N > 40 cells. D) Volume of viral induced assembly compartment as measured by pp28 staining. Bar graphs indicate mean with error

bars indicating SEM. No significance by unpaired T-test. N > 40 vIACs. E) Representative western blot of viral proteins in WT and H3K27me3 depleted cells during HCMV infection at 4 or 6dpi compared to mock (M) as indicated. Vinculin is shown as loading control.

4.6 Knockdown of several neuronal genes reduced HCMV spread and vIAC formation.

We next sought to determine if the transition from a fibroblast to neuronal expression profile is essential for HCMV infectivity. Following the observation that many of the genes differentially expressed in HCMV infection between WT and macroH2A1 KO cells were associated with axon formation and neurotransmitter trafficking, we hypothesized that HCMV hijacks these pathways for progeny maturation and spread. To test this hypothesis, we designed a targeted siRNA screen selecting 12 genes with low FDRs and large fold changes in expression between WT and macroH2A1 KO cells induced by HCMV at 72 hpi (**Figure 4.8 A-C**).

Following infection of WT cells with HCMV tagged with GFP, we transfected siRNAs to dampen the induction of these target genes later in infection (**Figure 4.10 A**). We confirmed that all siRNA targeted transcripts were reduced by at least 50% compared to their levels at 4 dpi in the condition treated with a non-targeting control (NC) siRNA (**Figure 4.10 B, Figure 4.8 D**). Upon initial infection, representative HCMV RNA and protein levels did not differ among any conditions (**Figure 4.8 E-F**). This indicates viral transcription and translation were not impacted by the siRNA treatment. We used supernatants harvested from the siRNA-treated HCMV-infected cells to set up GFP foci assays and measure plaque size. We found that several siRNA knockdowns caused a reduction in GFP foci to 40-70% of control levels though these groups did not reach significance (**Figure 4.10 C**). Knockdown of WWC1, however, did significantly reduce GFP foci. Interestingly, we also noted that several of the knockdown conditions produced viral progeny that generated smaller plaque sizes compared to the control. To investigate this observation, we imaged crystal violet plaques and quantified the area of these plaques (**Figure 4.9 A**). We found that five of our target genes, IFI27, KIF1A, LAMA1, NPTX2, and WWC1, had significantly smaller plaques compared to control (**Figure 4.10 D-E**), highlighting their importance to infection.

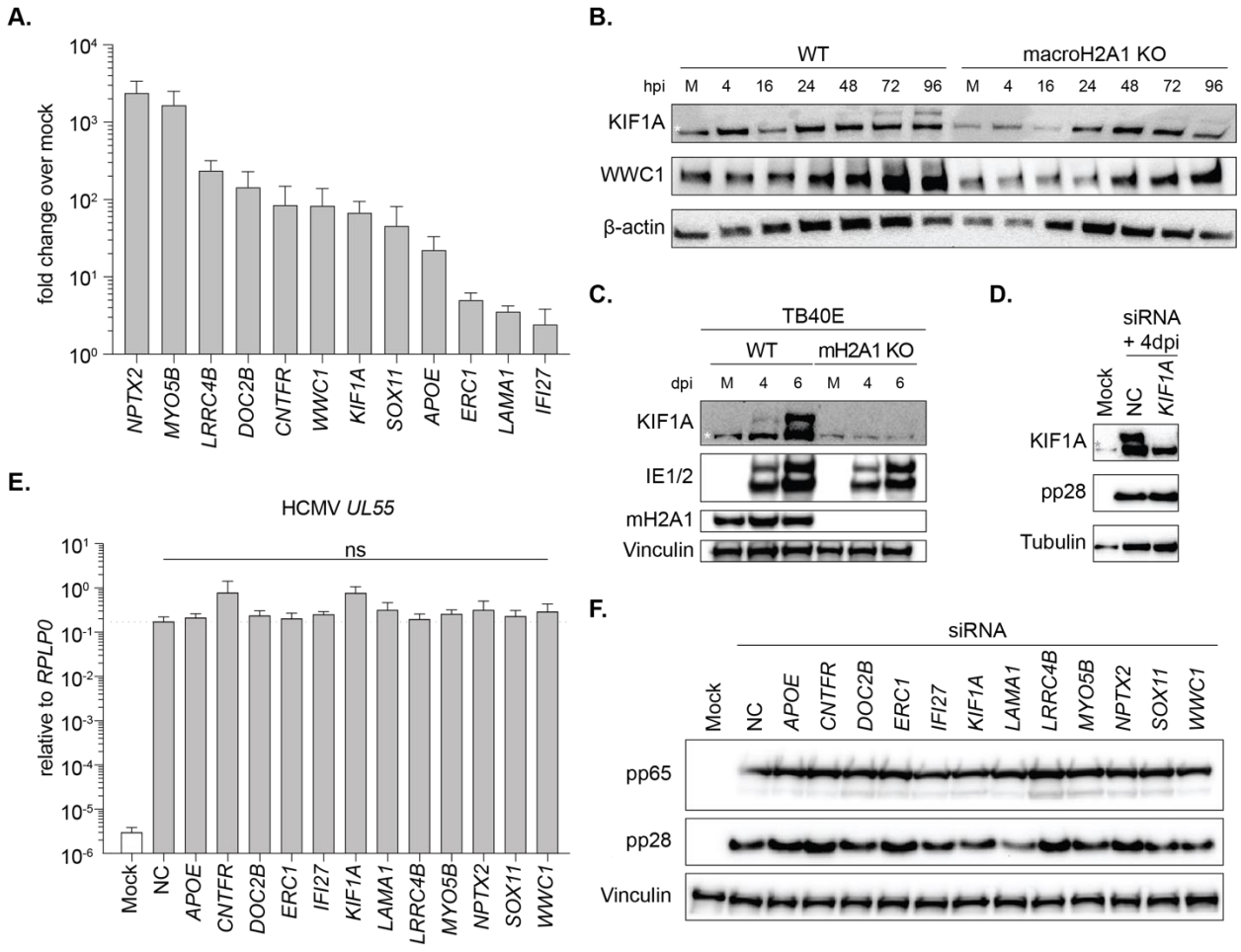

Figure 4.8. Gene expression analysis of siRNA screen during HCMV infection. A) RT-qPCR of target gene RNA levels during HCMV infection at 4 dpi. Bar graphs indicate mean with error bars indicating SEM. N=3 biological replicates. B) Representative western blot of neuronal proteins in WT and macroH2A1 KO cells during HCMV infection at 4, 16, 24, 48, 72, and 96 hpi compared to mock (M). Asterisk indicates a non-specific band. Actin is shown as loading control. C) Representative western blot of KIF1A in WT and macroH2A1 KO cells during *TB40EGFP* HCMV infection at 4 and 6 dpi compared to mock (M). Asterisk indicates a nonspecific band. Vinculin is shown as loading control. D) Representative western blot of siRNA knockdown in WT cells during HCMV infection at 4 dpi compared to mock (M). Asterisk indicates a non-specific band. Tubulin is shown as loading control and pp28 is shown as infection control. E) RT-qPCR of HCMV UL55 in siRNA treated cells during CMV infection. Expression is normalized to the non-targeting control treated mock-infected cells. Bar graphs show mean with error bars indicating SEM. N=3 biological replicates. No significance by ANOVA. F) Representative western blot of viral proteins pp65 and pp28 in siRNA knockdown in

WT cells during HCMV infection at 4 dpi compared to mock (M). Vinculin is shown as loading control.

Next, we investigated whether depletion of these five targets impacted HCMV-induced cellular remodeling and vIAC formation. We found that IFI27 and KIF1A KD cells had smaller nuclei and significantly smaller vIACs compared to control. Additionally, LAMA1, NPTX2, and WWC1 KD resulted in vIACs that were malformed with either a hollow or nonspherical appearance (**Figure 4.10 F-H and Figure 4.9 B-D**). Taken together, our results from this screen demonstrate that cells unable to induce these genes to a high level are unable to produce viral progeny that can spread efficiently, underscoring the significance of these genes in HCMV spread.

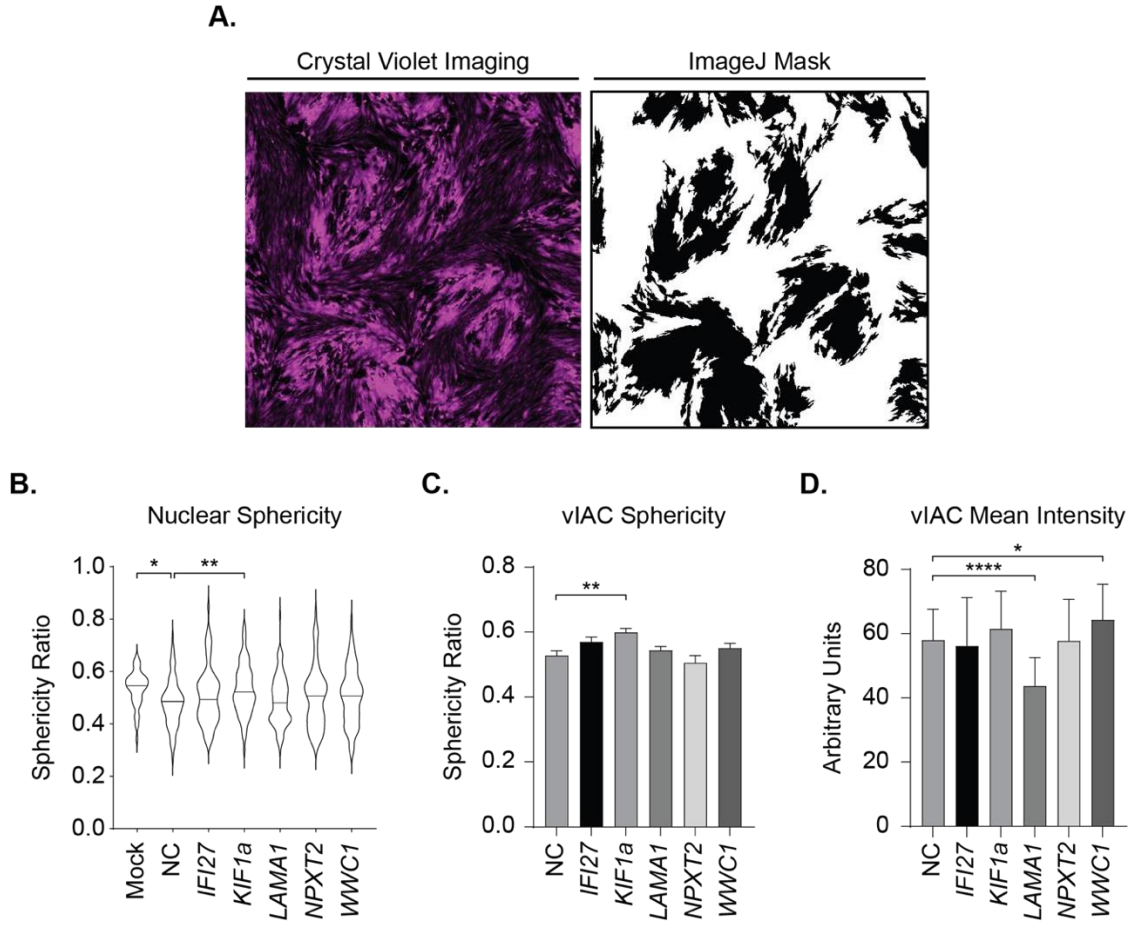

Figure 4.9. Image analysis of siRNA screen. A) Representative Cy-5 imaging of Crystal Violet stained HCMV plaques in HFF cells and subsequent ImageJ quantification. B) Nuclear sphericity of HCMV-infected WT and siRNA treated cells as indicated at 72 hpi. Violin plot depicts median and quartiles in dashed lines. * indicates $p < 0.05$ ANOVA with follow up Dunnett's test. N > 40 cells. C) Sphericity of viral-induced assembly compartment as measured by pp28 staining. Bar graphs show mean with error bars indicating SEM. No significance by unpaired T-test. N > 40 vIACs. D) Average intensity of viral-induced assembly compartments as measured by pp28 staining. Bar graphs show mean with error bars indicating SEM. * indicates $p < 0.05$ ANOVA with follow up Dunnett's test. N > 40 vIACs.

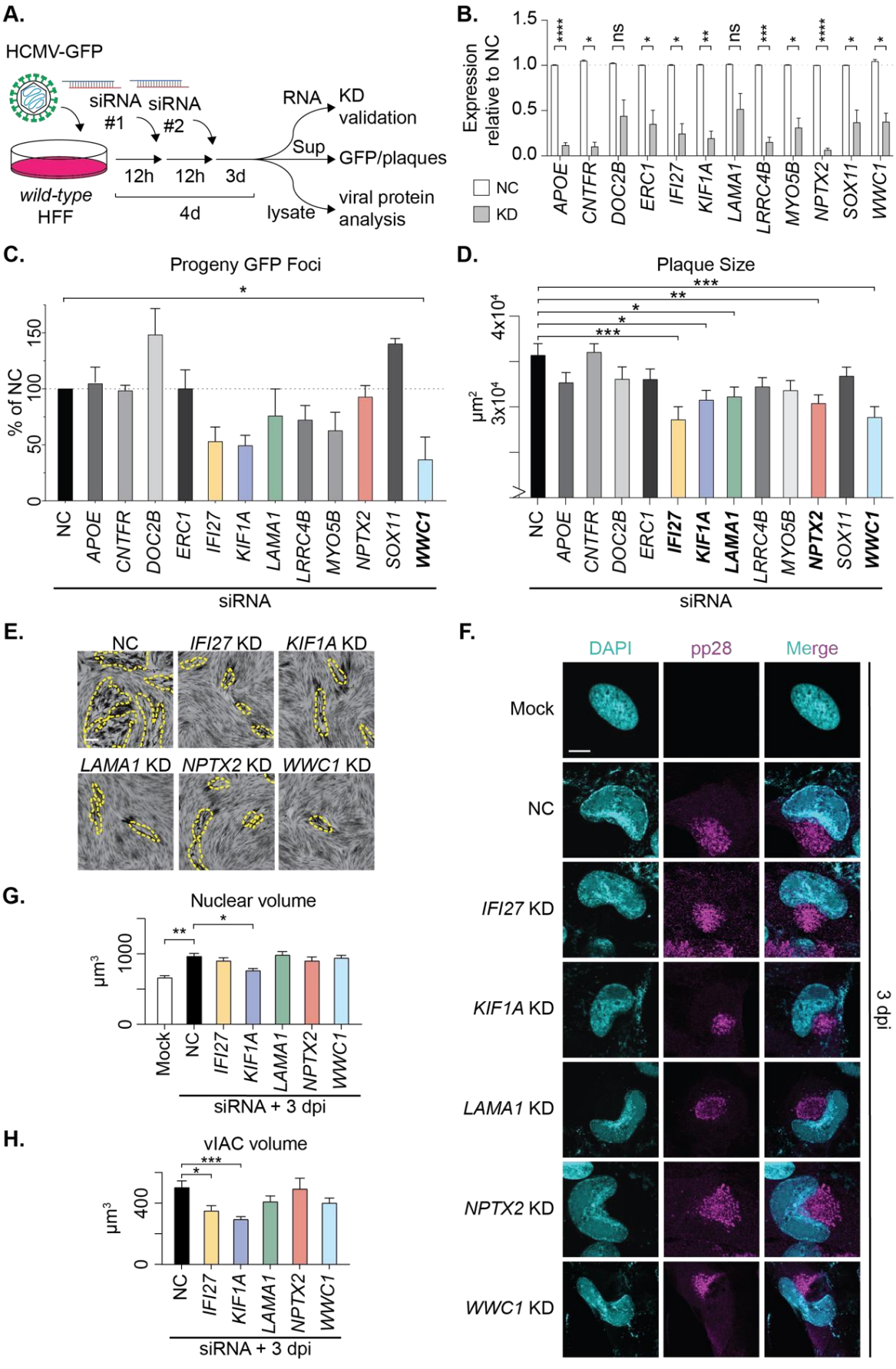
A.
HCMV-GFP
siRNA #1
siRNA #2
12h
12h
3d
4d
wild-type HFF
RNA
KD validation
Sup
GFP/plaques
lysate
viral protein analysis
B.
Expression relative to NC
NC
KD
APOE
CNTFR
DOC2B
ERC1
IFI27
KIF1A
LAMA1
LRRC4B
MYO5B
NPTX2
SOX11
WWC1
C.
Progeny GFP Foci
% of NC
siRNA
D.
Plaque Size
µm²
siRNA
E.
NC
IFI27 KD
KIF1A KD
LAMA1 KD
NPTX2 KD
WWC1 KD
F.
DAPI
pp28
Merge
Mock
NC
IFI27 KD
KIF1A KD
LAMA1 KD
NPTX2 KD
WWC1 KD
3 dpi
G.
Nuclear volume
µm³
Mock
siRNA + 3 dpi
H.
vIAC volume
µm³
siRNA + 3 dpi

Figure 4.10. Successful HCMV maturation requires induction of dormant neuronal proteins. A) Schematic of targeted siRNA screen methodology. B) RT-qPCR quantification of RNA levels of target genes during HCMV infection. These genes include APOE, a lipoprotein associated with Alzheimer's disease and synaptic vesicle release(45, 46); CNTFR, a ciliary neurotrophic factor receptor that supports motor neuron axons(47); DOC2B a calcium sensor that promotes synaptic vesicle release(48); ERC1, a cellular scaffolding protein(49); IFI27, an interferon-induced gene expressed in the cerebellum in response to viral CNS infection(50); KIF1A, a neuronal kinesin(30); LAMA1, a laminin essential for neurite growth(51, 52); LRRC4B, a transmembrane protein that regulates synapse formation(53); MYO5B, a myosin associated with polarity and axon development(54); NPTX2 (formerly NARP), a small molecule released in excitatory synapses(55); SOX11, a transcription factor associated with neuron development(56); and WWC1, a synaptic scaffolding protein(57). Knockdown of each gene at 4dpi is normalized to its expression in cells treated with the non-targeting control (NC) at 4 dpi. Bar graphs show mean with error bars indicating SEM. N=3 biological replicates. C) Quantification of GFP foci in cells infected with supernatant harvested from cells treated with indicated siRNA as depicted in (A). Bar graphs show mean with error bars indicating SEM. * indicates $P < 0.05$ by one way ANOVA with follow up Dunnett's test. N=3 biological replicates. D) Quantification of plaque area produced from supernatant harvested from cells treated with siRNA indicated. Those that reach statistical significance are bolded. Bar graphs show mean with error bars indicating SEM. * denotes $P < 0.05$, ** denotes $p < 0.01$, *** denotes $p < 0.001$ by one way ANOVA with follow up Dunnett's test. N > 300 plaques. E) Representative images of plaque sizes for those with significant differences as indicated. Yellow dashed line frames plaque example. Scale bar indicates 150 μm. F) Representative immunofluorescence images of HCMV-infected cells treated with indicated siRNA knockdown. DAPI is shown in cyan and pp28 is shown in magenta. Scale bar represents 10 μm. G) Quantification of nuclear volume in siRNA-treated cells infected with HCMV. Bar graph shows mean with error bars indicating SEM. * denotes $P < 0.05$, ** denotes $p < 0.01$ by one way ANOVA with follow up Dunnett's test. N > 60 cells. H) Quantification of viral induced assembly compartment (vIAC) volume in siRNA-treated cells infected with HCMV. Bar graph shows mean with error bars indicating SEM. * denotes $P < 0.05$, *** denotes $p < 0.001$ by one way ANOVA with follow up Dunnett's test. N > 60 vIACs.

4.7 HCMV IE1 is sufficient to drive expression of neuronal genes

Next, we investigated the mechanism of activation of these neuronal genes. HCMV immediate early protein IE1 directly binds the acidic patch on the nucleosome. This interaction is mediated by a region in its C-terminus called the chromatin-tethering domain (CTD) that specifically interacts with the host histone H2A(31). Because this region of H2A and the responsible amino acids are highly conserved between canonical H2A and macroH2A1(32) (**Figure 4.11 A,** underlined residues), we hypothesized that HCMV IE1 may also bind macroH2A1 in this region. Further, because HCMV IE1 is sufficient to

drive expression of several interferon stimulated genes (33), we hypothesized that through interacting with macroH2A1, IE1 may be responsible for the activation of neuronal genes that we observed.

To test this hypothesis, we expressed HCMV IE1, a mutant IE1 missing the CTD (IE1 ΔCTD), or luciferase as a control using a doxycycline inducible promoter in fibroblast cells (31, 33). We confirmed that doxycycline (dox) treatment drove robust expression of inducible IE1 or IE1 ΔCTD by 48 hours (**Figure 4.11 B**). Next, we measured the expression of 12 neuron-associated genes (as in **Figure 4.10**) by RT-qPCR. We found that compared to luciferase expression (Luc), expression of IE1 increased the transcript levels for all 12 genes, with 9 of 12 reaching statistical significance (**Figure 4.11 C**). We also examined the induction of COPA, a cluster 2 gene that increases in expression in both macroH2A1 KO and WT cells upon HCMV infection and found that this gene did not increase with IE1 expression, suggesting it is not regulated by IE1 or macroH2A1 (**Figure 4.11 C**). Importantly, we discovered that expression of IE1 ΔCTD induced expression of target neuronal transcripts to a lower degree than full length IE1. Specifically, 4 of 9 genes that were induced by IE1 were induced to a significantly lower level upon induction of IE1 ΔCTD (**Figure 4.11 C**). Further, we investigated the protein levels of KIF1A, which was robustly induced by IE1 expression, and discovered that despite the slight increase in transcript levels of

KIF1A upon expression of IE1 ΔCTD, we could not detect KIF1A by western blot (**Figure 4.11 D**). This finding indicates that the lower transcript levels induced by IE1 ΔCTD were not sufficient for protein expression of KIF1A. Taken together, these results demonstrate that IE1 is sufficient to drive expression of neuronal genes, likely through an interaction of the IE1 CTD with host histone macroH2A1.

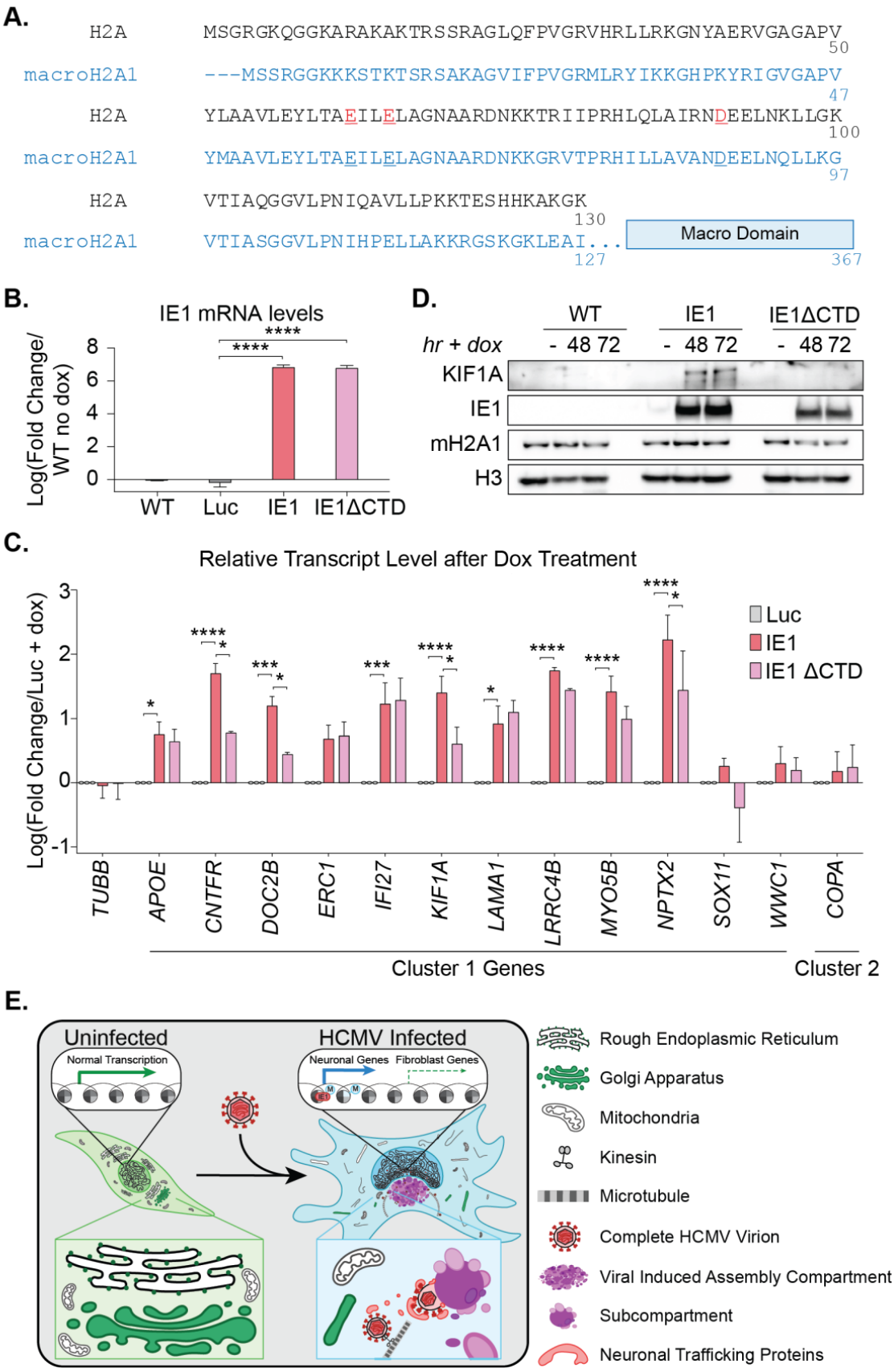
A.
H2A MSGRGKQGGKARAKAKTRSSRAGLQFPVGRVHRLLRKGNYAERVGAGAPV
50
macroH2A1 ---MSSRGGKKKSTKTSRSAKAGVIFPVGRMLRYIKKGHPKYRIGVGAPV
47
H2A YLAAVLEYLTAEILELAGNAARDNKKTRIIPRHLQLAIRNDEELNKLLGK
100
macroH2A1 YMAAVLEYLTAEILELAGNAARDNKKGRVTPRHILLAVANDEELNQLLKG
97
H2A VTIAQGGVLPNIQAVLLPKKTESHHKAKGK
130
macroH2A1 VTIASGGVLPNIHPELLAKKRGSKGKLEAI...
127
Macro Domain
367
B.
IE1 mRNA levels
Log(Fold Change/ WT no dox)
WT
Luc
IE1
IE1ΔCTD
D.
WT
IE1
IE1ΔCTD
hr + dox
- 48 72
- 48 72
- 48 72
KIF1A
IE1
mH2A1
H3
C.
Relative Transcript Level after Dox Treatment
Log(Fold Change/Luc + dox)
Luc
IE1
IE1 ΔCTD
TUBB
APOE
CNTFR
DOC2B
ERC1
IFI27
KIF1A
LAMA1
LRRC4B
MYO5B
NPTX2
SOX11
WWC1
COPA
Cluster 1 Genes
Cluster 2
E.
Uninfected
Normal Transcription
HCMV Infected
Neuronal Genes
Fibroblast Genes
Rough Endoplasmic Reticulum
Golgi Apparatus
Mitochondria
Kinesin
Microtubule
Complete HCMV Virion
Viral Induced Assembly Compartment
Subcompartment
Neuronal Trafficking Proteins

Figure 4.11. HCMV IE1 is sufficient to drive expression of dormant neuronal genes. A) Schematic of H2A and macroH2A1 homology in the histone fold domain. Residues previously demonstrated to facilitate binding of HCMV IE1 are shown in red in H2A and underlined to show conservation in macroH2A1. B) RT-qPCR quantification of RNA levels of viral IE1 in doxycycline (dox) inducible cell lines at 48 hours of treatment normalized to luciferase (Luc) levels. Bar graph shows mean with error bars indicating SEM. **** denotes $p < 0.0001$ by one way ANOVA with follow up Dunnett's test. N=3 biological replicates. C) RT-qPCR quantification of RNA levels of 12 cluster 1 genes in cells with dox-inducible IE1 or IE1 ΔCTD at 48 hours of dox treatment normalized to Luc. TUBB is shown as a negative control. COPA is shown as a representative cluster 2 gene. Bar graph shows mean with error bars indicating SEM. * denotes $P < 0.05$, ** denotes $p < 0.01$, *** denotes $p < 0.001$, **** denotes $p < 0.0001$ by one way ANOVA with follow up Dunnett's test. N=3 biological replicates. D) Representative western blot of IE1, KIF1A, and macroH2A1 in WT cells and cells with dox-inducible IE1 or IE1 ΔCTD when no dox was added (-) or at 48 and 72 hours after dox addition. H3 is shown as loading control. E) Model schematic. HCMV-infected cells upregulate numerous neuronal genes, through IE1, and these genes are required by the virus for proper cellular remodeling, formation of the viral assembly compartment, and viral maturation to promote viral spread.

4.8 Discussion

In this study, we demonstrated that human cytomegalovirus induces expression of numerous neuronal genes involved in synapse formation and neurotransmitter vesicle trafficking in a macroH2A1-dependent manner driven by viral IE1. We further showed that macroH2A1 and several of these induced neuronal genes are crucial to HCMV maturation and spread (**Figure 4.11 E**). Previous reports demonstrated that the HCMV protein IE1 can directly bind the acid patch of the canonical nucleosome (31, 34), which is highly conserved in macroH2A1(35). Here, we found that IE1 is sufficient to drive expression of macroH2A1-dependent neuronal genes, demonstrating a mechanism of action and suggesting that IE1 also binds to macroH2A1containing nucleosomes.. Our findings indicate that viral reprogramming of the host cell is dependent on host chromatin-controlled changes and uncovers previously unappreciated pathway critical for HCMV infection.

The formation of a vIAC and kidney-bean shaped nucleus was thought to be an exclusive feature of HCMV infection, however, these changes have also been observed in HSV-1 infection of neuron-like

cells (36). In fact, one of our identified neuronal genes important for HCMV maturation, *KIF1A*, a kinesin motor protein involved in axonal transport, was shown to be important for the spread of HSV-1 and pseudorabies virus (PRV) (37). These observations raise an interesting question about whether HCMV hijacking of neurotransmitter trafficking pathways is a retained evolutionary feature of many viruses or a novel pathway exploited specifically by HCMV. MacroH2A1 is also highly conserved and not rapidly evolving (38), suggesting that it is more likely to be HCMV that evolved to hijack this histone. Future work into the evolution of HCMV will uncover how these mechanisms of chromatin manipulation have developed.

Murine CMV was recently reported to control large scale transcriptional profiles and alter the identity of infected macrophages to escape innate immune response and increase spread (39). Our work builds on this finding in HCMV, suggesting that betaherpesviruses may drive cellular reprogramming for infection spread in various cell-type specific ways. Importantly, we find primarily structural genes associated with terminal differentiation to be upregulated during HCMV infection, as opposed to developmental genes. Taken together with the recent findings on murine CMV, our work suggests that HCMV cellular reprogramming is not limited to a particular set of genes, but rather is controlled through chromatin mechanisms. Furthermore, our discovery that HCMV upregulates genes associated with synapse formation and neurotransmitter trafficking for efficient spread provides a functional context for the previous findings wherein HCMV virions resemble synaptic-like vesicles in their lipid content (40).

It is important to note that these neurotransmitter pathways are dormant in uninfected fibroblast cells. Thus, there are no normal neuronal secretory functions that the virus must compete with, nor are there specific neuronal immune defenses to subvert. Furthermore, neuronal trafficking is one of the fastest and most efficient mechanisms by which to exit the cell (41). Therefore, HCMV has pinpointed and activated an entirely dormant pathway to both avoid competition and egress successfully and rapidly from the infected cell. Interestingly, the idea that ancient human retrovirus integration gave rise to the neuronal trafficking protein Arc (42) further supports the hypothesis that viral and neurotransmitter

trafficking rely on similar mechanisms. New screening methods may also uncover unknown strategies for chromatin manipulation through other factors to promote viral maturation (43, 44), though targeted approaches for chromatin may be required. Given our findings that HCMV induces expression of neuronal genes through chromatin manipulation, it is likely that many additional mechanisms of chromatin hijacking by viruses have yet to be uncovered.

Data Availability:
RNA-sequencing data can be found at GSE272267 (Reviewer token: wbszmgmmlhunpst)

Chapter 5: Discussion and Future Directions

5.1 Summary:

Herpesviruses are very large, complicated DNA viruses. Many of the human herpesviruses are known for their minor symptoms, such as sores and cold-like symptoms. However, herpesviruses can cause severe, even fatal, disease in neonates (1), are a major source of morbidity following transplantation (2, 3), and some are even known to be oncogenic (4). Nonhuman herpesviruses can have devastating agricultural and economic impacts in cattle (5), pigs (6), poultry (7), fish (8), and even mollusks (9). The extensive human health and economic burdens of herpersviruses highlight the need for continued research on the basic biology of herpesviruses.

The known human herpesviruses encode between 80-200 proteins depending on the virus (10). Despite the large number of potential targets, primary treatment for herpesviruses is the nucleoside analog, acyclovir and its derivatives (11), a drug originally approved by the FDA over 40 years ago. These drugs aim to reduce outbreaks or treat symptoms during outbreaks. Due to the establishment of a latent phase by all herpesviruses, no existing herpesvirus treatments are curative.

As nuclear replicating viruses, herpesviruses must compete with the host cell's existing nuclear environment to replicate. Assembled capsids must then navigate the crowded nuclear environment and exit the nucleus before they undergo final maturation in the cytosol. One important aspect of nuclear replication is the viral manipulation of host chromatin both as a regulatory element of the cell state and a physical barrier to replication and nuclear egress.

In this thesis, I have addressed knowledge gaps in the cellular mechanisms by which human herpesviruses HSV-1 and CMV efficiently produce progeny and spread from cell to cell. In chapter 2, we showed that heterochromatin markers macroH2A1 and H3K27me3 support the formation of chromatin channels used by HSV-1 capsids for nuclear egress. In chapter 3, I further refined our model on the role of H3K27me3, showing the mark directs capsid docking and the viral kinase Us3 for nuclear egress. Finally in chapter 5, I showed the heterochromatin marker macroH2A1, but not H3K27me3, supports HCMV maturation by driving transcription of neuronal genes in fibroblasts.

5.2 How are herpesviruses driving the large-scale chromatin and transcriptional changes during lytic infection?

Structure and function are intrinsically deeply connected in biology. Structure has long been used to infer functions and vice versa. With chromatin this relationship is especially linked, relaxed chromatin is transcribed and tightly coiled chromatin is inactive. Thus structural changes to chromatin correspond to transcription changes (12). The linked nature of the chromatin structure and transcription make it difficult to elucidate whether the changes to an infected cell are a result of structural changes to the chromatin or viral hijacking of transcription factors.

In chapter 2, I hypothesize that a general stress response, rather than a specific viral protein, might be the driving factor for the chromatin rearrangement during HSV-1 infection. This hypothesis is supported by similar transcription profiles in HSV-1 infected cells and cells experiencing heat or salt stress (13). In response to salt or osmotic stress, nuclear shape, chromatin structure and the transcriptional profile all change, though the order of these events has not been resolved (14). Mechanical forces applied to the nucleus to alter the shape also alter the transcriptional profile of the cell (15, 16). The linked change in nuclear structure and transcription profile are also observed in other diseases including cancers (17). HSV-1 infection also drives the large-scale nuclear remodeling as I reviewed in chapter 1. Observed

nuclear remodeling during infection, numerous data sets associating nuclear shape change with transcriptional profile changes, and infection transcriptional profiles matching those of other stressors support the hypothesis that the chromatin remodeling seen in infection is largely driven by nuclear stress.

In chapter 3, I report that the HSV-1 viral kinase Us3 is both sufficient and necessary to drive gross chromatin remodeling. In chapter 4, I report that HCMV protein IE1 is sufficient to induce transcription of the macroH2A1 dependent genes. A possible alterative hypothesis to transcriptional changes resulting from cellular stress, is that viral proteins more actively remodel chromatin to create the phenotypes seen during lytic herpesvirus infection.

The viral kinase Us3 extensively phosphorylates hosts and viral proteins (18–28). In chapter 3, I show phosphorylation data on several additional chromatin associated proteins. Extensive phosphorylation of chromatin associated proteins is not specific to HSV-1 infection and is commonly considered a response to DNA damage (29). Cellular responses to DNA damage lead to transcriptional changes (30). Together, the large-scale chromatin changes during infection, extensive phosphorylation of chromatin-associated proteins by Us3, and body of work on the chromatin response to DNA damage suggest that the hypotheses of chromatin remodeling during infection as a stress response and as driven by viral proteins are not mutually exclusive. Interestingly, recent work using 4-sU seq on a WT and Viral-Host Shutoff protein (VHS)-null HSV-1 concluded that both VHS protein and stress related transcription read-through work together to control host gene expression during infection (31).

Future experiments to investigate the contribution of Us3 to chromatin remodeling during infection can take advantage of the lower cost and increased ease of sequencing and chromatin profiling techniques. For example, comparing the transcription profile by RNA-seq on cells ectopically expressing Us3 and

cells infected with Us3-null virus to the changes seen in HSV-1 infection could identify changes in gene expression driven by Us3. Chromatin profiling techniques such as CUT&Run (32) on targets of Us3 phosphorylation, such as HDACs, in cells ectopically expressing Us3, cells infected with Us3-null virus, and cells infected with WT HSV-1 would help further elucidate the mechanisms of viral chromatin control. These experiments would not only help our understanding of HSV-1 biology, they would provide further insight into chromatin response to stress.

In chapter 4, I show that the CMV protein IE1 is sufficient to drive the expression of most of my target panel of macroH2A1 dependent neuronal genes. This increase was not seen in my control macroH2A1-independent gene. Additionally, in large microarray screens IE1 alone drove the expression of 25 interferon stimulated genes (33). Like Us3, some of IE1 functions are through regulation of HDACs (34). Unlike Us3, IE1 can directly interact with histones (35) and relax chromatin structure (36). Despite the change in transcription and local changes to chromatin structure, the expression of IE1 alone is not sufficient to remodel the host chromatin or induce the characteristic “kidney-bean” shape of an infected nucleus (33). IE1 is widely regarded as a “promiscuous” transcription factor (10). My work in chapter 4 and the previous work summarized above suggest IE1s primary function is as transcription factor rather than large scale chromatin remodeling.

In ongoing follow-up studies, I am further investigating this role of IE1 by comparing the transcription profile of cells with ectopic IE1, IE1ΔCTD, and additional immediate early HCMV transcription factor IE2 with the changes on transcription during HCMV infection. We are also working to acquire samples from cells infected with an IE1-degron-tagged virus for RNA-seq. These data together will help further define the role of IE1 as a transcription factor of host genes. Future work generating additional data sets with this ectopic expression and IE1-degron-tagged virus in macroH2A1 knockout cells could provide insight into macroH2A1’s role during HCMV infection and as a transcriptional activator. Finally, because IE1

was not sufficient to drive the expression of all cluster 1 genes in chapter 4, it is highly likely additional proteins drive transcription during CMV infection. Co-immunoprecipitation of macroH2A1 and IE1 during CMV infection, followed by mass spectrometry would help identify additional proteins and protein complexes that regulate transcription during CMV infection.

One initial observation that drove the work presented in chapter 4, was that the heterochromatin marker H3K9me3, as well as total chromatin visualized with Hoechst staining is polarized towards the vIAC (37). While neither macroH2A1 nor H3K27me3 were polarized towards the assembly compartment, macroH2A1 was required for this polarization. My course of investigation did not further elucidate a potential role for macroH2A1 in this nuclear and chromatin remodeling. Our RNA seq analysis resulted in over 3000 genes differentially regulated in macroH2A1 KO cells. It is possible that genes not targeted in the siRNA screen drive this nuclear rearrangement phenotype. Kif1A and IFI27 knockdown did exhibit some reduction in nuclear remodeling. Full knockout or pooled screening could also help elucidate the mechanism of macroH2A1 in nuclear remodeling. Chromatin profiling, including CUT&Run of H3K9me3 and Hi-C (38) would expand mechanistic understand of chromatin dynamics during CMV infection.

TEM of CMV infection at more expanded time points or with cryo-FIB milling (39) could be used to investigate open questions such as whether CMV also induces chromatin channels for nuclear egress.

5.3 How are co-localized heterochromatin marks driving different phenotypes?

MacroH2A1 localization in chromatin largely coincides with the histone mark H3K27me3(40). Both macroH2A1 and H3K27me3 are primarily associated with transcriptional repression. If the role of these markers are considered from a transcription standpoint, it might be surprising that in chapter 2 and 3 macroH2A1 and H3K27me3 have unique roles in HSV-1 infection. Even CUT&Tag data I present in

chapter 2 highlights a high degree of overlap in H3K27me3 and macroH2A1 on the host genome over the course of infection. In progress experiments will allow us to compare the transcriptional profiles of macroH2A1 knockout and H3K27me3 depleted cells both with and without HSV-1 infection. This RNA-sequencing will help add nuance to our understanding of macroH2A1 and H3K27me3 transcriptional regulation. Infected samples may also identify other proteins involved in the nuclear egress of HSV-1.

In chapter 4, I show an even more extreme difference between H3K27me3 and macroH2A1 roles during CMV infection. I found that while macroH2A1 KO significantly reduced progeny production and nuclear rearrangement, H3K27me3 depletion had a very modest impact on progeny production and no effect on nuclear remodeling. Differences in CMV infection may be explained by direct interaction of IE1 and the acidic patch of H2A-H2B (36). It is worth noting that while X-ray crystallography confirmed IE1 binding to the acidic patch, in reconstituted *in vitro* assays IE1 still interacted with H3 and H4 when H2A/H2B were not present (35). IE1 was additionally not sufficient to drive expression of all the screened macroH2A1 dependent genes. This suggests the possibility of an additional mechanism driving the phenotype difference between these heterochromatin marks.

One aspect that may help explain the difference between these marks comes from a more structural role for macroH2A. Upon establishing heterochromatin, H3K27me3 is deposited on nucleosomes first and is even required for the deposition of macroH2A1(41). Following insertion into chromatin, macroH2A then associates with several hundred kilobase regions, or broad domains, to act as a transcriptional repressor (40, 42). In comparison, H3K27me3 associated regions are narrow peaks, orders of magnitudes smaller at 221bps (43). In chapter 2, I show that macroH2A1 supports nuclear structure, expanding on previous work showing that macroH2A1 and macroH2A2 support nuclear architecture (44). In this same chapter, I show that though there are consistent changes in peripheral heterochromatin in H3K27me3 depleted cells, nuclear structure is impacted far less than in macroH2A1 KO cells. Additionally, in chapter 4 I show that macroH2A1 is required for nuclear remodeling during HCMV, while H3K27me3 depletion does not impact nuclear remodeling at all. Taken together, this data

supports a model in which macroH2A1 plays a role organizing chromatin on a much larger scale than H3K27me3, acting as an insulator to established heterochromatin. Future experiments to work towards elucidating the structural role of both H3K27me3 and macroH2A in healthy cell and herpesvirus infection could use atomic force microscopy to determine the nuclear rigidity of macroH2A1 KO and H3K27me3 depleted cells both without and during herpesvirus infection as was done in WT nuclei during HSV-1 infection (45).

It is important to note caveats to my work presented here. I was only able to partially deplete H3K27me3 prior to infection. The reduction of H3K27me3 was achieved with the small molecule inhibitor Tazemetostat (EPZ-6438), which only generates about a 75% reduction in H3K27me3 levels (46). In HFF-ts, Tazemetostat (a cytostatic inhibitor) reduced cell divisions limiting the removal of H3K27me3 from more constitutive chromatin regions. This short-term removal of H3K27me3 may also have “transcriptional memory” (47) further confounding the effects we observe. In fact, cells isolated from patients with Hutchinson-Gilford Progeria Syndrome (HGPS), a disease caused by lamin A mutation, retain normal nuclei structure until several passages after H3K27me3 depletion was observed (48). This suggests that our model may underestimate the structural role of H3K27me3. Future work could employ the dominant negative mutation H3K27M, which triggers hypomethylation of all H3K27 residues (49), to get a more complete picture of H3K27me3 role in structural support of the nucleus both with and without infection.

5.4 How conserved is nuclear egress and maturation in herpesviruses?

HSV-1 and the closely related alphaherpesvirus pseudorabies virus (PRV) are frequently used as a generalizable model for herpesvirus nuclear egress (50–53). This simplification of course offers numerous advantages including the comparative ease studying HSV-1 and PRV, the extensive body of literature on these viruses, and the availability of model systems and reagents. However, the work in this thesis highlights key differences in the nuclear egress pathway and subsequent maturation of the herpesviruses HSV-1 and CMV.

Herpesviruses infect an incredibly broad range of host species, with many species hosting numerous sub-families of herpesviruses. Despite the extensive number of species infected with herpesviruses, the host-range of known herpesviruses are highly restricted (10). Some human herpesviruses are so host limited that they are even unable to establish infection in closely related non-human primates. Detection of host-specific herpesviruses in such a broad range of species and higher sequence similarity between herpesviruses subfamilies than herpesviruses from the same host species has led researchers to conclude that herpesviruses infected a common ancestor hundreds of millions of years ago and evolved with their host species (54). Alphaherpesviruses likely diverged from other herpesviruses families 200 million years ago (55), and the most recent divergence occurred between HSV-1 and HSV-2 over 1.6 million years ago (56). The ancient evolution of these viruses, slower mutation rate, and high similarity between current laboratory strains of HSV-1 and samples recovered from ancient skeletons (57) highlight some of the difficulties with phylogeny-based evolution studies on herpesviruses and the need for more functional comparisons.

One difference between these herpesviruses I have discussed in this thesis is the different role of H3K27me3 in HSV-1 and CMV. In chapter 2, I show that H3K27me3 loss reduces infectious progeny significantly. In chapter 3, I showed that the nuclear egress in HSV-1 used H3K27me3 to direct viral kinase Us3 in nuclear egress. However, in chapter 4, I found that H3K27me3 loss only minimally effects CMV progeny production and release. Interestingly Us3 is not a conserved herpesvirus protein, rather a serine/threonine kinase Us3 homolog is only present in alphaherpesviruses (HSV-1, HSV-2, VZV, and PRV) (58). In alphaherpesviruses with Us3 deletion or kinase-dead mutations, normal nuclear egress is reduced, and bundles of multiple capsids are trapped in the perinuclear space (18, 21, 59). The abnormal nuclear egress in Us3null HSV-1 is very reminiscent of the observed nuclear egress in CMV. The CMV nuclear egress relies on “inclusions” containing several capsids folding in on themselves and allowing the virions to traverse the perinuclear space (60, 61). In cell culture, CMV produces much less progeny than HSV-1 and Us3-null virus is 10-100-fold less infective than WT virus.

Taken together, this suggests that it is possible that gain or loss of a single kinase over the course of herpesvirus evolution has resulted in significantly different egress pathways for alphaherpesvirus and other herpesviruses. Future work to test this hypothesis could examine whether Us3 phosphorylates components of the CMV NEC. If the target regions of Us3 kinase activity are conserved in the CMV NEC, follow-up studies could investigate the production of infective progeny by plaque assay and use TEM to monitor nuclear egress and virion in perinuclear inclusions in cells expressing HSV-1 Us3 and infected with CMV.

A more notable difference between the lytic replication cycles of HSV-1 and CMV is the formation of a viral induced assembly compartment (vIAC) outside the host nucleus (62). This vIAC formation is seen in the common cellular model for *in vitro* CMV experiments, fibroblasts. In commonly used *in vitro* model cell lines for HSV-1 infection, like epithelial and fibroblast lines, there is no observed vIAC formation. Recently, this understanding has been challenged by detection of vIAC in CNS derived cancer lines (CAD cells) infected with HSV-1(63, 64). As HSV1 has a latent phase in neuronal cells, it is not surprising that the infection cycle presents differently in CNS derived cells than fibroblast and epithelial cells. This opens up exciting questions for follow-up studies to address such as what factors in CAD cells are not present in fibroblast and epithelial cells that drive the formation of a vIAC during HSV-1 infection and how presence of a vIAC affects progeny production. This could be addressed by additional RNA sequencing on CAD cells infected with HSV-1 and mass-spectrometry on virions from fibroblast and CAD cells respectively. Comparison of lipid composition by mass spectrometry of virions grown in CAD cells vs published data of CMV virions and synaptic vesicles (65) could further elucidate potential roles of neuronal genes in herpesvirus packaging and maturation.

Additionally, generation of a CAD macroH2A1 KO cell line and subsequent infection with HSV-1 could help further elucidate whether macroH2A1 plays a structural role in vIAC and nuclear rearrangement when neuronal genes are expressed at a higher baseline and don’t require induction.

In the case of CMV infection, I showed in chapter 4 that the several neuronal genes helped drive formation of vIAC and that the viral protein IE1 is sufficient to drive the expression of many of these genes. The CMV protein IE1 does not have a homologous HSV-1 protein (58). Follow-up studies could address whether CMV protein IE1 expression during HSV-1 infection can drive the formation of a vIAC in fibroblast cells. This may provide insight on whether CMV's use of neuronal genes in packaging is evolutionarily retained from HSV-1's use of these proteins or an example of convergent evolution for the herpesviruses.

5.5 What is the impact of HCMV reprogramming of fibroblast cells *in vivo?*

MacroH2A1 is a complex regulator of chromatin. In neuronal differentiation macroH2A1 induces gene expression as a transcriptional activator (66). Conversely, in differentiated cells macroH2A1 acts as a barrier to reprogramming and represses genes involved in differentiation (42). My work in chapter 4 suggests that in the context of CMV infection, competing functions of macroH2A1 potentially regulate chromatin dynamics.

In chapter 4, I show that CMV infection drives the transcriptional state in infected fibroblast cells to be more like neuronal cells and neural progenitors than uninfected fibroblasts. Fibroblasts are not the only cell type reprogrammed by CMV infection. In murine CMV infection, macrophages infected with CMV assume an identity more "stem-cell like state" through disruption of *wnt* pathways (67). In development, fibroblasts are derived from both ectoderm and mesoderm depending on their location in the body (68). The HFF cells used in my studies are a skin fibroblast and would be derived from the same ectoderm embryonic layer as neurons (69). This is significant because as both HFF cells and neuronal progenitor cells are derived from ectoderm the question of whether CMV is truly reprogramming the cell or simply reverting to a common lineage "stem-like" state remains. To address this follow-up experiments RT-qPCR or larger scale RNA sequencing to analyze induction of neuronal genes in a fibroblast cell line that originates in the mesoderm cell layer could be performed.

A primary public health concern surrounding CMV is congenital infections. Congenital CMV is a common cause of sensorineural hearing loss and neurodisability (70). Neurodevelopment is a tightly regulated process. During *in utero* CMV infection in non-neuronal cell types, the induction of neuronal genes, including transcription factor *Sox11* and multiple members of the *wnt* signaling pathway, may confuse CNS development (71, 72). Much of the research on congenital CMV focuses on alterations to neural cells (73, 74). The work I present in chapter 4 suggests that future developmental work should consider dysregulation of cells surrounding the developing CNS as well.

5.6 How can understanding the function heterochromatin marks during infection help in a clinical setting?

H3K27me3 and the enzyme associated with depositing this histone mark, EZH2, are both dysregulated in multiple cancer subtypes (75). The association of EZH2 mutations with numerous cancers has resulted in the development of several small molecule inhibitors to target
EZH2 activity. The small molecule inhibitor used in the work presented in this thesis,
Tazemetostat, is the first and to date only FDA approved EZH2 inhibitor (76). Several others are in clinical trials and a less specific EZH1/EZH2 inhibitor was recently approved for use in Japan (77).
In chapter 2, I showed Tazemetostat could reduce infectious HSV-1 progeny production. In chapter 3, I showed that Tazemetostat treatment partially phenocopies Us3-null virus infection. Us3-null viruses have a significant reduction in neuroinvasiveness in *vivo* (78, 79). Mouse models treated with other EZH2 inhibitors had significant reduction in HSV-1 progeny production and spread in ganglia (80). My results as well as those from previous studies suggest that follow-up studies should investigate if Tazemetostat also reduces *in vivo* HSV-1 spread in neurons and the potential treatment options EZH2 inhibitors provide in HSV-1 encephalitis.

MacroH2A1 currently does not have any small molecule inhibitors available. In chapter 2 and 4, I show that macroH2A1 knockout significantly reduces HSV-1 and CMV progeny. Many aggressive cancers

are driven by macroH2A overexpression (81). Despite a broad role in transcription, macroH2A1 knockout in mice had limited negative phenotypes, with some studies even reporting positive effects on the mouse including improved insulin sensitivity, if macroH2A1 is knocked out after development (82). MacroH2A is highly conserved among mammals (83) indicating that mouse models would be effective tools to screen effects of macroH2A1 knockdown or blocking. The relative health of macroH2A1 KO mice and its role in numerous human diseases suggests it might be an effective target for drug design. Improved protein modeling software, such as AlphaFold3, can now predict small molecule interactions with protein structures allowing for *in silica* screening of hundreds of potential inhibitor interactions (84). *In silica* screens of existing molecules for macroH2A interaction, with follow-up cell and mice toxicity tests could identify ways macroH2A-targeted treatment, such as pretreatment of harvested stem cells to prevent reactivation of CMV following bone marrow transplant, could have eventual clinical application.

Chapter 6: Materials and Methods

6.1 Chapter 2 Materials and Methods:

Cells and viruses:

Primary human foreskin fibroblasts (HFFs), hTERT-immortalized HFFs, and hTERTimmortalized macroH2A1 knockout HFFs were cultured using standard methods with 10% FBS and 1% penicillin-streptomycin as previously described (46). Cells were grown at 37 °C with 5% CO_2 and tested for mycoplasma contamination approximately once a month.

The lab adapted strain of HSV-1, *syn 17*+(47), was used for all experiments unless otherwise noted. Monolayers of cells were infected for 1 hour at 37 °C as previously described (48). An MOI of 3 was used for all experiments, except for EM samples which used MOI of 10. Cells were collected at mock, 4-, 8-, and 12- hpi for western blot. Supernatant was collected at 8- and 12-hpi for plaque assays. HSV-1 infected samples were harvested for TEM at 18 hpi. Virus stock was grown by infecting Vero cells at an MOI of 0.0001. Virus was harvested ~60-80 hours post-infection and titered on U2OS cells to

determine stock plaque forming units per mL (PFU/mL). Experimental plaque assays were set up in Vero cells. Plaque assays were set up on serial 10-fold dilutions in serum-free DMEM. Virus was left on cells for 1 hour then aspirated. Cells were washed with 1X PBS (pH 7.46), and 2% methylcellulose overlay in DMEM with 2% FBS and 0.5% penicillin-streptomycin was added to wells. Plaques were fixed with 0.2% crystal violet between 96-100 hours post infection and plaques were counted by hand. All plaque assays were set up with 2 technical replicates.

Clinical isolates were acquired in 1994 and 1995 from oral swab collections. Samples were deidentified on collection. Patients provided daily home collections of oral swabs, and qPCR was used to detect how many days HSV was detected in these swabs. Patients that had detectable
HSV in only a few swabs were classified as “low-shedders” and patients that had a high percentage of days with positive swabs were classified as “high-shedders.” Stocks were a gift from the lab of Keith Jerome.

Table 1: Cell line sources.

Cell Line	Source
Human: RPE-1 (hTERTimmortalized)	Gift of E. Hatch Lab(49) (Invitrogen)
Human: Primary HFF	Gift of D. Galloway Lab
Human: HFF (hTERTimmortalized)	Gift of J. Kamil Lab(50)
African Green Monkey: Vero	Gift of A. Geballe Lab(51)

Knockout of macroH2A1:

MacroH2A1 guide RNA (gRNA, see Table 3) was cloned into TLCv2 (Addgene plasmid: 87360), a plasmid encoding doxycycline-inducible Cas9-2A-GFP and gRNA expression. To generate lentiviral

particles, $1.0x10^7$ HEK293T cells were transfected with 12 µg TLCV2_sg_mH2A1, 8 µg pMDL (Addgene plasmid: 12251), 4 µg VSVg, and 2.5 µg pREV (Addgene plasmid: 115989) using Attractene transfection reagent (Qiagen: 301005). Lentivirus was harvested at 24-, 48-, and 72-hours post-transfection, filtered through 0.2 µm filters, aliquoted, flash frozen with liquid nitrogen, and stored at -80C. 2 mL of thawed filtered lentivirus was used to transduce approximately $2.25x10^6$ HFF-T or $3x10^6$ RPE cells in 10 cm plates with 8 µg/mL polybrene (Millipore-Sigma: TR-1003-G). Cells were allowed to reach confluence before selection with 1 µg/mL puromycin for 3 days. Cells were then sorted by GFP positivity or counted by hemocytometer, plated at 1 cell per well into 96-well plates, and selected through serial expansion of colonies. Selected cells were screened for macroH2A1 knockout by western blot.

Infections with tazemetostat pretreatment:

HFFs and macroH2A1 KO HFFs were treated with DMSO or 10 µM of tazemetostat (MedChem: HY-13803) in DMSO for 3 days prior to infection. Cells were then infected at MOI of 3 and after 1 hour of incubation with virus, fresh media with 10µM Taz was added to previously treated cells. Control samples were treated with equivalent volumes of DMSO. Samples were harvested as above.

Western Blotting:

Western blotting was performed as previously described (46). Briefly, cells were counted, pelleted, resuspended in 1x NuPAGE lithium dodecyl sulfate (LDS) sample buffer (Fisher Scientific: NP007) + 5% 2-betamercaptoethanol at 300,000 cells per 200 µL, and boiled for 15 minutes. Protein lysates were separated by 13.5% SDS-PAGE gels using 1X NuPAGE MOPS buffer (Fisher Scientific: NP0001) at 75 volts for 30 minutes then 110 volts for 100 minutes, then wet transferred to a nitrocellulose membrane (Bio-Rad) at 100 volts for 70 minutes using Transfer Buffer (25 mM Tris Base, 100 mM glycine, 20% methanol). Membranes were ponceau stained and imaged. Membranes were blocked in 5% milk in Tris-buffered saline with Tween (TBST) for 1 hour, then probed with primary antibody overnight (see Table 2). Membranes were washed with TBST for thirty minutes, incubated with

secondary antibodies conjugated to horseradish peroxidase (α-mouse or α-rabbit; 1:5000) at room temperature for 1 hour, washed with TBST for thirty minutes, and detected using Clarity Western ECL Substrate (Bio-Rad: 1705061) and Chemidoc MP Imaging System (Bio-Rad). Images were formatted using Adobe Photoshop and Illustrator. Densitometry analysis was quantified using ImageJ.

Table 2: Sources and identification of antibodies used.

Antibody	Source	Identifier	Use (Concentration)
Mouse anti-actin	Abcam	Cat: 5441	WB (1:10,000)
Mouse anti-gH	Abcam	Cat: 110227	WB (1:1,000)
Rabbit anti-H3	Abcam	Cat: 1791	WB (1:20,000)
Rabbit anti-H3K27me3	Cell Signal Technologies	Cat: 9733T	WB/CUT&Tag (1:100) IF (1:500)
Rabbit anti-H3K9me3	Abcam	Cat: 8898	WB (1:1,000)
Rabbit anti-H4	Abcam	Cat: 10158	WB (1:1,000)
Mouse anti-ICP0	Santa Cruz Biotechnology	Cat: 53070	WB (1:1,000)
Mouse anti-ICP8	Abcam	Cat: 20194	IF (1:500)
Chicken anti-UL34	Kind gift of Richard Roller	N/A	WB (1:1000) IF (1:500)
Rabbit anti-macroH2A1	Abcam	Cat: 37264	WB (1:1,000) IF (1:500)
			CUT&Tag (1:100)
Rabbit anti-macroH2A1.1	Cell Signaling Technology	Cat: 12455S	WB (1:1,000)

Mouse anti-macroH2A1.2	Cell Signaling Technology	Cat: 4827S	WB (1:1,000)
Rabbit anti-macroH2A2	Active Motif	Cat: 39874	WB (1:1,000)
HRP-conjugated anti-VP16	Santa Cruz Biotechnology	Cat. 7546	WB (1:1,000)
Peroxidase-AffiniPure Goat Anti-Mouse	Jackson Immunoresearch Laboratories	Cat: 115-035003	WB (1:5,000)
Peroxidase-AffiniPure Goat Anti-Rabbit	Jackson Immunoresearch Laboratories	Cat: 111-035045	WB (1:5,000)
Rabbit anti-mouse IgG	Abcam	Cat: 46540	CUT&Tag (1:100)
Guinea pig anti-rabbit IgG	Antibodies Online	Cat: AB1N101961	CUT&Tag (1:100)
Goat anti-Rabbit IgG (H+L) AlexaFluor 568	ThermoFisher Scientific	Cat: A-11011	IF (1:300)
Goat anti-Mouse IgG (H+L) AlexaFluor 488	ThermoFisher Scientific	Cat: A-11001	IF (1:300)

Quantification of HSV-1 genomes by ddPCR:

Cells were harvested at the indicated times post-infection by trypsinization, washed with 1X PBS and centrifuged at 5000 xg for 2 minutes. Pellets were flash-frozen in liquid nitrogen and stored at -80 °C until processed. HSV-1 DNA within cells was isolated from frozen pellets using QIAamp DNAMini Kit (Qiagen: 51304).

Supernatants were harvested at the indicated times post-infection, centrifuged at > 3500 xg and filtered through 40 µm sterile syringe filters. DNA on the exterior of filtered capsids was digested for 1 hour at 25 °C with 20.3 units DNase (Qiagen: 79254) supplemented with 10 mM $MgCl_2$. DNase was inactivated at 75 °C for 10 minutes followed by vortexing. Capsids were digested with 3 mg/mL proteinase K (Fisher Scientific: BP1700) in 100 mM KCl, 25 mM EDTA, 10 mM Tris-HCl pH 7.4 and 1% Igepal for 1 hour at 50 °C. HSV-1 genomes from digested capsids were isolated using QIAamp DNAMini Kit.

A duplexed droplet digital PCR was performed to measure the levels of cellular or supernatant HSV-1 genomes on the QX100 droplet digital PCR system (Bio-Rad Laboratories, Hercules, CA) using a primer/probe set specific to HSV-1 gB. Cell numbers were determined using a primer/probe set specific to human Beta-globin, a reference gene that exists at two copies per cell. See Table 3 for oligonucleotide sequences, as have been previously established for HSV1(52). The digital droplet PCR (ddPCR) reaction mixture consisted of 12.5 µL of a 2X ddPCR
Supermix for Probes no dUTP (Bio-Rad: 1863024), 1.25 µL of each 20X primer-probe mix, and 10 µL of template DNA. 20 µL of each reaction mixture was loaded onto a disposable plastic cartridge (Bio-Rad: 1864008) with 70 µL of droplet generation oil (Bio-Rad: 1863005) and placed in the droplet generator (Bio-Rad). Droplets generated were transferred to a 96-well PCR plate (Bio-Rad 12001925), and PCR amplification was performed on a Bio-Rad C1000 Touch Thermal Cycler with the following conditions: 95 °C for 10 minutes, 40 cycles of 94 °C for 30 seconds, and 60 °C for 1 minute, followed by 98 °C for 10 minutes and ending at 4 °C. After amplification, the plate was loaded onto the droplet reader (Bio-Rad: QX200), and the droplets from each well of the plate were automatically read with droplet reader oil (Bio-Rad: 186-3004) at a rate of 32 wells per hour. Data were analyzed with QuantaSoft analysis software and quantitation of target molecules presented as copies per µL of PCR reaction. HSV-1 genome values were standardized to cellular β-globin levels. Experiments were completed in biological triplicate and statistical analysis was performed as indicated in figure legends using Prism v10 (GraphPad Software).

Table 3: Primers used for knockout and ddPCR

CRISPR MacroH2A1 gRNA	CCTCAATAGCAAGCCATCCTGT
HSV1_gB_qPCR_F1	CCGTCAGCACCTTCATCGA
HSV1_gB_qPCR_R1	CGCTGGACCTCCGTGTAGTC
HSV1_gB_probe1	6FAM-CCACGAGATCAAGGACAGCGGCC-BHQ1
beta-globin_qPCR_F1	TGAAGGCTCATGGCAAGAAA
beta-globin_qPCR_R1	GCTCACTCAGTGTGGCAAAGG
beta-globin_probe2_hex	/5HEX/TC CAG GTG AGC CAG GCC ATC ACT A/3BHQ_1/

Cleavage Under Targets & Tagmentation (CUT&Tag):

Two biological replicates per time point were obtained from independent infections. Protocol was adapted from the established CUT&Tag methods (20). Cells were harvested using trypsin, washed three times with ice-cold phosphate-buffered saline (PBS) via centrifugation at 600 xg for 3 minutes and counted using a hemocytometer. Nuclei from 600,000 cells were isolated by hypotonic lysis in 1 mL buffer NE1 (20 mM HEPES-KOH pH 7.9; 10 mM KCl; 0.5 mM spermidine; 0.1% Triton X-100; 20% Glycerol; Roche EDTA-free protease inhibitor) for 10 minutes on ice followed by centrifugation at 1300 xg for 4 minutes. Nuclei were resuspended in Wash buffer (20 mM HEPES-NaOH pH 7.5; 150 mM NaCl; 0.5 mM spermidine; Roche EDTAfree protease inhibitor) and counted using a hemocytometer. BioMag Plus Concanavalin A coated beads (Polysciences: 86057-3) were equilibrated with Binding buffer (20 mM HEPESKOH pH 7.9; 10 mM KCL; 1mM $CaCl_2$; 1 mM $MnCl_2$). Beads (5 µL) were mixed with aliquots of 75,000 nuclei and incubated at 25 °C for 10 minutes followed by magnetic separation of beads.

Beads were resuspended in 50 µL primary antibody [anti-mH2A1 (Abcam: ab37624), antiH3K27me3 (Cell Signaling:9733) or anti-mouse IgG (Abcam: ab46540) in Wash buffer supplemented with 2 mM EDTA and 0.1% bovine serum albumin (BSA) and incubated on a nutator at 4 °C overnight. The beads

were decanted on a magnet stand then resuspended in 50 µL secondary antibody [Guinea pig anti-rabbit IgG (Antibodies-Online: ABIN101961) 1:100] in Wash buffer supplemented with 2 mM EDTA and 0.1% BSA and incubated on a nutator at room temperature for 1 hour. The beads were decanted on a magnet stand and washed with 200 µL Wash buffer, then were resuspended in 50 µL pA-Tn5 (1:200) in 300-Wash buffer (Wash buffer containing 300 mM NaCl) and incubated on a nutator at room temperature for 1 hour. The beads were washed twice with 200 µL 300-Wash buffer, then resuspended in 50 µL Tagmentation buffer (300-Wash buffer supplemented with 10 mM $MgCl_2$) and incubated at 37 °C for 1 hour. Beads were then washed with 50 µL TAPS wash buffer (10 mM TAPS pH 8.5, 0.2 mM EDTA), then resuspended in 5 µL TAPS wash buffer supplemented with 0.1% SDS and incubated at 58 °C for 1 hour. SDS was neutralized on ice with 15 µL 0.67% Triton-X100. 2 µL of 10 mM indexed P5 and P7 primer solutions and 25 µL NEBnext High-Fidelity 2X Master Mix (New England BioLabs: ME541L) were added. Gap-filling and 15 cycles of PCR were performed using an MJ PTC-200 Thermocycler. Library clean-up was performed by incubating beads with 65 µL SPRI bead slurry for 5-10 minutes, then magnetization and two washes with 200 µL 80% ethanol. Libraries were eluted with 22 µL Tris-HCl pH 8.0 and 2 µL was used for Agilent 4200 Tapestation analysis. The barcoded libraries were mixed to achieve equimolar representation as desired aiming for a final concentration as recommended by the manufacturer for sequencing on an Illumina HiSeq 2500 2-lane Turbo flow cell.

CUT&Tag data processing:

CUT&Tag raw sequencing data were aligned to a custom genome made by concatenating human (hg38), HSV (JN555585.1), and E. coli (U00096.3 Escherichia coli str. K-12 substr. MG1655, complete genome). We performed alignments using bowtie2.

Domain calling:

Coverage at 100 bp windows of the human hg38 reference genome was calculated as number of reads of given length (120-1000 bp for the analyses presented here) that mapped at that window normalized by the factor N:

N= 10,000/(Total number of reads that mapped to E. coli genome)

Here 10,000 is an arbitrarily chosen number. We used *E. coli* DNA as a spike-in to normalize all datasets. We partitioned all chromosomes into domains of macroH2A1: domains had an enrichment that was two times the genome-wide median and at least four-fold higher than the IgG control. The normalized coverage at each base-pair from each replicate was averaged when combining multiple replicates. The normalized read density in 100 bp bins were then smoothed with a running average over the bins spanning +/- 1000 bp around each bin. We then calculated the genome-wide distribution of normalized read density and medians that were plotted in Figure S1. We averaged medians across WT macroH2A1 datasets (mock, 4, 8, and 12hpi), and multiplied the average by 2, to set the cutoff for domain definition for macroH2A1 datasets. We defined a similar cutoff for H3K27me3 datasets using H3K27me3 WT datasets.

Identifying domain level dynamics of macroH2A1 over time course of infection:

To measure changes in macroH2A1 across time points where the domain boundaries are not the same, we first concatenated domain definitions from all macroH2A1 datasets and then defined a set of non-overlapping intervals using the “disjoin” method of GenomicRanges R package (53). We then calculated the log2 ratio of macroH2A1 enrichment over IgG for the nonoverlapping regions for the mock, 4, 8, and 12hpi. The 4, 8, and 12hpi enrichments were then divided by the enrichment of the mock dataset to obtain change in macroH2A1 over time course at the non-overlapping regions. k-means clustering (k=6) using R(54) was performed on the matrix where the rows are the non-overlapping regions and the columns are change in macroH2A1 over mock at 4, 8, and 12hpi. We extended the non-overlapping regions by 5 bp on each end and then merged regions within each cluster using “reduce” method of

GenomicRanges, to obtain domains in each cluster. We recalculated change in macroH2A1 at 4, 8, and 12hpi over mock, which was used to plot heatmaps and boxplots shown in Figure 2.1 and Figure 2.2. H3K27me3 enrichment for WT and macroH2A1 KO cells was calculated at clustered macroH2A1

domains. The unique code for this work can be found here: https://doi.org/10.5281/zenodo.6783949

RNA sequencing:

Three biological replicates per time point were obtained from independent infections. Cells were harvested at the indicated times post-infection by trypsinization, washed with PBS and centrifuged at 5000 xg for 2 minutes. Pellets were lysed with TRIzol (Thermo Fisher: 15-596026) and total RNA was harvested according to manufacturer's instructions. RNAs were then treated with DNase (Qiagen: 79254) on RNeasy columns (Qiagen: 74104) per manufacturer's instructions. RNA was precipitated with 3 volumes ice-cold 96% ethanol, 1 volume 3 M sodium acetate pH 5.5, and 1 µL glycogen (Thermo Fischer: R055) overnight at -80 °C. Precipitated RNAs were pelleted at 15,000 xg and 4 °C for 30 minutes, washed with ice-cold 75% ethanol and spun as above for 10 min. RNA was resuspended in nuclease-free water.

RNA was quantified by Nanodrop and integrity analyzed with the 4200 Tapestation Bioanalyzer system (Agilent). 500 ng of total RNA with an RNA Integrity Number (RIN) greater than 9.5 were used to prepare sequencing libraries with the TruSeq® Stranded mRNA Library Prep Kit (Illumina: 20020594). Library concentrations were measured with Qubit dsDNA HS Assay Kit (Thermo Fisher: Q32854) then analyzed with Agilent High Sensitivity D5000 ScreenTape System and pooled. Libraries were sequenced with 100-bp paired-end reads on an Illumina NovaSeq 6000 SP sequencer at the Fred Hutch Genomics Core Facility RNA/4sU-RNA/Hi-C data processing: Fastq files were filtered to exclude reads that didn't pass Illumina's base call quality threshold. STAR v2.7.1(55) with 2-pass mapping was used to align paired-end reads to a combined reference of human genome build hg38 and HSV1 genome JN555585.1 (https://www.ncbi.nlm.nih.gov/nuccore/JN555585.1/). FastQC 0.11.9 (https://www.bioinformatics.babraham.ac.uk/projects/fastqc/) and RSeQC 4.0.0(56) were used for QC including insert fragment size, read quality, read duplication rates, gene body coverage and read

distribution in different genomic regions. FeatureCounts(57) in Subread 1.6.5 was used to quantify gene-level expression by strand-specific paired-end read counting.

Gene annotation were based on GENCODE V31 (https://www.gencodegenes.org/human/) and GCA_000859985.2_ViralProj15217 (https://www.ncbi.nlm.nih.gov/data-hub/genome/GCF_000859985.2/). For HSV1, annotated genes were collapsed into nonoverlapping transcribed regions, e.g. X indicating a transcribed region unique to gene X, X:Y indicating an overlapping transcribed region for genes X and Y, and so on.

Bioconductor package edgeR 3.26.8(58) was used to detect differential gene expression between sample groups. Genes with low expression were excluded by requiring at least one count per million in at least N samples (N is equal to the number of samples in the smaller group). The filtered expression matrix was normalized by TMM method (https://genomebiology.biomedcentral.com/articles/10.1186/gb-2010-11-3-r25) and subject to significance testing using quasi-likelihood pipeline implemented in edgeR. Genes were deemed differentially expressed if fold changes were greater than 2 in either direction and BenjaminiHochberg adjusted p-values were less than 0.01.

The intervals representing start and end of each gene were intersected with clustered macroH2A1 domains to obtain cluster assignments for genes. Intersection was performed using "intersect" function of bedtools(59). Genes that did not uniquely intersect with domains in a single cluster were discarded. The cluster assignments for genes were used for plotting total RNA fold changes in Figure S3. Gene Ontology analysis were performed using WebGestalt(60). Reads per kilobase of transcript per million reads mapped (RPKM) values for 4sU-RNA was obtained from GEO (GSE59717) and converted to transcripts per million (TPM). The TPM values across two 4sU-RNA replicates for each condition was averaged and box plots were generated similarly to total RNA.

For calculating eigenvector distributions, compartment wig file was downloaded from the following link:

https://4dn-open-data-public.s3.amazonaws.com/fourfront-webprod/wfoutput/b543cbf4-ce54https://4dn-open-data-public.s3.amazonaws.com/fourfront-webprod/wfoutput/b543cbf4-ce54-4d2d-8960-281528ff18a6/4DNFI342UZP1.bw4d2d-8960-281528ff18a6/4DNFI342UZP1.bw

Regions from compartment file intersecting with each domain cluster were extracted and the values were used for generating box plots shown in Figure 2.3.

Data availability:

The CUT&Tag and RNA-seq data can be found here: Series GSE209820

Immunofluorescence:

Cells were plated on poly-L coated glass coverslips the day prior to infection. Cells were then infected with HSV-1 at an MOI of 3 and collected at mock, 4-, 8-, and 12- hpi. For harvest cells were fixed with cold 4% PFA in 1X PBS for 15 minutes. Cells were permeabilized with 0.5% Triton-X in 1X PBS for 10 minutes, then blocked in 10% goat serum in 1X PBS for 1 hour, incubated with primary antibody (diluted as noted) in 3% BSA in 1X PBS for 1 hour. Slides were incubated with secondary antibodies at a dilution of 1:300 in 3% BSA in 1X PBS for 1 hour. Coverslips were fixed to microscope slides with Invitrogen™ ProLong™ Gold Antifade Mountant. Images were taken on Leica Stellaris Confocal with 63X oil objective at room temperature.

Electron Microscopy:

Cells were fixed in 2% paraformaldehyde and 2.5% glutaraldehyde in 0.1M sodium cacodylate buffer (pH 7.3) at 4 °C. Fixed cells were rinsed briefly in 1% sucrose in 50mM cacodylate (pH 7.2), then postfixed on ice for 30 mins in a solution of 1% osmium (EM Sciences: RT19152) and 0.8% potassium ferricyanide in 50mM cacodylate (pH 7.2). Cell pellets were washed twice briefly at 25 °C in 1% sucrose in 50mM cacodylate (pH 7.2), then washed in three changes of 50mM cacodylate (pH 7.2) for 5 min each. Cell pellets were treated with 0.2% tannic acid (Sigma-Aldrich: 1401-55-4) in 50 mM cacodylate (pH 7.2) for 15 minutes at 25 °C, then rinsed several times in water. Cells were dehydrated through a graded ethanol series and embedded in Epon 12 resin (Ted Pella: 18010). 70nm thin

sections were cut using an Ultracut UC7 ultramicrotome (Leica Mikrosysteme) and collected on 200 mesh formvar/carbon copper grids (Ted Pella: 01800). Sections were stained with 2% aqueous uranyl acetate and Reynolds lead citrate. Cell pellet sections were imaged using a Talos L120C microscope operated at 120kV with a Ceta-16M (4096 x 4096) camera (ThermoFisher Scientific).

All data were collected at spot size 5 with a 100um C2 aperture and 70um objective aperture.
For quantification, nuclei were targeted at 1250x and manually circled. Autofocus was set to 2.0um. Nuclei were then imaged at 11000x as a montage and stitched together automatically using SerialEM (Nexperion Inc). Stitched maps were exported as uncompressed 16-bit tif files for further analysis. For qualitative analysis, images were manually focused to -2.0um defocus and then 20 1-second frames were collected and drift-corrected using Velox software (Thermo Fisher Scientific, Eindhoven, NL). Final summed images were exported as 16-bit tif files and cropped using ImageJ.

Image analysis pipelines for counting capsids and for measuring chromatin density at the nuclear envelope were deployed in MATLAB R2020b. Scripts are available on the Fred Hutch GitHub repository. Capsid pipeline follows three steps: 1- nuclear boundaries identification, 2- capsid detection, 3- capsid classification. Nuclear boundaries were identified with user input, by outlining a freehand contour of the nucleus of interest, from which a binary mask is extracted, and its area and perimeter was calculated. Capsid detection was performed on the medianfiltered complement of the original image, using a Circular Hough Transform based algorithm, with phase coding for radii estimation (61), and search radius ranging from 10.6 to 31.7 nm. Capsids residing within the nuclear mask were then counted and classified. Detected capsids were classified in three categories (Empty, Intermediate and Full), depending on the distribution of the pixel grayscale intensities within the capsids relative to a normal distribution. Moreover, the distance of the capsids from the nearest nuclear membrane pixel was measured using a distance transform, and capsids within a 200nm distance from the nuclear membrane were counted.

Width of heterochromatin abutting the nuclear envelope was quantified by measuring the length of the binarized chromatin from 1D intensity profiles along the normal of the nuclear perimeter, sampled at every 10 perimeter pixels. Dense heterochromatin was binarized using global Otsu's thresholding method applied to the background-corrected complement of the contrast-adjusted original image. Noise from the binarized image was further reduced by applying a 2D order statistic filter using the minimum value of a varying domain interactively defined by the user, with default value of 8-by-8 pixels. The resulting heterochromatin density distribution was normalized to the total length of the nucleus' perimeter.

Live-cell imaging, tracking, and calculation of the mean squared displacement (MSD)

Cells were infected with HSV-1 VP26mCherry (a kind gift from Beate Sodeik; Sandbaumhüter *et al.*, 2013) and an MOI of 3. Nuclei were stained prior to imaging with Hoechst 33258 (Sigma Aldrich) diluted 1:1000 in cell culture media. Cells were imaged at indicated time points on a Nikon TI2 (Nikon) spinning-disk fluorescence microscope equipped with a Yokogawa W2 spinning-disk unit (Yokogawa), an Andor DU-888 X-11633 electron-multiplying charge-coupled device (EMCCD) camera (Andor Technology) and a 100x 1.49 numerical aperture (NA) Apo-TIRF objective (Nikon) resulting in 130 nm pixel size. The setup also included 405 nm, 488 nm, 561 nm, and 640 nm laser lines and respective filter sets. Physiological growth conditions were kept constant at 37°C, 5% CO2, using an environmental control system consisting of an objective heater and a humidified incubation chamber.

Cells were continuously imaged for 40 sec with a 561 nm wavelength laser in a single plane and a frame rate of 9.5 frame/sec. Single particle tracking was performed in ImageJ Fiji (Schindelin *et al.*, 2012) with the plugin TrackMate v.7.6.1 (Ershov *et al.*, 2022). Tracking settings were as follows: LoG detector, estimated diameter 0.8 µm, quality threshold 50, pre-processing with median filter, sub-pixel localization, spot filter "Signal/Noise ratio" >0.47, simple LAP tracker with the settings: linking max distance 0.5µm, gap-closing max distance 0.5µm, gap-closing max frame gap 1, track filter "Number of spots in the track" >20 spots. MSD analysis was performed using MotilityLab (http://2ptrack.net, accessed 17.02.2023)

based on the R-package CelltrackR (Wortel *et al.*, 2021). To calculate the maximum nuclear corral size, a non-linear fit with exponential plateau was fitted to the meanMSD curves using the model$Y = YM - (YM - Y0) \times \exp(-k \times x)$ with GraphPad Prism v.9.5.0. Y0 represents the starting population (in [μm^2]), K determines the rate constant (inverse of X [sec]), and YM represents the plateau (same units as Y). We then calculated the mean corral diameter using the following equation: $d_{corral} = d_{particle}\, 2 \times \sqrt{YM}$ (modified from Bosse *et al.*, 2015) where d_{corral} is the corral diameter, $d_{particle}$ is the 1044 estimated HSV-1 capsid size of 125 nm (Baker *et al.*,1990), and YM is the plateau of the 1045 respective MSD curve.

6.2 Chapter 3 Materials and Methods:

Cells and viruses:

hTERT-immortalized HFFs, HeLa cells, macroH2A1 knockout HeLa cells were cultured using standard methods with 10% FBS and 1% penicillin-streptomycin as previously described (Lynch et al., 2021) . Cells were grown at 37 °C with 5% CO_2 and tested for mycoplasma contamination approximately once a month.

The lab adapted strain of HSV-1, *syn 17+* (Brown et al., 1973) , was used for all experiments unless otherwise noted. Us3-null, UL31-null, and UL34-null HSV-1 mutants were a kind gift from Richard Roller(16, 27) . Monolayers of cells were infected for 1 hour at 37 °C as previously described (Lilley et al., 2005) . An MOI of 3 was used for all experiments, except for EM samples which used MOI of 10. Cells were collected at mock, 4-, 8-, and 12- hpi for western blot. Supernatant was collected at 8- and 12-hpi for plaque assays. HSV-1 infected samples were harvested for TEM at 18 hpi. Virus stock was grown by infecting Vero cells at an MOI of 0.0001. Virus was harvested ~60-80 hours post-infection and titered on U2OS cells to determine stock plaque forming units per mL (PFU/mL). Experimental plaque assays were set up in Vero cells. Plaque assays were set up on serial 10-fold dilutions in serum-free DMEM. Virus was left on cells for 1 hour then aspirated. Cells were washed with 1X PBS (pH

7.46), and 2% methylcellulose overlay in DMEM with 2% FBS and 0.5% penicillin-streptomycin was added to wells. Plaques were fixed with 0.2% crystal violet between 96-100 hours post infection and plaques were counted by hand. All plaque assays were set up with 2 technical replicates.

Knockout of macroH2A1:

MacroH2A1 guide RNA(22) was cloned into TLCv2 (Addgene plasmid: 87360), a plasmid encoding doxycycline-inducible Cas9-2A-GFP and gRNA expression. To generate lentiviral particles, $1.0x10^7$ HEK293T cells were transfected with 12 µg TLCV2_sg_mH2A1, 8 µg pMDL (Addgene plasmid: 12251), 4 µg VSVg, and 2.5 µg pREV (Addgene plasmid: 115989) using Attractene transfection reagent (Qiagen: 301005). Lentivirus was harvested at 24-, 48-, and 72hours post-transfection, filtered through 0.2 µm filters, aliquoted, flash frozen with liquid nitrogen, and stored at -80C. 2 mL of thawed filtered lentivirus was used to transduce approximately $3x10^6$ HeLa cells in 10 cm plates with 8 µg/mL polybrene (Millipore-Sigma: TR1003-G). Cells were allowed to reach confluence before selection with 1 µg/mL puromycin for 3 days. Plated at 1 cell per well into 96-well plates, and selected through serial expansion of colonies. Selected cells were screened for macroH2A1 knockout by western blot.

Infections with tazemetostat pretreatment:

HFFs or HeLa cells were treated with DMSO or 10 µM of tazemetostat (MedChem: HY-13803) in DMSO for 3 days prior to infection. Cells were then infected at MOI of 5 and after 1 hour of incubation with virus, fresh media with 10µM Taz was added to previously treated cells. Control samples were treated with equivalent volumes of DMSO. Samples were harvested as above.

Western Blotting:

Western blotting was performed as previously described (Lynch et al., 2021) . Briefly, cells were counted, pelleted, resuspended in 1x NuPAGE lithium dodecyl sulfate (LDS) sample buffer (Fisher Scientific: NP007) + 5% 2-betamercaptoethanol at 300,000 cells per 200 µL, and boiled for 15 minutes. Protein lysates were separated by 13.5% SDS-PAGE gels using 1X NuPAGE MOPS buffer (Fisher Scientific: NP0001) at 75 volts for 30 minutes then 110 volts for 100 minutes, then wet transferred to a nitrocellulose membrane (Bio-Rad) at 100 volts for 70 minutes using Transfer Buffer (25 mM Tris Base, 100 mM glycine, 20% methanol). Membranes were ponceau stained and imaged. Membranes were blocked in 5% milk in Tris-buffered saline with Tween (TBST) for 1 hour, then probed with primary antibody overnight (see Table 2). Membranes were washed with TBST for thirty minutes, incubated with secondary antibodies conjugated to horseradish peroxidase (α-mouse or α-rabbit; 1:5000) at room temperature for 1 hour, washed with TBST for thirty minutes, and detected using Clarity Western ECL Substrate (Bio-Rad: 1705061) and Chemidoc MP Imaging System (Bio-Rad). Images were formatted using Adobe Photoshop and Illustrator. Densitometry analysis was quantified using ImageJ.

Table 1: Sources and identification of antibodies used.

Antibody	Source	Identifier	Use (Concentration)
Mouse anti-actin	Abcam	Cat: 5441	WB (1:10,000)
Mouse anti-gH	Abcam	Cat: 110227	WB (1:1,000)
Rabbit anti-H3	Abcam	Cat: 1791	WB (1:20,000)
Rabbit anti-H3K27me3	Cell Signal Technologies	Cat: 9733T	WB/CUT&Tag (1:100) IF (1:500)
Mouse anti-ICP0	Santa Cruz	Cat: 53070	WB (1:1,000)

	Biotechnology		
Mouse anti-ICP8	Abcam	Cat: 20194	IF (1:500)
Chicken anti-UL34	Kind gift of Richard Roller	N/A	WB (1:1000) IF (1:500)
Peroxidase-AffiniPure Goat Anti-Mouse	Jackson Immunoresearch Laboratories	Cat: 115-035003	WB (1:5,000)
Peroxidase-AffiniPure Goat Anti-Rabbit	Jackson Immunoresearch Laboratories	Cat: 111-035045	WB (1:5,000)
Rabbit anti-mouse IgG	Abcam	Cat: 46540	CUT&Tag (1:100)
Guinea pig anti-rabbit IgG	Antibodies Online	Cat: AB1N101961	CUT&Tag (1:100)
Goat anti-Rabbit IgG (H+L) AlexaFluor 568	ThermoFisher Scientific	Cat: A-11011	IF (1:300)
Goat anti-Mouse IgG (H+L) AlexaFluor 488	ThermoFisher Scientific	Cat: A-11001	IF (1:300)

RNA sequencing:

Three biological replicates per time point were obtained from independent infections. Cells were harvested at the indicated times post-infection by trypsinization, washed with PBS and centrifuged at 5000 xg for 2 minutes. Pellets were lysed with TRIzol (Thermo Fisher: 15-596-026) and total RNA was harvested according to manufacturer's instructions. RNAs were then treated with DNase (Qiagen: 79254) on RNeasy columns (Qiagen: 74104) per manufacturer's

instructions. RNA was precipitated with 3 volumes ice-cold 96% ethanol, 1 volume 3 M sodium acetate pH 5.5, and 1 µL glycogen (Thermo Fischer: R055) overnight at -80 °C. Precipitated RNAs were pelleted at 15,000 xg and 4 °C for 30 minutes, washed with ice-cold 75% ethanol and spun as above for 10 min. RNA was resuspended in nuclease-free water.

RNA was quantified by Nanodrop and integrity analyzed with the 4200 Tapestation Bioanalyzer system (Agilent). 500 ng of total RNA with an RNA Integrity Number (RIN) greater than 9.5 were used to prepare sequencing libraries with the TruSeq® Stranded mRNA Library Prep Kit (Illumina: 20020594). Library concentrations were measured with Qubit dsDNA HS Assay Kit (Thermo Fisher: Q32854) then analyzed with Agilent High Sensitivity D5000 ScreenTape System and pooled. Libraries were sequenced with 100-bp paired-end reads on an Illumina NovaSeq 6000 SP sequencer at the Fred Hutch Genomics Core Facility

Transfection:

Cells were plated on poly-L coated glass coverslips the day prior to transfection. HeLa cells were transfected with 400 ng of plasmid DNA from Table 3 as indicated in figures using Attractene reagent and manufacturer protocol. Cells were fixed at 24 hours post-transfection and stained as described below.

Immunofluorescence:

Cells were plated on poly-L coated glass coverslips the day prior to infection. Cells were then infected with HSV-1 at an MOI of 3 and collected at mock, 10-, and 18- hpi or transfected as described above. For harvest cells were fixed with cold 4% PFA in 1X PBS for 15 minutes. Cells were permeabilized with 0.5% Triton-X in 1X PBS for 10 minutes, then blocked in 10% goat serum in 1X PBS for 1 hour, incubated with primary antibody (diluted as noted) in 3% BSA in 1X

PBS for 1 hour. Slides were incubated with secondary antibodies at a dilution of 1:300 in 3% BSA in 1X PBS for 1 hour. Coverslips were fixed to microscope slides with Invitrogen™ ProLong™ Gold Antifade Mountant. Images were taken on Leica Stellaris Confocal with 63X oil objective at room temperature.

Electron Microscopy:

Cells were fixed in 2% paraformaldehyde and 2.5% glutaraldehyde in 0.1M sodium cacodylate buffer (pH 7.3) at 4 °C. Fixed cells were rinsed briefly in 1% sucrose in 50mM cacodylate (pH 7.2), then postfixed on ice for 30 mins in a solution of 1% osmium (EM Sciences: RT19152) and 0.8% potassium ferricyanide in 50mM cacodylate (pH 7.2). Cell pellets were washed twice briefly at 25 °C in 1% sucrose in 50mM cacodylate (pH 7.2), then washed in three changes of 50mM cacodylate (pH 7.2) for 5 min each. Cell pellets were treated with 0.2% tannic acid (Sigma-Aldrich: 1401-55-4) in 50 mM cacodylate (pH 7.2) for 15 minutes at 25 °C, then rinsed several times in water. Cells were dehydrated through a graded ethanol series and embedded in Epon 12 resin (Ted Pella: 18010). 70nm thin sections were cut using an Ultracut UC7 ultramicrotome (Leica Mikrosysteme) and collected on 200 mesh formvar/carbon copper grids (Ted Pella: 01800). Sections were stained with 2% aqueous uranyl acetate and Reynolds lead citrate. Cell pellet sections were imaged using a Talos L120C microscope operated at 120kV with a Ceta-16M (4096 x 4096) camera (ThermoFisher Scientific).

All data were collected at spot size 5 with a 100um C2 aperture and 70um objective aperture. For quantification, nuclei were targeted at 1250x and manually circled. Autofocus was set to 2.0um. Nuclei were then imaged at 11000x as a montage and stitched together automatically using SerialEM (Nexperion Inc). Stitched maps were exported as uncompressed 16-bit tif files for further analysis. For qualitative analysis, images were manually focused to -2.0um defocus

and then 20 1-second frames were collected and drift-corrected using Velox software (Thermo Fisher Scientific, Eindhoven, NL). Final summed images were exported as 16-bit tif files and cropped using ImageJ.

6.3 Chapter 4 Materials and Methods

Cells and viruses

hTERT-immortalized HFFs, and hTERT-immortalized macroH2A1 knockout HFFs generated as previously described (22), were cultured using standard methods with 10% FBS and 1% penicillin-streptomycin as previously described (58). Cells were grown at 37°C with 5% CO_2 and routinely tested for mycoplasma contamination.

MRC5 cells with doxycycline inducible IE1, IE1 ΔCTD, or Luciferase were a kind gift from the lab of M. Nevels and used as previously described (31, 33). Briefly, cells were grown in DMEM with 10% tetracycline negative FBS, 1% penicillin-streptomycin, and 1mM sodium pyruvate. Confluent plates were seeded and after 3 days, the media was changed then cells were undisturbed for 7 days. After these 7 days, 2 µg/mL doxycycline was added to plates and refreshed every 24 hours. Cells were harvested at 48 hours and RNA was extracted using the NEB Total RNA kit and RT-qPCR was performed as described below.

The lab-adapted strain of HCMV *Towne* (59) was used for all experiments unless otherwise noted. GFP-*Towne* (60) and *TB40E*-GFP (61) were used for experiments indicated at an MOI of 1. Monolayers of cells were infected for 1 h at 37°C as previously described (62). Cells were collected at 4, 16, 24, 48,72, 96 hpi for western blot and RNA-sequencing. The supernatant was collected at 4 and 6 dpi for plaque assays. Virus stock was grown by infecting WT HFF cells at an MOI of 0.0001. The virus was harvested ~16-20 dpi and titered on HFF cells to determine stock plaque-forming units per ml (PFU/ml). Experimental plaque assays were set up in WT HFF cells. Plaque assays were set up as serial 10-fold dilutions in serum-free DMEM. The virus was left on the cells for 1 h and then aspirated. Cells were washed with 1× PBS (pH 7.46) and 2% methylcellulose overlay in DMEM with 2% FBS, and

0.5% penicillin-streptomycin was added to wells. Plaques were fixed with 0.2% crystal violet at 14 dpi and plaques were counted by hand. All plaque assays were set up with two technical replicates. In the case of GFP-tagged viruses, foci were read at 7 dpi using the Cy-5 filter on a Typhoon Trio Imager and quantified using FIJI is Just ImageJ version 2.1.0: Java 1.8.0_172 [64-bit].

Infections with tazemetostat pretreatment

HFFs were treated with DMSO or 10 μM of tazemetostat (HY-13803; MedChem) in DMSO for 3 d prior to infection as previously described(22). Cells were then infected at an MOI of 1, and after 1 h of incubation with the virus, fresh media with 10 μM tazemetostat was added to previously treated cells. Control samples were treated with equivalent volumes of DMSO.

Samples were harvested as above.

Western blotting

Western blotting was performed as previously described(58). Briefly, cells were counted, pelleted, resuspended in 1× NuPAGE lithium dodecyl sulfate (LDS) sample buffer (NP007; Thermo Fisher Scientific) + 5% β-mercaptoethanol at 300,000 cells per 200 μl, and boiled for 15 min. Protein lysates were separated by 13.5% SDS-PAGE gels using 1× NuPAGE MOPS buffer (NP0001; Thermo Fisher Scientific) at 75 V for 30 min, then 110 V for 100 min, and then wet transferred to a nitrocellulose membrane (Bio-Rad) at 100 V for 70 min using Transfer Buffer (25 mM Tris Base, 100 mM glycine, 20% methanol). Membranes were ponceau stained and imaged. Membranes were blocked in 5% milk in Tris-buffered saline with Tween (TBST) for 1 h and then probed with primary antibody overnight (**Table 1**). Membranes were washed with

TBST for 30 min, incubated with secondary antibodies conjugated to horseradish peroxidase (αmouse or α-rabbit; 1:5,000) at room temperature for 1 h, washed with TBST for 30 min, and detected using Clarity Western ECL Substrate (1705061; Bio-Rad) and Chemidoc MP Imaging System (Bio-Rad). Images were formatted using Adobe Photoshop and Illustrator.

Table 1. Antibodies used for western blot and immunofluorescence.

Antibody	Source	Identifier	Use (concentration)
Mouse anti-CMV IE1/2	Virusys Corporation	Cat: p1215	WB (1:5,000)
Mouse anti-CMV UL44	Virusys Corporation	Cat: CA006-100	WB (1:36,000)
Mouse anti-CMV pp28	Virusys Corporation	Cat: CA004-1	WB (1:4,000) IF (1:250)
Mouse anti-CMV pp65	Virusys Corporation	Cat: CA003-100	WB (1:2,000)
Mouse anti-CMV gB	Virusys Corporation	Cat: CA005-100	WB (1:4,000)
Rabbit anti-macroH2A1	Abcam	Cat: 37264	WB (1:1,000)
Mouse anti-Vinculin	Sigma Aldrich	Cat: V9131	WB (1:10,000)
Mouse anti-α-Tubulin	Thermo Fisher Scientific	Cat: 32-2500	IF (1:1000)
Mouse anti-α-Tubulin	Santa Cruz Biotechnology	Cat: sc-69969	WB (1:1,000)
Mouse anti-β-actin	Abcam	Cat: 5441	WB (1:10,000)
Rabbit anti-KIF1A	Abcam	Cat: ab180153	WB (1:2,500)

Rabbit anti-KIBRA (WWC1)	Cell Signaling Technologies	Cat: 8774S	WB (1:1,000)
Rabbit anti-H3	Abcam	Cat: 1791	WB (1:20,000)
Rabbit anti-H3K27me3	Cell Signaling Technologies	Cat: 9733T	WB (1:100)
Peroxidase-AffiniPure goat antirabbit	Jackson Immunoresearch Laboratories	Cat: 111-035-045	WB (1:5,000)
Peroxidase-AffiniPure goat antimouse	Jackson Immunoresearch Laboratories	Cat: 115-035-003	WB (1:5,000)
Goat anti-mouse IgG (H+L) AlexaFluor 555	Thermo Fisher Scientific	Cat: A-32727	IF (1:300)

Quantification of HSV-1 genomes by droplet digital (ddPCR)

Quantification was carried out as previously described (22). In brief, cells were harvested at the indicated times after infection by trypsinization, washed with 1× PBS, and centrifuged at 5,000 × *g* for 2 min. Pellets were flash-frozen in liquid nitrogen and stored at −80°C until processed. HCMV DNA within cells was isolated from frozen pellets using QIAamp DNAMini Kit (51304; Qiagen).

Supernatants were harvested at the indicated times after infection, centrifuged at >3,500 × *g,* and filtered through 40-μm sterile syringe filters. DNA on the exterior of filtered capsids was digested for 1 h at 25°C with 20.3 units DNase (79254; Qiagen) supplemented with 10 mM $MgCl_2$. DNase was inactivated at 75°C for 10 min followed by vortexing. Capsids were then digested with 3 mg/ml

proteinase K (BP1700; Thermo Fisher Scientific) in 100 mM KCl, 25 mM EDTA, 10 mM Tris-HCl pH 7.4, and 1% Igepal for 1 h at 50°C. HCMV genomes from digested capsids were isolated using QIAamp DNAMini Kit.

A duplexed droplet digital PCR was performed to measure the levels of cellular or supernatant HCMV genomes on the QX100 droplet digital PCR system (Bio-Rad Laboratories) using a primer/probe set specific to HCMV UL55. Cell numbers were determined using a primer/probe set specific to human Beta-globin, a reference gene that exists at two copies per cell. The ddPCR reaction mixture consisted of 12.5 µl of a 2× ddPCR Supermix for Probes no dUTP 628 (1863024; Bio-Rad), 1.25 µl of each 20× primer-probe mix (Table 2), and 10 µl of template DNA. 20 µl of each reaction mixture was loaded onto a disposable plastic cartridge (1864008; Bio-Rad) with 70 µl of droplet generation oil (1863005; Bio-Rad) and placed in the droplet generator (Bio-Rad). Droplets generated were transferred to a 96-well PCR plate (12001925; Bio-Rad), and PCR amplification was performed on a Bio-Rad C1000 Touch Thermal Cycler with the following conditions: 95°C for 10 min, 40 cycles of 94°C for 30 s, and 60°C for 1 min, followed by 98°C for 10 min, and ending at 4°C. After amplification, the plate was loaded onto the droplet reader (QX200; Bio-Rad) and the droplets from each well of the plate were automatically read with droplet reader oil (186–3004; Bio-Rad) at a rate of 32 wells per hour. Data were analyzed with QuantaSoft analysis software and the quantitation of target molecules presented as copies per microliter of the PCR reaction. HCMV genome values were standardized to cellular β-globin levels. Experiments were completed in biological triplicate and 640 statistical analysis was performed as indicated in figure legends using Prism v10 (GraphPad 641 Software).

Table 2: Primers and probes for ddPCR

Target	Forward Primer	Reverse Primer	Probe
HCMV UL55	TGGGCGAGG ACAACGAA	TGAGGCTGGG AAGCTGACAT	6FAM-TGGGCAACCACC GCACTGAGG-BHQ1
Human BetaGlobin	TGAAGGCTCA TGGCAAGAAA	GCTCACTCAGT GTGGCAAAGG	5HEX- TCCAGGTGAGCCAGGCCATCACTA3BHQ1

RNA sequencing

Three biological replicates per time point were obtained from independent infections. Cells were harvested at the indicated times after infection by trypsinization, washed with PBS, and centrifuged at 5,000 × *g* for 2 min. RNA was harvested using New England BioLabs Monarch® Total RNA Miniprep Kit (T2010S) as per kit instructions.

RNA was quantified by Nanodrop and integrity was analyzed with the 4200 Tapestation Bioanalyzer system (Agilent). 500 ng of total RNA with an RNA Integrity Number (RIN) >9.5 were used to prepare sequencing libraries with the TruSeq Stranded mRNA Library Prep Kit (20020594; Illumina). Library concentrations were measured with Qubit dsDNA HS Assay Kit (Q32854; Thermo Fisher Scientific) and then analyzed with Agilent High Sensitivity D5000

ScreenTape System and pooled. Libraries were sequenced with 100-bp paired-end reads on an Illumina NextSeq 2000 sequencer at the Fred Hutch Genomics Core Facility.

RNA-seq analysis

A concatenated fasta file was created using cDNA sequences from release 110 of Ensembl for the human genome and *Towne-HCMV* genome generated from sequencing map in Murphy e*t al.* 2003(63) and genbank sequences, which was then used to construct a Salmon index(64). Expression for each transcript was quantified from raw reads using Salmon v1.9 with libType set as automatic. DESeq2(65) (v1.30.1) in R (v4.0.3) was used first to perform all pairwise comparisons for WT and macroH2A1 KO both across time points and between the two genotypes. There were six time points each in biological triplicates, resulting in 36 datasets: six time points compared against each other for each genotype (15x2) and six time points compared between WT and macroH2A1 KO (6) A superset of genes was made by combining lists of genes with adjusted p-value £0.05 from each comparison. The expression matrix across genotypes and time points was transformed using the “rlog” function in DESeq2, and then the expression values for the superset of genes were extracted. The normalized read count for each gene was averaged across replicates, Z-transformed across time points and genotypes, and then the matrix of Z-scores was subjected to k-means clustering (k=4). Raw reads for ENCODE datasets were obtained and quantified with Salmon in the same manner as the CMV samples. CMV samples and ENCODE samples were loaded together in DESeq2 as a single DESeq dataset and transformed using the “rlog” function. Normalized expression values for genes in cluster 1 were then extracted to plot the distance matrix and principal components. The distance matrix was calculated using the “dist” function in R and plotted using the pheatmap package.

Principal component analysis was performed using the “prcomp” function in R and plotted using ggplot2. GO enrichment analysis was performed with WebGestalt(66). macroH2A and H3K27me3 enrichment at genes from different clusters were performed using published data for WT and

macroH2A.1 KO HFF cells. Enrichment was calculated across the whole gene (Gene start and Gene end definitions from Ensembl).

Targeted siRNA screen

HFFs were plated in 6-well plates and infected at MOI of 1 with HCMV-GFP Towne as described. Cells were transfected at 12 and 24 hours post infection with 25 pmol/well siRNA (Silencer select, Ambion distributed by Thermo Fisher) (**Table 3**) using lipofectamine RNAiMAX (Thermo Fisher). Non-targeting "Negative Control #1" (Cat. 4390843) was used as siRNA control. At 4 days post infection, supernatants were collected and flash frozen in liquid nitrogen for GFP-foci and plaque assay. Cells were pelleted and split, 75:25 for protein lysate and RNA respectively. Cells for protein lysate were lysed as previously described. Cell pellets for RNA extraction were flash frozen in liquid nitrogen and stored at -80C.

RT-qPCR

RNA was extracted by TRIzol (Invitrogen) and cDNA was generated using Iscript Reverse Transcription kit (Bio-Rad). RT-qPCR was performed using a CFX384 Touch Real-Time PCR 693 Detection System (Bio-Rad) and iTaq Universal SYBR Green One-Step kit (Bio-Rad). Primers for 694 RT-qPCR are described in Table 3.

Table 3. RT-qPCR primers and siRNA IDs.

Target	Forward RT-qPCR Primer	Reverse RT-qPCR Primer	Ambion Silencer Select siRNA (Cat. 4392420) ID:
APOE(67)	CCTCAAGAGCTGG TTCGAG	TCGGCGTTCAGTG ATTGTC	s532836
CNTFR	CACCTGTTCTCCAC CATCAA	CACAATGGTGAAC TCGTCAAAG	s3270
DOC2B	CAGGAGCCAGTAA GGCAAATA	GTCTTCATCTGTGA TCCCGTAG	s16033
ERC1	TCAGGCGAGAGAT AACACAATC	TGCTCTCCTTTACT TCCACATC	s22995
IFI27	CTGTCATTGCGAG GTTCTACT	ATTTGGGATAGTTG GCTCCTC	s194542
KIF1A	ACATGACACTCTCC GCTTATATC	CTTGGCATCACGG GAATAGA	s1827
LAMA1	CTGGACATAGCCA GCTCTAATG	GTATTCCATCCACG CGGTAATA	s531309
LRRC4B	AAGCGGCTGGAAT ACATCTC	ATGTCCTTGAGGTT GCACAT	s41228
MYO5B	GTGGCAGAAGAAG CCTACAA	CATACTTGGCTGAT ACCGTCTT	s532220
NPXT2	CCATTAGAAGAAG GCTCCCATT	ATGAAGACAGTCC AGTGCTTAC	s9696

SOX11	CCTCTTCCGCTAGTTGTGAAA	GGAGGAGGTGAGAAAGGAAATG	s224668
WWC1	CAAAGGAAAGCAGATGCAAGAG	GACTGCAGATACAGTGAGGATG	s23477
UL55	TGGGCGAGGACAACGAA	TGAGGCTGGGAAGCTGACAT	N/A
RPLP0	GCAGCATCTACAACCCTGAAG	CACTGGCAACATTGCGGAC	N/A
IE1(68)	CAAGTGACCGAGGATTGCAA	CACCATGTCCACTCGAACCTT	N/A

Immunofluorescence

As previously described (8), in brief: Cells were plated on poly-L coated glass coverslips the day prior to infection. Cells were then infected with HCMV at an MOI of 1 and collected at 72 hpi. For harvest, cells were fixed with cold 4% PFA in 1× PBS for 15 min. Cells were permeabilized with 0.5% Triton-X in 1× PBS for 15 min, then blocked in 10% human serum in 1× PBS for 1 h, incubated with primary antibody (diluted as noted in **Table 2**) in 10% human sera in 1× PBS for 1 h. Slides were incubated with secondary antibodies at a dilution of 1:300 in 3% BSA in 1×

PBS for 1 h. Coverslips were fixed to microscope slides with Invitrogen ProLong Gold Antifade Mountant or Vectashield (Tubulin stain). Images were taken on Leica Stellaris Confocal with 63× oil objective at room temperature. Images were formatted using Adobe Photoshop and Illustrator.

Images were analyzed using Bitplane Imaris v9.1.1. Labeled nuclei and vIACs were segmented using the Surfaces tool on DAPI and pp28 stains respectively, and average volumes, sphericity and mean fluorescence intensities were reported for each field.

Plaque area quantification

Once plaque assays were fixed (as per Cells and Virus section), plates were imaged on a Molecular Devices ImageXpress Micro high-content imaging system equipped with a Nikon 4x/0.2 Plan Apo objective. To provide a quantitative measurement of staining intensity, we acquired fluorescence images with a Cy5 filter set. Twenty-four overlapping fields were imaged per well, providing 73% coverage of the total well area.

Using FIJI is Just ImageJ version 2.1.0: Java 1.8.0_172 [64-bit] threshold was set to top 8% of pixel intensity (to account for well-to-well variation in crystal violet staining). The image was converted to binary and “analyze particles” feature was used to acquire area for particles over 1000 pixel units squared (**Figure 4.9 A**).

We also acquired transmitted light images of selected samples on a Nikon Eclipse Ti inverted microscope equipped with a Nikon 4x/0.2 Plan Apo objective. Images were acquired on a Photometrics Prime BSI Express sCMOS camera through an orange (580-610 nm) filter. This wavelength range was chosen to match the absorbance spectrum of crystal violet, thus maximizing staining contrast and ensuring high dynamic range.

Electron microscopy

Cells were fixed in 2% paraformaldehyde and 2.5% glutaraldehyde in 0.1 M sodium cacodylate buffer (pH 7.3) at 4°C. Fixed cells were rinsed briefly in 1% sucrose in 50 mM cacodylate (pH 7.2), then postfixed on ice for 30 min in a solution of 1% osmium tetroxide (RT19152; EM

Sciences) and 0.8% potassium ferricyanide in 50 mM cacodylate (pH 7.2). Cell pellets were washed twice briefly at 25°C in 1% sucrose in 50 mM cacodylate (pH 7.2) and then washed in three changes of 50 mM cacodylate (pH 7.2) for 5 min each. Cell pellets were treated with 0.2% tannic acid (1401-55-4; Sigma-Aldrich) in 50 mM cacodylate (pH 7.2) for 15 min at 25°C and then rinsed several times in water. Cells were dehydrated through a graded ethanol series and embedded in Epon 12 resin (18010; Ted Pella). 70-nm thin sections were cut using an Ultracut UC7 ultramicrotome (Leica Mikrosysteme) and collected on 200 mesh formvar/carbon coated copper grids (01800; Ted Pella). Sections were stained with 2% aqueous uranyl acetate and Reynolds lead citrate. Cell pellet sections were imaged using a Talos L120C microscope operated at 120 kV with a Ceta-16 M (4,096 × 4,096) camera (Thermo Fisher Scientific).

All data were collected at spot size 5 with a 100-µm C2 aperture and 70-µm objective aperture.

Images were formatted using Adobe Photoshop and Illustrator.

Image analysis was done using FIJI is Just ImageJ version 2.1.0: Java 1.8.0_172 [64-bit]. For analysis 2.5 micron by 2.5 micron grids were drawn on non-overlapping regions of cytosol.

“Freehand line tool” was used to trace all lengths of ER in the field of view and length of line was measured with ImageJ “Measure” function (**Figure 4.3 B**). Macro code for vIAC subcompartments can be found at: **10.5281/zenodo.11521560** (**Figure 4.3 D**).

Statistical Analysis

Graphs were generated and statistical analysis were run as marked in figure legends using GraphPad Prism v 9.1.2

Chapter7: Literature Cited

7.1 Chapter 1 Literature Cited:

1. Luger K, Mäder AW, Richmond RK, Sargent DF, Richmond TJ. 1997. Crystal structure of the nucleosome core particle at 2.8 Å resolution. *Nature*. 389(6648):251–60

2. Bannister AJ, Kouzarides T. 2011. Regulation of chromatin by histone modifications. *Cell Res*. 21(3):381–95

3. Wiles ET, Selker EU. 2017. H3K27 methylation: a promiscuous repressive chromatin mark. *Curr Opin Genet Dev*. 43:31–37

4. Saksouk N, Simboeck E, Déjardin J. 2015. Constitutive heterochromatin formation and transcription in mammals. *Epigenet Chromatin*. 8(1):3

5. Gamble MJ, Frizzell KM, Yang C, Krishnakumar R, Kraus WL. 2010. The histone variant macroH2A1 marks repressed autosomal chromatin, but protects a subset of its target genes from silencing. *Gene Dev*. 24(1):21–32

6. Trojer P, Reinberg D. 2007. Facultative Heterochromatin: Is There a Distinctive Molecular Signature? *Mol Cell*. 28(1):1–13

7. Jenuwein T, Allis CD. 2001. Translating the Histone Code. *Science*. 293(5532):1074–80

8. Lee J-S, Smith E, Shilatifard A. 2010. The Language of Histone Crosstalk. *Cell*. 142(5):682–85

9. Wiles ET, Selker EU. 2017. H3K27 methylation: a promiscuous repressive chromatin mark. *Curr Opin Genet Dev*. 43:31–37

10. Czermin B, Melfi R, McCabe D, Seitz V, Imhof A, Pirrotta V. 2002. Drosophila Enhancer of Zeste/ESC Complexes Have a Histone H3 Methyltransferase Activity that Marks Chromosomal Polycomb Sites. *Cell*. 111(2):185–96

11. Cao R, Wang L, Wang H, Xia L, Erdjument-Bromage H, et al. 2002. Role of Histone H3 Lysine 27 Methylation in Polycomb-Group Silencing. *Science*. 298(5595):1039–43

12. Cao Q, Wang X, Zhao M, Yang R, Malik R, et al. 2014. The central role of EED in the orchestration of polycomb group complexes. *Nat. Commun.* 5(1):3127

13. Kraft K, Yost KE, Murphy SE, Magg A, Long Y, et al. 2022. Polycomb-mediated genome architecture enables long-range spreading of H3K27 methylation. *Proc. Natl. Acad. Sci.* 119(22):e2201883119

14. Shumaker DK, Dechat T, Kohlmaier A, Adam SA, Bozovsky MR, et al. 2006. Mutant nuclear lamin A leads to progressive alterations of epigenetic control in premature aging. *Proc. Natl. Acad. Sci.* 103(23):8703–8

15. Liu Y, Yang Q. 2023. The roles of EZH2 in cancer and its inhibitors. *Méd. Oncol.* 40(6):167

16. Lowe BR, Maxham LA, Hamey JJ, Wilkins MR, Partridge JF. 2019. Histone H3 Mutations: An Updated View of Their Role in Chromatin Deregulation and Cancer. *Cancers*. 11(5):660

17. Gamble MJ, Kraus WL. 2010. Multiple facets of the unique histone variant macroH2A: From genomics to cell biology. *Cell Cycle*. 9(13):2568–74

18. Sun Z, Bernstein E. 2019. Histone variant macroH2A: from chromatin deposition to molecular function. *Essays Biochem*. 63(1):59–74

19. Costanzi C, Pehrson JR. 1998. Histone macroH2A1 is concentrated in the inactive X chromosome of female mammals. *Nature*. 393(6685):599–601

20. Gamble MJ, Frizzell KM, Yang C, Krishnakumar R, Kraus WL. 2010. The histone variant macroH2A1 marks repressed autosomal chromatin, but protects a subset of its target genes from silencing. *Gene Dev*. 24(1):21–32

21. Chakravarthy S, Gundimella SKY, Caron C, Perche P-Y, Pehrson JR, et al. 2005. Structural Characterization of the Histone Variant macroH2A. *Mol Cell Biol*. 25(17):7616–24

22. Muthurajan UM, McBryant SJ, Lu X, Hansen JC, Luger K. 2011. The Linker Region of MacroH2A Promotes Self-association of Nucleosomal Arrays*. *J Biol Chem*. 286(27):23852–64

23. Karras GI, Kustatscher G, Buhecha HR, Allen MD, Pugieux C, et al. 2005. The macro domain is an ADP-ribose binding module. *Embo J*. 24(11):1911–20

24. Douet J, Corujo D, Malinverni R, Renauld J, Sansoni V, et al. 2017. MacroH2A histone variants maintain nuclear organization and heterochromatin architecture. *J Cell Sci*. 130(9):1570–82

25. Fu Y, Lv P, Yan G, Fan H, Cheng L, et al. 2015. MacroH2A1 associates with nuclear lamina and maintains chromatin architecture in mouse liver cells. *Sci Rep-uk*. 5(1):17186

26. Hsu C-J, Meers O, Buschbeck M, Heidel FH. 2021. The Role of MacroH2A Histone Variants in Cancer. *Cancers*. 13(12):3003

27. Sporn JC, Kustatscher G, Hothorn T, Collado M, Serrano M, et al. 2009. Histone macroH2A isoforms predict the risk of lung cancer recurrence. *Oncogene*. 28(38):3423–28

28. Kapoor A, Goldberg MS, Cumberland LK, Ratnakumar K, Segura MF, et al. 2010. The histone variant macroH2A suppresses melanoma progression through regulation of CDK8. *Nature*. 468(7327):1105–9

29. Kadauke S, Blobel GA. 2009. Chromatin loops in gene regulation. *Biochim. Biophys. Acta (BBA) - Gene Regul. Mech.* 1789(1):17–25

30. Grubert F, Srivas R, Spacek DV, Kasowski M, Ruiz-Velasco M, et al. 2020. Landscape of cohesinmediated chromatin loops in the human genome. *Nature*. 583(7818):737–43

31. Andersson R, Sandelin A. 2020. Determinants of enhancer and promoter activities of regulatory elements. *Nat. Rev. Genet.* 21(2):71–87

32. Giammartino DCD, Polyzos A, Apostolou E. 2020. Transcription factors: building hubs in the 3D space. *Cell Cycle*. 19(19):2395–2410

33. Beagan JA, Phillips-Cremins JE. 2020. On the existence and functionality of topologically associating domains. *Nat. Genet.* 52(1):8–16

34. Yu M, Ren B. 2016. The Three-Dimensional Organization of Mammalian Genomes. *Annu. Rev. Cell Dev. Biol.* 33(1):1–25

35. Agarwal A, Korsak S, Choudhury A, Plewczynski D. 2023. The dynamic role of cohesin in maintaining human genome architecture. *BioEssays*. 45(10):e2200240

36. Stephens AD. 2020. Chromatin rigidity provides mechanical and genome protection. *Mutat.* Res.Fundam. Mol. Mech. Mutagen. 821:111712

37. Kim S, Yu N-K, Kaang B-K. 2015. CTCF as a multifunctional protein in genome regulation and gene expression. *Exp. Mol. Med.* 47(6):e166–e166

38. Nasmyth K, Haering CH. 2009. Cohesin: Its Roles and Mechanisms. *Genetics*. 43(1):525–58

39. Dorner D, Gotzmann J, Foisner R. 2007. Nucleoplasmic lamins and their interaction partners, LAP2α, Rb, and BAF, in transcriptional regulation. *FEBS J.* 274(6):1362–73

40. Bouzid T, Kim E, Riehl BD, Esfahani AM, Rosenbohm J, et al. 2019. The LINC complex, mechanotransduction, and mesenchymal stem cell function and fate. *J. Biol. Eng.* 13(1):68

41. Torvaldson E, Kochin V, Eriksson JE. 2015. Phosphorylation of lamins determine their structural properties and signaling functions. *Nucleus*. 6(3):166–71

42. Capell BC, Collins FS. 2006. Human laminopathies: nuclei gone genetically awry. *Nat. Rev. Genet.* 7(12):940–52

43. Horníková L, Bruštíková K, Huérfano S, Forstová J. 2022. Nuclear Cytoskeleton in Virus Infection. *Int J Mol Sci*. 23(1):578

44. O'Sullivan JM, Pai DA, Cridge AG, Engelke DR, Ganley ARD. 2013. The nucleolus: a raft adrift in the nuclear sea or the keystone in nuclear structure? *Biomol. Concepts*. 4(3):277–86

45. Orsolic I, Jurada D, Pullen N, Oren M, Eliopoulos AG, Volarevic S. 2016. The relationship between the nucleolus and cancer: Current evidence and emerging paradigms. *Semin. Cancer Biol.* 37:36–50

46. Parlato R, Kreiner G. 2013. Nucleolar activity in neurodegenerative diseases: a missing piece of the puzzle? *J. Mol. Med.* 91(5):541–47

47. Zierhut C, Funabiki H. 2015. Nucleosome functions in spindle assembly and nuclear envelope formation. *BioEssays*. 37(10):1074–85

48. Tsai RYL, Pederson T. 2014. Connecting the nucleolus to the cell cycle and human disease. *FASEB J.* 28(8):3290–96

49. Olson MOJ. 2004. Sensing Cellular Stress: Another New Function for the Nucleolus? *Sci.'s STKE*. 2004(224):pe10

50. Knipe DM, Howley P. 2013. *Fields Virology*. Lippincott Williams & Wilkins

51. Davison AJ. 2002. Evolution of the herpesviruses. *Vet. Microbiol.* 86(1–2):69–88

52. Looker KJ, Magaret AS, May MT, Turner KME, Vickerman P, et al. 2015. Global and Regional Estimates of Prevalent and Incident Herpes Simplex Virus Type 1 Infections in 2012. *Plos One*. 10(10):e0140765

53. Knipe DM, Howley P. 2013. *Fields Virology*. Lippincott Williams & Wilkins

54. Knipe DM, Cliffe A. 2008. Chromatin control of herpes simplex virus lytic and latent infection. *Nat Rev Microbiol*. 6(3):211–21

55. Ayoub HH, Chemaitelly H, Abu-Raddad LJ. 2019. Characterizing the transitioning epidemiology of herpes simplex virus type 1 in the USA: model-based predictions. *BMC Med.* 17(1):57

56. Kennedy PGE, Chaudhuri A. 2002. Herpes simplex encephalitis. *J. Neurol., Neurosurg. Psychiatry*. 73(3):237

57. Kłysik K, Pietraszek A, Nowakowska M, Karewicz A. 2018. Acyclovir in the Treatment of Herpes Viruses – A Review. *Curr. Med. Chem.* 27(24):4118–37

58. Sirtori C, Bosisio-Bestetti M. 1967. Nucleolar changes in KB tumor cells infected with herpes simplex virus. *Cancer Res.* 27(2):367–76

59. Love R, Wildy P. 1963. Cytochemical studies of the nucleoproteins of HeLa cells infected with Herpes virus. *J. Cell Biol.* 17(2):237–54

60. Dupuy-Coin AM, Arnoult J, Bouteille M. 1978. Quantitative correlation of morphological alterations of the nucleus with functional events during in vitro infection of glial cells with herpes simplex hominis (HSV 2). *J. Ultrastruct. Res.* 65(1):60–72

61. Dienes HP, Ramadori G, Falke D, Thoenes W. 1984. Electron microscopic observations on primary hepatocyte cultures infected with herpes simplex virus Types I and II. *Virchows Arch. B*. 46(1):321–32

62. Monier K, Armas JCG, Etteldorf S, Ghazal P, Sullivan KF. 2000. Annexation of the interchromosomal space during viral infection. *Nat Cell Biol*. 2(9):661–65

63. Simpson-Holley M, Baines J, Roller R, Knipe DM. 2004. Herpes Simplex Virus 1 UL31 and UL34 Gene Products Promote the Late Maturation of Viral Replication Compartments to the Nuclear Periphery. *J Virol*. 78(11):5591–5600

64. Simpson-Holley M, Colgrove RC, Nalepa G, Harper JW, Knipe DM. 2005. Identification and Functional Evaluation of Cellular and Viral Factors Involved in the Alteration of Nuclear Architecture during Herpes Simplex Virus 1 Infection. *J Virol*. 79(20):12840–51

65. Evilevitch A, Hohlbauch SV. 2022. Intranuclear HSV-1 DNA ejection induces major mechanical transformations suggesting mechanoprotection of nucleus integrity. *Proc National Acad Sci*. 119(9):e2114121119

66. Lewis HC, Kelnhofer-Millevolte LE, Brinkley MR, Arbach HE, Arnold EA, et al. 2023. HSV-1 exploits host heterochromatin for nuclear egress. *J. Cell Biol.* 222(9):e202304106

67. Bosse JB, Hogue IB, Feric M, Thiberge SY, Sodeik B, et al. 2015. Remodeling nuclear architecture allows efficient transport of herpesvirus capsids by diffusion. *Proc National Acad Sci*. 112(42):E5725–33

68. Aho V, Salminen S, Mattola S, Gupta A, Flomm F, et al. 2021. Infection-induced chromatin modifications facilitate translocation of herpes simplex virus capsids to the inner nuclear membrane. *Plos Pathog*. 17(12):e1010132

69. Arii J. 2021. Host and Viral Factors Involved in Nuclear Egress of Herpes Simplex Virus 1. *Viruses*. 13(5):754

70. Ryckman BJ, Roller RJ. 2004. Herpes Simplex Virus Type 1 Primary Envelopment: UL34 Protein Modification and the US3-UL34 Catalytic Relationship. *J Virol*. 78(1):399–412

71. Reynolds AE, Wills EG, Roller RJ, Ryckman BJ, Baines JD. 2002. Ultrastructural Localization of the Herpes Simplex Virus Type 1 U L 31, U L 34, and U S 3 Proteins Suggests Specific Roles in Primary Envelopment and Egress of Nucleocapsids. *J Virol*. 76(17):8939–52

72. Bahnamiri MM, Roller RJ. 2021. Mechanism of Nuclear Lamina Disruption and the Role of pUS3 in Herpes Simplex Virus 1 Nuclear Egress. *J Virol*. 95(10): e02432-20.

73. Park R, Baines JD. 2006. Herpes Simplex Virus Type 1 Infection Induces Activation and Recruitment of Protein Kinase C to the Nuclear Membrane and Increased Phosphorylation of Lamin B. *J Virol*. 80(1):494– 504

74. Myllys M, Ruokolainen V, Aho V, Smith EA, Hakanen S, et al. 2016. Herpes simplex virus 1 induces egress channels through marginalized host chromatin. *Sci Rep-uk*. 6(1):28844

75. Douet J, Corujo D, Malinverni R, Renauld J, Sansoni V, et al. 2017. MacroH2A histone variants maintain nuclear organization and heterochromatin architecture. *J Cell Sci*. 130(9):1570–82

76. Stephens AD, Liu PZ, Banigan EJ, Almassalha LM, Backman V, et al. 2018. Chromatin histone modifications and rigidity affect nuclear morphology independent of lamins. *Mol. Biol. Cell*. 29(2):220– 33

77. Mogensen TH. 2009. Pathogen Recognition and Inflammatory Signaling in Innate Immune Defenses. Clin. Microbiol. Rev. 22(2):240–73

78. Schneider WM, Chevillotte MD, Rice CM. 2014. Interferon-Stimulated Genes: A Complex Web of Host Defenses. *Annu. Rev. Immunol.* 32(1):513–45

79. Li T, Diner BA, Chen J, Cristea IM. 2012. Acetylation modulates cellular distribution and DNA sensing ability of interferon-inducible protein IFI16. *Proc National Acad Sci*. 109(26):10558–63

80. Orzalli MH, Conwell SE, Berrios C, DeCaprio JA, Knipe DM. 2013. Nuclear interferon-inducible protein 16 promotes silencing of herpesviral and transfected DNA. *Proc National Acad Sci*. 110(47):E4492–4501

81. Cliffe AR, Knipe DM. 2008. Herpes Simplex Virus ICP0 Promotes both Histone Removal and Acetylation on Viral DNA during Lytic Infection ▿ . *J Virol*. 82(24):12030–38

82. Kent JR, Zeng P-Y, Atanasiu D, Gardner J, Fraser NW, Berger SL. 2004. During Lytic Infection Herpes Simplex Virus Type 1 Is Associated with Histones Bearing Modifications That Correlate with Active Transcription. *J. Virol.* 78(18):10178–86

83. Lang F, Li X, Vladimirova O, Hu B, Chen G, et al. 2017. CTCF interacts with the lytic HSV-1 genome to promote viral transcription. *Sci Rep-uk*. 7(1):39861

84. Li X, Yu Y, Lang F, Chen G, Wang E, et al. 2021. Cohesin promotes HSV-1 lytic transcription by facilitating the binding of RNA Pol II on viral genes. *Virol. J.* 18(1):26

85. Kwiatkowski DL, Thompson HW, Bloom DC. 2009. The Polycomb Group Protein Bmi1 Binds to the Herpes Simplex Virus 1 Latent Genome and Maintains Repressive Histone Marks during Latency. *J Virol*. 83(16):8173–81

86. Bloom DC, Giordani NV, Kwiatkowski DL. 2010. Epigenetic regulation of latent HSV-1 gene expression. *Biochimica Et Biophysica Acta Bba - Gene Regul Mech*. 1799(3–4):246–56

87. Cliffe AR, Coen DM, Knipe DM. 2013. Kinetics of Facultative Heterochromatin and Polycomb Group Protein Association with the Herpes Simplex Viral Genome during Establishment of Latent Infection. *Mbio*. 4(1):e00590-12

88. Liang Y, Quenelle D, Vogel JL, Mascaro C, Ortega A, Kristie TM. 2013. A Novel Selective LSD1/KDM1A Inhibitor Epigenetically Blocks Herpes Simplex Virus Lytic Replication and Reactivation from Latency. *mBio*. 4(1):e00558-12

89. Messer HGP, Jacobs D, Dhummakupt A, Bloom DC. 2015. Inhibition of H3K27me3-Specific Histone Demethylases JMJD3 and UTX Blocks Reactivation of Herpes Simplex Virus 1 in Trigeminal Ganglion Neurons. *J. Virol.* 89(6):3417–20

90. Margueron R, Reinberg D. 2011. The Polycomb complex PRC2 and its mark in life. *Nature*. 469(7330):343–49

91. Arbuckle JH, Gardina PJ, Gordon DN, Hickman HD, Yewdell JW, et al. 2017. Inhibitors of the Histone Methyltransferases EZH2/1 Induce a Potent Antiviral State and Suppress Infection by Diverse Viral Pathogens. *Mbio*. 8(4):e01141-17

92. Lee JS, Raja P, Pan D, Pesola JM, Coen DM, Knipe DM. 2018. CCCTC-Binding Factor Acts as a Heterochromatin Barrier on Herpes Simplex Viral Latent Chromatin and Contributes to Poised Latent Infection. *Mbio*. 9(1):e02372-17

93. Washington SD, Edenfield SI, Lieux C, Watson ZL, Taasan SM, et al. 2018. Depletion of the Insulator Protein CTCF Results in Herpes Simplex Virus 1 Reactivation In Vivo. *J Virol*. 92(11):e00173-18

94. Washington SD, Singh P, Johns RN, Edwards TG, Mariani M, et al. 2019. The CCCTC Binding Factor, CTRL2, Modulates Heterochromatin Deposition and the Establishment of Herpes Simplex Virus 1 Latency In Vivo. *J. Virol.* 93(13):

95. Singh P, Neumann DM. 2021. Cohesin Subunit Rad21 Binds to the Herpes Simplex Virus 1 Genome near CTCF Insulator Sites during Latency In Vivo. *J. Virol.* 95(11):

96. Callé A, Ugrinova I, Epstein AL, Bouvet P, Diaz J-J, Greco A. 2008. Nucleolin Is Required for an Efficient Herpes Simplex Virus Type 1 Infection. *J. Virol.* 82(10):4762–73

97. Lymberopoulos MH, Bourget A, Abdeljelil NB, Pearson A. 2011. Involvement of the UL24 protein in herpes simplex virus 1-induced dispersal of B23 and in nuclear egress. *Virology*. 412(2):341–48

98. Lymberopoulos MH, Pearson A. 2007. Involvement of UL24 in herpes-simplex-virus-1-induced dispersal of nucleolin. *Virology*. 363(2):397–409

99. López MR, Schlegel EFM, Wintersteller S, Blaho JA. 2008. The major tegument structural protein VP22 targets areas of dispersed nucleolin and marginalized chromatin during productive herpes simplex virus 1 infection. *Virus Res.* 136(1–2):175–88

100. Greco A, Arata L, Soler E, Gaume X, Couté Y, et al. 2012. Nucleolin Interacts with US11 Protein of Herpes Simplex Virus 1 and Is Involved in Its Trafficking. *J. Virol.* 86(3):1449–57

101. Cannon MJ, Schmid DS, Hyde TB. 2010. Review of cytomegalovirus seroprevalence and demographic characteristics associated with infection. *Rev. Méd. Virol.* 20(4):202–13

102. Zanghellini F, Boppana SB, Emery VC, Griffiths PD, Pass RF. 1999. Asymptomatic Primary Cytomegalovirus Infection: Virologic and Immunologic Features. *J. Infect. Dis.* 180(3):702–7

103. Manicklal S, Emery VC, Lazzarotto T, Boppana SB, Gupta RK. 2013. The “Silent” Global Burden of Congenital Cytomegalovirus. *Clin. Microbiol. Rev.* 26(1):86–102

104. Azevedo LS, Pierrotti LC, Abdala E, Costa SF, Strabelli TMV, et al. 2015. Cytomegalovirus infection in transplant recipients. *Clinics*. 70(7):515–23

105. Christensen-Quick A, Vanpouille C, Lisco A, Gianella S. 2017. Cytomegalovirus and HIV Persistence: Pouring Gas on the Fire. *AIDS Res. Hum. Retroviruses*. 33(S1):S-23-S-30

106. Lurain NS, Chou S. 2010. Antiviral Drug Resistance of Human Cytomegalovirus. *Clin. Microbiol. Rev.* 23(4):689–712

107. Alwine JC. 2012. The Human Cytomegalovirus Assembly Compartment: A Masterpiece of Viral Manipulation of Cellular Processes That Facilitates Assembly and Egress. *PLoS Pathog.* 8(9):e1002878

108. Procter DJ, Furey C, Garza-Gongora AG, Kosak ST, Walsh D. 2020. Cytoplasmic control of intranuclear polarity by human cytomegalovirus. *Nature*, pp. 1–6

109. Buchkovich NJ, Maguire TG, Alwine JC. 2010. Role of the Endoplasmic Reticulum Chaperone BiP, SUN Domain Proteins, and Dynein in Altering Nuclear Morphology during Human Cytomegalovirus Infection. *J Virol*. 84(14):7005–17

110. Das S, Ortiz DA, Gurczynski SJ, Khan F, Pellett PE. 2014. Identification of Human Cytomegalovirus Genes Important for Biogenesis of the Cytoplasmic Virion Assembly Complex. *J Virol*. 88(16):9086–99

111. Camozzi D, Pignatelli S, Valvo C, Lattanzi G, Capanni C, et al. 2008. Remodelling of the nuclear lamina during human cytomegalovirus infection: role of the viral proteins pUL50 and pUL53. *J Gen Virol*. 89(3):731–40

112. Nevels M, Paulus C, Shenk T. 2004. Human cytomegalovirus immediate-early 1 protein facilitates viral replication by antagonizing histone deacetylation. *Proc. Natl. Acad. Sci.* 101(49):17234–39

113. Mücke K, Paulus C, Bernhardt K, Gerrer K, Schön K, et al. 2014. Human Cytomegalovirus Major Immediate Early 1 Protein Targets Host Chromosomes by Docking to the Acidic Pocket on the Nucleosome Surface. *J Virol*. 88(2):1228–48

114. Fang Q, Chen P, Wang M, Fang J, Yang N, et al. 2016. Human cytomegalovirus IE1 protein alters the higher-order chromatin structure by targeting the acidic patch of the nucleosome. *Elife*. 5:e11911

115. Mauch-Mücke K, Schön K, Paulus C, Nevels MM. 2020. Evidence for Tethering of Human Cytomegalovirus Genomes to Host Chromosomes. *Front. Cell. Infect. Microbiol.* 10:577428

116. Nitzsche A, Paulus C, Nevels M. 2008. Temporal Dynamics of Cytomegalovirus Chromatin Assembly in Productively Infected Human Cells ▿ . *J Virol*. 82(22):11167–80

117. Albright ER, Morrison K, Ranganathan P, Carter DM, Nishikiori M, et al. 2022. Human cytomegalovirus lytic infection inhibits replication-dependent histone synthesis and requires stem loop binding protein function. *Proc National Acad Sci*. 119(14):e2122174119

118. Nitzsche A, Steinhäußer C, Mücke K, Paulus C, Nevels M. 2012. Histone H3 Lysine 4 Methylation Marks Postreplicative Human Cytomegalovirus Chromatin. *J. Virol.* 86(18):9817–27

119. Cuevas-Bennett C, Shenk T. 2008. Dynamic Histone H3 Acetylation and Methylation at Human Cytomegalovirus Promoters during Replication in Fibroblasts. *J. Virol.* 82(19):9525–36

120. Groves IJ, Reeves MB, Sinclair JH. 2009. Lytic infection of permissive cells with human cytomegalovirus is regulated by an intrinsic 'pre-immediate-early' repression of viral gene expression mediated by histone post-translational modification. *J. Gen. Virol.* 90(10):2364–74

121. Lieberman PM. 2013. Keeping it quiet: chromatin control of gammaherpesvirus latency. *Nat Rev Microbiol*. 11(12):863–75

122. Matthews SM, Groves IJ, O'Connor CM. 2023. Chromatin control of human cytomegalovirus infection. *mBio*. 14(4):e00326-23

123. Nevels M, Paulus C, Shenk T. 2004. Human cytomegalovirus immediate-early 1 protein facilitates viral replication by antagonizing histone deacetylation. *P Natl Acad Sci Usa*. 101(49):17234–39

124. Martínez FP, Cruz R, Lu F, Plasschaert R, Deng Z, et al. 2014. CTCF Binding to the First Intron of the Major Immediate Early (MIE) Gene of Human Cytomegalovirus (HCMV) Negatively Regulates MIE Gene Expression and HCMV Replication. *J. Virol.* 88(13):7389–7401

125. Elder EG, Krishna BA, Poole E, Perera M, Sinclair J. 2021. Regulation of host and viral promoters during human cytomegalovirus latency via US28 and CTCF. *J. Gen. Virol.* 102(5):001609

126. Abraham CG, Kulesza CA. 2013. Polycomb Repressive Complex 2 Silences Human Cytomegalovirus Transcription in Quiescent Infection Models. *J. Virol.* 87(24):13193–205

127. Cavallo T, Graves K, Cole NL, Albrecht T. 1981. Cytomegalovirus: An Ultrastructural Study of the Morphogenesis of Nuclear Inclusions in Human Cell Culture. *J. Gen. Virol.* 56(1):97–104

128. Villinger C, Neusser G, Kranz C, Walther P, Mertens T. 2015. 3D Analysis of HCMV Induced-Nuclear Membrane Structures by FIB/SEM Tomography: Insight into an Unprecedented Membrane Morphology. *Viruses*. 7(11):5686–5704

129. Strang BL, Boulant S, Coen DM. 2010. Nucleolin Associates with the Human Cytomegalovirus DNA Polymerase Accessory Subunit UL44 and Is Necessary for Efficient Viral Replication. *J. Virol.* 84(4):1771– 84

130. Westdorp KN, Sand A, Moorman NJ, Terhune SS. 2017. Cytomegalovirus Late Protein pUL31 Alters Pre-rRNA Expression and Nuclear Organization during Infection. *J. Virol.* 91(18):

131. Al-Heeti OM, Cathro HP, Ison MG. 2022. Adenovirus Infection and Transplantation. *Transplantation*. 106(5):920–27

132. Majorant D, Qiu F, Kalil AC, Wilson N, Florescu DF. 2018. Adenovirus – a deadly disease in the solid organ transplant population – risk factors and outcomes. *Transplant P*. 50(10):3769–74

133. Marsh K, Tayler R, Pollock L, Roy K, Lakha F, et al. 2022. Investigation into cases of hepatitis of unknown aetiology among young children, Scotland, 1 January 2022 to 12 April 2022. *Eurosurveillance*. 27(15):

134. Baker JM, Buchfellner M, Britt W, Sanchez V, Potter JL, et al. 2022. Acute Hepatitis and Adenovirus Infection Among Children — Alabama, October 2021–February 2022. *Morbidity Mortal Wkly Rep*. 71(18):638–40

135. Hoke CH, Snyder CE. 2013. History of the restoration of adenovirus type 4 and type 7 vaccine, live oral (Adenovirus Vaccine) in the context of the Department of Defense acquisition system. *Vaccine*. 31(12):1623–32

136. Sandkovsky U, Vargas L, Florescu DF. 2014. Adenovirus: Current Epidemiology and Emerging Approaches to Prevention and Treatment. *Curr Infect Dis Rep*. 16(8):416

137. Avgousti DC, Herrmann C, Kulej K, Pancholi NJ, Sekulic N, et al. 2016. A core viral protein binds host nucleosomes to sequester immune danger signals. *Nature*. 535(7610):173–77

138. Lynch KL, Dillon MR, Bat-Erdene M, Lewis HC, Kaai RJ, et al. 2021. A viral histone-like protein exploits antagonism between linker histones and HMGB proteins to obstruct the cell cycle. *Curr Biol.* 31,23: 5227-5237.e7

139. Charman M, Weitzman MD. 2020. Replication Compartments of DNA Viruses in the Nucleus: Location, Location, Location. *Viruses*. 12(2):151

140. Pfitzner S, Hofmann-Sieber H, Bosse JB, Franken LE, Grünewald K, Dobner T. 2020. Fluorescent protein tagging of adenoviral proteins pV and pIX reveals 'late virion accumulation compartment.' *PLoS Pathog.* 16(6):e1008588

141. Lynch KL, Gooding LR, Garnett-Benson C, Ornelles DA, Avgousti DC. 2019. Epigenetics and the dynamics of chromatin during adenovirus infections. *Febs Lett*. 593(24):3551–70

142. Stein RW, Corrigan M, Yaciuk P, Whelan J, Moran E. 1990. Analysis of E1A-mediated growth regulation functions: binding of the 300-kilodalton cellular product correlates with E1A enhancer repression function and DNA synthesis-inducing activity. *J. Virol.* 64(9):4421–27

143. Arany Z, Newsome D, Oldread E, Livingston DM, Eckner R. 1995. A family of transcriptional adaptor proteins targeted by the E1A oncoprotein. *Nature*. 374(6517):81–84

144. Horwitz GA, Zhang K, McBrian MA, Grunstein M, Kurdistani SK, Berk AJ. 2008. Adenovirus Small e1a Alters Global Patterns of Histone Modification. *Science*. 321(5892):1084–85

145. Ferrari R, Pellegrini M, Horwitz GA, Xie W, Berk AJ, Kurdistani SK. 2008. Epigenetic Reprogramming by Adenovirus e1a. *Science*. 321(5892):1086–88

146. Ferrari R, Su T, Li B, Bonora G, Oberai A, et al. 2012. Reorganization of the host epigenome by a viral oncogene. *Genome Res*. 22(7):1212–21

147. Ferrari R, Gou D, Jawdekar G, Johnson SA, Nava M, et al. 2014. Adenovirus Small E1A Employs the Lysine Acetylases p300/CBP and Tumor Suppressor Rb to Repress Select Host Genes and Promote Productive Virus Infection. *Cell Host Microbe*. 16(5):663–76

148. Johnson JS, Osheim YN, Xue Y, Emanuel MR, Lewis PW, et al. 2004. Adenovirus Protein VII Condenses DNA, Represses Transcription, and Associates with Transcriptional Activator E1A. *J Virol*. 78(12):6459–68

149. Haruki H, Okuwaki M, Miyagishi M, Taira K, Nagata K. 2006. Involvement of Template-Activating Factor I/SET in Transcription of Adenovirus Early Genes as a Positive-Acting Factor. *J Virol*. 80(2):794–801

150. Haruki H, Gyurcsik B, Okuwaki M, Nagata K. 2003. Ternary complex formation between DNA-adenovirus core protein VII and TAF-Iβ/SET, an acidic molecular chaperone. *Febs Lett*. 555(3):521–27

151. Tang D, Kang R, Zeh HJ, Lotze MT. 2023. The multifunctional protein HMGB1: 50 years of discovery. Nat. Rev. Immunol. 23(12):824–41

152. Arnold EA, Kaai RJ, Leung K, Brinkley MR, Kelnhofer-Millevolte LE, et al. 2023. Adenovirusprotein VII binds the A-box of HMGB1 to repress interferon responses. *PLOS Pathog.* 19(9):e1011633

153. Xue Y, Johnson JS, Ornelles DA, Lieberman J, Engel DA. 2005. Adenovirus Protein VII Functions throughout Early Phase and Interacts with Cellular Proteins SET and pp32. *J Virol*. 79(4):2474–83

154. Carvalho T, Seeler JS, Ohman K, Jordan P, Pettersson U, et al. 1995. Targeting of adenovirus E1A and E4-ORF3 proteins to nuclear matrix-associated PML bodies. *J. cell Biol.* 131(1):45–56

155. Ullman AJ, Reich NC, Hearing P. 2007. Adenovirus E4 ORF3 Protein Inhibits the Interferon-Mediated Antiviral Response. *J Virol*. 81(9):4744–52

156. Stracker TH, Carson CT, Weitzman MD. 2002. Adenovirus oncoproteins inactivate the Mre11–Rad50–NBS1 DNA repair complex. *Nature*. 418(6895):348–52

157. Soriano AM, Crisostomo L, Mendez M, Graves D, Frost JR, et al. 2019. Adenovirus 5 E1A Interacts with E4orf3 To Regulate Viral Chromatin Organization. *J. Virol.* 93(10):

158. Lawrence FJ, McStay B, Matthews DA. 2006. Nucleolar protein upstream binding factor is sequestered into adenovirus DNA replication centres during infection without affecting RNA polymerase I location or ablating rRNA synthesis. *J. Cell Sci.* 119(12):2621–31

159. Lam YW, Evans VC, Heesom KJ, Lamond AI, Matthews DA. 2010. Proteomics Analysis of the Nucleolus in Adenovirus-infected Cells. *Mol Cell Proteomics*. 9(1):117–30

160. Reyes ED, Kulej K, Pancholi NJ, Akhtar LN, Avgousti DC, et al. 2017. Identifying Host Factors Associated with DNA Replicated During Virus Infection. *Mol Cell Proteomics*. 16(12):2079–97

161. Genoveso MJ, Hisaoka M, Komatsu T, Wodrich H, Nagata K, Okuwaki M. 2020. Formation of adenovirus DNA replication compartments and viral DNA accumulation sites by host chromatin regulatory proteins including NPM1. *FEBS J.* 287(1):205–17

162. Ugai H, Dobbins GC, Wang M, Le LP, Matthews DA, Curiel DT. 2012. Adenoviral protein V promotes a process of viral assembly through nucleophosmin 1. *Virology*. 432(2):283–95

163. Samad MA, Komatsu T, Okuwaki M, Nagata K. 2012. B23/nucleophosmin is involved in regulation of adenovirus chromatin structure at late infection stages, but not in virus replication and transcription. *J Gen Virol*. 93(Pt_6):1328–38

164. Samad MA, Okuwaki M, Haruki H, Nagata K. 2007. Physical and functional interaction between a nucleolar protein nucleophosmin/B23 and adenovirus basic core proteins. *Febs Lett*. 581(17):3283–88

165. Box JK, Paquet N, Adams MN, Boucher D, Bolderson E, et al. 2016. Nucleophosmin: from structure and function to disease development. *BMC Mol. Biol.* 17(1):19

166. Pfitzner S, Bosse JB, Hofmann-Sieber H, Flomm F, Reimer R, et al. 2021. Human Adenovirus Type 5 Infection Leads to Nuclear Envelope Destabilization and Membrane Permeability Independently of Adenovirus Death Protein. *Int J Mol Sci*. 22(23):13034

167. Tollefson AE, Scaria A, Hermiston TW, Ryerse JS, Wold LJ, Wold WS. 1996. The adenovirus death protein (E3-11.6K) is required at very late stages of infection for efficient cell lysis and release of adenovirus from infected cells. *J. Virol.* 70(4):2296–2306

168. Doan PTB, Nio K, Shimakami T, Kuroki K, Li Y-Y, et al. 2023. Super-Resolution Microscopy Analysis of Hepatitis B Viral cccDNA and Host Factors. *Viruses*. 15(5):1178

169. Moreau P, Cournac A, Palumbo GA, Marbouty M, Mortaza S, et al. 2018. Tridimensional infiltration of DNA viruses into the host genome shows preferential contact with active chromatin. *Nat Commun*. 9(1):4268

170. Porter SS, Liddle JC, Browne K, Pastrana DV, Garcia BA, et al. 2021. Histone Modifications in Papillomavirus Virion Minichromosomes. *mBio*. 12(1):e03274-20

171. Wang R, Lee J-H, Kim J, Xiong F, Hasani LA, et al. 2023. SARS-CoV-2 restructures host chromatin architecture. *Nat Microbiol*. 8(4):679–94

172. Washington SD, Musarrat F, Ertel MK, Backes GL, Neumann DM. 2018. CTCF Binding Sites in the Herpes Simplex Virus 1 Genome Display Site-Specific CTCF Occupation, Protein Recruitment, and Insulator Function. *J Virol*. 92(8):e00156-18

173. Kaya-Okur HS, Wu SJ, Codomo CA, Pledger ES, Bryson TD, et al. 2019. CUT&Tag for efficient epigenomic profiling of small samples and single cells. *Nat Commun*. 10(1):1930

174. Boftsi M, Whittle FB, Wang J, Shepherd P, Burger LR, et al. 2021. The adeno-associated virus 2 genome and Rep 68/78 proteins interact with cellular sites of DNA damage. *Hum. Mol. Genet.* 31(6):985–98

175. Majumder K, Boftsi M, Pintel DJ. 2019. Viral Chromosome Conformation Capture (V3C) Assays for Identifying Trans-interaction Sites between Lytic Viruses and the Cellular Genome. *Bio-Protoc.* 9(6):e3198

176. Vu A, Poyzer C, Roller R. 2016. Extragenic Suppression of a Mutation in Herpes Simplex Virus 1 UL34 That Affects Lamina Disruption and Nuclear Egress. *J. Virol.* 90(23):10738–51

177. Dembowski JA, DeLuca NA. 2018. Temporal Viral Genome-Protein Interactions Define Distinct Stages of Productive Herpesviral Infection. *Mbio*. 9(4):e01182-18

178. Kulej K, Avgousti DC, Sidoli S, Herrmann C, Fera AND, et al. 2017. Time-resolved Global and Chromatin Proteomics during Herpes Simplex Virus Type 1 (HSV-1) Infection. *Mol Cell Proteomics*. 16(4 suppl 1):S92–107

179. Dembowski JA, Dremel SE, DeLuca NA. 2017. Replication-Coupled Recruitment of Viral and Cellular Factors to Herpes Simplex Virus Type 1 Replication Forks for the Maintenance and Expression of Viral Genomes. *PLoS Pathog.* 13(1):e1006166

7.2 Chapter 2 Literature Cited:

1. Knipe DM, Cliffe A. 2008. Chromatin control of herpes simplex virus lytic and latent infection. *Nat Rev Microbiol*. 6(3):211–21

2. Monier K, Armas JCG, Etteldorf S, Ghazal P, Sullivan KF. 2000. Annexation of the interchromosomal space during viral infection. *Nat Cell Biol*. 2(9):661–65

3. Kulej K, Avgousti DC, Sidoli S, Herrmann C, Fera AND, et al. 2017. Time-resolved Global and Chromatin Proteomics during Herpes Simplex Virus Type 1 (HSV-1) Infection. *Mol Cell Proteomics*. 16(4 suppl 1):S92–107

4. Aho V, Mäntylä E, Ekman A, Hakanen S, Mattola S, et al. 2019. Quantitative Microscopy Reveals Stepwise Alteration of Chromatin Structure during Herpesvirus Infection. *Viruses*. 11(10):935

5. Johnson KE, Bottero V, Flaherty S, Dutta S, Singh VV, Chandran B. 2014. IFI16 Restricts HSV-1 Replication by Accumulating on the HSV-1 Genome, Repressing HSV-1 Gene Expression, and Directly or Indirectly Modulating Histone Modifications. Plos Pathog. 10(11):e1004503

6. Roller RJ, Johnson DC. 2021. Herpesvirus Nuclear Egress across the Outer Nuclear Membrane. *Viruses*. 13(12):2356

7. Arii J. 2021. Host and Viral Factors Involved in Nuclear Egress of Herpes Simplex Virus 1. *Viruses*. 13(5):754

8. Aho V, Salminen S, Mattola S, Gupta A, Flomm F, et al. 2021. Infection-induced chromatin modifications facilitate translocation of herpes simplex virus capsids to the inner nuclear membrane. *Plos Pathog*. 17(12):e1010132

9. Myllys M, Ruokolainen V, Aho V, Smith EA, Hakanen S, et al. 2016. Herpes simplex virus 1 induces egress channels through marginalized host chromatin. *Sci Rep-uk*. 6(1):28844

10. Chi P, Allis CD, Wang GG. 2010. Covalent histone modifications — miswritten, misinterpreted and mis-erased in human cancers. *Nat Rev Cancer*. 10(7):457–69

11. Margueron R, Reinberg D. 2011. The Polycomb complex PRC2 and its mark in life. *Nature*. 469(7330):343–49

12. Gamble MJ, Kraus WL. 2010. Multiple facets of the unique histone variant macroH2A: From genomics to cell biology. *Cell Cycle*. 9(13):2568–74

13. Kapoor A, Goldberg MS, Cumberland LK, Ratnakumar K, Segura MF, et al. 2010. The histone variant macroH2A suppresses melanoma progression through regulation of CDK8. *Nature*. 468(7327):1105–9

14. Douet J, Corujo D, Malinverni R, Renauld J, Sansoni V, et al. 2017. MacroH2A histone variants maintain nuclear organization and heterochromatin architecture. *J Cell Sci*. 130(9):1570–82

15. Fu Y, Lv P, Yan G, Fan H, Cheng L, et al. 2015. MacroH2A1 associates with nuclear lamina and maintains chromatin architecture in mouse liver cells. *Sci Rep-uk*. 5(1):17186

16. Aho V, Myllys M, Ruokolainen V, Hakanen S, Mäntylä E, et al. 2017. Chromatin organization regulates viral egress dynamics. *Sci Rep-uk*. 7(1):3692

17. Ghiraldini FG, Filipescu D, Bernstein E. 2021. Solid tumours hijack the histone variant network. *Nat Rev Cancer*. 21(4):257–75

18. Rickels R, Hu D, Collings CK, Woodfin AR, Piunti A, et al. 2016. An Evolutionary Conserved Epigenetic Mark of Polycomb Response Elements Implemented by Trx/MLL/COMPASS. *Mol Cell*. 63(2):318–28

19. Lue JK, Amengual JE. 2018. Emerging EZH2 Inhibitors and Their Application in Lymphoma. *Curr Hematol Malig R*. 13(5):369–82

20. Kaya-Okur HS, Wu SJ, Codomo CA, Pledger ES, Bryson TD, et al. 2019. CUT&Tag for efficient epigenomic profiling of small samples and single cells. *Nat Commun*. 10(1):1930

21. Weller SK, Coen DM. 2012. Herpes Simplex Viruses: Mechanisms of DNA Replication. *Csh Perspect Biol*. 4(9):a013011

22. Hennig T, Michalski M, Rutkowski AJ, Djakovic L, Whisnant AW, et al. 2018. HSV-1-induced disruption of transcription termination resembles a cellular stress response but selectively increases chromatin accessibility downstream of genes. *Plos Pathog*. 14(3):e1006954

23. Lieberman-Aiden E, Berkum NL van, Williams L, Imakaev M, Ragoczy T, et al. 2009. Comprehensive Mapping of Long-Range Interactions Reveals Folding Principles of the Human Genome. *Science*. 326(5950):289–93

24. Rao SSP, Huntley MH, Durand NC, Stamenova EK, Bochkov ID, et al. 2014. A 3D Map of the Human Genome at Kilobase Resolution Reveals Principles of Chromatin Looping. *Cell*. 159(7):1665–80

25. Cai W, Schaffer PA. 1992. Herpes simplex virus type 1 ICP0 regulates expression of immediate-early, early, and late genes in productively infected cells. *J Virol*. 66(5):2904–15

26. Naldinho-Souto R, Browne H, Minson T. 2006. Herpes Simplex Virus Tegument Protein VP16 Is a Component of Primary Enveloped Virions. *J Virol*. 80(5):2582–84

27. Lorentzen EU, Eing BR, Hafezi W, Manservigi R, Kühn JE. 2001. Replication-Competent Herpes simplex Virus Type 1 Mutant Expressing an Autofluorescent Glycoprotein H Fusion Protein. *Intervirology*. 44(4):232–42

28. Gao C, Chen L, Tang S-B, Long Q-Y, He J-L, et al. 2020. The epigenetic landscapes of histone modifications on HSV-1 genome in human THP-1 cells. *Antivir Res*. 176:104730

29. Gibson W, Roizman B. 1972. Proteins Specified by Herpes Simplex Virus VIII. Characterization and Composition of Multiple Capsid Forms of Subtypes 1 and 2. *J Virol*. 10(5):1044–52

30. Yu X-K, O'Connor CM, Atanasov I, Damania B, Kedes DH, Zhou ZH. 2003. ThreeDimensional Structures of the A, B, and CCapsids of Rhesus Monkey Rhadinovirus: Insights into GammaherpesvirusCapsid Assembly, Maturation, and DNAPackaging. *J Virol*. 77(24):13182–93

31. Bosse JB, Hogue IB, Feric M, Thiberge SY, Sodeik B, et al. 2015. Remodeling nuclear architecture allows efficient transport of herpesvirus capsids by diffusion. *Proc National Acad Sci*. 112(42):E5725–33

32. Baker TS, Newcomb WW, Booy FP, Brown JC, Steven AC. 1990. Three-dimensional structures of maturable and abortive capsids of equine herpesvirus 1 from cryoelectron microscopy. *J Virol*. 64(2):563–73

33. Muthurajan UM, McBryant SJ, Lu X, Hansen JC, Luger K. 2011. The Linker Region of MacroH2A Promotes Self-association of Nucleosomal Arrays*. *J Biol Chem*. 286(27):23852–64

34. Kozlowski M, Corujo D, Hothorn M, Guberovic I, Mandemaker IK, et al. 2018. MacroH2A histone variants limit chromatin plasticity through two distinct mechanisms. *Embo Rep*. 19(10):

35. Arbuckle JH, Gardina PJ, Gordon DN, Hickman HD, Yewdell JW, et al. 2017. Inhibitors of the Histone Methyltransferases EZH2/1 Induce a Potent Antiviral State and Suppress Infection by Diverse Viral Pathogens. *Mbio*. 8(4):e01141-17

36. Brach D, Johnston-Blackwell D, Drew A, Lingaraj T, Motwani V, et al. 2017. EZH2 inhibition by tazemetostat results in altered dependency on B-cell activation signaling in DLBCL. *Mol Cancer Ther*. 16(11):molcanther.0840.2016

37. Knutson SK, Kawano S, Minoshima Y, Warholic NM, Huang K-C, et al. 2014. Selective Inhibition of EZH2 by EPZ-6438 Leads to Potent Antitumor Activity in EZH2-Mutant Non-Hodgkin Lymphoma. *Mol Cancer Ther*. 13(4):842–54

38. Bosse JB, Virding S, Thiberge SY, Scherer J, Wodrich H, et al. 2014. Nuclear Herpesvirus Capsid Motility Is Not Dependent on F-Actin. *Mbio*. 5(5):e01909-14

39. Bjerke SL, Roller RJ. 2006. Roles for herpes simplex virus type 1 UL34 and US3 proteins in disrupting the nuclear lamina during herpes simplex virus type 1 egress. *Virology*. 347(2):261– 76

40. Simpson-Holley M, Baines J, Roller R, Knipe DM. 2004. Herpes Simplex Virus 1 UL31 and UL34 Gene Products Promote the Late Maturation of Viral Replication Compartments to the Nuclear Periphery. *J Virol*. 78(11):5591–5600

41. Leach NR, Roller RJ. 2010. Significance of host cell kinases in herpes simplex virus type 1 egress and lamin-associated protein disassembly from the nuclear lamina. *Virology*. 406(1):127–37

42. Bahnamiri MM, Roller RJ. 2021. Mechanism of Nuclear Lamina Disruption and the Role of pUS3 in Herpes Simplex Virus 1 Nuclear Egress. *J Virol*. 95(10):

43. Bigalke JM, Heuser T, Nicastro D, Heldwein EE. 2014. Membrane deformation and scission by the HSV-1 nuclear egress complex. *Nat Commun*. 5(1):4131–4131

44. Draganova EB, Thorsen MK, Heldwein EE. 2021. Nuclear Egress of Herpesviruses. *Curr Issues Mol Biol*. 41:125–70

45. Simpson-Holley M, Colgrove RC, Nalepa G, Harper JW, Knipe DM. 2005. Identification and Functional Evaluation of Cellular and Viral Factors Involved in the Alteration of Nuclear Architecture during Herpes Simplex Virus 1 Infection. *J Virol*. 79(20):12840–51

46. Lynch KL, Dillon MR, Bat-Erdene M, Lewis HC, Kaai RJ, et al. 2021. A viral histone-like protein exploits antagonism between linker histones and HMGB proteins to obstruct the cell cycle. *Curr Biol*

47. Brown SM, Ritchie DA, Subak-Sharpe JH. 1973. Genetic Studies with Herpes Simplex Virus Type 1. The Isolation of Temperature-sensitive Mutants, their Arrangement into Complementation Groups and Recombination Analysis Leading to a Linkage Map. *J Gen Virol*. 18(3):329–46

48. Lilley CE, Carson CT, Muotri AR, Gage FH, Weitzman MD. 2005. DNA repair proteins affect the lifecycle of herpes simplex virus 1. *P Natl Acad Sci Usa*. 102(16):5844–49

49. Hatch EM, Kulukian A, Holland AJ, Cleveland DW, Stearns T. 2010. Cep152 interacts with Plk4 and is required for centriole duplication. *J Cell Biol*. 191(4):721–29

50. Li G, Nguyen CC, Ryckman BJ, Britt WJ, Kamil JP. 2015. A viral regulator of glycoprotein complexes contributes to human cytomegalovirus cell tropism. *Proc National Acad Sci*. 112(14):4471–76

51. Child SJ, Greninger AL, Geballe AP. 2021. Rapid adaptation to human protein kinase R by a unique genomic rearrangement in rhesus cytomegalovirus. *Plos Pathog*. 17(1):e1009088

52. Aubert M, Boyle NM, Stone D, Stensland L, Huang M-L, et al. 2014. In vitro Inactivation of Latent HSV by Targeted Mutagenesis Using an HSV-specific Homing Endonuclease. *Mol Ther Nucleic Acids*. 3(2):e146

53. Lawrence M, Huber W, Pagès H, Aboyoun P, Carlson M, et al. 2013. Software for Computing and Annotating Genomic Ranges. *Plos Comput Biol*. 9(8):e1003118

54. Team RC. 2019. R: A Language and Environment for Statistical Computing. *R Foundation for Statistical Computing*

55. Dobin A, Davis CA, Schlesinger F, Drenkow J, Zaleski C, et al. 2013. STAR: ultrafast universal RNA-seq aligner. *Bioinformatics*. 29(1):15–21

56. Wang L, Wang S, Li W. 2012. RSeQC: quality control of RNA-seq experiments. *Bioinformatics*. 28(16):2184–85

57. Liao Y, Smyth GK, Shi W. 2014. featureCounts: an efficient general purpose program for assigning sequence reads to genomic features. *Bioinformatics*. 30(7):923–30

58. Robinson MD, McCarthy DJ, Smyth GK. 2010. edgeR: a Bioconductor package for differential expression analysis of digital gene expression data. *Bioinformatics*. 26(1):139–40

59. Quinlan AR, Hall IM. 2010. BEDTools: a flexible suite of utilities for comparing genomic features. *Bioinformatics*. 26(6):841–42

60. Liao Y, Wang J, Jaehnig EJ, Shi Z, Zhang B. 2019. WebGestalt 2019: gene set analysis toolkit with revamped UIs and APIs. *Nucleic Acids Res*. 47(W1):W199–205

61. Atherton TJ, Kerbyson DJ. 1999. Size invariant circle detection. *Image Vision Comput*. 17(11):795–803

7.3 Chapter 3 Literature Cited:

1. Luger K, Mäder AW, Richmond RK, Sargent DF, Richmond TJ. 1997. Crystal structure of the nucleosome core particle at 2.8 Å resolution. *Nature*. 389(6648):251–60

2. Trojer P, Reinberg D. 2007. Facultative Heterochromatin: Is There a Distinctive Molecular Signature? *Mol Cell*. 28(1):1–13

3. Shvedunova M, Akhtar A. 2022. Modulation of cellular processes by histone and non-histone protein acetylation. *Nat. Rev. Mol. Cell Biol.* 23(5):329–49

4. Gehani SS, Agrawal-Singh S, Dietrich N, Christophersen NS, Helin K, Hansen K. 2010. Polycomb Group Protein Displacement and Gene Activation through MSK-Dependent H3K27me3S28 Phosphorylation. *Mol. Cell*. 39(6):886–900

5. Valencia AM, Kadoch C. 2019. Chromatin regulatory mechanisms and therapeutic opportunities in cancer. *Nat. Cell Biol.* 21(2):152–61

6. Gallinari P, Marco SD, Jones P, Pallaoro M, Steinkühler C. 2007. HDACs, histone deacetylation and gene transcription: from molecular biology to cancer therapeutics. *Cell Res.* 17(3):195–211

7. Lee H, Rezai-Zadeh N, Seto E. 2004. Negative Regulation of Histone Deacetylase 8 Activity by Cyclic AMP-Dependent Protein Kinase A. *Mol. Cell. Biol.* 24(2):765–73

8. Seo S, Mathison A, Grzenda A, Podratz J, Calvo E, et al. 2018. Mechanisms Underlying the Regulation of HP1γ by the NGF-PKA Signaling Pathway. *Sci. Rep.* 8(1):15077

9. Schultz DC, Ayyanathan K, Negorev D, Maul GG, Rauscher FJ. 2002. SETDB1: a novel KAP-1-associated histone H3, lysine 9-specific methyltransferase that contributes to HP1mediated silencing of euchromatic genes by KRAB zinc-finger proteins. *Genes Dev.* 16(8):919– 32

10. Seki Y, Kurisaki A, Watanabe-Susaki K, Nakajima Y, Nakanishi M, et al. 2010. TIF1β regulates the pluripotency of embryonic stem cells in a phosphorylation-dependent manner. *Proc. Natl. Acad. Sci.* 107(24):10926–31

11. Bronshtein I, Kepten E, Kanter I, Berezin S, Lindner M, et al. 2015. Loss of lamin A function increases chromatin dynamics in the nuclear interior. *Nat. Commun.* 6(1):8044

12. Chang L, Li M, Shao S, Li C, Ai S, et al. 2020. Nuclear peripheral chromatin-lamin B1 interaction is required for global integrity of chromatin architecture and dynamics in human cells. *Protein Cell*. 13(4):258–80

13. Camps J, Erdos MR, Ried T. 2015. The role of lamin B1 for the maintenance of nuclear structure and function. *Nucleus*. 6(1):8–14

14. Knipe DM, Howley P. 2013. *Fields Virology*. Lippincott Williams & Wilkins

15. Monier K, Armas JCG, Etteldorf S, Ghazal P, Sullivan KF. 2000. Annexation of the interchromosomal space during viral infection. *Nat Cell Biol*. 2(9):661–65

16. Simpson-Holley M, Baines J, Roller R, Knipe DM. 2004. Herpes Simplex Virus 1 U L 31 and U L 34 Gene Products Promote the Late Maturation of Viral Replication Compartments to the Nuclear Periphery. *J Virol*. 78(11):5591–5600

17. Simpson-Holley M, Colgrove RC, Nalepa G, Harper JW, Knipe DM. 2005. Identification and Functional Evaluation of Cellular and Viral Factors Involved in the Alteration of Nuclear Architecture during Herpes Simplex Virus 1 Infection. *J Virol*. 79(20):12840–51

18. Bigalke JM, Heldwein EE. 2015. Nuclear Exodus: Herpesviruses Lead the Way. *Ann Rev Virol*. 3(1):1–23

19. Aho V, Myllys M, Ruokolainen V, Hakanen S, Mäntylä E, et al. 2017. Chromatin organization regulates viral egress dynamics. *Sci Rep-uk*. 7(1):3692

20. Myllys M, Ruokolainen V, Aho V, Smith EA, Hakanen S, et al. 2016. Herpes simplex virus 1 induces egress channels through marginalized host chromatin. *Sci Rep-uk*. 6(1):28844

21. Aho V, Salminen S, Mattola S, Gupta A, Flomm F, et al. 2021. Infection-induced chromatin modifications facilitate translocation of herpes simplex virus capsids to the inner nuclear membrane. *Plos Pathog*. 17(12):e1010132

22. Lewis HC, Kelnhofer-Millevolte LE, Brinkley MR, Arbach HE, Arnold EA, et al. 2023. HSV-1 exploits host heterochromatin for nuclear egress. *J. Cell Biol.* 222(9):e202304106

23. Chang YE, Roizman B. 1993. The product of the UL31 gene of herpes simplex virus 1 is a nuclear phosphoprotein which partitions with the nuclear matrix. *J. Virol.* 67(11):6348–56

24. Ye G-J, Vaughan KT, Vallee RB, Roizman B. 2000. The Herpes Simplex Virus 1 UL34 Protein Interacts with a Cytoplasmic Dynein Intermediate Chain and Targets Nuclear Membrane. *J. Virol.* 74(3):1355–63

25. Fuchs W, Klupp BG, Granzow H, Osterrieder N, Mettenleiter TC. 2002. The Interacting UL31 and UL34 Gene Products of Pseudorabies Virus Are Involved in Egress from the Host Cell Nucleus and Represent Components of Primary Enveloped but Not Mature Virions. *J Virol*. 76(1):364–78

26. Mou F, Forest T, Baines JD. 2007. US3 of Herpes Simplex Virus Type 1 Encodes a Promiscuous Protein Kinase That Phosphorylates and Alters Localization of Lamin A/C in Infected Cells. *J. Virol.* 81(12):6459–70

27. Ryckman BJ, Roller RJ. 2004. Herpes Simplex Virus Type 1 Primary Envelopment: UL34 Protein Modification and the US3-UL34 Catalytic Relationship. *J. Virol.* 78(1):399–412

28. Bjerke SL, Roller RJ. 2006. Roles for herpes simplex virus type 1 UL34 and US3 proteins in disrupting the nuclear lamina during herpes simplex virus type 1 egress. *Virology*. 347(2):261– 76

29. Purves FC, Roizman B. 1992. The UL13 gene of herpes simplex virus 1 encodes the functions for posttranslational processing associated with phosphorylation of the regulatory protein alpha 22. *Proc. Natl. Acad. Sci.* 89(16):7310–14

30. Coulter LJ, Moss HWM, Lang J, McGeoch DJ. 1993. A mutant of herpes simplex virus type 1 in which the UL13 protein kinase gene is disrupted. *J. Gen. Virol.* 74(3):387–95

31. Kato A, Yamamoto M, Ohno T, Tanaka M, Sata T, et al. 2006. Herpes Simplex Virus 1Encoded Protein Kinase UL13 Phosphorylates Viral Us3 Protein Kinase and Regulates Nuclear Localization of Viral Envelopment Factors UL34 and UL31. *J. Virol.* 80(3):1476–86

32. Bahnamiri MM, Roller RJ. 2021. Mechanism of Nuclear Lamina Disruption and the Role of pUS3 in Herpes Simplex Virus 1 Nuclear Egress. *J Virol*. 95(10):

33. Kulej K, Avgousti DC, Sidoli S, Herrmann C, Fera AND, et al. 2017. Time-resolved Global and Chromatin Proteomics during Herpes Simplex Virus Type 1 (HSV-1) Infection*. *Mol Cell Proteomics*. 16(4):S92–107

34. Kato A, Arii J, Shiratori I, Akashi H, Arase H, Kawaguchi Y. 2008. Herpes Simplex Virus 1 Protein Kinase Us3 Phosphorylates Viral Envelope Glycoprotein B and Regulates Its Expression on the Cell Surface. *J. Virol.* 83(1):250–61

35. Xiong R, Rao P, Kim S, Li M, Wen X, Yuan W. 2015. Herpes Simplex Virus 1 US3 Phosphorylates Cellular KIF3A To Downregulate CD1d Expression. *J. Virol.* 89(13):6646–55

36. Kuny CV, Chinchilla K, Culbertson MR, Kalejta RF. 2010. Cyclin-Dependent Kinase-Like Function Is Shared by the Beta- and Gamma- Subset of the Conserved Herpesvirus Protein Kinases. *PLoS Pathog.* 6(9):e1001092

37. Gao C, Chen L, Tang S-B, Long Q-Y, He J-L, et al. 2020. The epigenetic landscapes of histone modifications on HSV-1 genome in human THP-1 cells. *Antivir Res*. 176:104730

38. Francois AK, Rohani A, Loftus M, Dochnal S, Hrit J, et al. 2024. Single-genome analysis reveals a heterogeneous association of the herpes simplex virus genome with H3K27me2 and the reader PHF20L1 following infection of human fibroblasts. *mBio*. 15(4):e03278-23

39. Donaldson JG. 2003. Multiple Roles for Arf6: Sorting, Structuring, and Signaling at the Plasma Membrane*. *J. Biol. Chem.* 278(43):41573–76

40. Fu L, Wang X, Yang Y, Chen M, Kuerban A, et al. 2023. Septin11 promotes hepatocellular carcinoma cell motility by activating RhoA to regulate cytoskeleton and cell adhesion. *Cell Death Dis.* 14(4):280

41. Juaire KD, Lapouge K, Becker MMM, Kotova I, Michelhans M, et al. 2021. Structural and Functional Impact of SRP54 Mutations Causing Severe Congenital Neutropenia. *Structure*. 29(1):15-28.e7

42. Ohta A, Yamauchi Y, Muto Y, Kimura H, Nishiyama Y. 2011. Herpes simplex virus type 1 UL14 tegument protein regulates intracellular compartmentalization of major tegument protein VP16. *Virol. J.* 8(1):365

43. Gao J, Hay TJM, Banfield BW. 2017. The Product of the Herpes Simplex Virus 2 UL16 Gene Is Critical for the Egress of Capsids from the Nuclei of Infected Cells. *J. Virol.* 91(10):10.1128/jvi.00350-17

44. Wang J, Wu K, Ni L, Li C, Peng R, et al. 2023. Effects of US7 and UL56 on Cell-to-Cell Spread of Human Herpes Simplex Virus 1. *Viruses*. 15(11):2256

45. Muradov JH, Finnen RL, Gulak MA, Hay TJM, Banfield BW. 2021. pUL21 regulation of pUs3 kinase activity influences the nature of nuclear envelope deformation by the HSV-2 nuclear egress complex. *PLoS Pathog.* 17(8):e1009679

46. Cliffe AR, Arbuckle JH, Vogel JL, Geden MJ, Rothbart SB, et al. 2015. Neuronal Stress Pathway Mediating a Histone Methyl/Phospho Switch Is Required for Herpes Simplex Virus Reactivation. *Cell Host Microbe*. 18(6):649–58

47. Bonito-Oliva A, Södersten E, Spigolon G, Hu X, Hellysaz A, et al. 2016. Differential regulation of the phosphorylation of Trimethyl-lysine27 histone H3 at serine 28 in distinct populations of striatal projection neurons. *Neuropharmacology*. 107:89–99

48. Palomer E, Carretero J, Benvegnù S, Dotti CG, Martin MG. 2016. Neuronal activity controls Bdnf expression via Polycomb de-repression and CREB/CBP/JMJD3 activation in mature neurons. *Nat. Commun.* 7(1):11081

49. Klopfleisch R, Klupp BG, Fuchs W, Kopp M, Teifke JP, Mettenleiter TC. 2006. Influence of Pseudorabies Virus Proteins on Neuroinvasion and Neurovirulence in Mice. *J. Virol.* 80(11):5571–76

50. Arbuckle JH, Gardina PJ, Gordon DN, Hickman HD, Yewdell JW, et al. 2017. Inhibitors of the Histone Methyltransferases EZH2/1 Induce a Potent Antiviral State and Suppress Infection by Diverse Viral Pathogens. *Mbio*. 8(4):e01141-17

7.4 Chapter 4 Literature Cited:

1. Cannon MJ, Schmid DS, Hyde TB. 2010. Review of cytomegalovirus seroprevalence and demographic characteristics associated with infection. Rev. Méd. Virol. 20(4):202–13

2. Fowler K, Mucha J, Neumann M, Lewandowski W, Kaczanowska M, et al. 2022. A systematic literature review of the global seroprevalence of cytomegalovirus: possible implications for treatment, screening, and vaccine development. BMC Public Heal. 22(1):1659

3. Zanghellini F, Boppana SB, Emery VC, Griffiths PD, Pass RF. 1999. Asymptomatic Primary Cytomegalovirus Infection: Virologic and Immunologic Features. J. Infect. Dis. 180(3):702–7

4. Manicklal S, Emery VC, Lazzarotto T, Boppana SB, Gupta RK. 2013. The “Silent” Global Burden of Congenital Cytomegalovirus. *Clin Microbiol Rev*. 26(1):86–102
5. Azevedo LS, Pierrotti LC, Abdala E, Costa SF, Strabelli TMV, et al. 2015. Cytomegalovirus infection in transplant recipients. *Clinics*. 70(7):515–23

6. Christensen-Quick A, Vanpouille C, Lisco A, Gianella S. 2017. Cytomegalovirus and HIV Persistence: Pouring Gas on the Fire. *AIDS Res. Hum. Retroviruses*. 33(S1):S-23-S-30

7. Alwine JC. 2012. The Human Cytomegalovirus Assembly Compartment: A Masterpiece of Viral Manipulation of Cellular Processes That Facilitates Assembly and Egress. *Plos Pathog*. 8(9):e1002878

8. Procter DJ, Furey C, Garza-Gongora AG, Kosak ST, Walsh D. 2020. Cytoplasmic control of intranuclear polarity by human cytomegalovirus. *Nature*. 587(7832):109–14

9. Procter DJ, Banerjee A, Nukui M, Kruse K, Gaponenko V, et al. 2018. The HCMV Assembly Compartment Is a Dynamic Golgi-Derived MTOC that Controls Nuclear Rotation and Virus Spread. *Dev Cell*. 45(1):83-100.e7

10. Tandon R, Mocarski ES. 2012. Viral and host control of cytomegalovirus maturation. *Trends Microbiol*. 20(8):392–401

11. Severi B, Landini MP, Govoni E. 1988. Human Cytomegalovirus morphogenesis: an ultrastructural study of the late cytoplasmic phases. *Arch. Virol.* 98(1–2):51–64

12. Pignatelli S, Monte PD, Landini MP, Severi B, Nassiri R, et al. 2007. Cytomegalovirus Primary Envelopment at Large Nuclear Membrane Infoldings: What’s New? *J Virol*. 81(13):7320–22

13. Tooze J, Hollinshead M, Reis B, Radsak K, Kern H. 1993. Progeny vaccinia and human cytomegalovirus particles utilize early endosomal cisternae for their envelopes. *Eur. J. cell Biol.* 60(1):163–78

14. Walsh D, Perez C, Notary J, Mohr I. 2005. Regulation of the Translation Initiation Factor eIF4F by Multiple Mechanisms in Human Cytomegalovirus-Infected Cells. *J. Virol.* 79(13):8057– 64

15. Jenuwein T, Allis CD. 2001. Translating the Histone Code. *Science*. 293(5532):1074–80

16. Lee J-S, Smith E, Shilatifard A. 2010. The Language of Histone Crosstalk. *Cell*. 142(5):682– 85

17. Talbert PB, Henikoff S. 2021. Histone variants at a glance. *J. Cell Sci.* 134(6):jcs244749

18. Costanzi C, Pehrson JR. 1998. Histone macroH2A1 is concentrated in the inactive X chromosome of female mammals. *Nature*. 393(6685):599–601

19. Gamble MJ, Frizzell KM, Yang C, Krishnakumar R, Kraus WL. 2010. The histone variant macroH2A1 marks repressed autosomal chromatin, but protects a subset of its target genes from silencing. *Gene Dev*. 24(1):21–32

20. Dell'Orso S, Wang AH, Shih H-Y, Saso K, Berghella L, et al. 2016. The Histone Variant MacroH2A1.2 Is Necessary for the Activation of Muscle Enhancers and Recruitment of the Transcription Factor Pbx1. *Cell Rep.* 14(5):1156–68

21. Ma H, Su L, Xia W, Wang W, Tan G, Jiao J. 2021. MacroH2A1.2 deficiency leads to neural stem cell differentiation defects and autism-like behaviors. *EMBO Rep.* 22(7):e52150

22. Lewis HC, Kelnhofer-Millevolte LE, Brinkley MR, Arbach HE, Arnold EA, et al. 2023. HSV-1 exploits host heterochromatin for nuclear egress. *J. Cell Biol.* 222(9):e202304106

23. Albright ER, Morrison K, Ranganathan P, Carter DM, Nishikiori M, et al. 2022. Human cytomegalovirus lytic infection inhibits replication-dependent histone synthesis and requires stem loop binding protein function. *Proc. Natl. Acad. Sci.* 119(14):e2122174119

24. Craighead JE, Kanich RE, Almeida JD. 1972. Nonviral Microbodies with Viral Antigenicity Produced in Cytomegalovirus-Infected Cells. *J. Virol.* 10(4):766–75

25. Pepperl S, Münster J, Mach M, Harris JR, Plachter B. 2000. Dense Bodies of Human Cytomegalovirus Induce both Humoral and Cellular Immune Responses in the Absence of Viral Gene Expression. *J. Virol.* 74(13):6132–46

26. Büscher N, Paulus C, Nevels M, Tenzer S, Plachter B. 2015. The proteome of human cytomegalovirus virions and dense bodies is conserved across different strains. *Méd. Microbiol. Immunol.* 204(3):285–93

27. Dunham I, Kundaje A, Aldred SF, Collins PJ, Davis CA, et al. 2012. An integrated encyclopedia of DNA elements in the human genome. *Nature*. 489(7414):57–74

28. Luo Y, Hitz BC, Gabdank I, Hilton JA, Kagda MS, et al. 2019. New developments on the Encyclopedia of DNA Elements (ENCODE) data portal. *Nucleic Acids Res.* 48(D1):D882–89

29. Lue JK, Amengual JE. 2018. Emerging EZH2 Inhibitors and Their Application in Lymphoma. *Curr Hematol Malig R*. 13(5):369–82

30. Kondo M, Takei Y, Hirokawa N. 2012. Motor Protein KIF1A Is Essential for Hippocampal Synaptogenesis and Learning Enhancement in an Enriched Environment. *Neuron*. 73(4):743– 57

31. Mücke K, Paulus C, Bernhardt K, Gerrer K, Schön K, et al. 2014. Human Cytomegalovirus Major Immediate Early 1 Protein Targets Host Chromosomes by Docking to the Acidic Pocket on the Nucleosome Surface. *J Virol*. 88(2):1228–48

32. Chakravarthy S, Gundimella SKY, Caron C, Perche P-Y, Pehrson JR, et al. 2005. Structural Characterization of the Histone Variant macroH2A. *Mol Cell Biol*. 25(17):7616–24

33. Knoblach T, Grandel B, Seiler J, Nevels M, Paulus C. 2011. Human Cytomegalovirus IE1 Protein Elicits a Type II Interferon-Like Host Cell Response That Depends on Activated STAT1 but Not Interferon-γ. *PLoS Pathog.* 7(4):e1002016

34. Nitzsche A, Paulus C, Nevels M. 2008. Temporal Dynamics of Cytomegalovirus Chromatin Assembly in Productively Infected Human Cells. *J Virol*. 82(22):11167–80

35. Luger K, Mäder AW, Richmond RK, Sargent DF, Richmond TJ. 1997. Crystal structure of the nucleosome core particle at 2.8 Å resolution. *Nature*. 389(6648):251–60

36. White S, Kawano H, Harata NC, Roller RJ. 2020. Herpes Simplex Virus Organizes Cytoplasmic Membranes To Form a Viral Assembly Center in Neuronal Cells. *J. Virol.* 94(19):

37. Scherer J, Hogue IB, Yaffe ZA, Tanneti NS, Winer BY, et al. 2020. A kinesin-3 recruitment complex facilitates axonal sorting of enveloped alpha herpesvirus capsids. *PLoS Pathog.* 16(1):e1007985

38. Guberovic I, Farkas M, Corujo D, Buschbeck M. 2023. Evolution, structure and function of divergent macroH2A1 splice isoforms. *Semin. Cell Dev. Biol.* 135:43–49

39. Baasch S, Giansanti P, Kolter J, Riedl A, Forde AJ, et al. 2021. Cytomegalovirus subverts macrophage identity. *Cell*. 184(14):3774-3793.e25

40. Liu STH, Sharon-Friling R, Ivanova P, Milne SB, Myers DS, et al. 2011. Synaptic vesicle-like lipidome of human cytomegalovirus virions reveals a role for SNARE machinery in virion egress. *Proc. Natl. Acad. Sci.* 108(31):12869–74

41. Martin TFJ. 2003. Tuning exocytosis for speed: fast and slow modes. *Biochim. Biophys. Acta (BBA) - Mol. Cell Res.* 1641(2–3):157–65

42. Pastuzyn ED, Day CE, Kearns RB, Kyrke-Smith M, Taibi AV, et al. 2018. The Neuronal Gene Arc Encodes a Repurposed Retrotransposon Gag Protein that Mediates Intercellular RNA Transfer. *Cell*. 172(1–2):275-288.e18

43. Finkel Y, Nachshon A, Aharon E, Arazi T, Simonovsky E, et al. 2024. A virally encoded highresolution screen of cytomegalovirus dependencies. *Nature*, pp. 1–8

44. Moreno I, Rodríguez-Sánchez I, Schafer X, Munger J. 2022. Human cytomegalovirus induces neuronal enolase to support virally mediated metabolic remodeling. *Proc. Natl. Acad. Sci.* 119(49):e2205789119

45. Lane-Donovan C, Herz J. 2017. ApoE, ApoE Receptors, and the Synapse in Alzheimer's Disease. *Trends Endocrinol. Metab.* 28(4):273–84

46. Dumanis SB, DiBattista AM, Miessau M, Moussa CEH, Rebeck GW. 2013. APOE genotype affects the pre-synaptic compartment of glutamatergic nerve terminals. *J. Neurochem.* 124(1):4–14

47. DeChiara TM, Vejsada R, Poueymirou WT, Acheson A, Suri C, et al. 1995. Mice lacking the CNTF receptor, unlike mice lacking CNTF, exhibit profound motor neuron deficits at birth. *Cell*. 83(2):313–22

48. Groffen AJ, Martens S, Arazola RD, Cornelisse LN, Lozovaya N, et al. 2010. Doc2b Is a High-Affinity Ca2+ Sensor for Spontaneous Neurotransmitter Release. *Science*. 327(5973):1614–18

49. Sala K, Corbetta A, Minici C, Tonoli D, Murray DH, et al. 2019. The ERC1 scaffold protein implicated in cell motility drives the assembly of a liquid phase. *Sci. Rep.* 9(1):13530

50. Lucas TM, Richner JM, Diamond MS. 2016. The Interferon-Stimulated Gene Ifi27l2a Restricts West Nile Virus Infection and Pathogenesis in a Cell-Type- and Region-Specific Manner. *J. Virol.* 90(5):2600–2615

51. Ichikawa-Tomikawa N, Ogawa J, Douet V, Xu Z, Kamikubo Y, et al. 2012. Laminin α1 is essential for mouse cerebellar development. *Matrix Biol.* 31(1):17–28

52. Flanagan LA, Rebaza LM, Derzic S, Schwartz PH, Monuki ES. 2006. Regulation of human neural precursor cells by laminin and integrins. *J. Neurosci. Res.* 83(5):845–56

53. Kim S, Burette A, Chung HS, Kwon S-K, Woo J, et al. 2006. NGL family PSD-95–interacting adhesion molecules regulate excitatory synapse formation. *Nat. Neurosci.* 9(10):1294–1301

54. Liu Y, Xu X-H, Chen Q, Wang T, Deng C-Y, et al. 2013. Myosin Vb controls biogenesis of post-Golgi Rab10 carriers during axon development. *Nat. Commun.* 4(1):2005

55. Chang MC, Park JM, Pelkey KA, Grabenstatter HL, Xu D, et al. 2010. Narp regulates homeostatic scaling of excitatory synapses on parvalbumin-expressing interneurons. *Nat. Neurosci.* 13(9):1090–97

56. Bergsland M, Werme M, Malewicz M, Perlmann T, Muhr J. 2006. The establishment of neuronal properties is controlled by Sox4 and Sox11. *Genes Dev.* 20(24):3475–86

57. Ji Z, Li H, Yang Z, Huang X, Ke X, et al. 2019. Kibra Modulates Learning and Memory via Binding to Dendrin. *Cell Rep.* 26(8):2064-2077.e7

58. Lynch KL, Dillon MR, Bat-Erdene M, Lewis HC, Kaai RJ, et al. 2021. A viral histone-like protein exploits antagonism between linker histones and HMGB proteins to obstruct the cell cycle. *Curr. Biol.* 31(23):5227-5237.e7

59. Kemble G, Duke G, Winter R, Spaete R. 1996. Defined large-scale alterations of the human cytomegalovirus genome constructed by cotransfection of overlapping cosmids. *J. Virol.* 70(3):2044–48

60. Marchini A, Liu H, Zhu H. 2001. Human Cytomegalovirus with IE-2 (UL122) Deleted Fails To Express Early Lytic Genes. *J. Virol.* 75(4):1870–78

61. Sampaio KL, Cavignac Y, Stierhof Y-D, Sinzger C. 2005. Human Cytomegalovirus Labeled with Green Fluorescent Protein for Live Analysis of Intracellular Particle Movements. *J Virol*. 79(5):2754–67

62. Kim ET, Roche KL, Kulej K, Spruce LA, Seeholzer SH, et al. 2019. SAMHD1 Modulates Early Steps during Human Cytomegalovirus Infection by Limiting NF-κB Activation. *Cell Rep.* 28(2):434-448.e6

63. Murphy E, Yu D, Grimwood J, Schmutz J, Dickson M, et al. 2003. Coding potential of laboratory and clinical strains of human cytomegalovirus. *Proc. Natl. Acad. Sci.* 100(25):14976– 81

64. Patro R, Duggal G, Love MI, Irizarry RA, Kingsford C. 2017. Salmon provides fast and biasaware quantification of transcript expression. *Nat. Methods*. 14(4):417–19

65. Love MI, Huber W, Anders S. 2014. Moderated estimation of fold change and dispersion for RNA-seq data with DESeq2. *Genome Biol.* 15(12):550

66. Liao Y, Wang J, Jaehnig EJ, Shi Z, Zhang B. 2019. WebGestalt 2019: gene set analysis toolkit with revamped UIs and APIs. *Nucleic Acids Res.* 47(W1):W199–205

67. Lee E-G, Tulloch J, Chen S, Leong L, Saxton AD, et al. 2020. Redefining transcriptional regulation of the APOE gene and its association with Alzheimer's disease. *PLoS ONE*. 15(1):e0227667

68. Arend KC, Ziehr B, Vincent HA, Moorman NJ. 2016. Multiple Transcripts Encode FullLength Human Cytomegalovirus IE1 and IE2 Proteins during Lytic Infection. *J. Virol.* 90(19):8855–65

7.5 Chapter 5 Literature Cited:

1. Samies NL, James SH. 2020. Prevention and treatment of neonatal herpes simplex virus infection. *Antivir. Res.* 176:104721

2. Azevedo LS, Pierrotti LC, Abdala E, Costa SF, Strabelli TMV, et al. 2015. Cytomegalovirus infection in transplant recipients. *Clinics*. 70(7):515–23

3. Kotton CN, Kumar D, Caliendo AM, Huprikar S, Chou S, et al. 2018. The Third International Consensus Guidelines on the Management of Cytomegalovirus in Solid-organ Transplantation. *Transplantation*. 102(6):900–931

4. Pei Y, Wong JH, Robertson ES. 2020. Herpesvirus Epigenetic Reprogramming and Oncogenesis. *Annu. Rev. Virol.* 7(1):309–31

5. Sayers RG. 2017. Associations between exposure to bovine herpesvirus 1 (BoHV-1) and milk production, reproductive performance, and mortality in Irish dairy herds. *J. Dairy Sci.* 100(2):1340–52

6. Liu Q, Kuang Y, Li Y, Guo H, Zhou C, et al. 2022. The Epidemiology and Variation in Pseudorabies Virus: A Continuing Challenge to Pigs and Humans. *Viruses*. 14(7):1463

7. Davidson I. 2020. Out of Sight, but Not Out of Mind: Aspects of the Avian Oncogenic Herpesvirus, Marek's Disease Virus. *Animals*. 10(8):1319
8. Klafack S, Schröder L, Jin Y, Lenk M, Lee P-Y, et al. 2022. Development of an attenuated vaccine against Koi Herpesvirus Disease (KHVD) suitable for oral administration and immersion. *npj Vaccines*. 7(1):106

9. Renault T, Bouquet AL, Maurice J-T, Lupo C, Blachier P. 2014. Ostreid Herpesvirus 1 Infection among Pacific Oyster (Crassostrea gigas) Spat: Relevance of Water Temperature to Virus Replication and Circulation Prior to the Onset of Mortality. *Appl. Environ. Microbiol.* 80(17):5419–26

10. Knipe DM, Howley P. 2013. *Fields Virology*. Lippincott Williams & Wilkins

11. Kłysik K, Pietraszek A, Nowakowska M, Karewicz A. 2018. Acyclovir in the Treatment of Herpes Viruses – A Review. *Curr. Med. Chem.* 27(24):4118–37

12. Oudelaar AM, Higgs DR. 2021. The relationship between genome structure and function. *Nat. Rev. Genet.* 22(3):154–68

13. Hennig T, Michalski M, Rutkowski AJ, Djakovic L, Whisnant AW, et al. 2018. HSV-1-induced disruption of transcription termination resembles a cellular stress response but selectively increases chromatin accessibility downstream of genes. *Plos Pathog*. 14(3):e1006954

14. Finan JD, Guilak F. 2010. The effects of osmotic stress on the structure and function of the cell nucleus. *J. Cell. Biochem.* 109(3):460–67

15. Jain N, Iyer KV, Kumar A, Shivashankar GV. 2013. Cell geometric constraints induce modular gene-expression patterns via redistribution of HDAC3 regulated by actomyosin contractility. *Proc. Natl. Acad. Sci.* 110(28):11349–54

16. Kirby TJ, Lammerding J. 2018. Emerging views of the nucleus as a cellular mechanosensor. *Nat. Cell Biol.* 20(4):373–81

17. Lope-Planelles A de, González-Novo R, Madrazo E, Peralta-Carrero G, Rodríguez MPC, et al. 2023. Mechanical stress confers nuclear and functional changes in derived leukemia cells from persistent confined migration. *Cell. Mol. Life Sci.* 80(11):316

18. Mou F, Wills EG, Park R, Baines JD. 2008. Effects of Lamin A/C, Lamin B1, and Viral US3 Kinase Activity on Viral Infectivity, Virion Egress, and the Targeting of Herpes Simplex Virus UL34-Encoded Protein to the Inner Nuclear Membrane. *J. Virol.* 82(16):8094–8104

19. Leach N, Bjerke SL, Christensen DK, Bouchard JM, Mou F, et al. 2007. Emerin Is Hyperphosphorylated and Redistributed in Herpes Simplex Virus Type 1-Infected Cells in a Manner Dependent on both UL34 and US3. *J Virol*. 81(19):10792–803

20. Kato A, Arii J, Shiratori I, Akashi H, Arase H, Kawaguchi Y. 2008. Herpes Simplex Virus 1 Protein Kinase Us3 Phosphorylates Viral Envelope Glycoprotein B and Regulates Its Expression on the Cell Surface. *J. Virol.* 83(1):250–61

21. Xiong R, Rao P, Kim S, Li M, Wen X, Yuan W. 2015. Herpes Simplex Virus 1 US3 Phosphorylates Cellular KIF3A To Downregulate CD1d Expression. *J. Virol.* 89(13):6646–55

22. Morris JB, Hofemeister H, O'Hare P. 2007. Herpes Simplex Virus Infection Induces Phosphorylation and Delocalization of Emerin, a Key Inner Nuclear Membrane Protein. *J Virol*. 81(9):4429–37

23. Gershburg S, Geltz J, Peterson KE, Halford WP, Gershburg E. 2015. The UL13 and US3 Protein Kinases of Herpes Simplex Virus 1 Cooperate to Promote the Assembly and Release of Mature, Infectious Virions. *PLoS ONE*. 10(6):e0131420

24. Mou F, Forest T, Baines JD. 2007. US3 of Herpes Simplex Virus Type 1 Encodes a Promiscuous Protein Kinase That Phosphorylates and Alters Localization of Lamin A/C in Infected Cells. *J. Virol.* 81(12):6459–70

25. Morimoto T, Arii J, Tanaka M, Sata T, Akashi H, et al. 2009. Differences in the Regulatory and Functional Effects of the Us3 Protein Kinase Activities of Herpes Simplex Virus 1 and 2. *J. Virol.* 83(22):11624–34

26. Poon APW, Benetti L, Roizman B. 2006. US3 and US3.5 Protein Kinases of Herpes Simplex Virus 1 Differ with Respect to Their Functions in Blocking Apoptosis and in Virion Maturation and Egress. *J. Virol.* 80(8):3752–64

27. Poon APW, Gu H, Roizman B. 2006. ICP0 and the US3 protein kinase of herpes simplex virus 1 independently block histone deacetylation to enable gene expression. *Proc. Natl. Acad. Sci.* 103(26):9993–98

28. Poon APW, Liang Y, Roizman B. 2003. Herpes Simplex Virus 1 Gene Expression Is Accelerated by Inhibitors of Histone Deacetylases in Rabbit Skin Cells Infected with a Mutant Carrying a cDNA Copy of the Infected-Cell Protein No. 0. *J. Virol.* 77(23):12671–78

29. Capozzo I, Iannelli F, Francia S, Fagagna F d'Adda di. 2017. Express or repress? The transcriptional dilemma of damaged chromatin. *FEBS J.* 284(14):2133–47

30. Adam S, Polo SE. 2014. Blurring the line between the DNA damage response and transcription: The importance of chromatin dynamics. *Exp. Cell Res.* 329(1):148–53

31. Friedel CC, Whisnant AW, Djakovic L, Rutkowski AJ, Friedl M-S, et al. 2020. Dissecting Herpes Simplex Virus 1-Induced Host Shutoff at the RNA Level. *J. Virol.* 95(3):10.1128/jvi.01399-20

32. Skene PJ, Henikoff S. 2017. An efficient targeted nuclease strategy for high-resolution mapping of DNA binding sites. *eLife*. 6:e21856

33. Knoblach T, Grandel B, Seiler J, Nevels M, Paulus C. 2011. Human Cytomegalovirus IE1 Protein Elicits a Type II Interferon-Like Host Cell Response That Depends on Activated STAT1 but Not Interferon-γ. *PLoS Pathog.* 7(4):e1002016

34. Nevels M, Paulus C, Shenk T. 2004. Human cytomegalovirus immediate-early 1 protein facilitates viral replication by antagonizing histone deacetylation. *Proc. Natl. Acad. Sci.* 101(49):17234–39

35. Mücke K, Paulus C, Bernhardt K, Gerrer K, Schön K, et al. 2014. Human Cytomegalovirus Major Immediate Early 1 Protein Targets Host Chromosomes by Docking to the Acidic Pocket on the Nucleosome Surface. *J Virol*. 88(2):1228–48

36. Fang Q, Chen P, Wang M, Fang J, Yang N, et al. 2016. Human cytomegalovirus IE1 protein alters the higher-order chromatin structure by targeting the acidic patch of the nucleosome. *eLife*. 5:e11911

37. Procter DJ, Furey C, Garza-Gongora AG, Kosak ST, Walsh D. 2020. Cytoplasmic control of intranuclear polarity by human cytomegalovirus. *Nature*. 587(7832):109–14

38. Belton J-M, McCord RP, Gibcus JH, Naumova N, Zhan Y, Dekker J. 2012. Hi–C: A comprehensive technique to capture the conformation of genomes. *Methods*. 58(3):268–76

39. STRUNK KM, WANG K, KE D, GRAY JL, ZHANG P. 2012. Thinning of large mammalian cells for cryo-TEM characterization by cryo-FIB milling. *J. Microsc.* 247(3):220–27

40. Gamble MJ, Frizzell KM, Yang C, Krishnakumar R, Kraus WL. 2010. The histone variant macroH2A1 marks repressed autosomal chromatin, but protects a subset of its target genes from silencing. *Gene Dev*. 24(1):21–32

41. Ruiz PD, Gamble MJ. 2018. MacroH2A1 chromatin specification requires its docking domain and acetylation of H2B lysine 20. *Nat. Commun.* 9(1):5143

42. Gaspar-Maia A, Qadeer ZA, Hasson D, Ratnakumar K, Leu NA, et al. 2013. MacroH2A histone variants act as a barrier upon reprogramming towards pluripotency. *Nat. Commun.* 4(1):1565

43. Cai Y, Zhang Y, Loh YP, Tng JQ, Lim MC, et al. 2021. H3K27me3-rich genomic regions can function as silencers to repress gene expression via chromatin interactions. *Nat. Commun.* 12(1):719

44. Douet J, Corujo D, Malinverni R, Renauld J, Sansoni V, et al. 2017. MacroH2A histone variants maintain nuclear organization and heterochromatin architecture. *J Cell Sci*. 130(9):1570–82

45. Evilevitch A, Hohlbauch SV. 2022. Intranuclear HSV-1 DNA ejection induces major mechanical transformations suggesting mechanoprotection of nucleus integrity. *Proc National Acad Sci*. 119(9):e2114121119

46. Veronezi GMB, Ramachandran S. 2024. Nucleation and spreading maintain Polycomb domains every cell cycle. *Cell Rep.* 43(4):114090

47. D'Urso A, Brickner JH. 2017. Epigenetic transcriptional memory. *Curr. Genet.* 63(3):435–39

48. Shumaker DK, Dechat T, Kohlmaier A, Adam SA, Bozovsky MR, et al. 2006. Mutant nuclear lamin A leads to progressive alterations of epigenetic control in premature aging. *Proc. Natl. Acad. Sci.* 103(23):8703–8

49. Bender S, Tang Y, Lindroth AM, Hovestadt V, Jones DTW, et al. 2013. Reduced H3K27me3 and DNA Hypomethylation Are Major Drivers of Gene Expression in K27M Mutant Pediatric High-Grade Gliomas. *Cancer Cell*. 24(5):660–72

50. Mettenleiter TC. 2002. Herpesvirus Assembly and Egress. *J. Virol.* 76(4):1537–47

51. Bigalke JM, Heldwein EE. 2015. Nuclear Exodus: Herpesviruses Lead the Way. *Ann Rev Virol*. 3(1):1–23

52. Roller RJ, Johnson DC. 2021. Herpesvirus Nuclear Egress across the Outer Nuclear Membrane. *Viruses*. 13(12):2356

53. Klupp BG, Mettenleiter TC. 2023. The Knowns and Unknowns of Herpesvirus Nuclear Egress. *Annu. Rev. Virol.* 10(1):305–23

54. Davison AJ. 2002. Evolution of the herpesviruses. *Vet. Microbiol.* 86(1–2):69–88

55. McGeoch DJ, Cook S, Dolan A, Jamieson FE, Telford EAR. 1995. Molecular Phylogeny and Evolutionary Timescale for the Family of Mammalian Herpesviruses. *J. Mol. Biol.* 247(3):443–58

56. Wertheim JO, Smith MD, Smith DM, Scheffler K, Pond SLK. 2014. Evolutionary Origins of Human Herpes Simplex Viruses 1 and 2. *Mol. Biol. Evol.* 31(9):2356–64

57. Guellil M, Dorp L van, Inskip SA, Dittmar JM, Saag L, et al. 2022. Ancient herpes simplex 1 genomes reveal recent viral structure in Eurasia. *Sci. Adv.* 8(30):eabo4435

58. Soh TK, Ognibene S, Sanders S, Schäper R, Kaufer BB, Bosse JB. 2024. A proteome-wide structural systems approach reveals insights into protein families of all human herpesviruses. *bioRxiv*. 2024.07.16.603793

59. Klupp BG, Granzow H, Mettenleiter TC. 2001. Effect of the pseudorabies virus US3 protein on nuclear membrane localization of the UL34 protein and virus egress from the nucleus. *J. Gen. Virol.* 82(10):2363–71

60. Buser C, Walther P, Mertens T, Michel D. 2007. Cytomegalovirus Primary Envelopment Occurs at Large Infoldings of the Inner Nuclear Membrane. *J Virol*. 81(6):3042–48

61. Pignatelli S, Monte PD, Landini MP, Severi B, Nassiri R, et al. 2007. Cytomegalovirus Primary Envelopment at Large Nuclear Membrane Infoldings: What's New? *J Virol*. 81(13):7320–22
62. Alwine JC. 2012. The Human Cytomegalovirus Assembly Compartment: A Masterpiece of Viral Manipulation of Cellular Processes That Facilitates Assembly and Egress. *Plos Pathog*. 8(9):e1002878

63. White S, Kawano H, Harata NC, Roller RJ. 2020. Herpes Simplex Virus Organizes Cytoplasmic Membranes To Form a Viral Assembly Center in Neuronal Cells. *J. Virol.* 94(19):

64. White S, Roller R. 2024. Herpes simplex virus type-1 cVAC formation in neuronal cells is mediated by dynein motor function and glycoprotein retrieval from the plasma membrane. *J. Virol.* 98(7):e00713-24

65. Liu STH, Sharon-Friling R, Ivanova P, Milne SB, Myers DS, et al. 2011. Synaptic vesicle-like lipidome of human cytomegalovirus virions reveals a role for SNARE machinery in virion egress. *Proc. Natl. Acad. Sci.* 108(31):12869–74

66. Ma H, Su L, Xia W, Wang W, Tan G, Jiao J. 2021. MacroH2A1.2 deficiency leads to neural stem cell differentiation defects and autism-like behaviors. *EMBO Rep.* 22(7):e52150

67. Baasch S, Giansanti P, Kolter J, Riedl A, Forde AJ, et al. 2021. Cytomegalovirus subverts macrophage identity. *Cell*. 184(14):3774-3793.e25

68. Plikus MV, Wang X, Sinha S, Forte E, Thompson SM, et al. 2021. Fibroblasts: Origins, definitions, and functions in health and disease. *Cell*. 184(15):3852–72

69. Kiecker C, Bates T, Bell E. 2016. Molecular specification of germ layers in vertebrate embryos. *Cell. Mol. Life Sci.* 73(5):923–47

70. Salomè S, Corrado FR, Mazzarelli LL, Maruotti GM, Capasso L, et al. 2023. Congenital cytomegalovirus infection: the state of the art and future perspectives. *Front. Pediatr.* 11:1276912

71. Rosso SB, Inestrosa NC. 2013. WNT signaling in neuronal maturation and synaptogenesis. *Front. Cell. Neurosci.* 7:103

72. Inestrosa NC, Varela-Nallar L. 2015. Wnt signalling in neuronal differentiation and development. *Cell Tissue Res.* 359(1):215–23

73. Roark HK, Jenks JA, Permar SR, Schleiss MR. 2020. Animal Models of Congenital Cytomegalovirus Transmission: Implications for Vaccine Development. *J. Infect. Dis.* 221(Supplement_1):S60–73

74. Zhou Y-P, Mei M-J, Wang X-Z, Huang S-N, Chen L, et al. 2022. A congenital CMV infection model for follow-up studies of neurodevelopmental disorders, neuroimaging abnormalities, and treatment. *JCI Insight*. 7(1):e152551

75. Nichol JN, Dupéré-Richer D, Ezponda T, Licht JD, Miller WH. 2016. Chapter Three H3K27 Methylation A Focal Point of Epigenetic Deregulation in Cancer. *Adv. Cancer Res.* 131:59–95

76. Mullard A. 2020. FDA approves an inhibitor of a novel 'epigenetic writer.' *Nat. Rev. Drug Discov.* 19(3):156–156

77. Dou F, Tian Z, Yang X, Li J, Wang R, Gao J. 2022. Valemetostat: First approval as a dual inhibitor of EZH1/2 to treat adult T-cell leukemia/lymphoma. *Drug Discov. Ther.* 16(6):297–99

78. Klopfleisch R, Klupp BG, Fuchs W, Kopp M, Teifke JP, Mettenleiter TC. 2006. Influence of Pseudorabies Virus Proteins on Neuroinvasion and Neurovirulence in Mice. *J. Virol.* 80(11):5571–76

79. Olsen LM, Ch'ng TH, Card JP, Enquist LW. 2006. Role of Pseudorabies Virus Us3 Protein Kinase during Neuronal Infection. *J. Virol.* 80(13):6387–98

80. Arbuckle JH, Gardina PJ, Gordon DN, Hickman HD, Yewdell JW, et al. 2017. Inhibitors of the Histone Methyltransferases EZH2/1 Induce a Potent Antiviral State and Suppress Infection by Diverse Viral Pathogens. *Mbio*. 8(4):e01141-17

81. Hsu C-J, Meers O, Buschbeck M, Heidel FH. 2021. The Role of MacroH2A Histone Variants in Cancer. *Cancers*. 13(12):3003

82. Hurtado-Bagès S, Guberovic I, Buschbeck M. 2018. The MacroH2A1.1 – PARP1 Axis at the Intersection Between Stress Response and Metabolism. *Front. Genet.* 9:417

83. Guberovic I, Farkas M, Corujo D, Buschbeck M. 2023. Evolution, structure and function of divergent macroH2A1 splice isoforms. *Semin. Cell Dev. Biol.* 135:43–49

84. Abramson J, Adler J, Dunger J, Evans R, Green T, et al. 2024. Accurate structure prediction of biomolecular interactions with AlphaFold 3. *Nature*. 630(8016):493–500